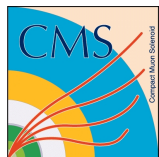

2 **Consolidation and longevity studies on CMS**
3 **Resistive Plate Chamber system in the context**
4 **of upgrade of CMS Muon System towards High**
5 **Luminosity LHC**

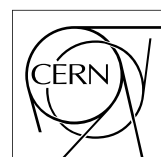
6

Alexis Fagot

7



Thesis to obtain the degree of
Doctor of Philosophy in Physics
Academic years 2012-2018





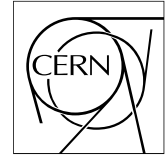
Universiteit Gent
Faculteit Wetenschappen
Vakgroep Fysica en Sterrenkunde

⁹ Promotoren: Dr. Michael Tytgat
Prof. Dr. Dirk Ryckbosch

¹⁰ Universiteit Gent
¹¹ Faculteit Wetenschappen
¹² Vakgroep Fysica en Sterrenkunde
¹³ Proeftuinstraat 86, B-9000 Gent, België
¹⁴ Tel.: +32 9 264.65.28
¹⁵ Fax.: +32 9 264.66.97



Thesis to obtain the degree of
Doctor of Philosophy in Physics
Academic years 2012-2018



Acknowledgements

¹⁸ Ici on remerciera tous les gens que j'ai pu croiser durant cette aventure et qui m'ont permis de
¹⁹ passer un bon moment

Gent, ici la super date de la mort qui tue de la fin d'écriture
21 *Alexis Fagot*

Table of Contents

23	Acknowledgements	i
24	Nederlandse samenvatting	vii
25	English summary	ix
26	1 Introduction	1-1
27	2 Investigating the TeV scale	2-1
28	2.1 The Standard Model of Particle Physics	2-2
29	2.1.1 A history of particle physics	2-2
30	2.1.2 Construction and test of the model	2-11
31	2.1.3 Investigating the TeV scale	2-12
32	2.2 The Large Hadron Collider & the Compact Muon Solenoid	2-14
33	2.2.1 LHC, the most powerful particle accelerator	2-14
34	2.2.1.1 Particle acceleration	2-15
35	2.2.2 CMS, a multipurpose experiment	2-18
36	2.2.2.1 The silicon tracker, core of CMS	2-20
37	2.2.2.2 The calorimeters, measurement of particle's energy	2-20
38	2.2.2.3 The muon system, corner stone of CMS	2-22
39	3 Muon Phase-II Upgrade	3-1
40	3.1 High Luminosity LHC and muon system requirements	3-2
41	3.2 Necessity for improved electronics	3-5
42	3.3 New detectors and increased acceptance	3-8
43	3.3.1 Improved forward resistive plate chambers	3-9
44	3.3.2 Gas electron multipliers	3-12
45	3.3.3 Installation schedule	3-19
46	3.4 Implications of the different upgrades on the Level-1 Trigger. Improvement of physics performance.	3-20
47	3.5 Ecofriendly gas studies	3-24
49	4 Physics of Resistive plate chambers	4-1
50	4.1 Principle	4-1
51	4.2 Rate capability and time resolution of Resistive Plate Chambers	4-3
52	4.2.1 Operation modes	4-3
53	4.2.2 Standard gas mixture for RPCs operated in collider experiments	4-5
54	4.2.3 Detector designs and performance	4-10
55	4.2.3.1 Double gap RPC	4-12
56	4.2.3.2 Multigap RPC (MRPC)	4-13
57	4.2.3.3 Charge distribution and performance limitations	4-17

58	4.3	Signal formation	4-19
59	4.3.1	Energy loss at intermediate energies	4-20
60	4.3.2	Primary ionization	4-24
61	4.3.3	Development and propagation of avalanches	4-28
62	4.3.4	Drift and diffusion of the electron cloud	4-32
63	4.3.5	Space charge effect & streamers	4-34
64	4.4	Effect of atmospherical conditions on the detector's performance	4-38
65	5	Longevity studies and Consolidation of the present CMS RPC subsystem	5-1
66	5.1	Testing detectors under extreme conditions	5-1
67	5.1.1	The Gamma Irradiation Facilities	5-3
68	5.1.1.1	GIF	5-3
69	5.1.1.2	GIF++	5-5
70	5.2	Preliminary tests at GIF	5-7
71	5.2.1	Resistive Plate Chamber test setup	5-7
72	5.2.2	Data Acquisition	5-10
73	5.2.3	Geometrical acceptance of the setup layout to cosmic muons	5-10
74	5.2.3.1	Description of the simulation layout	5-10
75	5.2.3.2	Simulation procedure	5-12
76	5.2.3.3	Results	5-13
77	5.2.4	Photon flux at GIF	5-13
78	5.2.4.1	Expectations from simulations	5-13
79	5.2.4.2	Dose measurements	5-18
80	5.2.5	Results and discussions	5-19
81	5.3	Longevity tests at GIF++	5-19
82	5.3.1	Description of the Data Acquisition	5-23
83	5.3.2	RPC current, environmental and operation parameter monitoring	5-24
84	5.3.3	Measurement procedure	5-24
85	5.3.4	Longevity studies results	5-24
86	6	Conclusions and outlooks	6-1
87	6.1	Conclusions	6-1
88	6.2	Outlooks	6-1
89	A	A data acquisition software for CAEN VME TDCs	A-1
90	A.1	GIF++ DAQ file tree	A-1
91	A.2	Usage of the DAQ	A-2
92	A.3	Description of the readout setup	A-3
93	A.4	Data read-out	A-3
94	A.4.1	V1190A TDCs	A-4
95	A.4.2	DataReader	A-6
96	A.4.3	Data quality flag	A-10
97	A.5	Communications	A-12
98	A.5.1	V1718 USB Bridge	A-13
99	A.5.2	Configuration file	A-13
100	A.5.3	WebDCS/DAQ intercommunication	A-17
101	A.5.4	Example of inter-process communication cycle	A-18
102	A.6	Software export	A-18

103	B Details on the offline analysis package	B-1
104	B.1 GIF++ Offline Analysis file tree	B-1
105	B.2 Usage of the Offline Analysis	B-2
106	B.2.1 Output of the offline tool	B-3
107	B.2.1.1 ROOT file	B-3
108	B.2.1.2 CSV files	B-5
109	B.3 Analysis inputs and information handling	B-6
110	B.3.1 Dimensions file and IniFile parser	B-6
111	B.3.2 TDC to RPC link file and Mapping	B-7
112	B.4 Description of GIF++ setup within the Offline Analysis tool	B-9
113	B.4.1 RPC objects	B-9
114	B.4.2 Trolley objects	B-10
115	B.4.3 Infrastructure object	B-11
116	B.5 Handeling of data	B-12
117	B.5.1 RPC hits	B-12
118	B.5.2 Clusters of hits	B-13
119	B.6 DAQ data Analysis	B-14
120	B.6.1 Determination of the run type	B-15
121	B.6.2 Beam time window calculation for efficiency runs	B-16
122	B.6.3 Data loop and histogram filling	B-17
123	B.6.4 Results calculation	B-18
124	B.6.4.1 Rate normalisation	B-18
125	B.6.4.2 Rate and activity	B-20
126	B.6.4.3 Strip masking tool	B-22
127	B.6.4.4 Output CSV files filling	B-24
128	B.7 Current data Analysis	B-29

¹²⁹

Nederlandse samenvatting –Summary in Dutch–

¹³⁰

¹³¹ Le resume en Neerlandais (j'aurais peut-être pu apprendre la langue juste pour ça...).

English summary

¹³³ Le meme résume mais en Anglais (on commencera par la hein!).

List of Figures

134

135	2.1	Through the gold foil experiment Rutherford could show that most of the mass of atoms was contained in a positively charged nucleus and could then propose a more accurate atomic model than that of Thomson.	2-3
136	2.2	Figure 2.2a: Meson octet. Figure 2.2b: Baryon octet. Figure 2.2c: Baryon decuplet.	2-8
137	2.3	The elementary particles of the Standard Model are showed along with their names and properties. Their interactions with the strong, weak and electromagnetic forces have been explicated using color squares. In the left column, the scalar higgs boson is depicted, while the central is focused on the matter particles, the fermions, and the right on the force carriers, the gauge bosons. The role of the Higgs boson in electroweak symmetry breaking is highlighted, and the corresponding way properties of the various particles differ in the (high-energy) symmetric phase (top) and the (low-energy) broken-symmetry phase (bottom) are showed.	2-11
138	2.4	CERN accelerator complex.	2-15
139	2.5	Pictures of the different accelerators. From top to bottom: first the LINAC 2 and the <i>Pb</i> source of LINAC 3. Then the Booster and the LEIR. Finally, the PS, the SPS and the LHC.	2-16
140	2.6	Figure 2.6a: schematics of the LHC cryodipoles. 1: Superconducting Coils, 2: Beam pipe, 3: Heat exchanger Pipe, 4: Helium-II Vessel, 5: Superconducting Bus-bar, 6: Iron Yoke, 7: Non-Magnetic Collars, 8: Vacuum Vessel, 9: Radiation Screen, 10: Thermal Shield, 11: Auxiliary Bus-bar Tube, 12: Instrumentation Feed Throughs, 13: Protection Diode, 14: Quadrupole Bus-bars, 15: Spool Piece Bus-bars. Figure 2.6b: magnetic field and resulting motion force applied on the beam particles.	2-17
141	2.7	Figure 2.7a: picture of the LHC quadrupoles. Figure 2.7b: magnetic fields and resulting focussing force applied on the beam by 2 consecutive quadrupoles.	2-18
142	2.8	Picture of the CMS barrel. The red outer layer is the muon system hosted into the red iron return yokes. The calorimeters are the blue cylinder inside in magnet solenoid and the tracker is the inner yellow cylinder built around the beam pipe.	2-19
143	2.9	View of the CMS apparatus and of its different components.	2-19
144	2.10	Slice showing CMS sub-detectors and how particles interact with them.	2-20
145	2.11	CMS tracker.	2-20
146	2.12	Figure 2.12a: picture of the ECAL. Figure 2.12b: picture of the lead tungstate crystals composing the ECAL.	2-21
147	2.13	CMS hadron calorimeter barrel.	2-21
148	2.14	A quadrant of the muon system, showing DTs (yellow), RPCs (blue), and CSCs (green).	2-22
149	2.15	Figure 2.15a: Barrel wheel with its detector rings and return yokes. Figure 2.15b: CSC endcap disk with the 2 CSC stations. The outer station is made of 10 deg detectors while the inner station is made of 20 deg detectors. Figure 2.15c: RPC endcap disk. The inner station is not equipped and the inner CSC station can be seen.	2-23
150			
151			
152			
153			
154			
155			
156			
157			
158			
159			
160			
161			
162			
163			
164			
165			
166			
167			
168			
169			
170			
171			
172			
173			

- 174 2.16 Figure 2.16a: Cross section of a DT module showing the two superlayers measur-
 175 ing the ϕ coordinate, perpendicular to the cross section plane, and the superlayer
 176 measuring the η coordinate, placed in between the two others with honeycomb and
 177 parallel to the cross section plane. The DT detector is sandwiched in between 2
 178 RPCs whose readout strips are perpendicular to the cross section plane, measuring
 179 the ϕ coordinate. Figure 2.16b: A DT cell is shown together with its electric field.
 180 The path of a muon through a superlayer is shown. 2-23
- 181 2.17 Figure 2.17a: cathode strips and anode wire layout of a CSC panel. Figure 2.17b
 182 avalanche development and charge collection by anode wires and induction on cath-
 183 ode strips inside of a CSC panel. 2-24
- 184 2.18 Muon track reconstruction through the 6 panels of a CMS CSC using the infor-
 185 mation of anode wire groups and cathode strip charge distribution combined with
 186 comparator bits to decide on which half strip the muon is more likely to have passed. 2-24
- 187 2.19 Double gap layout of CMS RPCs. Muons passing through the gas volumes will cre-
 188 ate electron-ions pairs by ionising the gas. this ionisation will immediately translate
 189 into a developing avalanche. 2-25
- 190 3.1 Detailed timeline projection of for LHC and HL-LHC operation until 2039 show-
 191 ing the evolution of the instantaneous and integrated luminosity as designed (Fig-
 192 ure 3.1a) and in the ultimate case where the instantaneous luminosity is increased to
 193 $7.5 \times 10^{34} \text{ cm}^{-2}\text{s}^{-1}$ (Figure 3.1b) [20, 22]. 3-2
- 194 3.2 Absorbed dose in the CMS cavern after an integrated luminosity of 3000 fb. Using
 195 the interaction point as reference, R is the transverse distance from the beamline and
 196 Z is the distance along the beamline. 3-3
- 197 3.3 A quadrant of the muon system, showing DTs (yellow), RPCs (blue), and CSCs
 198 (green). The locations of new forward muon detectors for Phase-II are contained
 199 within the dashed box and indicated in red for GEM stations (ME0, GE1/1, and
 200 GE2/1) and dark blue for improved RPC (iRPC) stations (RE3/1 and RE4/1). 3-4
- 201 3.4 Figure 3.4a: Extrapolated fraction of failing channels of the present DT MiC1 elec-
 202 tronics as a function of the integrated luminosity for different scenari until LS4. Fig-
 203 ure 3.4b: Comparison of the current (left) and upgraded (right) DT data processing.
 204 So far, the data is sent to service cavern of CMS facility via copper-to-optical-fiber
 205 translators (CuOF) by each MiC1. There, data including RPCs and outer hadron
 206 calorimeter is combined into trigger primitives (TPG) and transmitted by the Twin-
 207 Mux system to CMS Track Finder. The time-to-digital converter (TDC) data is col-
 208 lected and sent to the CMS data acquisition system (DAQ) by the micro read-out
 209 server (μ ROS). After the upgrade, the TDC data will be sent via optical links to
 210 a patch panel inside the experimental cavern by each MiC2, and transferred to the
 211 back-end, where triggering and event building will be performed. 3-6
- 212 3.5 Figure 3.5a: The event loss fractions as a function of the instantaneous luminosity is
 213 compared for CFEBs (Phase-1) and DCFEBs (Phase-II) at different CSC locations.
 214 HL-LHC luminosity is marked with the dashed brown line. Figure 3.5b: Comparison
 215 of the current (left) and upgraded (right) CSC data processing. A part of the con-
 216 nections in between ALCTs and DCFEBs, and the trigger mother boards (TMBs)
 217 and data acquisition mother boards (DMBs) will be upgraded toward optical data
 218 transfer. The detector dependent units (DDUs) used as interface in between CSCs'
 219 front-end electronics and the CMS DAQ will be replaced by new FED boards. 3-7
- 220 3.6 Comparison of the simulated time residuals in between reconstructed and true muon
 221 times without (blue) and with (red) the upgraded RPC link system. 3-8

222	3.7	RMS of the multiple scattering displacement as a function of muon p_T for the proposed forward muon stations. All of the electromagnetic processes such as bremsstrahlung and magnetic field effect are included in the simulation.	3-9
225	3.8	Simulation of the impact of RPC hit inclusion onto the local trigger primitive efficiency in station 3 (left) and station 4 (right). The contribution of iRPC starts above $ \eta = 1.8$	3-9
228	3.9	Expected hit rate due to neutrons, photons, electrons and positrons at HL-HLC instantaneous luminosity of $5 \times 10^{34} \text{ cm}^{-2}\text{s}^{-1}$ in RE3/1 and RE4/1 chambers. The sensitivities of iRPCs used in the simulation for each particle are reported and differ from one endcap disk to another as the energies of the considered particles varies with the increasing distance from the interaction point.	3-10
233	3.10	Measured average charge per avalanche as a function of the effective electric field for different gas gap thickness in double gap RPCs using HPL electrodes.	3-11
235	3.11	The PETIROC time jitter as a function of the input signal amplitude, measured with and without internal clocks.	3-12
237	3.12	Schematics of a GEM showing the cathode on top, the GEM foil separating the gas volume into the drift region, in between the cathode and foil, and the induction region, in between the GEM foil and the anode, and the anode on which a 2D readout is installed. A negative voltage is applied on the cathode while the anode is connected to the ground.	3-13
242	3.13	Left: Picture of a CMS GEM foil provided by a scanning electron microscope. Right: Representation of the electric field lines in a GEM hole and of the amplification that electrons and ions undergo in the hole's volume due to the very intense electric field.	3-14
245	3.14	Schematic representation of CMS triple GEMs. The gas volume is divided into 4 areas. The drift area is the region where the primary electrons are created before being amplified a first time while passing through the first GEM foil. Then the process of drift and amplification is repeated twice in following two transfer areas and GEM foils. Finally, the charges have been amplified enough to induce current in the read-out strips while in the last drift area. The dimensions, potentials and electric fields are provided.	3-14
252	3.15	Simulated efficiency and rate of the standalone Level-1 muon trigger using tracks reconstructed in CSCs and all GEM stations compared with Phase-I values in the case where only CSCs are used or CSCs+GE1/1. The zones of inefficiency of the CSC subsystem are compensated by the addition of GEMs during Phase-II and the trigger rates is kept from increasing due to the high luminosity.	3-15
255	3.16	Figure 3.16a: Simulated resolution of the muon direction measurement $\Delta\phi$ with Phase-II conditions. In the second endcap station, the resolution is compared in the case of CSCs (ME2/1) alone and CSCs+GEMs (GE2/1+ME2/1) while a similar resolution measurement is given in the case of the first station (GE1/1+ME1/1). Figure 3.16b: The addition of GEM detectors on stations 1 and 2 (ME0 is considered to contribute to station station 1) as redundant system to CSCs allows to improve the muon momentum improvement through a more accurate measurement of the local bending angles ϕ_1 and ϕ_2	3-16
265	3.17	Schematics of the data communication chain for DAQ of the GEM subsystems. The sending of trigger data via optical links to the CSC OTMBs is only done for GE1/1 and GE2/1 to match the data with ME1/1 and ME2/1.	3-16

268 3.18 Figure 3.18a: Energy spectrum of GIF++ ^{137}Cs source as measured by the GE1/1
 269 detector installed in GIF++. Figure 3.18b: Evolution of the normalized gain of the
 270 GE1/1 detector installed at in GIF++ as a function of the integrated charge per unit
 271 area. The first part of the study, up to a charge of 55 mC/cm^2 had been done in the
 272 former Gamma Irradiation Facility (GIF) that has now been dismantled following
 273 the construction of GIF++. No variation of the normalized gain can be observed
 274 after an accumulation of 110 mC/cm^2 3-17

275 3.19 Figure 3.19a: Comparison of the gas gain as a function of the divider voltage before
 276 and after the irradiation of a triple-GEM by neutrons in CHARM. Figure 3.19b:
 277 Comparison of the gas gain as a function of the divider voltage before and after the
 278 irradiation of a triple-GEM by alpha particles. 3-18

279 3.20 Data flow of the Level-1 Trigger during Phase-II operations. 3-20

280 3.21 Comparison of Phase-II DT trigger primitives algorithmic efficiency for segments
 281 obtained with 2 super-layers (quality $\geq 6/8$) and 1 super-layer only (quality = 4/4).
 282 The simulation was done by generating 2×10^6 muons. The candidate tracks with
 283 correct time identification is showed with open symbols. 3-21

284 3.22 Simulated spatial (3.22a) and angular (3.22b) resolution of the algorithm using 8
 285 aligned hits in both super-layers (quality = 8/8) and 4 aligned hits in only one super-
 286 layer (quality = 4/4). The contribution of intermediate quality tracks (6 aligned hits)
 287 is negligible in the angular range shown. [Be careful to update this caption as it
 288 uses a text to close to the published one.] 3-21

289 3.23 Efficiency of the L1 trigger in the endcap region after Phase-II upgrade in the case
 290 CSC/GEM/RPC hits are requested in at least 2 stations out of four (3.23a) and in all
 291 four stations (3.23b). 3-22

292 3.24 Resolution of the LCT ambiguous events thanks to the combination of CSC and
 293 iRPC readout data. Using CSCs only, 2 pairs of hits are possible. 3-23

294 3.25 The angular resolution on reconstructed muon tracks in the GEM overlap region
 295 $2.0 < |\eta| < 2.15$ is compared for Phase-II conditions in the case CSC are alone
 296 (Figure 3.25a) and in the case the GEMs' data, including ME0, is combined to which
 297 of CSCs (Figure 3.25b). 3-23

298 3.26 Comparison of L1 trigger performances for prompt muons with and without the
 299 addition of GEMs in the region $2.1 < |\eta| < 2.4$ at Phase-II conditions. GEMs would
 300 allow a reduction of the trigger accept rate by an order of magnitude (Figure 3.26a)
 301 while increasing the trigger efficiency (Figure 3.26b). 3-24

302 3.27 The efficiency (solid lines) and streamer probability (dashed lines) of HFO/CO_2
 303 (Figure 3.27a) and CF_3I/CO_2 (Figure 3.27b) based gas mixtures as a function of
 304 the effective high-voltage are compared with the present CMS RPC gas mixture
 305 represented in black. The detector used for the study is a single gap RPC with similar
 306 properties than CMS RPCs. The streamer probability is defined as the proportion of
 307 events with a deposited charge greater than 20 pC 3-25

308 4.1 Different phases of the avalanche development in the RPC gas volume subjected to
 309 a constant electric field E_0 . a) An avalanche is initiated by the primary ionisation
 310 caused by the passage of a charged particle through the gas volume. b) Due to
 311 its growing size, the avalanche starts to locally influence the electric field. c) The
 312 electrons, lighter than the cations reach the anode first. d) The ions reach the cathode.
 313 While the charges have not recombined, the electric field in the small region around
 314 the avalanche stays affected and locally blinds the detector. 4-2

- 315 4.2 Movement of the charge carriers in an RPC. Figure 4.2a: Voltage across an RPC
 316 whose electrode have a relative permittivity of 5 at the moment the tension s applied.
 317 Figure 4.2b: After the charge carriers moved, the electrodes are charged and there
 318 is no voltage drop over the electrodes anymore. The full potential is applied on the
 319 gas gap only. Figure 4.2c: The streamer discharge initiated by a charged particle
 320 transports electrons and cations towards the anode and cathode respectively. 4-4
- 321 4.3 Typical oscilloscope pulses in streamer mode (Figure 4.3a) and avalanche mode(Figure 4.3b).
 322 In the case of streamer mode, the very small avalanche signal is visible. 4-4
- 323 4.4 Rate capability comparison for the streamer and avalanche mode of operation. An
 324 order of magnitude in rate capability for a maximal efficiency drop of 10% is gained
 325 by using the avalanche mode over the streamer mode. 4-5
- 326 4.5 Comparison of the charge distribution of signals induced by cosmic muons in an
 327 RPC operated with a gas mixture of argon, butane and bromotrifluoromethane (CF_3Br).
 328 The Ar/C_4H_{10} is kept constant at 60/40 in volume while the total amount of CF_3Br
 329 in the mixture is varied: 0% (Figure 4.5a), 4% (Figure 4.5b) and 8% (Figure 4.5c) [39]. 4-6
- 330 4.6 Comparison of the efficiency and streamer probability, defined as the fraction of
 331 events with an induced charge 10 times larger than that of the average avalanche,
 332 with and without irradiation by a 24 GBq ^{137}Cs source of an RPC successively
 333 operated with a 90/10 mixture $C_2H_2F_4/i-C_4H_{10}$ (Figure 4.6a) and a 70/5/10/15
 334 mixture of $Ar/i-C_4H_{10}/CO_2/C_2H_2F_4$ (Figure 4.6b) [40]. 4-6
- 335 4.7 Comparison of the fast charge ratio with and without irradiation by a 24 GBq ^{137}Cs
 336 source of an RPC successively operated with a 90/10 mixture $C_2H_2F_4/i-C_4H_{10}$
 337 (Figure 4.7a) and a 70/5/10/15 mixture of $Ar/i-C_4H_{10}/CO_2/C_2H_2F_4$ (Figure 4.7b).
 338 The results are provided for both single gap and double gap operation [40]. 4-7
- 339 4.8 Efficiency (circles and stars with 30 mV and 100 mV thresholds respectively) and
 340 streamer probability (opened circles) as function of the operating voltatge of a 2 mm
 341 single gap HPL RPC flushed with a gas mixture containing (a) 5%, (b) 2%, (c) 1%
 342 and (d) no SF_6 [42]. 4-8
- 343 4.9 Evolution of the efficiency, working voltage, and voltage at 50% of maximum ef-
 344 ficiency for CMS Barrel (Figure 4.9a) and Endcap (Figure 4.9b) RPCs obtained
 345 through yearly voltage scans since 2011. The working voltage of each RPC is up-
 346 dated after each voltage scan to ensure optimal operation [57]. 4-9
- 347 4.10 Comparison of the rate capability of 8 mm and 2 mm wide RPCs. The lines are
 348 linear fits on the data [59]. 4-10
- 349 4.11 Distributions of the induced charge of fast signals on 2 mm (Figure 4.11a) and 8 mm
 350 (Figure 4.11b) RPCs exposed to a radiation rate of 100 Hz/cm². Average induced
 351 charge of fast signals as a function of the high voltage applied on 2 mm and 8 mm
 352 RPCs (Figure 4.11c). In the case of the 2 mm RPC, a saturation of the pre-amplifier
 353 was observed. The average of the distribution is underestimated and the median is
 354 showed together with the average to account for this bias [59]. 4-11
- 355 4.12 Time distributions of the leading, trailing, and average of both leading and traling
 356 edges for 2 mm (top row) and 8 mm (bottom row) RPCs exposed to a 100 Hz/cm²
 357 radiation rate. The data was collected with RPCs operated at the voltage correspond-
 358 ing to the knee of the efficiency distribution, defined as the point where 95% of the
 359 maximum efficiency is obtained [59]. 4-12

- 360 4.13 Possible double-gap RPC layouts: a) "standard" 1D double-gap RPC, as used in
 361 CMS experiment, where the anodes are facing each other and a 1D read-out plane
 362 is sandwiched in between them, b) double read-out double-gap RPC as used in AT-
 363 LAS experiment, where the cathodes are facing each other and 2 read-out planes are
 364 used on the outer surfaces. This last layout can offer the possibility to use a 2D
 365 reconstruction by using orthogonal read-out planes. 4-13
- 366 4.14 Comparison of performance of CMS double and single gap RPCs using cosmic
 367 muons [55]. Figure 4.14a: Comparison of efficiency sigmoids. Figure 4.14b: Volt-
 368 age distribution at 95% of maximum efficiency. Figure 4.14c: $\Delta_{10\%}^{90\%}$ distribution. . . 4-13
- 369 4.15 Representation of different RPC layouts (wide gap on Figure (a), double gap on
 370 Figure (b) and multigap on Figure (c)), of the corresponding sensitive volume in
 371 gray, and of the associated avalanche size [45]. 4-14
- 372 4.16 Time distributions of the leading, trailing, and average of both leading and trailing
 373 edges for multigap RPCs consisting in two 4 mm (Figure 4.16a) and four 2 mm
 374 (Figure 4.16b) exposed to a 100 Hz/cm² radiation rate. The data was collected with
 375 RPCs operated at the voltage corresponding to the knee of the efficiency distribution,
 376 defined as the point where 95% of the maximum efficiency is obtained [45]. 4-15
- 377 4.17 Presentation of a study of a possible ALICE MRPC cell using 250 μm gas gaps,
 378 620 μm outer glass electrodes, and 550 μm inner floating electrodes (Figure 4.17a),
 379 and of its time resolution performance as a function of the applied high voltage for
 380 different radiation levels referred through different filter settings of the 740 GBq
¹³⁷Cs source the former CERN GIF facility [60]. 4-15
- 382 4.18 Particle identification applied to electrons in the STAR experiment. The identifica-
 383 tion is performed combining ToF and dE/dx measurements [65]. 4-16
- 384 4.19 Comparison of the detector performance of ALICE ToF MRPC [66] at fixed applied
 385 voltage (in blue) and at fixed effective voltage (in red). The effective voltage is kept
 386 fixed by increasing the applied voltage accordingly to the current drawn by the detector. 4-17
- 387 4.20 Ratio between total induced and drifting charge have been simulated for single gap,
 388 double-gap and multigap layouts [67]. The total induced charge for a double-gap
 389 RPC is a factor 2 higher than for a multigap. 4-18
- 390 4.21 Charge spectra have been simulated for single gap, double-gap and multigap lay-
 391 outs [67]. It appears that when single gap shows a decreasing spectrum, double and
 392 multigap layouts exhibit a spectrum whose peak is detached from the origin. The
 393 detachment gets stronger as the number of gaps increases. 4-18
- 394 4.22 The maximal theoretical efficiency is simulated for single gap, double-gap and multi-
 395 gap layouts [67] at a constant gap thickness of 2 mm and using an effective Townsend
 396 coefficient of 9 mm⁻¹. 4-19
- 397 4.23 Mass stopping power as a function of $\beta\gamma = p/Mc$ for positive muons in copper [68].
 398 The total stopping power is indicated with solid line and local components with
 399 dashed lines. the vertical bands are used to indicate boundaries between different
 400 approximations used at different energy range. 4-19
- 401 4.24 Mean mass stopping power for liquid hydrogen, as used in bubble chambers, gaseous
 402 helium, carbon, aluminum, iron, tin, and lead without the inclusion of radiative effect
 403 at higher $\beta\gamma$ necessary for pions and muons in denser materials [68]. 4-21
- 404 4.25 Mean excitation energies normalized to the atomic number as adopted by the ICRU [68,
 405 72, 73]. 4-22
- 406 4.26 Mean mass stopping power at minimum ionization as a function of the atomic num-
 407 ber [68]. 4-22

408	4.27 Example of straggling function $f(\Delta)$ of particles passing through 1.2 cm of Argon 409 gas with a $\beta\gamma$ of 3.6 and represented with a solid line. The original Landau distribu- 410 tion is showed with a dashed line [74].	4-23
411	4.28 Evolution of straggling functions $f(\Delta)$ of particles passing through a volume of 412 Argon gas with a $\beta\gamma$ of 3.6 with increasing thickness x [74].	4-23
413	4.29 Photo-absorption cross section as computed by HEED for nobles gases with different 414 electric shell numbers [70].	4-25
415	4.30 Photo-absorption cross section as computed by HEED for typical RPC gas mix- 416 tures [70]. The RPC mixture with CO_2 corresponds to the mixture used by CALICE 417 SDHCAL [78] while the other one was foreseen for the experiment ATLAS [79] but 418 has been changed since then.	4-26
419	4.31 Distributions of number of electrons (left) and energy loss (right) for a 5 GeV/c 420 muon passing through 1.2 mm of Helium (Figure 4.31a), Argon (Figure 4.31b) or a 421 typical RPC gas mixture (Figure 4.31c) [70].	4-27
422	4.32 Figure 4.32a: Mean cluster density for muons through different gas volumes [70]. 423 Figure 4.32b: Distribution of the number of electrons per cluster for a 5 GeV/c 424 muon traveling through a mixture of 96.7% $C_2H_2F_4$, 3% i- C_4H_{10} and 0.3% SF_6 [70, 425 79].	4-28
426	4.33 Townsend and attachment coefficient for a typical 96.7/3/0.3 mixture of $C_2H_2F_4$ /i- 427 C_4H_{10} / SF_6 , at a temperature $T = 296.15$ K and a pressure $P = 1013$ hPa [70, 79]. .	4-29
428	4.34 Comparison of the distribution law of Furry and the Poisson law for $\bar{n} = 5$ [82]. .	4-29
429	4.35 Single-electron avalanche size distribution in a proportionnal counter filled with 430 methylal at different E/p values. (a) 70, (b) 76.5, (c) 105, (d) 186.5, (e) 426V/cm torr [83].	4-30
431	4.36 Figure 4.36a: Comparison of avalanche size distributions for different values of 432 Townsend and attachment coefficients. The effective Townsend coefficient is the 433 same for both distributions. Figure 4.36b: Fluctuation in avalanche size for avalanche 434 started by a single electron with $\alpha = 13 \text{ mm}^{-1}$ and $\eta = 3.5 \text{ mm}^{-1}$ [79].	4-32
435	4.37 Figure 4.37a: Electron mean drift velocity v_D in pure $C_2H_2F_4$ and typical RPC 436 gas mixtures. Figure 4.37b: Transverse diffusion coefficient in pure $C_2H_2F_4$ and a 437 typical RPC gas mixture. Figure 4.37c: Longitudinal diffusion coefficient in pure 438 $C_2H_2F_4$ and a typical RPC gas mixture. All results are given with a pressure $P =$ 439 760 Torr and a temperature $T = 296.15$ K [70].	4-33
440	4.38 Comparison of the free charge carriers in the gas after a time $t = 7.90$ ns in the case 441 where no diffusion is taken into account to simulate the avalanche (Figure 4.38a) 442 and in the case where the diffusion is implemented (Figure 4.38b) [70].	4-33
443	4.39 Schematic representation of an avalanche and of the electric field deformation it 444 causes due to the local concentration of charge carriers [51].	4-35
445	4.40 Evolution of the charge induced by an avalanche started by a single electron in a 446 1.2 mm thick RPC with an applied electric field of 54 kV/cm in the case space 447 charge is not taken into account (Figure 4.40a) and in the case it is implemented into 448 the simulation (Figure 4.40b). The total induced charge is correlated to the size of 449 the avalanche [70].	4-36
450	4.41 Distributions of charge carriers within the gas volume of a 1.2 mm thick RPC and 451 the corresponding deformation of the electric field at different time steps with an 452 applied electric field of 55.5 kV/cm [70].	4-37
453	4.42 Representation of the weighting field in the volume of a RPC and the resulting in- 454 duced current in the strip placed at 1 V and its neighbour connected to the ground. 455 The induced current corresponds, as can be understood from Formula 4.22 [51].	4-38
456	4.43 Schematics of CMS RPC FEE logic.	4-39

457	4.44	Equivalence in between the charge of the induced signal in input of the CMS FEE and the signal strength on the output of the pre-amplifier.	4-39
458			
459	4.45	Description of the principle of a CFD. A comparison of threshold triggering (left) and constant fraction triggering (right) is shown in Figure 4.45a. Constant fraction triggering is obtained thanks to zero-crossing technique as explained in Fig- ure 4.45b. The signal arriving at the input of the CFD is split into three components. A first one is delayed and connected to the inverting input of a first comparator. A second component is connected to the noninverting input of this first comparator. A third component is connected to the noninverting input of another comparator along with a threshold value connected to the inverting input. Finally, the output of both comparators is fed through an AND gate.	4-40
460			
461			
462			
463			
464			
465			
466			
467			
468	4.46	Typical efficiency sigmoid of a CMS RPC detector. The black dots correspond to the data, the blue line to the sigmoid fit and the opened cross to the knee and working extracted from the fit line.	4-41
469			
470			
471	4.47	Effect of the temperature variation on the rate (Figure 4.47a) and the efficiency (Fig- ure 4.47b) of a RPC [84].	4-42
472			
473	4.48	Effect of the pressure variation on the rate (Figure 4.48a) and the efficiency (Fig- ure 4.48b) of a RPC [85].	4-43
474			
475	5.1	Figure 5.1a: The integrated charge per region (Barrel, Endcap) is extrapolated to HL-LHC integrated luminosity (3000 fb^{-1}) using the data accumulated in 2016 in every HV channels. Figure 5.1b: The hit rate per region (Barrel, Endcap) is linearly extrapolated to HL-LHC highest instantaneous luminosity ($5 \times 10^{34} \text{ cm}^{-2}\text{s}^{-1}$) using the rate as a function of instantaneous luminosity recorded by RPCs in 2017 showing a linear dependence.	5-2
476			
477			
478			
479			
480			
481	5.2	Background Fluka simulation compared to 2016 Data at $L = 10^{34} \text{ cm}^{-2}\text{s}^{-1}$ in the fourth endcap disk region. A mismatch in between simulation and data can be ob- served.	5-3
482			
483			
484	5.3	Layout of the test beam zone called X5c GIF at CERN. Photons from the radioactive source produce a sustained high rate of random hits over the whole area. The zone is surrounded by 8 m high and 80 cm thick concrete walls. Access is possible through three entry points. Two access doors for personnel and one large gate for material. A crane allows installation of heavy equipment in the area.	5-4
485			
486			
487			
488			
489	5.4	^{137}Cs decays by β^- emission to the ground state of ^{137}Ba (BR = 5.64%) and via the 662 keV isomeric level of ^{137}Ba (BR = 94.36%) whose half-life is 2.55min.	5-5
490			
491	5.5	Floor plan of the GIF++ facility. When the facility downstream of the GIF++ takes electron beam, a beam pipe is installed along the beam line (z-axis). The irradiator can be displaced laterally (its center moves from $x = 0.65 \text{ m}$ to 2.15 m), to increase the distance to the beam pipe.	5-5
492			
493			
494			
495	5.6	Simulated unattenuated current of photons in the xz plane (Figure 5.6a) and yz plane (Figure 5.6b) through the source at $x = 0.65 \text{ m}$ and $y = 0 \text{ m}$. With angular correction filters, the current of 662 keV photons is made uniform in xy planes.	5-6
496			
497			
498	5.7	Signals from the RPC strips are shaped by the FEE described on Figure 5.7a. Out- put LVDS signals are then read-out by a TDC module connected to a computer or converted into NIM and sent to scalers. Figure 5.7b describes how these converted signals are put in coincidence with the trigger.	5-7
499			
500			
501			

- 502 5.8 Description of the RPC setup. Dimensions are given in mm. A tent containing RPCs
 503 is placed at 1720 mm from the source container. The source is situated in the center
 504 of the container. RE-4-2-BARC-161 chamber is 160 mm inside the tent. This way,
 505 the distance between the source and the chambers plan is 2060 mm. Figure 5.8a
 506 provides a side view of the setup in the xz plane while Figure 5.8b shows a top view
 507 in the yz plane. 5-8
- 508 5.9 RE-4-2-BARC-161 chamber is inside the tent as described in Figure 5.8. In the top
 509 right, the two scintillators used as trigger can be seen. This trigger system has an
 510 inclination of 10° relative to horizontal and is placed above half-partition B2 of the
 511 RPCs. PMT electronics are shielded thanks to lead blocks placed in order to protect
 512 them without stopping photons from going through the scintillators and the chamber. 5-8
- 513 5.10 Hit distributions over all 3 partitions of RE-4-2-BARC-161 chamber is showed on
 514 these plots. Top, middle and bottom figures respectively correspond to partitions A,
 515 B, and C. These plots show that some events still occur in other half-partitions than
 516 B2, which corresponds to strips 49 to 64, in front of which the trigger is placed, con-
 517 tributing to the inefficiency of detection of cosmic muons. In the case of partitions
 518 A and C, the very low amount of data can be interpreted as noise. On the other hand,
 519 it is clear that a little portion of muons reach the half-partition B1, corresponding to
 520 strips 33 to 48. 5-9
- 521 5.11 Results are derived from data taken on half-partition B2 only. On the 18th of June
 522 2014, data has been taken on chamber RE-2-BARC-161 at building 904 (Prevessin
 523 Site) with cosmic muons providing us a reference efficiency plateau of $(97.54 \pm$
 524 $0.15)\%$ represented by a black curve. A similar measurement has been done at GIF
 525 on the 21st of July with the same chamber giving a plateau of $(78.52 \pm 0.94)\%$
 526 represented by a red curve. 5-10
- 527 5.12 Representation of the layout used for the simulations of the test setup. The RPC is
 528 represented as a yellow trapezoid while the two scintillators as blue cuboids looking
 529 at the sky. A green plane corresponds to the muon generation plane within the sim-
 530 ulation. Figure 5.8a shows a global view of the simulated setup. Figure 5.8b shows
 531 a zommed view that allows to see the 2 scintillators as well as the full RPC plane. . . 5-11
- 532 5.13 γ flux $F(D)$ is plot using values from table 5.1. As expected, the plot shows similar
 533 attenuation behaviours with increasing distance for each absorption factors. 5-14
- 534 5.14 Figure 5.14a shows the linear approximation fit done via formulae 5.7 on data from
 535 table 5.2. Figure 5.14b shows a comparison of this model with the simulated flux
 536 using a and b given in figure 5.14a in formulae 5.4 and the reference value $D_0 =$
 537 50 cm and the associated flux for each absorption factor F_0^{ABS} from table 5.1 . . . 5-16
- 538 5.15 Dose measurements has been done in a plane corresponding to the tents front side.
 539 This plan is 1900 mm away from the source. As explained in the first chapter, a
 540 lens-shaped lead filter provides a uniform photon flux in the vertical plan orthogonal
 541 to the beam direction. If the second line of measured fluxes is not taken into account
 542 because of lower values due to experimental equipments in the way between the
 543 source and the tent, the uniformity of the flux is well showed by the results. 5-18
- 544 5.16 5-19
- 545 5.17 Evolution of the maximum efficiency for RE2 (5.17a) and RE4 (5.17b) chambers
 546 with increasing extrapolated γ rate per unit area at working point. Both irradiated
 547 (blue) and non irradiated (red) chambers are shown. 5-20
- 548 5.18 Evolution of the working point for RE2 (5.18a) and RE4 (5.18b) with increasing
 549 extrapolated γ rate per unit area at working point. Both irradiated (blue) and non
 550 irradiated (red) chambers are shown. 5-21

551	5.19 Evolution of the maximum efficiency at HL-LHC conditions, i.e. a background hit 552 rate per unit area of 300 Hz/cm ² , with increasing integrated charge for RE2 (5.19a) 553 and RE4 (5.19b) detectors. Both irradiated (blue) and non irradiated (red) chambers 554 are shown. The integrated charge for non irradiated detectors is recorded during test 555 beam periods and stays small with respect to the charge accumulated in irradiated 556 chambers.	5-21
557	5.20 Comparison of the efficiency sigmoid before (triangles) and after (circles) irradiation 558 for RE2 (5.20a) and RE4 (5.20b) detectors. Both irradiated (blue) and non irradiated 559 (red) chambers are shown.	5-22
560	5.21 Evolution of the Bakelite resistivity for RE2 (5.21a) and RE4 (5.21b) detectors. Both 561 irradiated (blue) and non irradiated (red) chambers are shown.	5-22
562	5.22 Evolution of the noise rate per unit area for the irradiated chamber RE2-2-BARC-9 563 only.	5-23
564	A.1 (A.1a) View of the front panel of a V1190A TDC module [95]. (A.1b) View of the 565 front panel of a V1718 Bridge module [96]. (A.1c) View of the front panel of a 6U 566 6021 VME crate [97].	A-3
567	A.2 Module V1190A <i>Trigger Matching Mode</i> timing diagram [95].	A-4
568	A.3 Structure of the ROOT output file generated by the DAQ. The 5 branches (<code>EventNumber</code> , 569 <code>number_of_hits</code> , <code>Quality_flag</code> , <code>TDC_channel</code> and <code>TDC_TimeStamp</code>) are visible on 570 the left panel of the ROOT browser. On the right panel is visible the histogram cor- 571 responding to the variable <code>nHits</code> . In this specific example, there were approximately 572 50k events recorded to measure the gamma irradiation rate on the detectors. Each 573 event is stored as a single entry in the <code>TTree</code>	A-10
574	A.4 The effect of the quality flag is explained by presenting the content of <code>TBranch</code> 575 <code>number_of_hits</code> of a data file without <code>Quality_flag</code> in Figure A.4a and the con- 576 tent of the same <code>TBranch</code> for data corresponding to a <code>Quality_flag</code> where all TDCs 577 were labelled as <code>GOOD</code> in Figure A.4b taken with similar conditions. It can be noted 578 that the number of entries in Figure A.4b is slightly lower then in Figure A.4a due 579 to the excluded events.	A-12
580	A.5 Using the same data as previously showed in Figure A.4, the effect of the quality 581 flag is explained by presenting the reconstructed hit multiplicity of a data file with- 582 out <code>Quality_flag</code> in Figure A.5a and the reconstructed content of the same RPC 583 partition for data corresponding to a <code>Quality_flag</code> where all TDCs were labelled as 584 <code>GOOD</code> in Figure A.5b taken with similar conditions. The artificial high content of bin 585 0 is completely suppressed.	A-12
586	A.6 WebDCS DAQ scan page. On this page, shifters need to choose the type of scan 587 (Rate, Efficiency or Noise Reference scan), the gamma source configuration at the 588 moment of data taking, the beam configuration, and the trigger mode. These in- 589 formation will be stored in the DAQ ROOT output. Are also given the minimal 590 measurement time and waiting time after ramping up of the detectors is over before 591 starting the data acquisition. Then, the list of HV points to scan and the number of 592 triggers for each run of the scan are given in the table underneath.	A-14

593	B.1	Example of expected hit time distributions in the cases of efficiency (Figure B.1a) and noise/gamma rate per unit area (Figure B.1b) measurements as extracted from the raw ROOT files. The unit along the x-axis corresponds to ns. The fact that "the" muon peak is not well defined in Figure B.1a is due to the contribution of all the RPCs being tested at the same time that don't necessarily have the same signal arrival time. Each individual peak can have an offset with the ones of other detectors. The inconsistancy in the first 100 ns of both time distributions is an artefact of the TDCs and are systematically rejected during the analysis.	B-15
594			
595	B.2	The effect of the quality flag is explained by presenting the reconstructed hit multiplicity of a data file without <code>Quality_flag</code> . The artificial high content of bin 0 is the effect of corrupted data.	B-18
596			
597	B.3	Display of the masking tool page on the webDCS. The window on the left allows the shifter to edit <code>ChannelsMapping.csv</code> . To mask a channel, it only is needed to set the 3rd field corresponding to the strip to mask to 0. It is not necessary for older mapping file formats to add a 1 for each strip that is not masked as the code is versatile and the default behaviour is to consider missing mask fields as active strips. The effect of the mask is directly visible for noisy channels as the corresponding bin turns red. The global effect of masking strips will be an update of the rate value showed on the histogram that will take into consideration the rejected channels.	B-23
598			
599			
600			
601			
602			
603			
604			
605			
606			
607			
608			
609			
610			
611			

List of Tables

612

613	3.1	Details of the greenhouse fluorinated gases used in CMS and of their GWP [23].	3-24
614	4.1	Properties of the most used electrode materials for RPCs.	4-3
615	5.1	Total photon flux ($E\gamma \leq 662$ keV) with statistical error predicted considering a 616 ^{137}Cs activity of 740 GBq at different values of the distance D to the source along 617 the x-axis of irradiation field [92].	5-13
618	5.2	Correction factor c is computed thanks to formulae 5.5 taking as reference $D_0 =$ 619 50 cm and the associated flux F_0^{ABS} for each absorption factor available in table 5.1.	5-15
620	5.3	The data at D_0 in 1997 is taken from [92]. In a second step, using Equations 5.8 621 and 5.9, the flux at D can be estimated in 1997. Then, taking into account the 622 attenuation of the source activity, the flux at D can be estimated at the time of the 623 tests in GIF in 2014. Finally, assuming a sensitivity of the RPC to γ $s = 2 \times 10^{-3}$, 624 an estimation of the hit rate per unit area is obtained.	5-17
625	A.1	Inter-process communication cycles in between the webDCS and the DAQ through 626 file string signals.	A-19

List of Acronyms

627

628

List of Acronyms

629

630

A

631

633 AFL

Almost Full Level

634 ALCTs

anode local charged track boards

635

636

B

637

639 BARC

Bhabha Atomic Research Centre

640 BLT

Block Transfer

641 BMTF

Barrel Muon Track Finder

642 BNL

Brookhaven National Laboratory

643 BR

Branching Ratio

644

645

C

646

648 CAEN

Costruzioni Apparecchiature Elettroniche Nucleari S.p.A.

649 CERN

European Organization for Nuclear Research

650 CFD

Constant Fraction Discriminator

651 CFEBs

cathode front-end boards

652 CMB

Cosmic Microwave Background

653 CMS

Compact Muon Solenoid

654 CSC

Cathode Strip Chamber

655 CuOF

copper-to-optical-fiber translators

656

657

D

658

660 DAQ

Data Acquisition

661 DCS

Detector Control Software

662 DQM

Data Quality Monitoring

663	DT	Drift Tube
664		
665		
666	E	
667		
668	ECAL	electromagnetic calorimeter
669	EMTF	Endcap Muon Track Finder
670		
671		
672	F	
673		
674	FCC	Future Circular Collider
675	FEE	Front-End Electronics
676	FEB	Front-End Board
677	FWHM	full-width-at-half-maximum
678		
679		
680	G	
681		
682	GE-/-	Find a good description
683	GE1/1	Find a good description
684	GE2/1	Find a good description
685	GEANT	GEometry ANd Tracking - a series of software toolkit platforms developed by CERN
686		
687	GEB	GEM Electronics board
688	GEM	Gas Electron Multiplier
689	GIF	Gamma Irradiation Facility
690	GIF++	new Gamma Irradiation Facility
691	GWP	Global Warming Potential
692		
693		
694	H	
695		
696	HCAL	hadron calorimeter
697	HL-LHC	High Luminosity LHC
698	HPL	High-pressure laminate
699	HV	High Voltage
700		
701		
702	I	
703		
704	ICRU	International Commission on Radiation Units & Measurements
705	iRPC	improved RPC

706	IRQ	Interrupt Request
707	ISR	Intersecting Storage Rings
708		
709		
710	L	
711		
712	LEIR	Low Energy Ion Ring
713	LEP	Large Electron-Positron
714	LHC	Large Hadron Collider
715	LS1	First Long Shutdown
716	LS2	Second Long Shutdown
717	LS3	Third Long Shutdown
718	LV	Low Voltage
719	LVDS	Low-Voltage Differential Signaling
720		
721		
722	M	
723		
724	MiC1	first version of Minicrate electronics
725	mip's	minimum ionizing particles
726	MC	Monte Carlo
727	MCNP	Monte Carlo N-Particle
728	ME-/	Find good description
729	ME0	Find good description
730	MRPC	Multigap RPC
731		
732		
733	N	
734		
735	NIM	Nuclear Instrumentation Module logic signals
736		
737		
738	O	
739		
740	OH	Optohybrid Board
741	OMTF	Overlap Muon Track Finder
742		
743		
744	P	
745		
746	PAI	Photo-Absorption Ionisation
747	PAIR	Photo-Absorption Ionisation with Relaxation
748	PMT	PhotoMultiplier Tube

749 PS Proton Synchrotron
750 PU pile-up

751

752

753 Q

754

755 QCD Quantum Chromodynamics
756 QED Quantum Electrodynamics

757

758

759 R

760

761 RE-/ Find a good description
762 RE2/2 Find a good description
763 RE3/1 Find a good description
764 RE3/2 Find a good description
765 RE4/1 Find a good description
766 RE4/2 Find a good description
767 RE4/3 Find a good description
768 RMS Root Mean Square
769 ROOT a framework for data processing born at CERN
770 RPC Resistive Plate Chamber

771

772

773 S

774

775 SC Synchrocyclotron
776 SLAC Stanford Linear Accelerator Center
777 SM Standard Model
778 SPS Super Proton Synchrotron
779 SUSY supersymmetry

780

781

782 T

783

784 TDC Time-to-Digital Converter
785 TDR Technical Design Report
786 ToF Time-of-flight
787 TPG trigger primitives

788

789

790 W

791

792 webDCS Web Detector Control System

793

794

795

796

797 YETS Year End Technical Stop

1

Introduction

798

799

2

800

801

Investigating the TeV scale

802 „We may regard the present state of the universe as the effect of the
803 past and the cause of the future. An intellect which at any given
804 moment knew all of the forces that animate nature and the mutual
805 positions of the beings that compose it, if this intellect were vast
806 enough to submit the data to analysis, could condense into a single
807 formula the movement of the greatest bodies of the universe and that
808 of the lightest atom; for such an intellect nothing could be uncertain
809 and the future just like the past would be present before its eyes.”
810 - Pierre Simon de Laplace, *A Philosophical Essay on Probabilities*, 1814

811 Throughout history, physics experiment became more and more powerful in order to investigate
812 finer details of nature and helped understanding the elementary blocks of matter and the
813 fundamental interactions that bond them in the microscopic world. Nowadays, the Standard
814 Model (SM) of particle physics is the most accurate theory designed to explain the behaviour of
815 particles and was able to make very precise predictions that are constantly verified, although some
816 hints of new physics are visible as bricks are still missing to have a global comprehension of the
817 Universe.

818 To highlight the limits of the SM and test the different alternative theories, ever more powerful
819 machines are needed. This is in this context that the Large Hadron Collider (LHC) has been
820 thought and built to accelerate and collide particles at energies exceeding anything that had been
821 done before. Higher collision energies and high pile-up imply the use of enormous detectors to
822 measure the properties of the interaction products. The Compact Muon Solenoid (CMS) is a
823 multipurpose experiment that have been designed to study the proton-proton collisions of the LHC
824 and give answers on various high energy physics scenari. Nevertheless, the luminosity delivered by
825 the collider will in the future be increased to levels beyond the original plans to improve its
826 discovery potential giving no choice to experiments such as CMS to upgrade their technologies to
827 cope with the increased radiation levels and detection rates.

828 **2.1 The Standard Model of Particle Physics**

829 In this early 21st century it is now widely accepted that matter is made of elementary blocks
830 referred to as *elementary particles*. The physics theory that classifies and describes the best the
831 behaviour and interaction of such elementary particles is the so called Standard Model that
832 formalizes 3 of the 4 fundamental interactions (electromagnetic, weak and strong interactions). It's
833 development took place during the 20th century thanks to a strong collaboration in between the
834 theoretical and experimental physicists.

835 **2.1.1 A history of particle physics**

836 The idea that nature is composed of elementary bricks, called *atomism*, is not contemporary as it
837 was already discussed by Indian or Greek philosophers during antiquity. In Greece, atomism has
838 been rejected by Aristotelianism as the existence of *atoms* would imply the existence of a void that
839 would violate the physical principles of Aristotle philosophy. Aristotelianism has been considered
840 as a reference in the European area until the 15th century and the Italian *Rinascimento* where ancient
841 text and history started to be more deeply studied. The re-discovery of Platon's philosophy would
842 allow to open the door to alternative theories and give a new approach to natural sciences where
843 experimentation would become central. A new era of knowledge was starting. By the beginning of
844 the 17th century, atomism was re-discovered by philosophers and the very first attempt to estimate
845 an *atom* size would be provided by Magnetus in 1646. Although his *atoms* correspond to what
846 would nowadays be called *molecules*, Magnetus achieved feats by calculating that the number of
847 molecules in a grain of incense would be of the order of 10^{18} simply by considering the time
848 necessary to smell it everywhere in a large church after the stick was lit on. It is now known that
849 this number only falls short by 1 order of magnitude.

850 An alternative philosophy to atomism popularized by Descartes was corpuscularianism. Built on
851 ever divisible corpuscles, contrary to atoms, its principles would be mainly used by alchemists like
852 Newton who would later develop a corpuscular theory of light. Boyle would combine together

853 ideas of both atomism or corpuscularianism leading to mechanical philosophy. The 18th century
 854 have seen the development of engineering providing philosophical thought experiments with
 855 repeatable demonstration and a new point of view to explain the composition of matter and
 856 Lavoisier would greatly contribute to chemistry and atomism by publishing in 1789 a list of 33
 857 chemical elements corresponding to what is now called *atoms*. In the early 19th century Dalton
 858 would summarize the knowledge on composition of matter and Fraunhofer would invent the
 859 spectrometer and discover the spectral lines. The rise of atomic physics, chemistry and
 860 mathematical formalism would unravel the different atomic elements and ultimately, the 20th
 861 century would see the very first sub-atomic particles.

862 **Discovery of the inner structure of the atom**

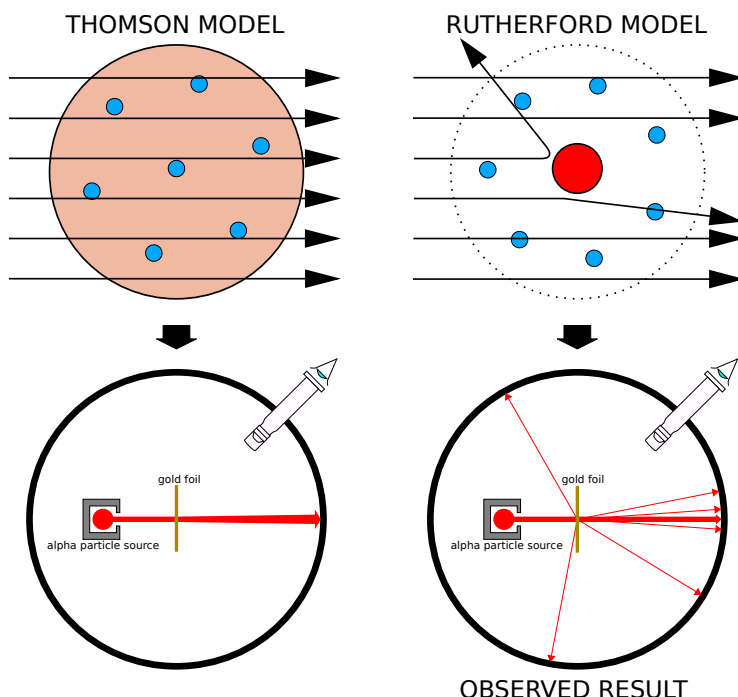


Figure 2.1: Through the gold foil experiment Rutherford could show that most of the mass of atoms was contained in a positively charged nucleus and could then propose a more accurate atomic model than that of Thomson.

863 The negative *electron* would be the first to be discovered in 1897 by Thomson after 3 decades of
 864 research on cathode rays by proving that the electrification observed in an electroscope, as reported
 865 by Perrin, was due to the rays themselves and that they had to be composed of electrically charged
 866 particles. In 1900, Becquerel would show the *beta rays* emitted by radium had the same charge
 867 over mass ratio than what measured by Thomson for cathode rays, pointing to electrons as a
 868 constituent of atoms. In 1907, Rutherford and Royds showed that *alpha* particles, once captured in
 869 a tube and subjected to an electric spark causing an electron avalanche, where helium ions as they
 870 could combine with 2 electrons to form a ${}^4\text{He}$. This discovery was directly followed by the
 871 constraint of the atom structure in 1909 through the gold foil experiment in which the deflection

angle of alpha particles fired at a very thin gold foil was measured and highlighted atoms where mainly empty with nearly all its mass contained into a tiny positively charged *nucleus*. With these two observations, he could formulate the Rutherford model of the atom in 1911, shown together with the Thomson plum pudding model in Figure 2.1. The link in between atomic number and number of positive and negative charges contained into the atoms would fast be understood and the different kind of element transmutation appeared to be purely nuclear processes making clear that the electromagnetic nature of chemical transformation could not possibly change nuclei. Thus a new branch in physics appeared to study nuclei exclusively: the nuclear physics.

Moreover, in 1913 quantum physics would be introduced into the atomic model by Bohr based on the assumptions of Plank to explain spectral lines, and other observed quantum effects. The same year, Moseley would confirm Bohr's model and Debye would extend it by introducing elliptical orbits.

By studying alpha emission and the product of their interaction with nitrogen gas, Rutherford reported in 1919 the very first nuclear reaction leading to the discovery that the hydrogen nucleus was composed of a single positively charged particle that was later baptised *proton*. This idea came from 1815 Prout's hypothesis proposing that all atoms are composed of "*protyles*" (i.e. hydrogen atoms). By using scintillation detectors, Rutherford could highlight typical hydrogen nuclei signature and understand that the impact of alpha particles with nitrogen would knock out an hydrogen nucleus and produce an oxygen 17, as explicated in Formula 2.1 and would then postulate that protons are building bricks of all elements.



With this assumption and the discovery of isotopes together with Aston, elements with identical atomic number but different masses, Rutherford would propose that all elements' nuclei but hydrogen's are composed of both charged particles, protons, and of chargeless particles, which he called *neutrons*, and that these neutral particles would help maintaining nuclei as one, as charged protons were likely to electrostatically repulse each other, and introduced the idea of a new force, a *nuclear* force. Though the first idea concerning neutrons was a bond state of protons and electrons as it was known that the beta decay, emitting electrons, was taking place in the nucleus, it was then showed that such a model would hardly be possible due to Heisenberg's uncertainty principle and by the recently measured *spin* of both protons and electrons. The spin, discovered through the study of the emission spectrum of alkali metals, would be understood as a "two-valued quantum degree of freedom" and formalized by Pauli and extended by Dirac, to take the relativist case into account. Measured to be $\frac{1}{2}\hbar$ for both, it was impossible to arrange an odd number of half integer spins and obtain a global nucleus spin that would be integer. Finally, in 1932, following the discovery of a new neutral radiation, Chadwick could discover the neutron as an uncharged particle with a mass similar to that of the proton whose half integer spin would reveal to be the solution to explain the nuclear spin.

Development of the Quantum Electrodynamics

Historically, the development of the quantum theory revolved around the question of emission and absorption of discrete amount of energy through light. Einstein used the initial intuition of Plank about the black-body radiation to develop in 1905 a model to explain the photoelectric effect in which light was described by discrete quanta now called *photons*. For this model, Einstein introduced the concept of wave-particle duality as classical theory was not able to describe the

914 phenomenon. With the new understanding of atoms and of their structure, classical theories also
 915 proved unable to explain atoms stability. Indeed, using classical mechanics, electrons orbiting
 916 around a nucleus should radiate an energy proportionnal to their angular momentum and thus loose
 917 energy through time and the spectrum of energy emission should then be continuous, but it was
 918 known since the 19th century and the discovery of spectral lines that the emission spectrum of
 919 material was discrete.

920 This was Bohr who first suggested that a quantum description of the atom was necessary in 1913.
 921 Using the correspondence principle stating that are large enough numbers the quantum calculations
 922 should give the same results than the classical theory, he proposed the very first quantum model of
 923 the hydrogen atom explaining the line spectrum by introducing the principal quantum number n
 924 describing the electron shell. This model would then be improved by Sommerfeld that would
 925 quantize the z-component of the angular momentum, leading to a the second and third quantum
 926 numbers, or azimuthal and magnetic quantum number, l and m defining for the second the orbital
 927 angular momentum of the electrons on their shells and thus, the shape of the orbital, and for the
 928 third the available orbital on the subshell for each electron. Nevertheless, although the model was
 929 not only limited to sperical orbitals anymore, making the atom more realistic, the Zeeman effect
 930 couldn't be completely explained by just using n , l and m . A solution would be brought after the
 931 discovery of Pauli in 1924, as Uhlenbeck, Goudsmid, and Kronig proposed in 1925 the idea of
 932 intrinsic rotation of the electron, introducing a new angular momentum vector associated to the
 933 particle itself, and not to the orbital, and associated to a new quantic number s , the *spin* projection
 934 quantum number explaining the lift of degeneracy to an even number of energy levels.

935 The introduction of the *spin* happened 1 year after another attempt of improvement of the theory
 936 was made by De Broglie in his PhD thesis. The original formulation of the quantum theory only
 937 considered photons as energy quanta behaving as both waves and particles. De Broglie proposed
 938 that all matter are described by waves and that there momentum is proportional to the oscillation of
 939 quantized electromagnetic field oscillators. This interpretation was able to reproduce the previous
 940 version of the quantum energy levels by showing that the quantum condition involves an integer
 941 multiple of 2π , as shown by Formula 2.2.

$$p = \hbar k \Leftrightarrow \int pdx = \hbar \int kdx = 2\pi\hbar n \quad (2.2)$$

942 Although the intuition of De Broglie about the wave-particle duality of all matter, his interpretation
 943 was semiclassical and it's in 1926 that the first fully quantum mechanical wave-equation would be
 944 introduced by Schrödinger to describe electron-like particles, reproducing the previous
 945 semiclassical formulation without inconsistencies. This complexe equation describes the evolution
 946 of the wave function Ψ of the quantum system, defined by it's position vector \mathbf{r} and time t as an
 947 energy conservation law, in which the hamiltonian of the system \hat{H} is explicit, by solving the
 948 Equation 2.3.

$$i\hbar \frac{\partial}{\partial t} |\Psi(\mathbf{r}, t)\rangle = \hat{H} |\Psi(\mathbf{r}, t)\rangle \quad (2.3)$$

949 In 1927, Dirac would go further in his paper about emission and absorption of radiation by
 950 proposing a second quantization not only of the physical process at play but also of the
 951 electromagnetic field, providing the ingredients to the first formulation of *Quantum*
 952 *Electrodynamics (QED)* and the description of photon emission by electrons dropping into a lower
 953 energy state in which the final number of particles is different than the initial one. To complete this

model to the many-body wave functions of identical particles, Jordan included creation and annihilation operators for fields obeying Fermi-Dirac statistics leading to a model describing particles that would be referred to as *fermions*. Nevertheless, in order to properly treat electromagnetism, the incorporation of the relativity theory developed by Einstein. Including gravity into quantum physics still is a challenge nowadays, but in 1928 Pauli and Jordan would show that special relativity's coordinate transformations could be applied to quantum fields as the field commutators were Lorentz invariant. Finally derived the same year, the Dirac equation, shown as Equation 2.4, similarly to Schrödinger's equation, is a single-particle equation but it incorporates special relativity in addition to quantum mechanics rules. It features the 4×4 gamma matrices γ^μ built using 2×2 Pauli matrices and unitary matrix, the 4-gradient ∂_μ , the rest mass m of any half integer spin massive particle described by the wave function $\psi(x, t)$, also called a Dirac spinor, and the speed of light c . In addition to perfectly reproduce the results obtained with quantum mechanics so far, it also provided with *negative-energy solutions* that would later be interpreted as a new form of matter, *antimatter* and give a theoretical justification to the Pauli equation that was phenomenologically constructed to account for the spin as in the non-relativistic limit, the Dirac equation is similar.

$$i\hbar\gamma^\mu\partial_\mu\psi - mc\psi = 0 \quad (2.4)$$

The successes of the QED was soon followed with theoretical problems as computations of any physical process involving photons and charged particles were showed to be only reliable at the first order of perturbation theory. At higher order of the theory, divergent contributions were appearing giving nonsensical results. Only two effects were contributing to these infinities.

- The self-energy of the electron (or positron), the energy that the particle has due its own interaction with its environment.
- The vacuum polarization, virtual electron–positron pairs produced by a background electromagnetic field in the vacuum which is not an "empty" space. These virtual pairs affect the charge and current distributions generated by the original electromagnetic field.

Solving this apparent problem was done by carefully defining the concepts of each observables, for example mass or charge, as these quantities are understood within the context of a non-interacting field equation, and that from the experiment point of view, they are abstractions as what is measured are "renormalized observables" shifted from there "bare" value by the interaction taking place in the measuring process. The infinities needed to be connected to corrections of mass and charge as those are fixed to finite values by experiment. This was the intuition of Bethe in 1947 who successfully computed the effect of such *renormalization* in the non-relativist case. Fully covariant formulations of QED including renormalization was achieved by 1949 by Tomonaga, Schwinger, Feynman and Dyson and Feynman is now famous for his association of diagrams to the term of the scattering matrix, greatly simplifying the representation and computation of interactions as the diagrams directly corresponded the measurable physical processes and would then be used in every quantum field theories. With the resolution of infinities, QED had mostly reached its final form, being still today the most accurate physical theory and would serve as a model to build all other quantum field theories.

993 **Development of the quark model and Quantum Chromodynamics**

994 To explain the nuclear force that holds *nucleons* (protons and neutrons) together, Yukawa
 995 theoretically proposed in 1934 the existence of a force carrier called *meson* due to it's predicted
 996 mass in the range in between the electron and nucleon masses. Discovered in 1936 by Anderson
 997 and Neddermeyer, and confirmed using bubble chambers in 1937 by Street and Stevenson, a first
 998 meson candidate was observed in the decay products of cosmic rays. Assuming it had the same
 999 electric charge than electrons and protons, this particle was observed to have a curvature due to
 1000 magnetic field that was sharper than protons but smoother than electrons resulting in a mass in
 1001 between that of electrons and protons. But its properties were not compatible with Yukawa's theory,
 1002 which was emphasized by the discovery of a new candidate in 1947, again in cosmic ray products
 1003 using photographic emulsions.

1004 This new candidate, although it had a similar mass than the already believed *meson*, would rather
 1005 decay into it. For distinction, the first candidate would then be renamed "*mu meson*" when the
 1006 second would be the "*pi meson*". The *mu meson* was behaving like a heavy electron and didn't
 1007 participate in the strong interaction whereas the pion was believed to be the carrier of the nuclear
 1008 interaction. This lead to classify the *mu* in a new category of particles called *leptons* together with
 1009 the electron that shared similar properties and *the neutrino*, and be renamed *muon*. The *pi meson*
 1010 was finally found to be a triplet of particles: a positively charged, a negatively charged, and a
 1011 neutral particle. The neutral *pi meson* has been more difficult to identify as it wouldn't leave tracks
 1012 on emulsions nor on bubble chambers and needed to be studied via it's decay products. It was
 1013 ultimately identified in University of California's cyclotron in 1950 through the observation of its
 1014 decay into 2 photons.

1015 Also discovered in 1947 but in cloud chamber photographs, the *K meson* as also been an important
 1016 step towards the establishment of the Standard Model. A triplet of particle, 2 charged and a neutral,
 1017 with a mass roughly half that of a proton, were reported. These particles were baptised *K meson* in
 1018 contrast to the "light" *pi* and *mu* "L-mesons". The particularity of the *K* were there very slow
 1019 decays with a typical lifetime of the order of 10^{-10} s much greater than the 10^{-23} s of *pi*-proton
 1020 reactions. The concept of *strangeness*, a new quantum number was then introduced by Pais as an
 1021 attempt to explain this phenomenon as *strange* particles appeared as a pair production of a strange
 1022 and anti-strange particle.

1023 With the development of synchrotrons, the particle *zoo* would grow to several dozens during the
 1024 1950s as higher energies were reachable through acceleration. In 1961, a first classification system,
 1025 called Eightfold Way, was proposed by Gell-Mann and finding its roots in the
 1026 Gell-Mann–Nishijima formula, which relates the electric charge Q , the third component of the
 1027 isospin I_3 , the *baryon* number B and the strangeness S , as explicated in Formula 2.5. The isospin
 1028 was a quantum number introduced in 1932 to explain symmetries of the newly discovered neutron
 1029 using representation theory of SU(2). The baryon number, was introduced by Nishijima as a
 1030 quantum number for baryons, i.e. particles of the same family as nucleons. The mesons were
 1031 classified in an octet and baryons of spin $\pm \frac{1}{2}$ and $\pm \frac{3}{2}$ were respectively classified into an octet and
 1032 a decuplet, as shown in Figure 2.2. To complete the baryon decuplet, Gell-Mann predicted the
 1033 existance of baryon Ω^- which would later be discovered in 1964.

$$Q = I_3 + \frac{1}{2}(B + S) \quad (2.5)$$

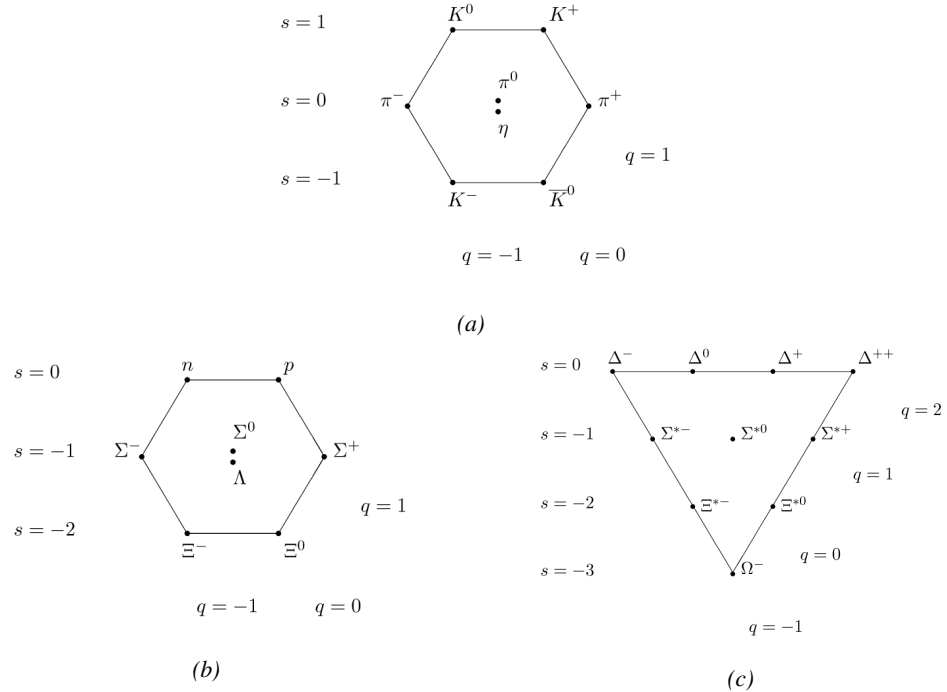


Figure 2.2: Figure 2.2a: Meson octet. Figure 2.2b: Baryon octet. Figure 2.2c: Baryon decuplet.

1034 Strong of this classification using an SU(3) flavor symmetry, Gell-Mann, and independently Zweig,
 1035 would propose a full theoretical model in which *hadrons* (strongly interacting particles, i.e. mesons
 1036 and baryons) were not elementary particles anymore. They would rather be composed with 3
 1037 flavors of particles called *quarks* and there anti-particles. The 3 flavors were called *up*, *down* and
 1038 *strange*. *Up* and *down* would be used to explain the nucleons and non-strange mesons, while
 1039 *strange* would come into the composition of hadrons showing strangeness. *Up* and *down* flavors
 1040 would be discovered in 1968 thanks to the deep inelastic scattering experiments conducted at the
 1041 Stanford Linear Accelerator Center (SLAC), and *strange* could only be indirectly validated
 1042 eventhough it provided a robust explanation to *kaon* (K) and *pion* (π). However, in the decade
 1043 following the Gell-Mann-Zweig quark model proposition, several improvement to the model were
 1044 brought, first by Glashow and Bjorken the same year that predicted the existence of a fourth quark
 1045 flavor, the *charm*, that would equalize the then known number of quarks and leptons and finally in
 1046 1973 by Kobayashi and Maskawa that would increase the number of quarks to 6 to explain the
 1047 experimental observation of CP violation. These two quarks would been refered to as *top* and
 1048 *bottom* for the first time in 1975. It's only after these additions to the quark model that finally the
 1049 *charm* would be discovered in 1974 at both SLAC and Brookhaven National Laboratory (BNL). A
 1050 meson where the *charm* was bond with an *anti-charm*, called J/ψ , would help convince the physics
 1051 community of the validity of the model. The *top* would be discovered soon after in 1977 in
 1052 Fermilab and indicate the existence of the *bottom* that would resist to discovery until Fermilab's
 1053 experiments CDF and D \emptyset in 1995 due its very large mass and the energy needed to produce it.
 1054 As remarked by Struminsky, the original quark model proposal composed of 3 quarks should
 1055 possess an additional quantum number due to mesons such as Ω^- or Δ^{++} . Indeed, these mesons
 1056 are composed of 3 identical quarks, respectively 3 *strange* and *up* quark, with parallel spins, which

1057 should be forbidden by the exclusion principle. Independently, Greenberg and Han-Nambu
 1058 proposed an additional SU(3) degree of freedom possessed by the quarks, that would later be
 1059 referred to as *color charge gauge*, that could interact through *gluons*, the gauge boson octet
 1060 corresponding to this degree of freedom. Nevertheless, as observing free quarks proved to be
 1061 impossible, two visions of the quarks were argued mainly due to the failures to observe these
 1062 particles free to prove their existence. On one side, Gell-Mann proposed to see quarks as
 1063 mathematical construct instead of real particles, as they are always confined, implying that quantum
 1064 field theory would not describe entirely the strong interaction. Opposed to this vision, Feynman on
 1065 the contrary argued that quarks were real particles, that he would call *partons*, that should be
 1066 described as all other particles by a distribution of position and momentum. The implications of
 1067 quarks as point-like particles would be verified at SLAC and the concept of *color* would be added
 1068 to the quark model in 1973 by Fritzsch and Leutwyler together with Gell-Mann to propose a
 1069 description of the strong interaction through the theory of Quantum Chromodynamics (QCD). The
 1070 discovery the same year of asymptotic freedom within the QCD by Gross, Politzer and Wilczek,
 1071 allowed for very precise predictions thanks to the perturbation theory. Nowadays, the confinement
 1072 of quarks is studied in experiments such as ALICE, through exploration of the quark-gluon plasma.

1073 **The Weak interaction, spontaneous symmetry breaking, the Higgs mechanism and the**
 1074 **Electroweak unification**

1075 The weak interaction is the process that causes radioactive decays. Thanks to the neutron discovery,
 1076 Fermi could explain in 1934 the beta radiations through the beta decay process in which the neutron
 1077 decays into a proton by emitting an electron. Though the missing energy observed during this
 1078 process triggered a huge debate about the apparent non conservation of energy, momentum and spin
 1079 of the process, Fermi, as Pauli before him, proposed that the missing energy was due to a neutral
 1080 not yet discovered particle that would then be baptised *neutrino*. The impossibility to detect such a
 1081 particle would leave some members of the scientific community sceptical, but hints of energy
 1082 conservation and of the existence of the neutrino were provided by measuring the energy spectrum
 1083 of electrons emitted through beta decay, as there was a strict limit on their energy. It's only 30 years
 1084 later in 1953 that it would be discovered by the team of Cowan and Reines using the principle of
 1085 inverse beta decay described through Formula 2.6. The experiment consisted in placing water tanks
 1086 sandwiched in between liquid scintillators near a nuclear reactor with an estimated neutrino flux of
 1087 $5 \times 10^{13} \text{ cm}^{-2} \text{s}^{-1}$. However, in order to explain the absence of some reactions in the experiment of
 1088 Cowan and Reines, and constraint the beta decay theory of Fermi and extend it to the case of the
 1089 muon, Konopinski and Mahmoud proposed in 1953 that the muon decay would eject a particle
 1090 similar to the neutrino and thus predicted the existence of a muon neutrino that would be different
 1091 than the one involved in the beta decay, related to the electron. With this, the idea of lepton number
 1092 would arise. The muon neutrino would successfully be detected in 1962 by Lederman, Schwartz and
 1093 Steinberger.

$$\bar{\nu} + p \rightarrow n + e^+ \quad (2.6)$$

1094 The theory could not be valid though as the probability of interaction, called cross-section, would
 1095 have been increasing without bound with the square of the energy. Fermi assumed in a two vector
 1096 current coupling but Lee and Yang noted that an axial current could appear and would violate
 1097 parity. The experiment of Wu in 1956 would confirm the parity violation and Gamow and Teller
 1098 would try to account for it by describing Fermi's interaction through allowed (parity-violating) and

1099 superallowed (parity-conserving) decays. But the success of QED as a quantum field theory would
1100 spark the development of such a theory to describe the weak interaction.

1101 As previously discussed, the great success of QED was built on an underlying symmetry,
1102 interpreted as a gauge invariance so that the effect of the force is the same in all space-time
1103 coordinates, and of the possibility to renormalize it in order to absorb the infinities. Independently in
1104 1958, Glashow, and Salam and Ward used 1957 Schwinger ideas about vector intermediary for the
1105 decay processes, could find a way to unite both the electromagnetic and weak interaction into a
1106 gauge theory involving 4 gauge bosons, 3 of which were massive and carried out the weak
1107 interaction and a massless boson carrying the electromagnetic interaction. Among the 3 massive
1108 bosons, 2 were charged and 1 was neutral, similarly to the previously theorized *pi meson* vector of
1109 the Yukawa model and all have a mass much greater than nucleons and thus a very short life time
1110 implying a finite very short range contrary to the contact interaction originally proposed by Fermi.

1111 Breakthrough in other fields of physics contributed in giving theoretical support and interpretation
1112 to the unified electroweak theory. The stepping stone would be the use of spontaneous symmetry
1113 breaking that was inspired to Nambu at the end of the 1950s following the development of the BCS
1114 superconductivity mechanism in 1957. Cooper had shown that BCS pairs, pairs of electrons bound
1115 together at low temperature, could have lower energy than the Fermi energy and where responsible
1116 for superconductivity. This lead to the discovery of Goldstone-Nambu bosons as a result of the
1117 spontaneous breaking of the chiral symmetry in a theory describing nucleons and mesons
1118 developped by Nambu and Jona-Lasinio in 1961, and now understood as a low-energy
1119 approximation of QCD. Simmilarly to mechanism of energy gap appearance in superconductivity,
1120 the nucleon mass is suggested to the result of a self-energy of a fermion field and is studied through
1121 a four-fermion interaction in which, as a consequence of the symmetry, bound states of
1122 nucleon-antinucleon pairs appear and can be regarded as virtual pions. Though the symmetry is
1123 maintained in the equations, the ground state is not preserved. Goldstone would later the same year
1124 show that the bound states corresponds to spinless bosons with zero mass.

1125 Although the model in itself didn't revolutionize particle physics, spontaneous symmetry breaking
1126 would be generalized to quantum field theories. As all fundamental interactions are described using
1127 gauge theories based on underlying symmetries, processes such as the chiral symmetry breaking
1128 would be introduced soon after the publication of Nambu and Jona-Lasinio. In 1962, Anderson,
1129 following an idea of Schwinger who suggested that zero-mass vector bosons were not necessarily
1130 required to describe the conservation of baryons contrary to the bosons emerging from chiral
1131 symmetry breaking, discussed the implications of spontaneous symmetry breaking in particles
1132 physics. A model was finally independently built in 1964 by Brout and Englert, Higgs, and
1133 Guralnik, Hagen, and Kibble, who discovered that combining an additional field into a gauge
1134 theory in order to break the symmetry, the resulting gauge bosons acquire a nonzero mass.
1135 Moreover, Higgs stated that this implied the existence of at least one new massive, i.e.
1136 self-interacting, scalar boson, that are now known as *Higgs bosons* corresponding to this additional
1137 field. The Higgs mechanism today specifically refers to the process through which the gauge
1138 bosons of the weak interaction acquire mass. In 1968, Weinberg could point to the Higgs
1139 mechanism to integrate a Higgs field into a new version of the electroweak theory in which the
1140 spontaneous symmetry breaking mechanism of the Higgs field would explicitely explain the masses
1141 of the weak interaction gauge bosons and the zero-mass of photons.

2.1.2 Construction and test of the model

The Standard Model of particle physics was built in the middle of the 1970s after the experimental confirmation of the existence of quarks. It is based on the assembly of the models previously introduced and describing the fundamental interactions, except for gravitation, and their gauge bosons as well as the way elementary "matter" particles interact with the fields associated with these force carriers. In this sense, the development of QED and the unification of the electroweak interaction, of the Yukawa interaction and of QCD, and of the Higgs mechanism made it possible to explain most of contemporary physics.

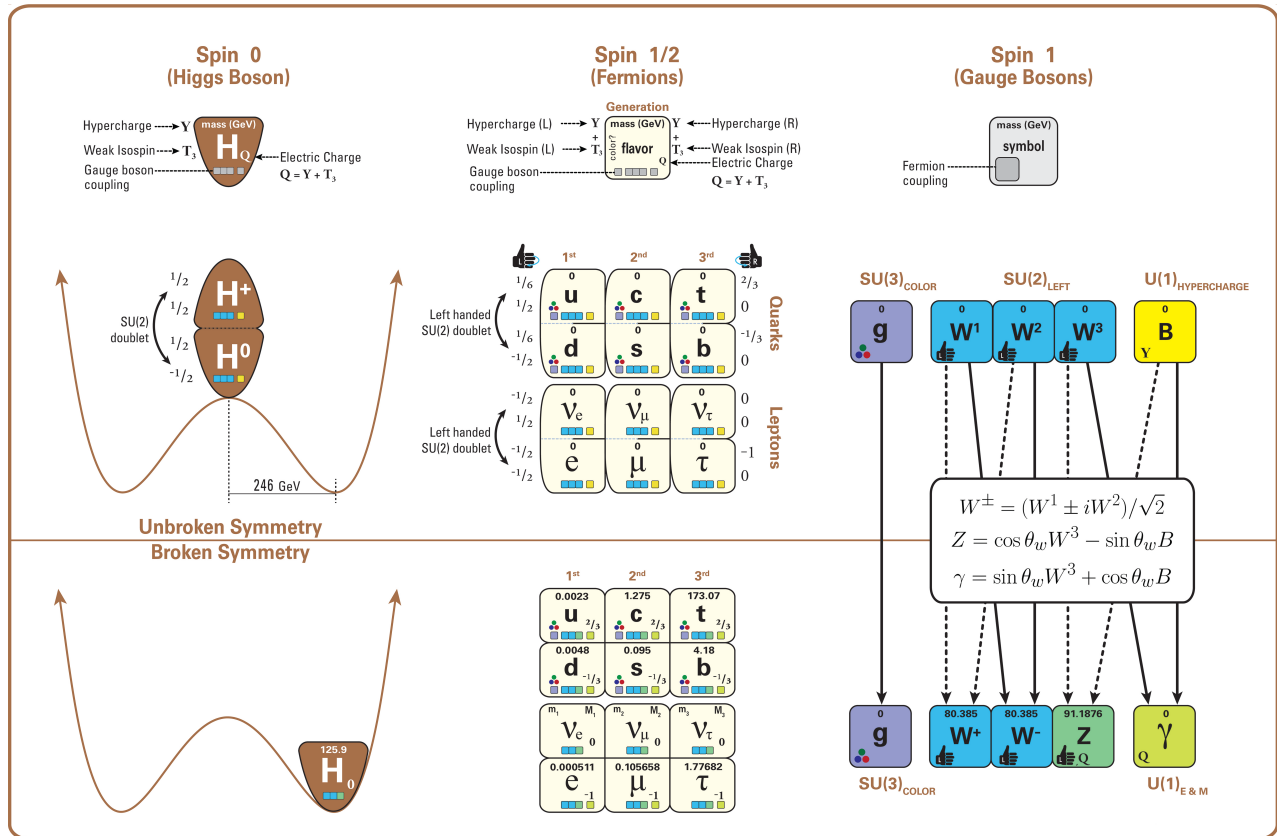


Figure 2.3: The elementary particles of the Standard Model are showed along with their names and properties. Their interactions with the strong, weak and electromagnetic forces have been explicited using color squares. In the left column, the scalar higgs boson is depicted, while the central is focused on the matter particles, the fermions, and the right on the force carriers, the gauge bosons. The role of the Higgs boson in electroweak symmetry breaking is highlighted, and the corresponding way properties of the various particles differ in the (high-energy) symmetric phase (top) and the (low-energy) broken-symmetry phase (bottom) are showed.

In the SM, "matter" particles, are described by 12 fermion fields of spin $\frac{1}{2}$ obeying the Fermi-Dirac statistics, i.e. subjected to the Pauli exclusion principle. To each fermion is associated its corresponding antiparticle. The fermions are classified according to the way they interact and, thus, according to the charges they carry. 6 of them are classified as quarks (u, d, c, s, t , and b) and are subjected to all interactions and the 6 others as leptons ($e^-, \mu^-, \tau^-, \nu_e, \nu_\mu$, and ν_τ). Leptons are

not subjected to the strong interaction and among them, the 3 neutrinos only interact weakly as they are neutral particles, which explains why they are so difficult to detect. The gauge boson fields are the gluons g for the strong interaction, the photon γ for the electromagnetic interaction and the weak bosons W^+ , W^- , and Z^0 for the weak interaction. Finally, the Higgs field H^0 is responsible, through the spontaneous symmetry breaking, of the mixing of the massless electroweak boson fields W_1 , W_2 , W_3 , and B leading to the observable states γ , W^+ , W^- , and Z^0 that can gain mass while interacting with the Higgs field. This picture of the SM is summarized through Figure 2.3 where the antifermions are not showed.

When the model was first finalized, the existence of the weak gauge bosons, of the charm, of the third quark generation composed of top and bottom quarks to explain the observed CP violation was not proven but the predictions were measured with good precision in the years following. First, the charm quark would be discovered in 1974, followed by the bottom quark in 1977. The weak bosons would be discovered during the next decade in 1983. The top quark would resist until 1995 due to its very large mass but would offer the last piece of the elementary QCD particles. The very last predicted elementary particle of the model that was not observed yet would prove to be very difficult to observe. The Higgs boson needed the start of the LHC to finally be observed in 2012. A few years more of tests were necessary to measure its properties to confirm the observation of a scalar boson compatible with the predicted Higgs boson H^0 . Even though only quark-antiquark (mesons) and 3 quark states (baryons) were observed, exotic hadrons were not forbidden by QCD and no limit of quark is imposed by the theory. Moreover, gluons could form bond states by themselves and with quarks. These two types of states are called *glueballs* and *hybrid hadrons*. For decades, experiments have been conducted without confirmation of such possible states existing. Nevertheless, in 2014, tetraquarks were observed by LHCb, one of LHC's main experiments, and in 2015, the same experiment reported the discovery of pentaquarks making the SM one of the best tested theories of physics.

2.1.3 Investigating the TeV scale

Even though the SM is a well tested theory, several hints of physics going beyond its scope have been observed. First of all, gravity is not explained through this model and huge difficulties are encountered when trying to include gravitation. The strength of gravitational interaction is expected to be negligible at the scale of elementary particles, nevertheless, adding gravitation in the perspective of developing a "*theory of everything*" leads to divergent integrals that could not be fixed through renormalization.

Moreover, the SM considers neutrinos to be massless but it was shown in the late 1960s by the Homestake experiment that the flux of solar neutrinos (i.e. ν_e) measured didn't match the predicted values due to neutrino oscillations, confirmed in the early 2000s by the Sudbury Neutrino Observatory. This oscillation implies that neutrinos that can be observed are a superposition of massive neutrino states. The research on neutrino oscillation is already quite advanced with experiments looking at atmospheric, reactor or beam neutrinos in order to determine the elements of the mixing matrix similar to the CKM matrix describing the mixing of quarks. Nevertheless, no answer to the origin of neutrino mass is provided.

Another intriguing fact is that the universe is dominated by matter. However, the SM predicted that matter and antimatter should have been created in equal amounts and no mechanism is able to explain this matter-antimatter asymmetry. Although this asymmetry is seen from the visible universe, it may be possible that other unknown regions of the Universe are dominated by

1199 antimatter. Another possibility to explain the apparent asymmetry would be the existence of a
1200 electric dipole in any fundamental particle that would permit matter and antimatter particles to
1201 decay at different rates.

1202 The discrepancy of velocity dispersion of stars in galaxies with respect to the visible mass they
1203 contain is known since the end of the 19th century where Kelvin proposed that this problem could
1204 be solved if a "great majority of [the stars] would be dark bodies". Throughout the 20th century,
1205 physicists like Kapteyn, Zwicky, showed the first hints of a "dark matter" by studying star
1206 velocities and galactic clusters, followed by robust measurements of galaxy rotation curves by
1207 Babcock which suggested that the mass-to-luminosity ratio was different from what would be
1208 expected from watching the visible light. Later in the 1970s, Rubin and Ford from direct light
1209 observations and Rogstad and Shostak from radio measurements showed that the radial velocity of
1210 visible objects in galaxies was increasing with increasing distance to the center of the galaxy.
1211 Finally observation of lensing effect by galaxy clusters, temperature distribution of hot gas in
1212 galaxies and clusters, and the anisotropies in the Cosmic Microwave Background (CMB) kept on
1213 pointing to a "dark matter". From all the data accumulated, the visible matter would only account
1214 to no more than 5% of the total content on the visible universe. Alternative theories have tried to
1215 investigate modified versions of the General Relativity as this theory is only well tested at the scale
1216 of the solar system but is not sufficiently tested on wider ranges or even theories in which
1217 gravitation is not a fundamental force but rather an emergent one, but so far, such theories have
1218 difficulties to reproduce all the experimental observations as easily as through dark matter.

1219 A possible theory to offer dark matter candidates would be supersymmetry (SUSY) which proposes
1220 a relationship in between bosons and fermions. In this model, each elementary particle, through a
1221 spontaneous spacetime symmetry breaking mechanism would have a *super partner* from the other
1222 family of particles. On top of providing heavy dark matter candidates, supersymmetry could also
1223 help solving the *Hierarchy problem*, the very large scale difference in between the weak interaction
1224 and gravity, although, as mentioned before, in the case gravity is found not to be a fundamental
1225 force, this problem would automatically fade.

1226 All these different aspects of physics beyond the Standard Model of particle physics and the
1227 Standard model itself can be tested through the use of very energetic and intense hadron and ion
1228 colliders. The LHC at CERN is a perfect tool to seek answers to these open questions except maybe
1229 for the gravity as gravity is extremely weak at particles level. For example, one of LHCb
1230 experiment's goal is to investigate CP-violation and thus baryonic asymmetry. In 2017, the
1231 collaboration has announced to have so far a 3.3σ statistical significance over a CP-violation
1232 through the study of the decays of Λ_b^0 and $\overline{\Lambda}_b^0$ into a proton (or antiproton) and 3 pions. Many
1233 analysis teams are also working hard on supersymmetry both in ATLAS and CMS collaborations,
1234 the two multipurpose experiments of LHC, even though no evidence of a supersymmetrical theory
1235 was seen, the few hint having the tendency to confirm the standard model. These experiments also
1236 have the possibility to investigate ways to explain Majorana neutrino mass through Yukawa
1237 interactions of scalar particles.

1238 The higher the center-of-mass energy, the smaller details the experiments will be able to see, the
1239 heavier the potential particle creation barrier will be, the stronger the cross-section of certain rare
1240 decay channels will be. As a comparison, with collisions happening at 14 TeV, the LHC is
1241 approximately 2 orders of magnitude more sensitive to the Higgs than the Tevatron was with its
1242 already very powerful 2 TeV. All these advantages eventually lead to new discoveries and deeper
1243 understanding of the models describing our Universe. But the LHC only is a step forward to gather
1244 more precise tests of the Standard Model and new knowledge about the physics beyond it. A

1245 successful physics campaign will probably serve to justify the building of new accelerators with
1246 even greater discovery potential like for example the Future Circular Collider (FCC) that would
1247 push even further the study of the unanswered questions of contemporary physics.

1248 2.2 The Large Hadron Collider & the Compact Muon Solenoid

1249 Throughout its history, CERN has played a leading role in high energy particle physics. Large
1250 regional facilities such as CERN were thought after the second world war in an attempt to increase
1251 international scientific collaboration and allows scientists to share the forever increasing costs of
1252 experiment facilities required due to the need for increasing the energy in the center of mass to
1253 deeper probe matter. The construction of the first accelerators at the end of the 50s, the
1254 Synchrocyclotron (SC) and the Proton Synchrotron (PS), was directly followed by the first
1255 observation of antinuclei in 1965 [1]. Strong from the experience of the Intersecting Storage
1256 Rings (ISR), the very first proton-proton collider that showed hints that protons are not elementary
1257 particles, the Super Proton Synchrotron (SPS) was built in the 70s to investigate the structure of
1258 protons, the preference for matter over antimatter, the state of matter in the early universe or exotic
1259 particles, and lead to the discovery in 1983 of the W and Z bosons [2–5]. These newly discovered
1260 particles and the electroweak interaction would then be studied in details by the Large
1261 Electron-Positron (LEP) collider that will help to prove in 1989 that there only are three
1262 generations of elementary particles [6]. The LEP would then be dismantled in 2000 to allow for the
1263 LHC to be constructed in the existing tunnel.

1264 2.2.1 LHC, the most powerful particle accelerator

1265 The LHC has always been considered as an option to the future of CERN. At the moment of the
1266 construction of the LEP beneath the border between France and Switzerland, the tunnel was built in
1267 order to accomodate what would be a Large Hadron Collider with a dipole field of 10 T and a beam
1268 energy in between 8 and 9 TeV [7] directly followed in 1985 with the creation of a 'Working Group
1269 on the Scientific and Technological Future of CERN' to investigate such a collider [8]. The
1270 decision was finally taken almost 10 years later, in 1994, to construct the LHC in the LEP tunnel [9]
1271 and the approval of the 4 main experiments that would take place at the 4 interaction points would
1272 come in 1997 [10] and 1998 [11]:

- 1273 • ALICE [12] has been designed in the purpose of studying quark-gluon plasma that is
1274 believed to have been a state of matter that existed in the very first moment of the universe.
- 1275 • ATLAS [13] and CMS [14] are general purpose experiments that have been designed with
1276 the goal of continuing the exploration of the Standard Model and investigate new physics.
- 1277 • LHCb [15] has been designed to investigate the preference of matter over antimatter in the
1278 universe through the CP violation.

1279 These large scale experiments, as well as the full CERN accelerator complex, are displayed on
1280 Figure 2.4. The LHC is a 27 km long hadron collider and the most powerful accelerator used for
1281 particle physics since 2008 [16]. The LHC was originally designed to collide protons at a
1282 center-of-mass energy of 14 TeV and luminosity of $10^{34} \text{ cm}^{-2}\text{s}^{-1}$, as well as Pb ions at a
1283 center-of-mass energy of 2.8 TeV/A with a peak luminosity of $10^{27} \text{ cm}^{-2}\text{s}^{-1}$. Run 1 of LHC,

when the center-of-mass energy only was half of the nominal LHC energy, was enough for both CMS and ATLAS to discover the Higgs boson [17] and for LHCb to discover pentaquarks [18] and confirm the existence of tetraquarks [19]. Nevertheless, after the Third Long Shutdown (LS3) (2024-2026), the accelerator will be in the so called High Luminosity LHC (HL-LHC) configuration [20], increasing its instantaneous luminosity to $10^{35} \text{ cm}^{-2}\text{s}^{-1}$ for pp collisions and to $4.5 \times 10^{27} \text{ cm}^{-2}\text{s}^{-1}$, boosting the discovery potential of the LHC. The HL-LHC phase should last at least another 10 years depending on the breakthrough this machine would lead to. Already a new accelerating device, the FCC, as been proposed to prepare the future of high energy physics after the LHC.

CERN's Accelerator Complex

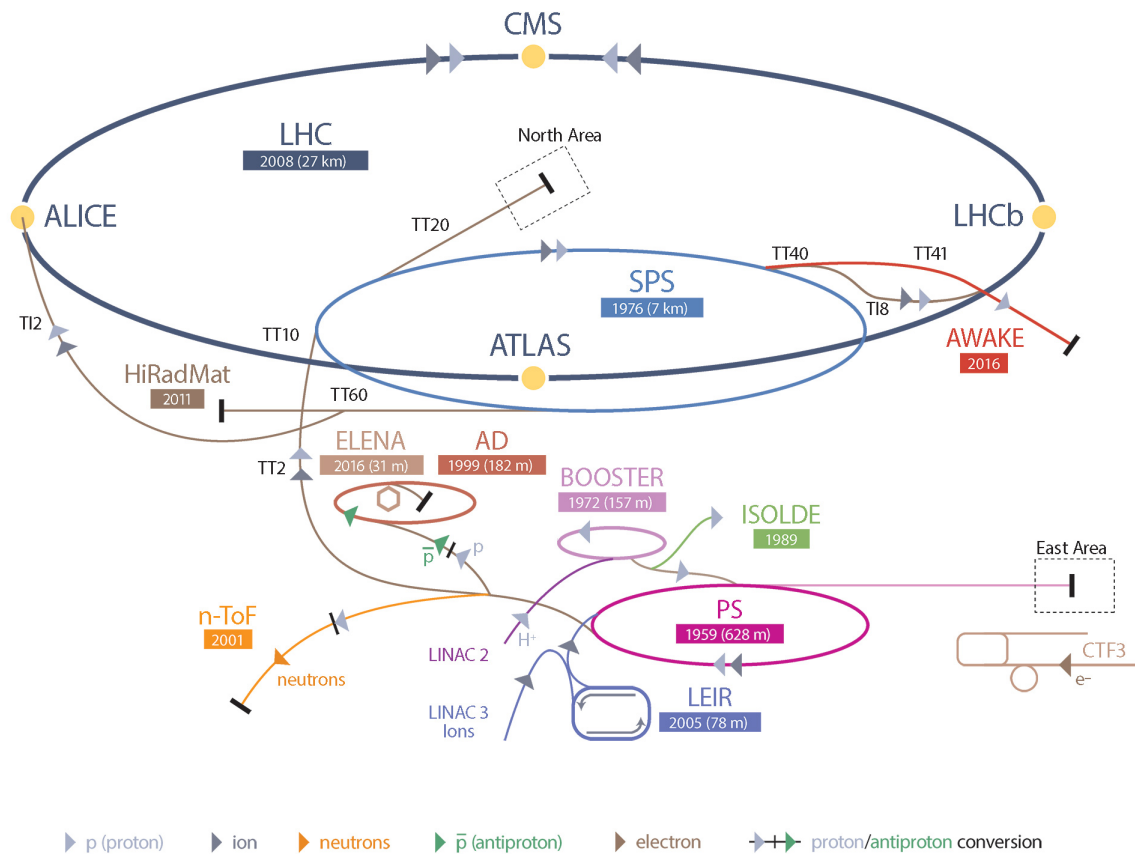


Figure 2.4: CERN accelerator complex.

2.2.1.1 Particle acceleration

The LHC is the last of a long series of accelerating devices. Before being accelerated by the LHC, the particles need to pass through different acceleration stages. All these acceleration stages are visible on Figure 2.4 and pictures of the accelerators are showed in Figure 2.5. The story of accelerated protons at CERN starts with a bottle of hydrogen gas injected into the

1298 source chamber of the linear particle accelerator *LINAC 2* in which a strong electric field strips
 1299 the electron off the hydrogen molecules only to keep their nuclei, the protons. The cylindrical
 1300 conductors, alternatively positively or negatively charged by radiofrequency cavities, accelerate
 1301 protons by pushing them from behind and pulling them from the front and ultimately give them an
 1302 energy of 50 MeV, increasing their mass by 5% in the process.

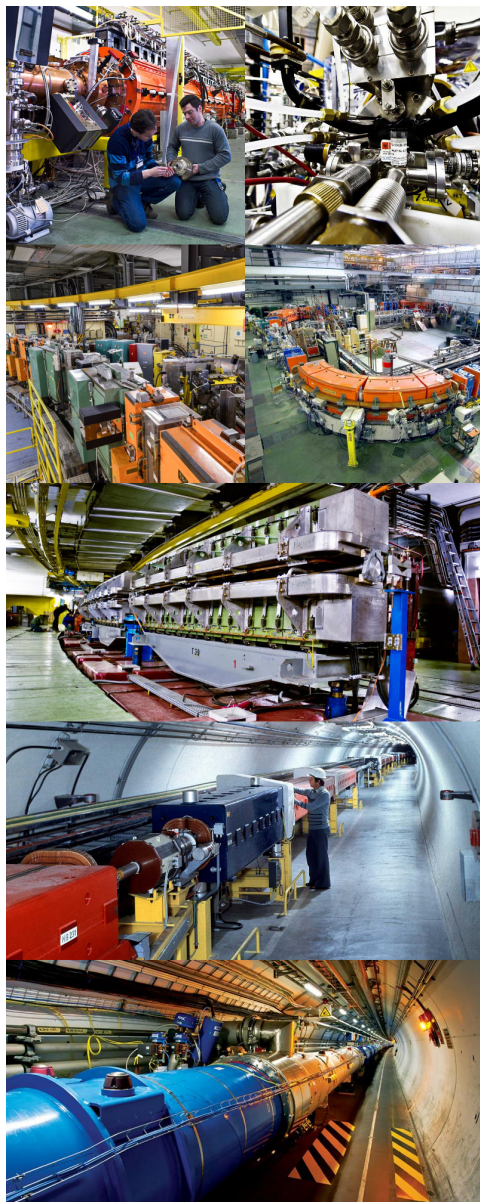


Figure 2.5: Pictures of the different accelerators. From top to bottom: first the LINAC 2 and the Pb source of LINAC 3. Then the Booster and the LEIR. Finally, the PS, the SPS and the LHC.

1303 When exiting the LINAC 2, the protons are divided into 4 bunches and injected into the 4
 1304 superimposed synchrotron rings of the *Booster* where they are then accelerated to reach an energy

of 1.4 GeV before being injected into the PS. Before the Booster was operational in 1972, the protons were directly injected into the PS from the LINAC 2 but the low injection energy limited the amount of protons that could be accelerated at once by the PS. With the Booster, the PS accepts approximately 100 times more particles.

The 4 proton bunches are thus sent as one to the PS where their energy eventually reaches 26 GeV. Since the 70s, the main goal of this 628 m circumference synchrotron has been to supply other machines with accelerated particles. Nowadays, not only the PS accelerates protons, it also accelerates heavy ions from the *Low Energy Ion Ring (LEIR)*. Indeed, the LHC experiments are not only designed to study *pp*-collisions but also *Pb*-collisions. Lead is first injected into the dedicated linear collider *LINAC 3*, that accelerate the ions using the same principle than LINAC 2. Electrons are stripped off the lead ions all along the acceleration process and eventually, only bare nuclei are injected in the LEIR whose goal is to transform the long ion pulses received into short dense bunches for LHC. Ions injected and stored in the PS were accelerated by the LEIR from 4.2 MeV to 72 MeV.

Directly following the PS, is finally the last acceleration stage before the LHC, the 7 km long *SPS*. The SPS accelerates the protons to 450 GeV and inject proton in both LHC accelerator rings that will increase their energy up to 7 TeV. When the LHC runs with heavy lead ions for ALICE and LHCb, ions are injected and accelerated to reach the energy of 2.8 TeV/A.

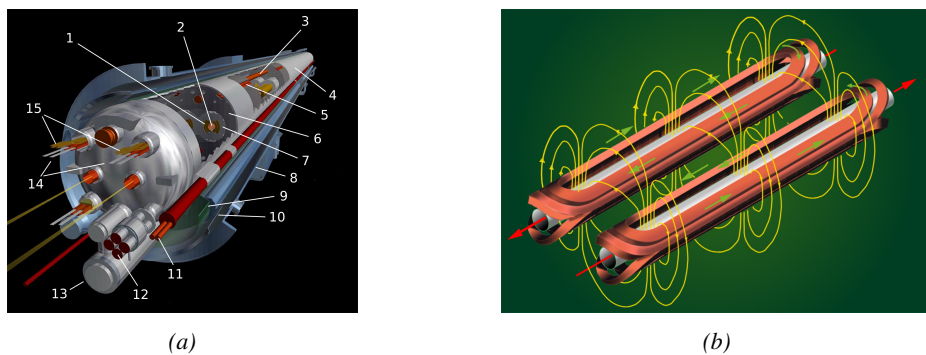


Figure 2.6: Figure 2.6a: schematics of the LHC cryodipoles. 1: Superconducting Coils, 2: Beam pipe, 3: Heat exchanger Pipe, 4: Helium-II Vessel, 5: Superconducting Bus-bar, 6: Iron Yoke, 7: Non-Magnetic Collars, 8: Vacuum Vessel, 9: Radiation Screen, 10: Thermal Shield, 11: Auxiliary Bus-bar Tube, 12: Instrumentation Feed Throughs, 13: Protection Diode, 14: Quadrupole Bus-bars, 15: Spool Piece Bus-bars. Figure 2.6b: magnetic field and resulting motion force applied on the beam particles.

The LHC beams are not continuous and are rather organised in bunch of particles. When in *pp*-collision mode, the beams are composed of 2808 bunches of 1.15×10^{11} protons separated by 25 ns. When in *Pb* collision mode, the 592 *Pb* bunches are on the contrary composed of 2.2×10^8 ions separated by 100 ns. The two parallel proton beams of the LHC are contained in a single twin-bore magnet due to the space restriction in the LEP tunnel. Indeed, building 2 completely separate accelerator rings next to each other was impossible. The dipoles of the 1232 twin-bore magnets are showed in Figure 2.6 alongside the magnetic field generated along the dipole section to accelerate the particles. The dipoles generate a nominal field of 8.33 T, needed to give protons and lead nucleons their nominal energy. Some 392 quadrupoles, presented in Figure 2.7, are also used to focus the beams, as well as other multipoles to correct smaller imperfections.

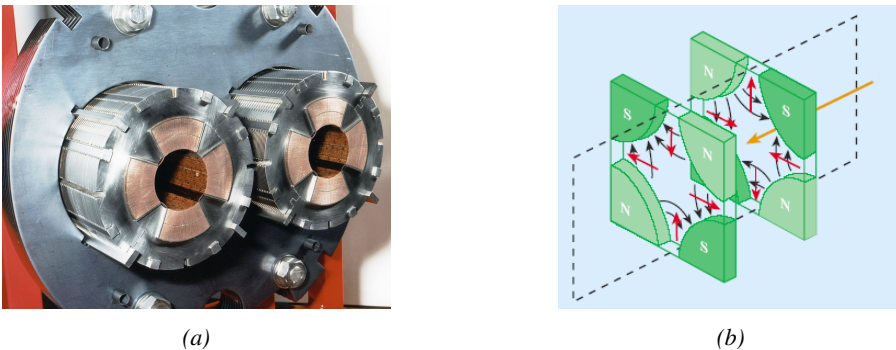


Figure 2.7: Figure 2.7a: picture of the LHC quadrupoles. Figure 2.7b: magnetic fields and resulting focussing force applied on the beam by 2 consecutive quadrupoles.

1333 2.2.2 CMS, a multipurpose experiment

1334 Among the four main LHC experiments is the Compact Muon Solenoid used as a multipurpose tool
 1335 to investigate the SM and physics beyond its scope. Proposed through a letter of intention in
 1336 1992 [14], and as its name suggests, this very compact detector's uses the muons as a clear tag of
 1337 most of SM and new physics interesting channels. In the original 1997 Technical Design
 1338 Report (TDR) [21], the very first sentences were stating that "*Muons are an unmistakable signature*
 1339 *of most of the physics LHC is designed to explore. The ability to trigger on and reconstruct muons*
 1340 *at the highest luminosities is central to the concept of CMS, the Compact Muon Solenoid.*" CMS
 1341 participated in the discovery of the Higgs boson and the measurement of its properties and
 1342 couplings together with ATLAS and is also actively involved in the search for SUSY and heavy ion
 1343 collisions. Other exotic physics are also being investigated using the data collected by CMS.
 1344 The CMS apparatus in itself is the heaviest detector ever built starring a 15m diameter and a 29 m
 1345 length for a total weight of 14 kT. A thick 4 T solenoid magnet located at the beam interaction
 1346 point hosts trackers and calorimeters. Extending in all directions around the magnet, heavy iron
 1347 return yokes are installed to extend the magnetic field and support a muon system. The apparatus
 1348 consists of a barrel, referring to the magnet and the detectors contained in it and the part of the
 1349 muon system built directly in the cylinder around the magnet, and of 2 endcaps in the forward and
 1350 backward region of the detector that closes the apparatus and complete the detection coverage
 1351 along the beam line. A front view on the barrel is provided in Figure 2.8 while a detailed view of
 1352 the apparatus is given in Figure 2.9.
 1353 In order to efficiently detect all long living particles and measure their properties with good
 1354 precision, the CMS detector uses an onion like layout around the interaction point in order to
 1355 maximize the covered solid angle. As detailed in Figure 2.10, in the innermost region of the
 1356 detector, closest to the interaction point, the silicon tracker records the trajectory of charged
 1357 particles. Around it, the electromagnetic calorimeter (ECAL) stops and measures the energy
 1358 deposition of electrons and photons. In the next layer, the hadron calorimeter (HCAL), hadrons are
 1359 stopped and their energy measured. These layers are contained inside of the magnet of CMS, the
 1360 superconducting solenoid. Outside of the magnet are the muon chambers embedded into iron return
 1361 yokes used to control the magnetic field and give muons, the only particles traveling completely
 1362 through the whole detector, a double bending helping in reconstructing their energy and trajectory.
 1363 Note that photons and neutral hadrons are differentiated from electrons and charged hadrons in the

¹³⁶⁴ calorimeters by the fact that don't interact with the silicon tracker and that they are not influenced
¹³⁶⁵ by the magnetic field.

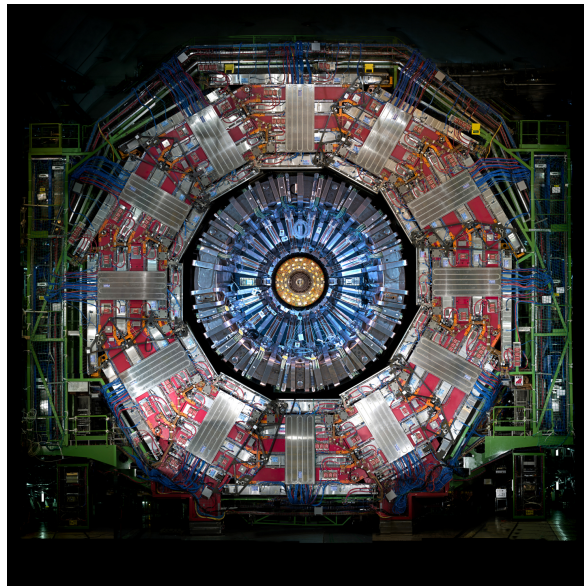


Figure 2.8: Picture of the CMS barrel. The red outer layer is the muon system hosted into the red iron return yokes. The calorimeters are the blue cylinder inside in magnet solenoid and the tracker is the inner yellow cylinder built around the beam pipe.

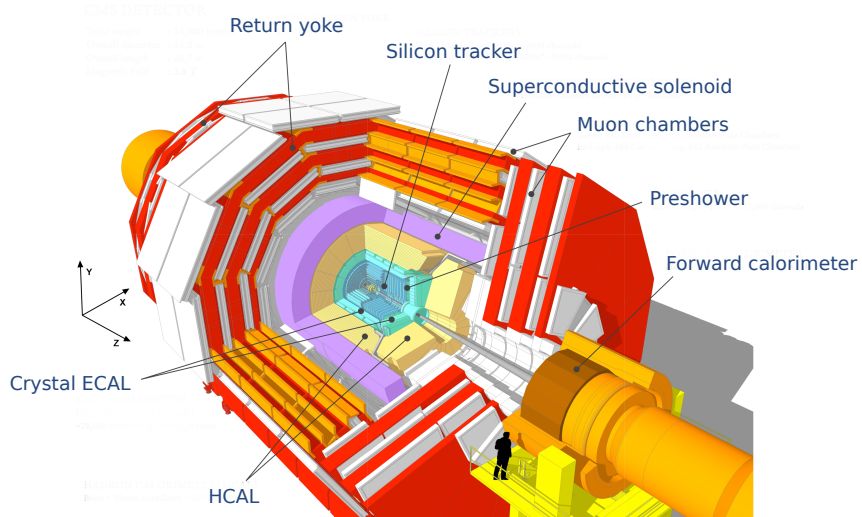


Figure 2.9: View of the CMS apparatus and of its different components.

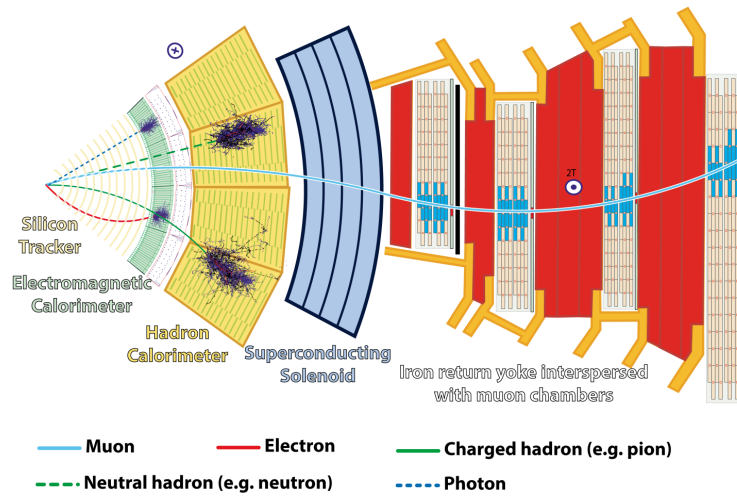


Figure 2.10: Slice showing CMS sub-detectors and how particles interact with them.

2.2.2.1 The silicon tracker, core of CMS

The silicon tracker visible on Figure 2.11 is divided into 2 different sub-systems: the *pixel detector* at the very core and the *microstrip detector* around it. This system is composed of 75 million individual readout channels with up to 6000 channels per squared centimeter for the pixels making it the world's biggest silicon detector. This density allows for measurements of the particle tracks with a precision of the order of $10\ \mu\text{m}$. This is necessary to reconstruct all the different interaction vertices with precision and have a precise measure of the curvature of the charged particles traveling through the magnetic field to estimate their charge and momentum.

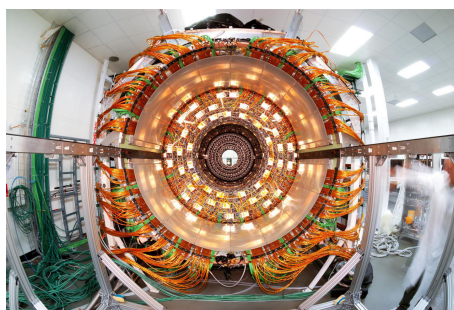


Figure 2.11: CMS tracker.

2.2.2.2 The calorimeters, measurement of particle's energy

The ECAL directly surrounding the tracker is composed of crystals of lead tungstate, PbWO_4 , a very dense but optically transparent material used to stop high energy electrons and photons. These crystal blocks basically are extremely dense scintillators which scintillate in fast, short light bursts proportionally to the energy deposition. The light is yielded rapidly and contained at 80% in the corresponding 25 ns lasting bunch crossing. Each crystal is isolated from the other by the carbon fiber matrix they are embedded in. It is composed of a barrel containing more than 60,000 crystals

1381 and of closing endcaps containing another 15,000 crystals. In front of the ECAL endcap is installed
 1382 a preshower detector made out of two layers of lead and silicon strip detectors to increase the
 1383 spatial resolution close to the beam line for pion-photon and single-double photon discrimination
 1384 purposes. Figure 2.12 shows the calorimeter inside of the magnet and the crystals.

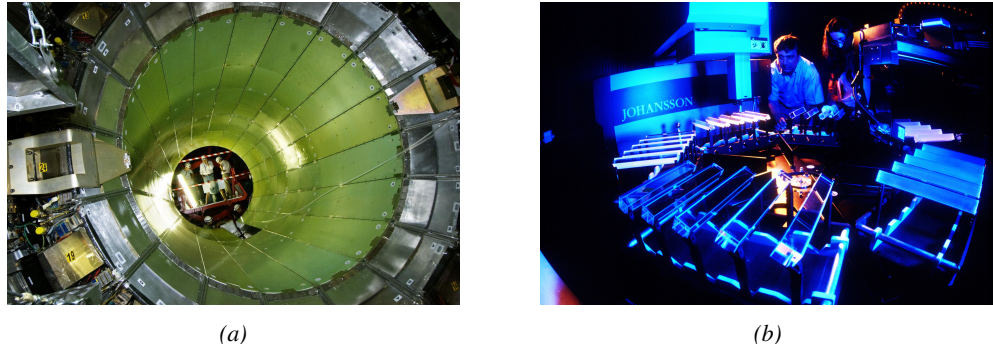


Figure 2.12: Figure 2.12a: picture of the ECAL. Figure 2.12b: picture of the lead tungstate crystals composing the ECAL.

1385 The next layer is the HCAL measuring the hadrons momentum and providing indirect hints of non
 1386 interacting neutral particles, such as neutrinos, as missing transverse momentum. Several layers of
 1387 brass or steel are interleaved with plastic scintillators readout by photodiodes using
 1388 wavelength-shifting fibers. The HCAL is also composed of a barrel, showed in Figure 2.13 and of
 1389 endcaps. It also features forward calorimeters on both sides of CMS in the region very close to the
 1390 beam line at high pseudorapidity ($3.0 < |\eta| < 5.0$). The role of these forward calorimeters, made
 1391 using steel and quartz fibers, is to measure very energetic hadrons.



Figure 2.13: CMS hadron calorimeter barrel.

1392 Finally, in the outer region of the apparatus, a muon system is used to trigger on potentially
 1393 interesting event by identifying muons. Indeed, the muon system is a very important part of the
 1394 CMS trigger infrastructure designed to efficiently select data from the enormous data flow received
 1395 by the detectors as the LHC delivers collisions at a rate of 40 MHz with a pile-ip of 20 to 30
 1396 collisions per bunch crossing during Phase-I and up to 200 during Phase-II, representing billions of
 1397 interactions per second among which a large quantity are low energy collisions that are not likely to
 1398 produce new reactions, and which is physically impossible for nowadays technologies to cope with.
 1399 Working at a maximum rate of 100 kHz, the trigger system is able to select the 100,000 more

interesting events by looking at the energy distribution of the interaction products and clear signatures like muons reconstructed by the muon system. the vast majority of these events will not finally be stored after physics tests are applied.

2.2.2.3 The muon system, corner stone of CMS

The challenge for the muon system is to provide a robust and fast measurement of muons. Three different subsystems, and soon 4 after LS2, compose the muon system as showed in Figure 2.14 in which a quadrant of the CMS detector focused on muon system. Drift Tube (DT) are found in the barrel region covering the low pseudorapidity region where particles transverse momentum is lower and Cathode Strip Chamber (CSC) are found in the endcap region covering higher pseudorapidity region closer to beam line where particles have a stronger momentum. The redundancy of the system is insured by Resistive Plate Chamber (RPC) in both the barrel and endcap region. Nevertheless, the region closest to the beam line ($|\eta| > 1.8$) was not equipped with RPCs. This lack of redundancy in the high pseudo rapidity region will be solved during LS2, the following Year End Technical Stop (YETS) in 2021 and 2022, and LS3 where the necessary services, detectors and Link System, that collects the data and synchronizes them, will be installed.

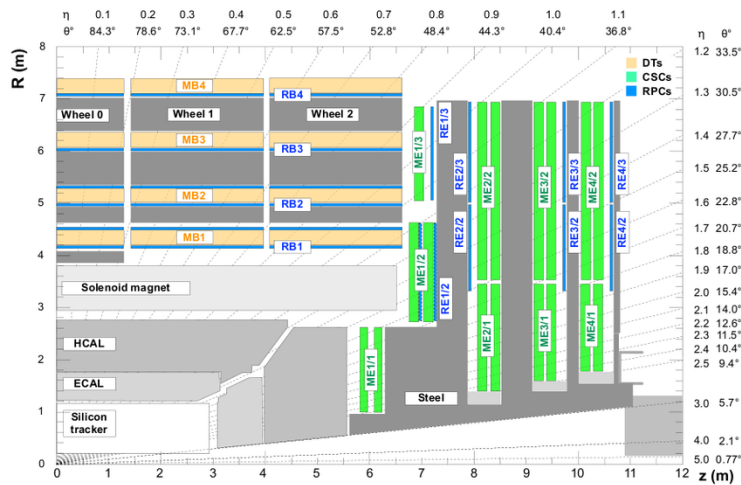


Figure 2.14: A quadrant of the muon system, showing DTs (yellow), RPCs (blue), and CSCs (green).

The barrel region is divided into 5 *wheels* made out of 4 *rings* of detectors with iron return yokes in between them whereas the endcaps are made out of 4 disks, each divided into pseudorapidity stations, 2 for CSCs (except for the first disk where 3 stations are equipped) and 3 for RPCs, although only 2 RPCs stations are equipped at present. The wheels and disks are showed in Figure 2.15. So far, each subsystem was dedicated to a particular task. DTs, in the barrel, and CSCs, in the endcaps, are used mainly for their spatial resolution. Indeed, DTs' resolution is of the order of 100 μm along both the $(r - \phi)$ and $(r - z)$ components while the resolution of CSCs is similar but varies in a range from 50 μm to 140 μm depending on the distance to the beamline. On the other hand, RPCs are used for their time resolution as they can deliver an information on the muon tracks within 1.5 ns. The 250 CMS DTs, found in the barrel covering the pseudorapidity region $0 < |\eta| < 1.2$ and whose structure is shown in Figure 2.16, are composed of 3 *superlayers* of DT cells. Two of these

superlayers are dedicated to measuring the ϕ coordinate of the muons and while the last one measures the η (or z) coordinate. Each superlayer consists on 4 layers of 60 to 70 DT cells arranged in quincunx to allow for a precise reconstruction of the muon path through the DT layers. Each DT cell is a rectangular aluminium gas volume with a central anode wire. Cathode strips are placed on the narrow surface of the cells and electrode strips are placed on the wide surface to help shaping the electric field to ensure a consistent drift velocity of electrons in the drift volume. These detectors are operated using a 85/15 mixture of Ar and CO_2 .

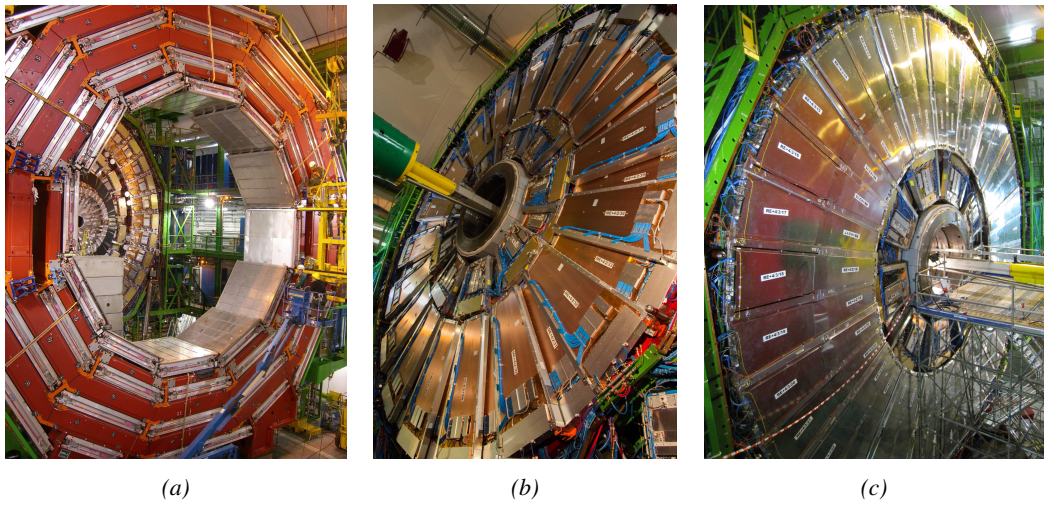


Figure 2.15: Figure 2.15a: Barrel wheel with its detector rings and return yokes. Figure 2.15b: CSC endcap disk with the 2 CSC stations. The outer station is made of 10 deg detectors while the inner station is made of 20 deg detectors. Figure 2.15c: RPC endcap disk. The inner station is not equipped and the inner CSC station can be seen.

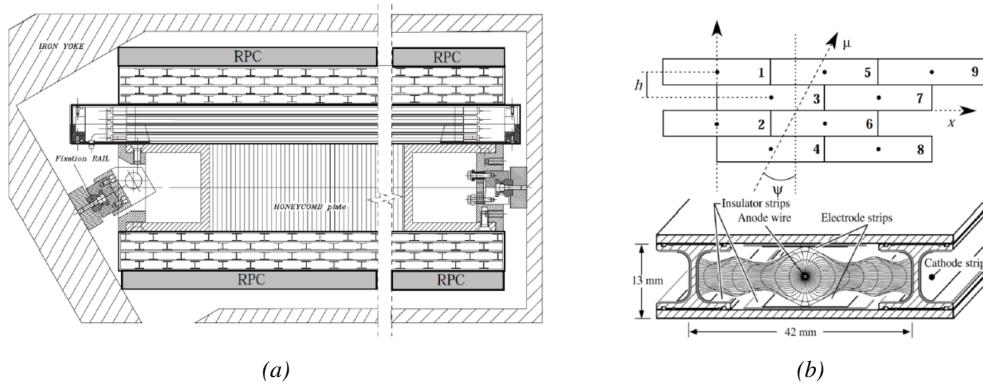


Figure 2.16: Figure 2.16a: Cross section of a DT module showing the two superlayers measuring the ϕ coordinate, perpendicular to the cross section plane, and the superlayer measuring the η coordinate, placed in between the two others with honeycomb and parallel to the cross section plane. The DT detector is sandwiched in between 2 RPCs whose readout strips are perpendicular to the cross section plane, measuring the ϕ coordinate. Figure 2.16b: A DT cell is shown together with its electric field. The path of a muon through a superlayer is shown.

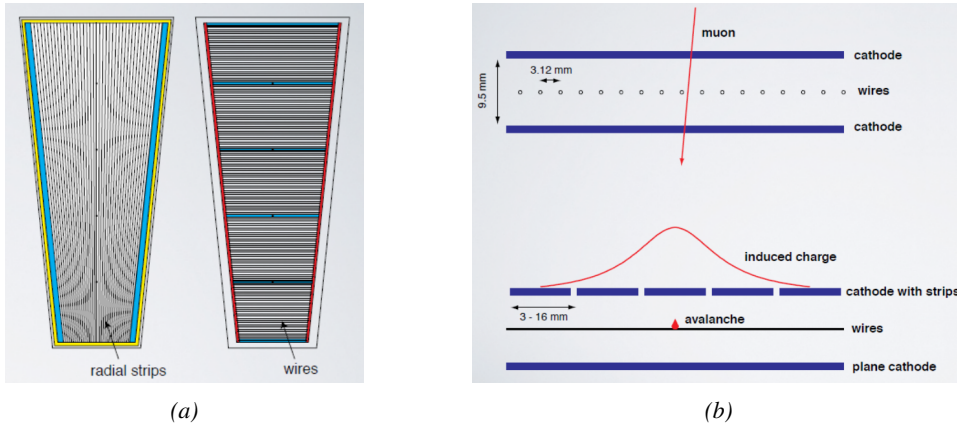


Figure 2.17: Figure 2.17a: cathode strips and anode wire layout of a CSC panel. Figure 2.17b avalanche development and charge collection by anode wires and induction on cathode strips inside of a CSC panel.

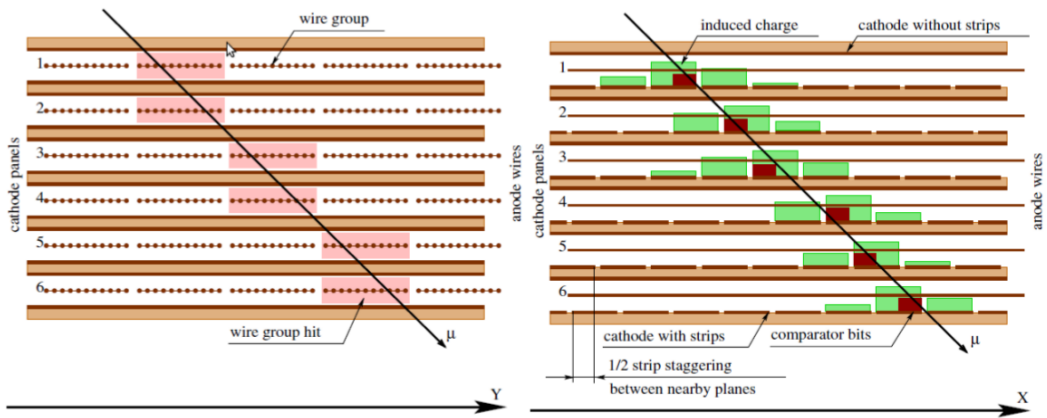


Figure 2.18: Muon track reconstruction through the 6 panels of a CMS CSC using the information of anode wire groups and cathode strip charge distribution combined with comparator bits to decide on which half strip the muon is more likely to have passed.

1434 The 540 CMS CSCs, found in the endcaps covering the pseudorapidity region $0.9 < |\eta| < 2.5$ and
 1435 described through Figure 2.17, are composed of 6 panels of CSC, each panel consisting in a wide
 1436 gas volume of 9.5 mm (7 mm in the case of ME1/1 station) containing anode wires and whose
 1437 surfaces are cathodes. The top cathode is a wide copper plane of the size of the gas volume. The
 1438 bottom cathode is divided into thin trapezoidal copper strips radially arranged to measure the
 1439 azimuthal coordinate ϕ with a pitch ranging from 8 to 16 mm. The $0.50 \mu\text{m}$ anode wires are placed
 1440 perpendicularly to the strips to measure radial coordinate r and are grouped by 10 to 15 with a wire
 1441 to wire space of 3.2 mm. In the specific case of ME1/1 placed against the HCAL endcap, the
 1442 $0.30 \mu\text{m}$ anode wires have a wire to wire distance of 2.5 mm and are not disposed perpendicularly
 1443 to the strips but slightly tilted by an angle of 29 deg to compensate for the lorentz force due to the
 1444 very strong local magnetic field of 4 T. These detectors are operated with a 40/50/10 mixture of
 1445 Ar, CO_2 and CF_4 . Combining the information of the multiple CSC panels, the detectors achieve a
 1446 very precise measurement of the muon track.

Despite their excellent spatial resolution, the wire chambers (DTs and CSCs) are limited in terms of time resolution by the fact that the charge needs to drift towards the anode wire and be collected before having the confirmation that a particle was detected as the drift volume is not used to develop avalanches. Indeed, the stronger electric field close to the anode wire triggers the avalanche and the gain of the detector. Due to the drift, the time resolution is thus limited at best to approximately 2 to 3 ns. In addition, even though the intrinsic time resolution of the tracking chambers is rather good compared to the 25 ns in between successive collisions, the processing time of the trigger system doesn't allow for very fast triggering as it provides a time precision of only 12.5 ns. Thus, detectors fully dedicated to timing measurement have been installed as a redundant system. These detectors are RPCs, also gaseous detectors but that use current induction instead of charge collection allowing for a time resolution of the order of 1.5 ns only. Theoretically, depending on the design used, RPCs could reach a time resolution of the order of 10 ps but in the context of LHC where bunch crossing happen every 25 ns, a time resolution of 1.5 ns is sufficient to accurately assign the right bunch crossing to each detected muon.

The 1056 RPCs equipping the CMS muon system both in the barrel and endcap regions and covering the pseudorapidity region $0 < |\eta| < 1.6$ are composed of two layers of RPC *gaps* as described in Figure 2.19. Each gap consists in two resistive electrodes made out of 2 mm thick Bakelite enclosing a 2 mm thick gas volume containing a 95.2/4.5/0.3 mixture of $C_2H_2F_4$, $i - C_4H_{10}$ and SF_6 . Due to this geometry, the electric field inside of a gap is homogeneous and linear at every point in the gas translating into a uniform development of avalanches in the gas volume as soon as a passing muon ionises the gas. The two gaps sandwich a readout copper strip plane. A negative voltage is applied on the outer electrodes, used as cathodes, and the inner electrodes, the anodes, are simply connected to the ground as well as the readout panel that picks up the current induced by the accumulated charge of the growing avalanches in one or both of the gas gaps. This OR system allows for a lower gain (i.e. a lower electric field) on both gaps to reach the maximal efficiency of such a detector.

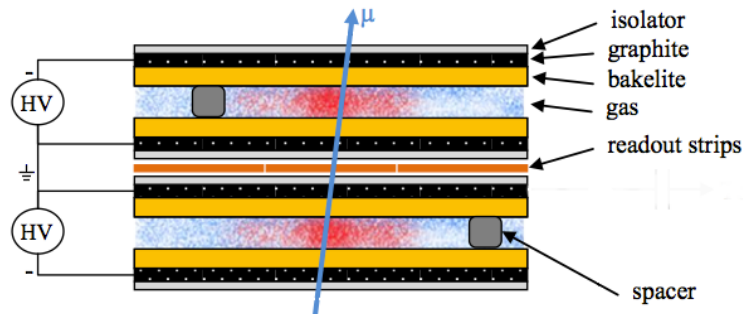


Figure 2.19: Double gap layout of CMS RPCs. Muons passing through the gas volumes will create electron-ion pairs by ionising the gas. this ionisation will immediately translate into a developing avalanche.

3

1473

1474

Muon Phase-II Upgrade

1475 The very first proton beam successfully circulated in the LHC in September 2008 directly followed
1476 by an incident leading to mechanical damage that would delay the LHC program for a year until
1477 November 2009, the very first collisions at a center-of-mass energy of 7 TeV taking place in March
1478 2010. The energy of the beam would be increased after a First Long Shutdown (LS1) starting early
1479 2013 after less than 3 years of data taking. Nevertheless, this first data taking period at only 7 TeV
1480 was sufficient to claim the discovery of a new particle compatible with the Higgs boson in July
1481 2012. During the 2 years of shutdown, the upgrade of the accelerator allowed for several
1482 maintenances along the beam pipes, repair and consolidation of magnet connection and
1483 high-current splices. But not only the LHC was upgraded. Indeed, the experiments at the 4
1484 collision points also took the advantage of this time to upgrade their system in prevision of the next
1485 LHC run (Run-II) until 2018 and the Second Long Shutdown (LS2) as the luminosity and energy of
1486 the beam would be continuously increasing. By the end of Run-II, the luminosity will have reached
1487 twice its nominal value when the center-of-mass energy has already got close to its nominal value
1488 by reaching an historical 13 TeV for the first time in 2017.
1489 The next long shutdown will occur at the end of this year and will again be the occasion for similar
1490 maintenance and consolidation in prevision of Run-III and the future upgrade of LS3. Still, the
1491 main occupation of LS2 on LHC side will be the upgrade of LHC injectors. On the experiments
1492 side, LHCb and ALICE will, in a very tight schedule, implement major upgrades while ATLAS and
1493 CMS will wait until LS3 to upgrade their detectors in prevision of high luminosity *LHC-Phase-II*.
1494 ALICE main challenge is an upgrade of their apparatus to cope with the 50 kHz $Pb - Pb$
1495 collisions. Similarly, LHCb will upgrade their frontend readout electronics to cope with the full
1496 40 MHz collisions delivered by LHC. ATLAS will perform standard maintenance and CMS will
1497 focus on the urgent upgrade of the pixel detector and on the installation of new muon detectors in
1498 order to take profit of LS2 time to mitigate the upgrade of detectors foreseen during LS3. Run-III
1499 will start in 2021 with the LHC at its nominal center-of-mass energy and will bring LHC-Phase-I to
1500 an end at the end of 2023. By then the luminosity will only increase to reach 2.5 times the nominal
1501 luminosity but during these 3 years of run, the LHC will deliver as much integrated luminosity as

1502 what what brought during the almost 7 years of both Run-I and II of data taking. Phase-I will end
1503 with an overall 300 fb^{-1} delivered.

1504 3.1 High Luminosity LHC and muon system requirements

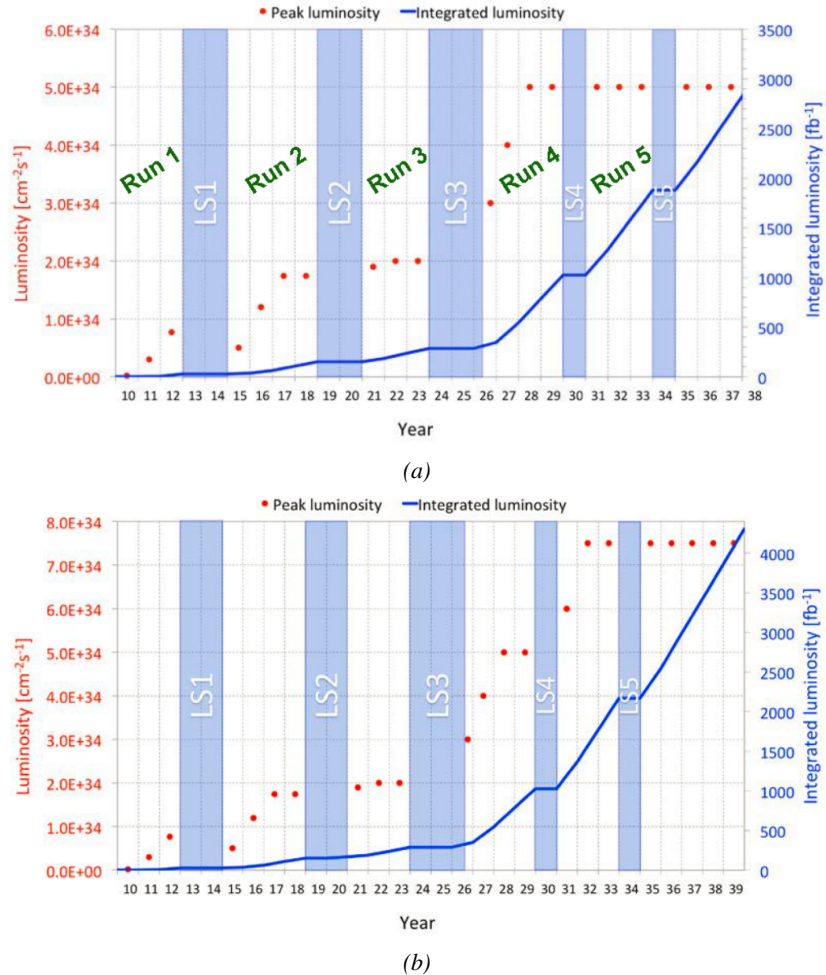


Figure 3.1: Detailed timeline projection of for LHC and HL-LHC operation until 2039 showing the evolution of the instantaneous and integrated luminosity as designed (Figure 3.1a) and in the ultimate case where the instantaneous luminosity is increased to $7.5 \times 10^{34} \text{ cm}^{-2}\text{s}^{-1}$ (Figure 3.1b) [20, 22].

1505 After approximately 15 years of operation, the LHC will undergo a new series of upgrade during
1506 the LS3 in order to boost its discovery potential as showed in Figure 3.1. This moment onward is
1507 what is referred to HL-LHC or Phase-II. The goal is to aim for a luminosity 5 to 7 times stronger
1508 than the nominal one trying to reach even 10 times this value if possible. Increasing the luminosity
1509 means that the beam size at the collision points needs to be reduced to boost the number of
1510 collisions per bunch crossing. For this purpose, new focusing and bending magnets, and collimators
1511 will be installed at the collision points as well as newly developed "crab cavities" that will tilt the

1512 particle bunches just prior to the collisions by giving them transverse momentum and thus
 1513 increasing their meeting area. In addition, the full proton injection line will be upgraded.
 1514 Over its full lifetime, the HL-LHC is expected to deliver an outstanding integrated luminosity of
 1515 3000 fb^{-1} leading, in the case of Higgs studies to measuring the couplings of the boson to a
 1516 precision of 2 to 5% thanks to the estimated 15 millions of Higgs created every year providing a
 1517 more precise measurement of potential deviations from the theoretical predictions. SUSY and
 1518 heavy gauge boson studies would also see their mass range limits pushed away by at least 1 TeV
 1519 and could lead to a new breakthrough. SUSY is a particularly important topic as it could give an
 1520 answer to why the Higgs boson can stay so light while coupled to heavy particles by introducing
 1521 the contributions of the super partners on top of providing dark matter candidates. Finally, the
 1522 increase of luminosity will give the possibility to investigate "exotic" mode like for example the
 1523 models introducing extra dimensions to explain the hierarchy problem.
 1524 On the experiments side, the pile-up (PU) will be increased up to 150 to 200 interactions per bunch
 1525 crossing in ATLAS and CMS, making necessary an strong upgrade of the trigger system and of the
 1526 inner trackers and of the calorimeters. Both ATLAS and CMS will also need to upgrade the muon
 1527 trigger at the level of the endcaps mainly focusing on the coverage near the beam line in order to
 1528 increase the detection acceptance and event selection. Moreover, the increased luminosity will also
 1529 lead to an increased background rate and a faster ageing of the detectors. This PhD work takes
 1530 place into this very specific context of muon detector consolidation and certification for the
 1531 HL-LHC period in order to provide the CMS experiment with robust new detectors and confirm
 1532 that the present system will survive through the next 20 years of HL-LHC.

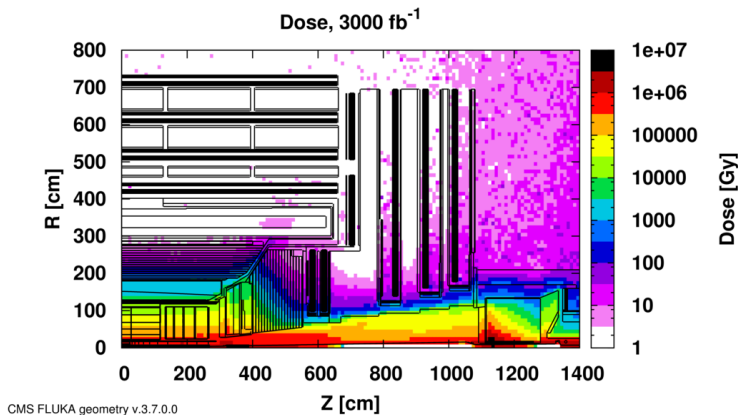


Figure 3.2: Absorbed dose in the CMS cavern after an integrated luminosity of 3000 fb . Using the interaction point as reference, R is the transverse distance from the beamline and Z is the distance along the beamline.

1533 The end of 2018 will mark the beginning of LS2 and the start of Phase-II upgrade activities. From
 1534 the HL-LHC period onwards, i.e. past LS3, the performance degradation due to integrated radiation
 1535 as well as the average number of inelastic collisions per bunch crossing, seen as pile-up into the
 1536 detectors' readout that far exceeds this of the original LHC plans, will rise substantially and
 1537 become a major challenge for all of the LHC experiments, like CMS, that were forced to address an
 1538 upgrade program for Phase-II [23]. Dealing with the data from the muon detectors will force to
 1539 upgrade the detectors and electronics towards the most recent technologies. Simultaneously, this
 1540 will push new latency requirements onto the Level-1 trigger and the Data Acquisition (DAQ) that

will only be fulfilled by upgrading the system with electronics having deeper buffering and faster processing. Simulations of the expected distribution of absorbed dose in the CMS detector under HL-LHC conditions show, in Figure 3.2, that detectors placed close to the beam line will have to withstand high irradiation, the radiation dose being of the order of a few tens of Gy.

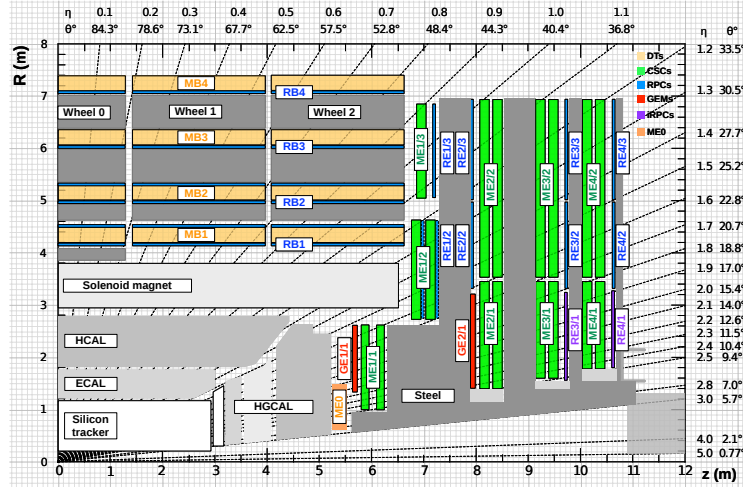


Figure 3.3: A quadrant of the muon system, showing DTs (yellow), RPCs (blue), and CSCs (green). The locations of new forward muon detectors for Phase-II are contained within the dashed box and indicated in red for GEM stations (ME0, GE1/1, and GE2/1) and dark blue for improved RPC (iRPC) stations (RE3/I and RE4/I).

The increase of irradiation close to the beam line will affect the background rate seen by the muon detectors in this area and tracking muons will prove to be difficult as this region is not yet equipped with all the detectors that were already foreseen for Phase-I. Improving this situation will come with the increase of hit numbers recorded along the particle track to reduce the ambiguity on muon versus background detection. Moreover, the measurement of small production cross-section and/or decay branching ratio processes, such as the Higgs boson coupling to charge leptons, and in particular to muons, or the $B_s \rightarrow \mu^+ \mu^-$ decay, is of major interest and specific upgrades in the forward regions of the detector will be required to maximize the physics acceptance to the largest possible solid angle.

To ensure proper trigger performance within the present coverage, the muon system will be completed with new chambers and the electronics of the present system will need to be upgraded to ensure an efficient triggering. Figure 3.3 shows the addition of Gas Electron Multiplier (GEM) and improved RPC (iRPC) in the pseudo-rapidity region $1.6 < |\eta| < 2.4$ to complete the redundancy of the already existing CSCs as originally scheduled in the CMS Technical Proposal [24]. A first step into this direction will be taken by installing GEMs on the first endcap disk in position GE1/1 during LS2, during which preparations for the future installation of more GEMs and RPCs will take place by installing the needed services. During the YETS following LS2, iRPCs will be installed on the third and fourth endcap disks in position RE3/I and RE4/I, and more GEMs will equip the second endcap in position GE2/1 and the inner layer, closest to the HCAL endcap called ME0 during LS3, finally completing the redundant coverage of the muon system and extending it a little by extending the reach to $|\eta| = 2.8$, the redundancy in the region $2.4 < |\eta| < 2.8$ being maintained by the 6 GEM layers contained in each ME0 detector that provide enough tracking points to

1567 efficiently reject neutron-induced background.

1568 Nevertheless, the region beyond $|\eta| > 2.8$ and extending to $|\eta| = 5.0$ only is covered by the
1569 forward HCAL detectors and lack redundant muon detector coverage. Extensions of the tracker in
1570 the context of HL-LHC will increase its coverage up to $|\eta| = 4.0$ but the identification of muons
1571 and measurement of their energy with reasonable precision only using the tracker is nearly
1572 impossible. Thus, this increased tracker coverage range needs to be put in parallel with a matching
1573 muon detector and will open doors to multi-lepton final states in which leptons are likely to have a a
1574 low transverse momentum and to be found near the beam line.

1575 Finally, as the muon system is composed only of gaseous detectors, strong environmental concerns
1576 have risen over the last years as the European directives will restrict the use of fluorine based gas
1577 mixtures. Both the CSC and RPC subsystems, using CF_4 , $C_2H_2F_4$, or SF_6 , will need to adapt
1578 their working gas in order to strongly reduce the greenhouse potential of the mixtures released into
1579 the atmosphere due to gas leaks.

1580 3.2 Necessity for improved electronics

1581 Drift Tubes and Cathode Strip Chambers are important components used to identify and measure
1582 muons, especially thanks to their spatial resolution of the order of $100\ \mu m$. Nevertheless, the
1583 luminosity and irradiation during HL-LHC will cause serious event loss and ageing on the
1584 electronics of these subsystems that will comprise the triggering and data transferring needs of
1585 CMS. Thus, electronics upgrade are foreseen to address these expected problems. While only the
1586 RPCs' electronic system is able to operate under Phase-II requirements, DTs and CSCs will need to
1587 improve their trigger accept rate and latency to ensure that Level-1 trigger threshold stays at the
1588 same level [25], and DAQ data transfer rate, that respectively need to achieve a minimum of
1589 $500\ kHz$, get down to $12.5\ \mu s$ [26], and increase to $1082\ Gbit/s$ DTs and to $1026\ Gbit/s$ for CSCs.
1590 As of today, the Level-1 trigger accept rate of DTs doesn't reach $300\ kHz$ while this of CSCs is
1591 bellow $250\ kHz$ but the foreseen upgrades are expected to increase the rate way beyond the
1592 requirement in the of DTs and up to $4\ MHz$ for CSCs [23].

1593 The first version of Minicrate electronics (MiC1) used by DTs don't allow for high enough trigger
1594 rate. In addition to this problem, it was showed that these electronics contain components that are
1595 not radiation hard enough to sustain HL-LHC conditions and thus, a too large number of channels
1596 may fail due to radiations. Considering the most optimistic scenario, at least 19% of the channels
1597 could have failed by LS4, as explicitated in Figure 3.4, far before the end of the HL-LHC campain.
1598 The MiC1 will be replaced on each detector by an improved version referred to as MiC2 while
1599 front-end electronics and high-voltage modules will not need any replacement. On the other hand,
1600 CSCs showed that there electronics would be able to live through the 10 years of Phase-II but the
1601 limited buffer depth might cause memory overflows and readout inefficiencies with a fraction of
1602 event loss ranging from 5 to more than 10% at an instantaneous luminosity similar to which of
1603 HL-LHC depending on the expected background, as showed on Figure 3.5 through the different
1604 detector positions. Thus the replacement of CSCs' cathode front-end boards (CFEBs) by digital
1605 ones, DCFEBs, with deeper buffer would permit to make event loss negligible and satisfy HL-LHC
1606 requirements [23].

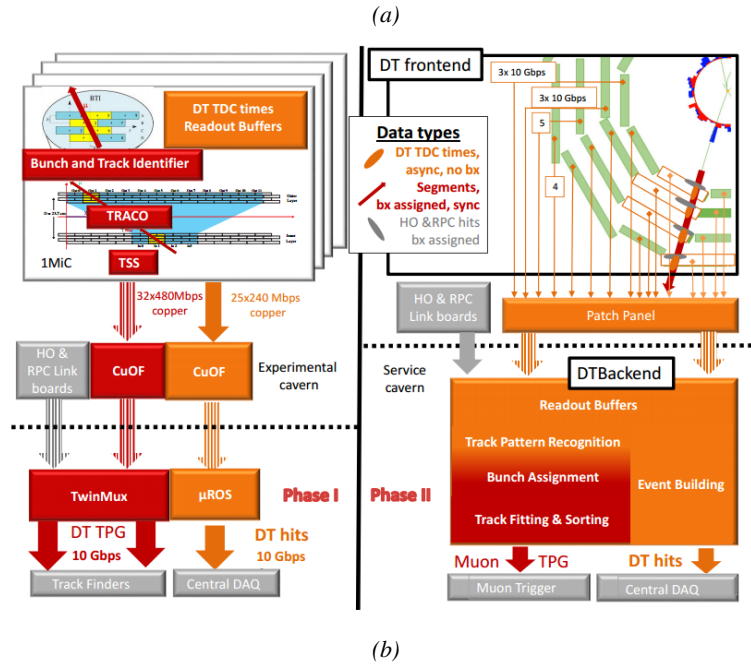
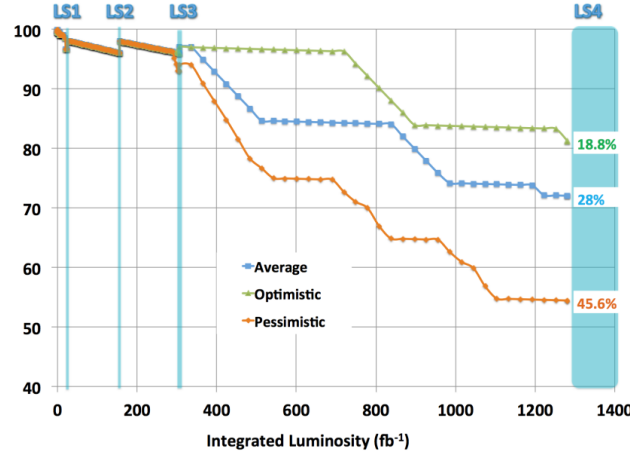


Figure 3.4: Figure 3.4a: Extrapolated fraction of failing channels of the present DT MiC1 electronics as a function of the integrated luminosity for different scenari until LS4. Figure 3.4b: Comparison of the current (left) and upgraded (right) DT data processing. So far, the data is sent to service cavern of CMS facility via copper-to-optical-fiber translators (CuOF) by each MiC1. There, data including RPCs and outer hadron calorimeter is combined into trigger primitives (TPG) and transmitted by the TwinMux system to CMS Track Finder. The time-to-digital converter (TDC) data is collected and sent to the CMS data acquisition system (DAQ) by the micro read-out server (μ ROS). After the upgrade, the TDC data will be sent via optical links to a patch panel inside the experimental cavern by each MiC2, and transferred to the back-end, where triggering and event building will be performed.

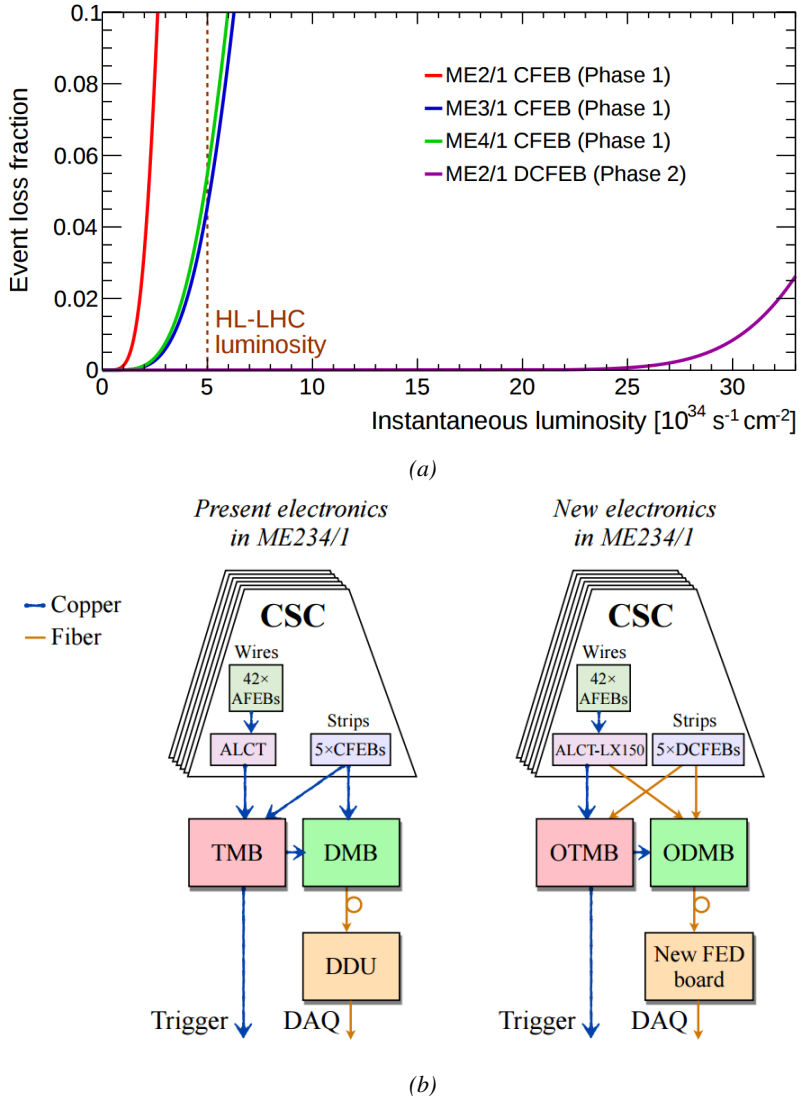


Figure 3.5: Figure 3.5a: The event loss fractions as a function of the instantaneous luminosity is compared for CFEBs (Phase-1) and DCFEBs (Phase-II) at different CSC locations. HL-LHC luminosity is marked with the dashed brown line. Figure 3.5b: Comparison of the current (left) and upgraded (right) CSC data processing. A part of the connections in between ALCTs and DCFEBs, and the trigger mother boards (TMBs) and data acquisition mother boards (DMBs) will be upgraded toward optical data transfer. The detector dependent units (DDUs) used as interface in between CSCs' front-end electronics and the CMS DAQ will be replaced by new FED boards.

All these new DT and CSC electronics will be connected to the trigger electronics via optical links to ensure a faster communication. The main change will come from the new DT minicrate modules which will not anymore be responsible for trigger and event building logic which will be transferred to the back-end electronics instead located in the service cavern via the patch pannels to which the Time-to-Digital Converter (TDC) data will be sent. The trigger and data transfer logic will barely change for CSCs. The existing copper cable connections of cathode and anode FEBs (CFEBs, and

1613 AFEBs which data is transmitted through the ALCTs) toward the trigger and data mother boards
 1614 (TMBs and DMBs) will simply be replaced by optical fibers and the TMBs and DMBs upgraded
 1615 with optical versions (OTMBS and ODMBs). As a new feature, the full anode wire data from
 1616 ALCTs will be sent to the ODMBs causing a lack of FPGA memory resources in these ALCT
 1617 boards that will thus need replacement.

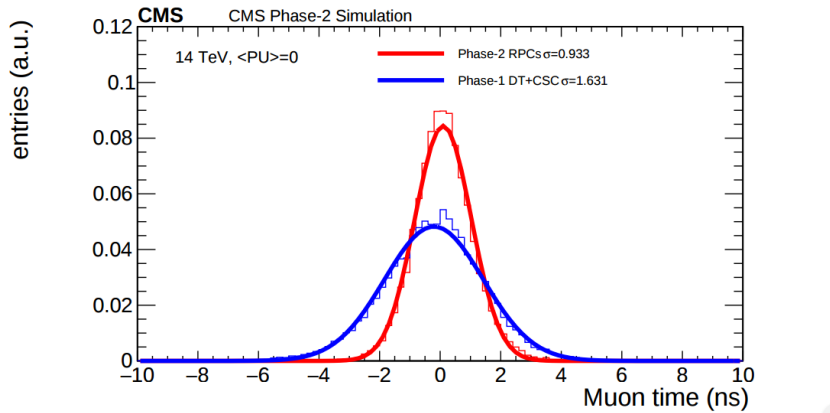


Figure 3.6: Comparison of the simulated time residuals in between reconstructed and true muon times without (blue) and with (red) the upgraded RPC link system.

1618 The upgrade on the side of Resistive Plate Chambers will then not come from their on-board
 1619 electronics but from the Link System located in the service cavern of CMS and that connects the
 1620 front-end electronics data of RPCs into CMS trigger processors. The main motivation for such an
 1621 upgrade is that the electronic board composing the link system are built using obsolete components
 1622 and weak components that can easily suffer from the electromagnetic noise. These components
 1623 may be the source of failing channels throughout Phase-II. Moreover, these link boards were
 1624 originally designed only to match RPC digitized signals with the corresponding bunch crossing.
 1625 Due to this feature, the time resolution of the full RPC chain is thus limited to 25 ns and does not
 1626 exploit the full time resolution of the detectors. This would make the synchronization of the RPC
 1627 system easier and allow to have a finer offline background removal within the 25 ns in between
 1628 bunch crossings thanks to the order of magnitude gained in terms of time resolution.
 1629 Upgrading RPC link system will require the installation of 1376 new link boards and 216 control
 1630 boards. The new boards will make use of the recent progress made with fast FPGAs and will be a
 1631 great improvement to the ASICs formerly used as they will be able to process signals from several
 1632 detectors in parallel. The benefit from using the full RPC time resolution thanks to the upgraded
 1633 link system can be seen through Figure 3.6 where the resolution of the RPC system itself is better
 1634 than which of DTs and CSCs that was used until now.

1635 3.3 New detectors and increased acceptance

1636 In the present muon system, the redundancy of was assured by RPCs used for their good timing
 1637 performances. The extension of the muon system towards higher pseudo-rapidity in order to
 1638 complete the redundancy in this very region and to contribute to the precision of muon momentum
 1639 measurements will require muon chambers with a spatial resolution less or comparable to the

1640 contribution muon of multiple scattering through the detector volume [21]. Most of the plausible
 1641 physics is covered only considering muons with $p_T < 100$ GeV thus, in order to match CMS
 1642 requirements, a spatial resolution of $\mathcal{O}(\text{few mm})$ will be necessary for the proposed new RPC
 1643 stations while the GEMs will need a resolution better than 1 mm, as showed by the simulation in
 1644 Figure 3.7.

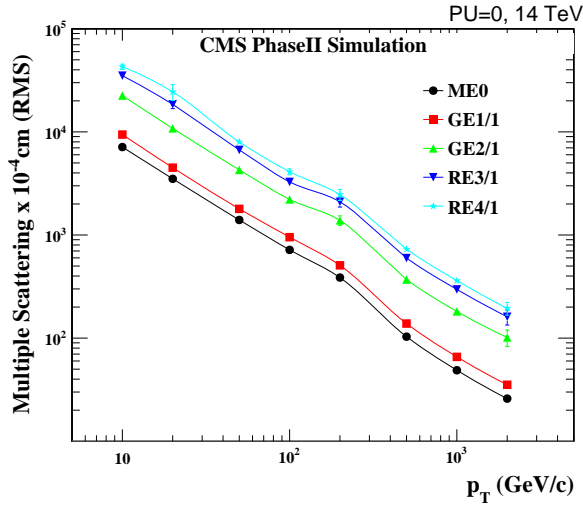


Figure 3.7: RMS of the multiple scattering displacement as a function of muon p_T for the proposed forward muon stations. All of the electromagnetic processes such as bremsstrahlung and magnetic field effect are included in the simulation.

1645 3.3.1 Improved forward resistive plate chambers

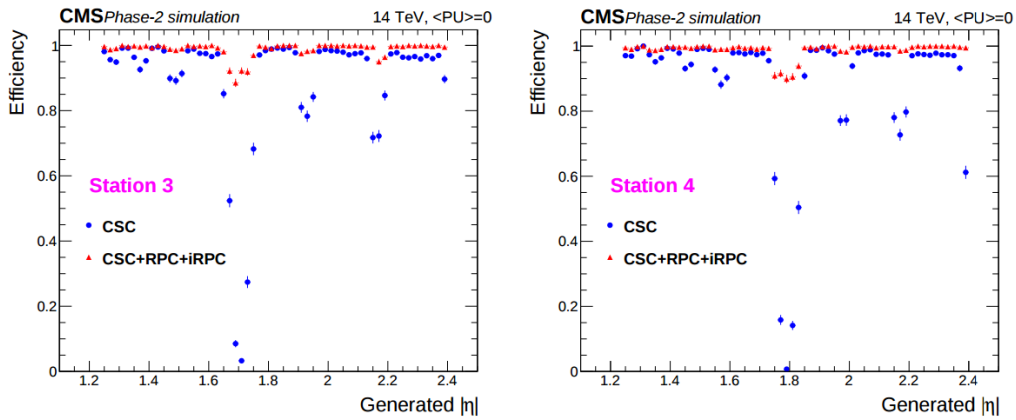


Figure 3.8: Simulation of the impact of RPC hit inclusion onto the local trigger primitive efficiency in station 3 (left) and station 4 (right). The contribution of iRPC starts above $|\eta| = 1.8$.

1646 Figure 3.3 shows that the iRPCs that will equip the third and fourth endcap disks in position RE3/1
 1647 and RE4/1 will finally be the partners of the CSCs in position ME3/1 and ME4/1 and complete

Phase-I plans but bringing the needed upgrades in the scope of Phase-II as the older chambers are not suitable to equip the forward region of CMS due to HL-LHC rates and charge deposition. By completing the redundancy, more track along the muon trajectory will be available and the lever arm will be improved. The benefits from extending the redundancy of the muon system with iRPCs to the forward most region is showed in Figure 3.8 in which the trigger efficiency is showed with and without RPCs in which it is possible to see that the efficiency of CMS trigger with the complete redundancy is improved is above 95% in the region $|\eta| > 1.8$ as the iRPCs help filling the holes in the CSC system.

The detectors that will be installed in the coming years will be similar to the already existing RPC system. 18 of the new chambers, each spanning 20° in φ around the beam axis with 96 radially oriented trapezoidal read-out strips, will cover each muon endcap disk leading to the production of 72 iRPCs. The main difference with the old RPC chambers is that these detectors will not have readout strips segmented in η as by using fast front-end electronics the strips will be read-out on both sides allowing for a radial spatial resolution of the order of 2 cm in order to contribute to the better reconstruction of muon in the forward region where the bending of muons by the magnetic field is low. This is motivated by the fact that, in the case a η segmentation was used, at least 5 pseudorapidity partitions would have been necessary to reach the minimal radial spatial resolution (≈ 20 cm). Having only one strip read-out from both along the chamber reduces by 60% the total number of channels and the necessary cabling and allows for a better spatial resolution. The strip pitch will range from 6.0 mm (5.9 mm) on the high pseudo-rapidity end to 12.3 mm (10.9 mm) on the low one on position RE3/1 (RE4/1). The spatial resolution in the direction perpendicular to the strips should reach approximately 3 mm, better than the minimal needed resolution (Figure 3.7), and the overall time resolution of the new installation will be equally 1.5 ns, as for the present due to the same link system being used.

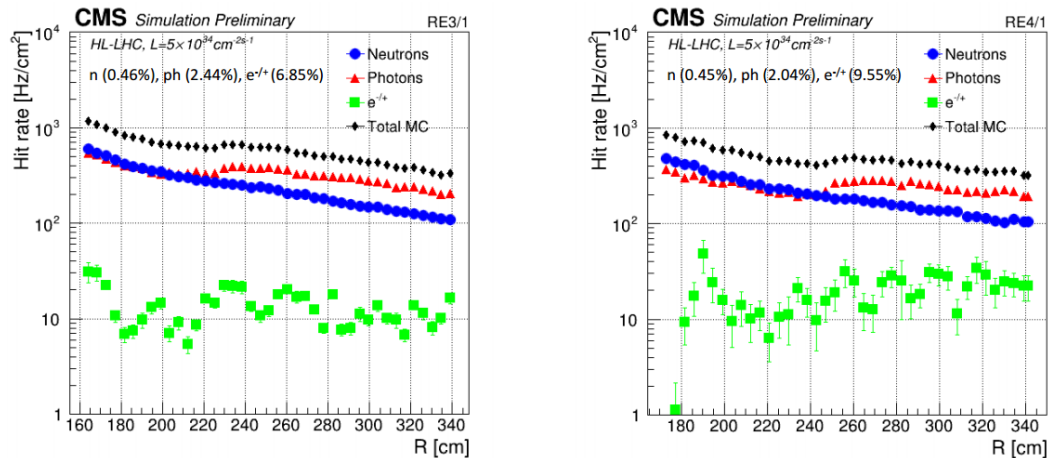


Figure 3.9: Expected hit rate due to neutrons, photons, electrons and positrons at HL-HLC instantaneous luminosity of $5 \times 10^{34} \text{ cm}^{-2}\text{s}^{-1}$ in RE3/1 and RE4/1 chambers. The sensitivities of iRPCs used in the simulation for each particle are reported and differ from one endcap disk to another as the energies of the considered particles varies with the increasing distance from the interaction point.

Nevertheless, having only a single strip instead of pseudo-rapidity segmentation will increase the probability of double hits in the same channel. This probability was estimated to be low enough as

it shouldn't exceed 0.7%. This estimation was made assuming an average hit rate per unit area of 600 Hz/cm² in the iRPCs (see Figure 3.9), a cluster size (average number of strips fired per muon) of 2, a strip active area of 158.4 × 0.87 cm² and a safety factor 3 leading to an estimated rate per strip of 380 kHz corresponding to an average time interval of 2600 ns in between 2 consecutive hits. The time for a signal to go through the full strip length is about 10 ns to which can be added 1 ns of dead time and 2 TDC clock cycles of 2.5 ns for a minimal time interval of 16 ns necessary to avoid ambiguities. The probability of having ambiguous double hits in a strip in then the ratio in between this minimal time interval in between 2 consecutive hits and the average time interval estimated from the rate the detectors are subjected to.

The instantaneous luminosity at HL-LHC being very high, the rates at the level of the new chambers needed to be simulated in order to understand the necessary requirements for these detectors. The simulated results for different background components (neutrons, photons, electrons and positrons) are showed in Figure 3.9 assuming known sensitivities to these particles. It is showed that on average over the iRPC areas the rates would be of the order of 600 Hz/cm² (600 Hz/cm² seen in RE3/1 and 480 Hz/cm² in RE4/1) [27]. Thus, taking into account a safety factor of about 3, it was decided that improved RPCs should at least be certified for rates reaching 2 kHz/cm² which would be achieved thanks to several improvements on the design and on the electronics. The detectors design will be based on the existing RPC design as they will be double gaps. Similarly to the existing RPC system, the electrode material will be HPL although the thickness of the electrodes and of the gas gap will be reduced to 1.4 mm as a thinner gas gap leads to a decrease of deposited charge per avalanche as showed in Figure 3.10. The smaller the gas gap, the more the detector becomes sensitive to gap non-uniformities across the electrode planes making a gap of 1.4 mm a good compromise in between these two competing factors.

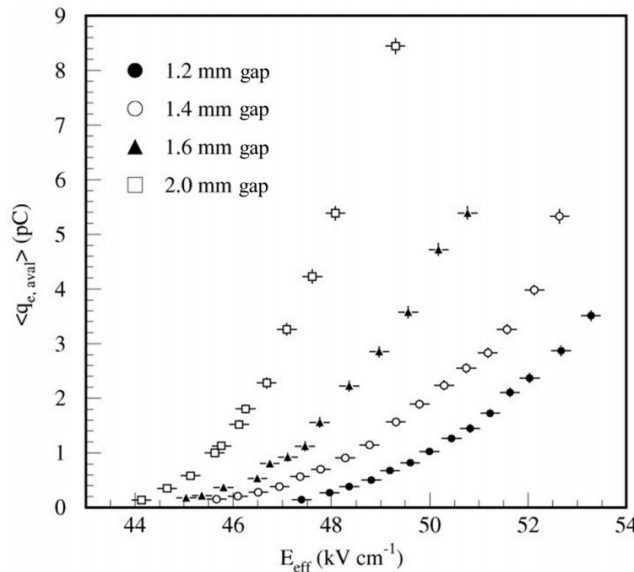


Figure 3.10: Measured average charge per avalanche as a function of the effective electric field for different gas gap thickness in double gap RPCs using HPL electrodes.

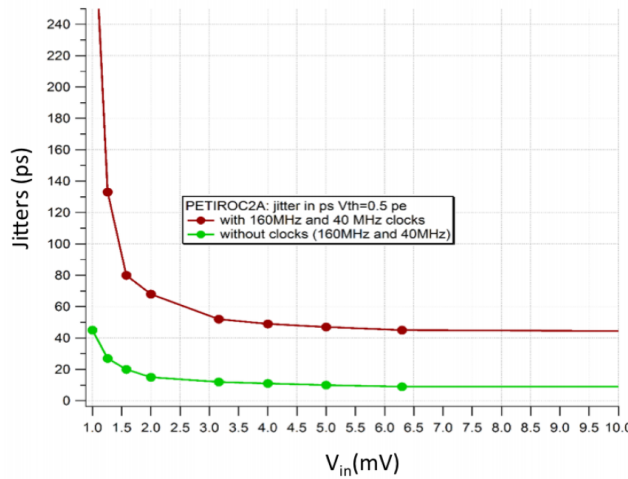


Figure 3.11: The PETIROC time jitter as a function of the input signal amplitude, measured with and without internal clocks.

1697 A lower charge deposition inside of the detector volume means a slower ageing and a longer
 1698 lifetime for detectors subjected to high irradiation. But, in order to take advantage of the lower
 1699 detector gain, more sensitive electronics are required so that the part of gain that was formerly done
 1700 in the gas volume can be moved to the electronics. Achieving this with the technology developed
 1701 more than 10 years ago for the present system is not possible as the signal over noise ratio of such
 1702 electronics doesn't allow to detect charges as low as 10 fC. Moreover, the new front-end electronics
 1703 will need to be radiation hard to survive to more than 10 years of HL-LHC conditions. The new
 1704 technology that has been chosen is based on the PETIROC ASIC manufactured by OMEGA and is
 1705 a 64-channel ASIC called CMS RPCROC on which the original SiGe technology will be replaced
 1706 by CMOS to increase its radiation hardness while keeping fast pre-amplification and discrimination
 1707 with a very low jitter that can reach less than 20 ps if no internal clock is used, as can be seen from
 1708 Figure 3.11. The ASIC is associated with an FPGA which purpose is to measure time thanks to a
 1709 TDC with a time resolution of 50-100 ps developed by Tsinghua University and that will provide a
 1710 measurement of the signal position along the strip with a precision of a few cm by measuring the
 1711 signal timing on both ends of the strips. In order to read-out all 96 strips, 3 ASICs and 3 TDCs,
 1712 each having 64 channels, are hosted on a front-end board attached to the chamber.
 1713 [Wait for the analysis of 2018 GIF++ data to add interesting information about the time and spatial
 1714 resolution measured during test beam periods.]

1715 3.3.2 Gas electron multipliers

1716 In the region closer to the interaction point where the spatial resolution is requested to be better
 1717 than 1 mm for the new detectors (at least for GE1/1 and ME0, GE2/1 being in the same order of
 1718 requested spatial resolution than the new iRPCs that will equip the third and fourth endcaps), the
 1719 choice has been made to use triple GEMs, micro pattern gaseous detectors, in the place of RPCs.
 1720 The GE1/1 project had been the first to be approved and demonstrators had been installed in CMS
 1721 already during LS1. The rest of the detectors will be installed during LS2 while the GE2/1 and ME0
 1722 projects are still under development. ME0, GE1/1 and GE2/1 will be installed respectively next to

¹⁷²³ the HCAL endcap, on the first and on the second muon endcap disks as can be seen from Figure 3.3.

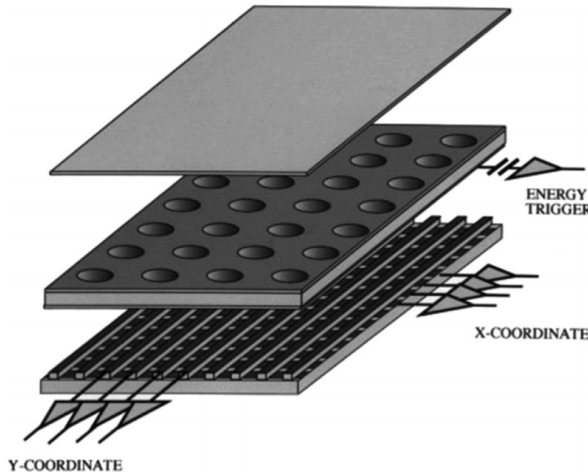


Figure 3.12: Schematics of a GEM showing the cathode on top, the GEM foil separating the gas volume into the drift region, in between the cathode and foil, and the induction region, in between the GEM foil and the anode, and the anode on which a 2D read-out is installed. A negative voltage is applied on the cathode while the anode is connected to the ground.

¹⁷²⁴ Gas Electron multipliers are gaseous detectors [28] which gas volume is confined in between 2
¹⁷²⁵ planar electrodes, the anode serving as read-out panel. The gas volume is divided in 2 or more
¹⁷²⁶ regions by a single or multiple *GEM foils* as showed in Figure 3.12. These foils are very thin, of the
¹⁷²⁷ order of a few tens of μm , and are pierced with holes as can be seen in Figure 3.13. Both surfaces
¹⁷²⁸ of the GEM foils are clad with copper in order to apply a strong electric field in between each side
¹⁷²⁹ that will generate very strong potentials in the holes. The gas region contained in between the
¹⁷³⁰ cathode and the GEM foil is called the drift region as the electric field is not strong enough to cause
¹⁷³¹ avalanches and thus start an amplification. The primary electrons drift toward the foil and are
¹⁷³² accelerated and amplify by the very high potential within the holes, as showed in Figure 3.13. Then
¹⁷³³ the electrons reach the second drift region in which they will induce signal on the read-out located
¹⁷³⁴ on the anode. By restraining the amplification process at the level of the holes, the electrons can
¹⁷³⁵ stay in a very confined space and thus induce a very localized current, providing the GEMs with a
¹⁷³⁶ very good spatial resolution.

¹⁷³⁷ In order to achieve a stronger amplification, the amplification process can be repeated several times
¹⁷³⁸ in a row. The GEMs that will be used in CMS are triple GEM detectors operated with a 70/30 gas
¹⁷³⁹ mixture of Ar/CO_2 . They contain 3 GEM foils and thus 3 electron amplifications, as can be seen in
¹⁷⁴⁰ Figure 3.14. The GEM foils used in CMS are 50 μm foils clad with 5 μm of copper on each side.
¹⁷⁴¹ The foils are pierced with double-canonical holes which inner and outer diameters are respectively
¹⁷⁴² 50 and 70 μm which are placed 140 μm from each other in an hexagonal pattern, as showed in
¹⁷⁴³ Figure 3.13. These detectors have a time resolution better than 10 ns and reach very good spatial
¹⁷⁴⁴ resolutions of less than 200 μrad as indeed the position of the hits is not measured along the strips
¹⁷⁴⁵ but following the azimuthal angle granularity of the radially organized trapezoidal strips.

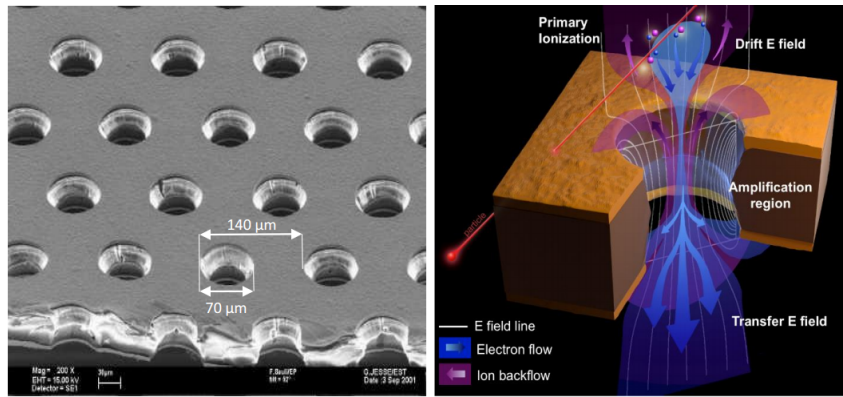


Figure 3.13: Left: Picture of a CMS GEM foil provided by a scanning electron microscope. Right: Representation of the electric field lines in a GEM hole and of the amplification that electrons and ions undergo in the hole's volume due to the very intense electric field.

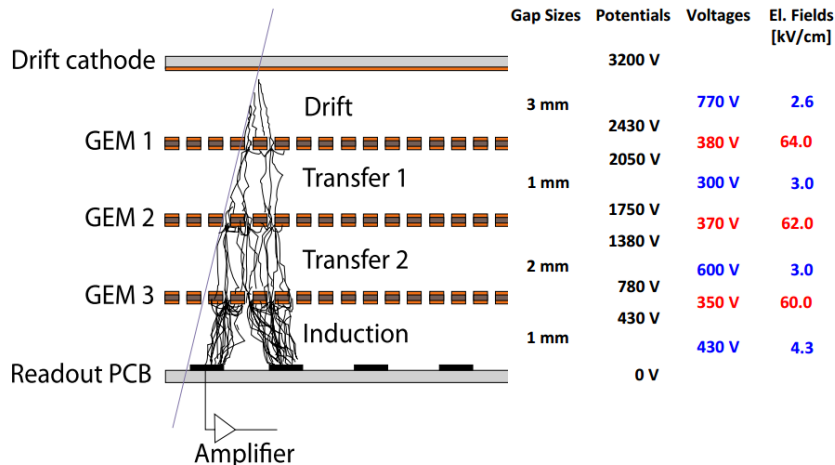


Figure 3.14: Schematic representation of CMS triple GEMs. The gas volume is divided into 4 areas. The drift area is the region where the primary electrons are created before being amplified a first time while passing through the first GEM foil. Then the process of drift and amplification is repeated twice in following two transfer areas and GEM foils. Finally, the charges have been amplified enough to induce current in the read-out strips while in the last drift area. The dimensions, potentials and electric fields are provided.

1746 The GEM Upgrade is divided into 3 subsystems as GE1/1 was the first approved project [29] and
 1747 that the detectors will already be installed during LS2. GE2/1 and ME0, on the other hand, will
 1748 profit of the R&D knowledge and skills developed for GE1/1 while the requirements for each
 1749 subsystem are different as they are not placed at the same distance from the interaction point. In
 1750 this very forward region, a different position with respect to the center of the detector can change
 1751 dramatically the conditions in which the detectors will have to be operated. In terms of rate
 1752 capability, GE2/1, which is the furthest, is required to withstand $2.1 \text{ kHz}/\text{cm}^2$ while GE1/1 needs
 1753 to be better than $10 \text{ kHz}/\text{cm}^2$ and ME, better than $150 \text{ kHz}/\text{cm}^2$. In terms of ageing with respect
 1754 to charge deposition, ME0 needs to be certified to $840 \text{ mC}/\text{cm}^2$, GE1/1 to $200 \text{ mC}/\text{cm}^2$ and

1755 GE2/1 only to 9 mC/cm². All 3 detectors need to have a time resolution better than 10 ns and an
 1756 angular resolution better than 500 µrad.

1757 On each GE1/1 ring, 36 super chambers, consisting of 2 single GEM layers and spanning 10°, will
 1758 be installed covering the pseudo-rapidity region $1.6 < |\eta| < 2.2$ together with ME1/1 CSCs and the
 1759 reach of the muon system will be improved thanks to the GE2/1 that will overlap with the GE1/1
 1760 and cover a region from $|\eta| > 1.6$ to $|\eta| < 2.4$ and complete the redundancy of ME2/1. The super
 1761 chambers, built with 2 triple GEM layers each consisting of 4 single GEM modules due to the
 1762 rather large surface of the GE2/1 chambers, that will be installed on the first ring of the second
 1763 endcap will span 20° each, hence, a total of 72 chambers will be assembled to equip the muon
 1764 system. Finally, the ME0 installed near the HCAL endcap will cover the region $2.0 < |\eta| < 2.8$ and
 1765 this subsystem will consist in super modules of 6 layers of triple GEM detectors covering an
 1766 azimuthal angle of 20° leading to the construction of 216 single detectors.

1767 All these new GEM detectors will be using a similar internal layout which is described in
 1768 Figure 3.14. The incoming muons will create detectable electron-ion pairs in the 3 mm thick drift
 1769 volume in which an electric field of 2.6 kV/cm is applied for the electrons to drift to the first GEM
 1770 foil on which a very intense field of 64 kV/cm is applied over a distance of only 60 µm which
 1771 allows for an average electronic gain of 20 to 25. After the first amplification stage, the electrons
 1772 drift over the 1 mm separating the 2 first GEM foils thanks to an electric field of 3.0 kV/cm and are
 1773 again amplified by a factor 20 to 25 while going through the second GEM foil to which is applied
 1774 an electric field of 62 kV/cm. The electron drift another 2 mm towards the last GEM foil through a
 1775 field of 3.0 kV/cm and are multiplied one last time from a similar factor passing through the
 1776 60 kV/cm of the last GEM foil holes. Finally, they drift along the 1 mm of the induction volume in
 1777 a field of 4.3 kV/cm to reach the trapezoidal strips on the read-out PCB used as anode. The total
 1778 detector gain is approximately of the order of 10^4 and the resulting output signal is both due to the
 1779 induction of moving charges in the induction volume and of charge pick-up once they read the
 1780 read-out strips.

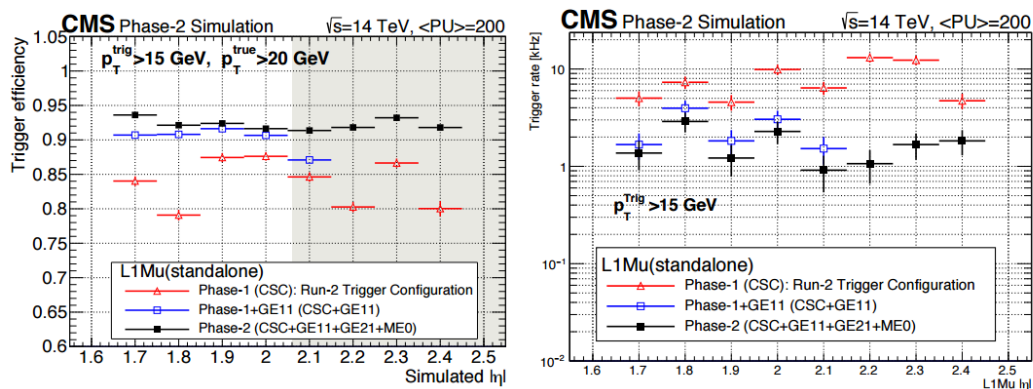


Figure 3.15: Simulated efficiency and rate of the standalone Level-1 muon trigger using tracks reconstructed in CSCs and all GEM stations compared with Phase-I values in the case where only CSCs are used or CSCs+GE1/1. The zones of inefficiency of the CSC subsystem are compensated by the addition of GEMs during Phase-II and the trigger rates is kept from increasing due to the high luminosity.

1781 Adding the GEMs into the forward region of the muon system will allow to strongly enhance the
 1782 Level-1 Trigger performance by reducing the inefficiency regions and the trigger rate as showed in

1783 Figure 3.15. Moreover, benefiting from the good spatial and angular resolution of the GEMs, the
 1784 precision into the muon measurement will also be greatly improved by the addition of GEMs as can
 1785 be seen from the simulation presented in Figure 3.16.

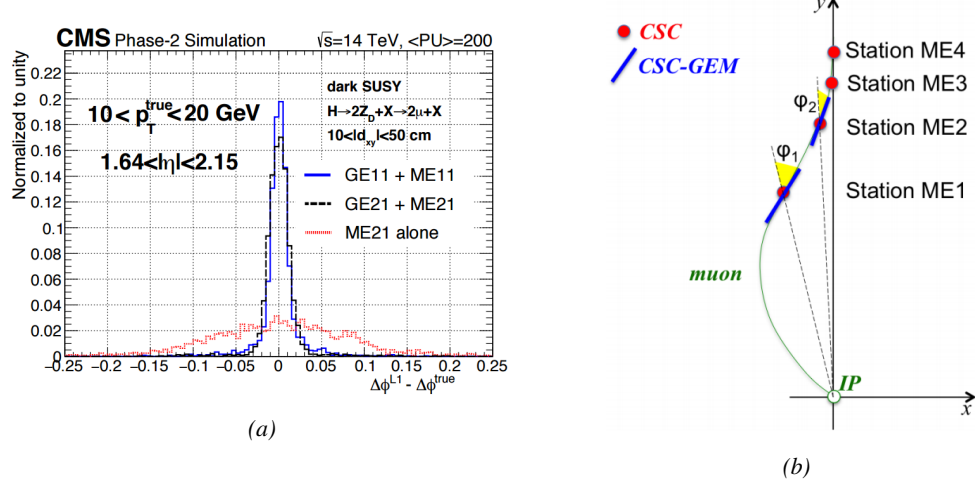


Figure 3.16: Figure 3.16a: Simulated resolution of the muon direction measurement $\Delta\phi$ with Phase-II conditions. In the second endcap station, the resolution is compared in the case of CSCs (ME2/I) alone and CSCs+GEMs (GE2/I+ME2/I) while a similar resolution measurement is given in the case of the first station (GE1/I+ME1/I). Figure 3.16b: The addition of GEM detectors on stations 1 and 2 (ME0 is considered to contribute to station station 1) as redundant system to CSCs allows to improve the muon momentum improvement through a more accurate measurement of the local bending angles ϕ_1 and ϕ_2 .

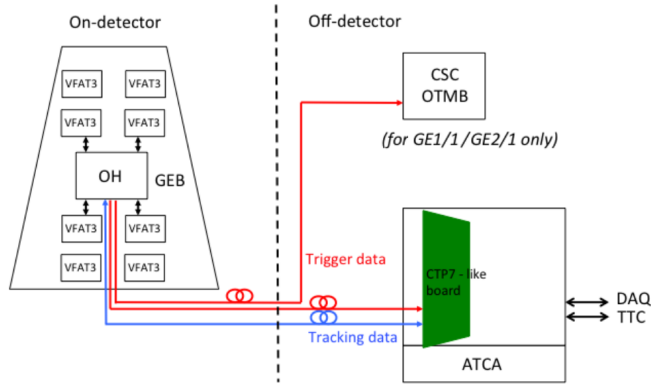


Figure 3.17: Schematics of the data communication chain for DAQ of the GEM subsystems. The sending of trigger data via optical links to the CSC OTMBs is only done for GE1/I and GE2/I to match the data with ME1/I and ME2/I.

1786 The read-out of GEMs will use the same technology. The anode planes used as read-out PCBs and
 1787 referred to as GEM Electronics board (GEB) host on their outer surface VFAT3 ASICS that connect
 1788 to a total of 128 strips for a very fine angular granularity. Along the endcap radius, the strips are
 1789 divided into 8 pseudo-rapidity partitions. In the case of GE1/I and ME0, each η -partition consist in

1790 384 read-out strips connected into 3 VFAT3 ASICs and offering a while the large GE2/1 partitions
 1791 contain twice as many channels. Both GE1/1 and GE2/1 strips have an angular pitch of $474\text{ }\mu\text{m}$
 1792 while this of ME0 is twice larger due to its proximity with the interaction point. The VFAT3 ASICs
 1793 allow for a latency better than the $12.5\text{ }\mu\text{s}$ required by CMS Level-1 Trigger and there frequencies
 1794 goes up to 1 MHz. They are connected into the Optohybrid Board (OH) and this full ensemble
 1795 (GEB+VAT3+OH) constitute the on-chamber electronics. The OH is then sending the data to the
 1796 modules constituting the DAQ of the GEM system via optical fibers. These back-end electronics
 1797 modules are located in the service cavern of CMS and host CMS communication devices, used to
 1798 have a common clock, and control and links to the Endcap Muon Track Finder (EMTF) system.
 1799 Moreover, GE1/1 and GE2/1 also have links with the CSC OTMBs as the OH of these 2
 1800 subsystems send data into these boards. This communication chain can be seen in Figure 3.17.
 1801 The detectors that will placed in CMS will have to live through Phase-II without significant
 1802 performance degradation to ensure an efficient data taking and the possibility to investigate more
 1803 exotic physics. As the 3 GEM subsystems will be using the same detector technology, the choice
 1804 was made to certify the GEMs in the worst of the 3 environments, i.e. the ME0 station located right
 1805 behind the HCAL. According to FLUKA simulation, including all the latest foreseen upgrades into
 1806 the CMS detector geometry, it was shown that the maximal hit rate expected in ME0 would be of
 1807 the order of 50 kHz/cm^2 with contributions of neutrons (6 kHz/cm^2), photons (35 kHz/cm^2), and
 1808 electrons and positrons (8 kHz/cm^2) resulting in a charge deposition a little lower than
 1809 300 mC/cm^2 after 10 years of HL-LHC [23]. It is necessary to understand the classical ageing
 1810 effects on the GEMs but also premature ageing due to contaminants in the gas mixture leading to
 1811 polymerization on the surface of the GEM foils during operation and the effect of discharges on the
 1812 detector operations if they have to happen during their lifetime.

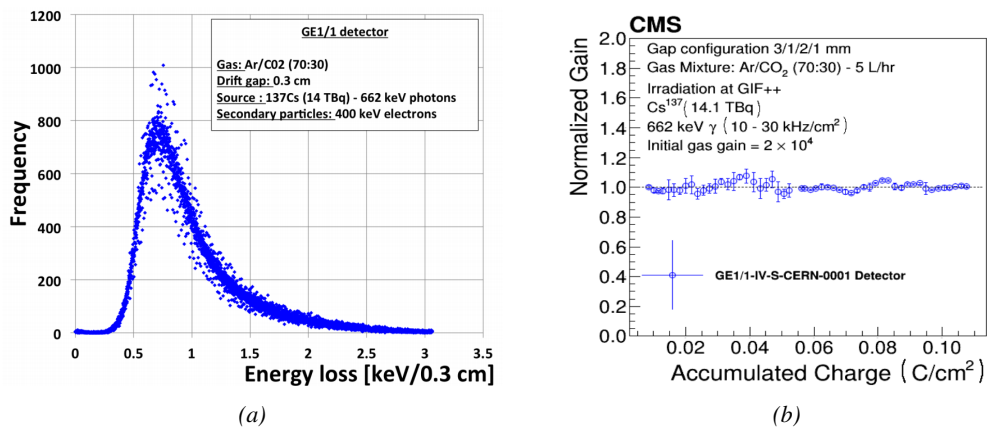


Figure 3.18: Figure 3.18a: Energy spectrum of GIF^{++} ^{137}Cs source as measured by the GE1/1 detector installed in GIF^{++} . Figure 3.18b: Evolution of the normalized gain of the GE1/1 detector installed at in GIF^{++} as a function of the integrated charge per unit area. The first part of the study, up to a charge of 55 mC/cm^2 had been done in the former Gamma Irradiation Facility (GIF) that has now been dismantled following the construction of GIF^{++} . No variation of the normalized gain can be observed after an accumulation of 110 mC/cm^2 .

1813 To characterize the classical ageing effects, a campaign is being conducted in the new Gamma
 1814 Irradiation Facility (GIF^{++}) of CERN where a GE1/1 detector operated at its nominal gain is
 1815 placed 50 cm from the facility's 14 TBq ^{137}Cs source which emits gammas at an energy of

662 keV. In order to spot any ageing of the detector, the effective gain is kept monitored, as can be seen in Figure 3.18b, as its variations gives clues about different aspects of the detector such as the geometry of the holes, the electric field configuration or the gas composition. The monitoring of the gamma energy distribution, showed on Figure 3.18a, can give an idea on the evolution of the performance of the chamber and finally, the evolution of the currents through time also is a good indicator of the appearance of dark current in the detector that would be due to the emission of electrons by thin insulating layers of the detector subjected to a long lasting irradiation known as Malter effect. At the time the Technical Design Report (TDR) for the Phase-II upgrade of the muon system was written [23], the GEM group had reported a total integrated charge of 110 mC/cm^2 which, if compared with 10 years of HL-LHC operation, represents a safety factor of 18 for the GE1/1 subsystem and a factor 37 for the GE2/1 subsystem but only 39% of the total expected ME0 integrated charge. It is estimated that reaching the total integrated charge necessary to certify the detectors for Phase-II operation will take another 2 to 3 years. Nevertheless, the present status of the longevity study shows no degradation of the performance of the detector installed in GIF++ as can be seen through Figure 3.18.

Aside of the classical ageing tests, outgassing of the different materials composing the GEMs have been conducted by placing the different materials to be tested into an outgassing box that consists in a stainless steel cylinder through which the CMS GEM 70/30 gas mixture of Ar/CO_2 with the possible contaminants is flowed while the detector is exposed to the continuous irradiation of a radioactive source and the heat is raised to enhance the outgassing. From the detector that was placed into this outgassing box, only one component was identified to cause loss of performance due to outgassing. This component was the polyurethane *Cell-Pack* used to coat the internal frame of the GEMs and the polymerization on its surface caused a 20% decrease of the gas gain. this polyurethane was replaced with a new one for which no outgassing effect causing a loss of performance was reported.

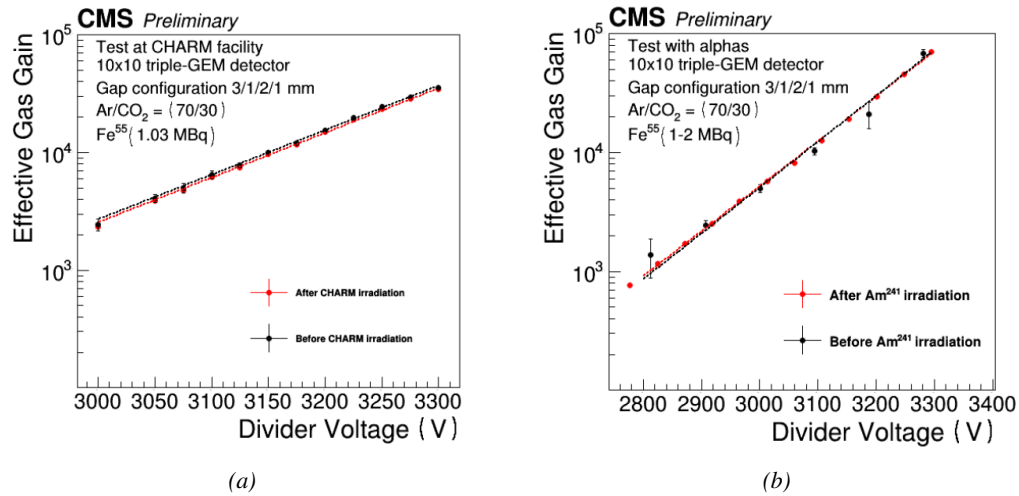


Figure 3.19: Figure 3.19a: Comparison of the gas gain as a function of the divider voltage before and after the irradiation of a triple-GEM by neutrons in CHARM. Figure 3.19b: Comparison of the gas gain as a function of the divider voltage before and after the irradiation of a triple-GEM by alpha particles.

Finally, even though the triple-GEM technology makes the detectors safe of discharges thanks to its

several amplification stages that allow to reach high gas gain using a relatively low electric field applied on the foils and to the distance separating the last foil from the read-out panel that is high enough to prevent discharging from developing all the way to the read-out, and hence, be stopped before it can cause any harm, it is important to have a good understanding of the discharge probability to ensure a safe operation over long periods. In order to further prevent discharges to develop in the detector volume, the GEM foils' power supply have been sectorized and protection resistors have been installed to limit the energy available for the discharge development. To reproduce the high-energy neutron background conditions of CMS, a GE1/1 detector have been placed in the CHARM facility of CERN. This facility allows to irradiate the detectors with a neutron fluence as high as $2.5 \times 10^8 / \text{cm}^2$. The detectors were operated with a slightly higher gain of 3.5×10^4 . It was measured that the discharge probability for a GEM operated under CMS conditions was of 2.85×10^{-9} per heavily ionizing particle with a 95% confidence level that would correspond to 225 discharges per cm^2 in ME0, 17 in GE1/1 and 12 in GE2/1 during the full HL-LHC period. According to Figure 3.19a, no degradation of the performance was observed after the irradiation at CHARM were 24 discharges per unit area were reported. Nevertheless, another test were the detector was exposed to a 5.5 MeV alpha source and were 450 discharges per unit area were reported didn't show any drop of performances either, as can be seen in Figure 3.19b.

3.3.3 Installation schedule

The previous discussion on the different upgrade projects makes it clear that a lot of work is schedule for CMS to be ready at the end of LS3 for HL-LHC. Conducting all the upgrades of the muon system together with upgrades of the other subsystems like the replacement of the Tracker and of part of the ECAL, will prove to be very difficult as the opening of CMS to access the Barrel will be done by fully opening the endcaps leaving only the first disk to be accessible. Thus, most subsystems have planed early installation over LS2, and the following YETS until LS3 in order to give more space to LS3 schedule.

First of all, LS2 will see the installation of GE1/1 detectors, all the on-detector schedule of CSCs and the installation of the necessary services for the improved RPCs to be installed later, such as the HV and LV power supply lines, the gas and cooling lines or signal cables. CSCs will have a huge work to do during LS2 as they will need to extract all of their detectors to refurbish them with upgraded DCFEB and ALCT mezzanine boards. The GE1/1 services were installed during LS1 together with a few demonstrator and only the detectors needs to be integrated into the first endcap disk. The detectors are presently being built and tested at the different assembly site to prepare for a smooth LS2 work.

The work of GEMs will be continued during the following YETS during which is planned the installation of the GE2/1 stations to only leave the ME0 to be installed during LS3. The iRPC program will follow a similar path as the new detectors will be installed during the YETS preceding LS3 in prevision of the fact that the endcap disks will not be accessible during LS3. This way, all the subsystems, but DTs, made great effort on planing their installation and integration within CMS only to have to deal with off-detector issues during the LS3 period, such as the replacement of ODMBs and HV system in the case of CSCs or the upgrade of the RPC Link System. Finally, during LS3 are schedules the replacement of DT minicrates electronics and the installation and integration of ME0 GEMs together with the HGCal.

3.4 Implications of the different upgrades on the Level-1 Trigger. Improvement of physics performance.

The upgrades of the different subsystems will have a subsequent impact on the Level-1 Trigger. Indeed, although its main scheme will not be affected, the efficiency of the trigger in identifying muons and provide the DAQ with good and fast trigger that can cope with HL-LHC instantaneous luminosity is a major improvement. In addition to the upgrade of the muon system in terms of trigger accept rate and latency, the Level-1 Trigger will get extra information in including the Tracker Trigger into its Muon Track Finder logic and combine the L1 Muon Trigger with Tracker and Calorimeter Triggers to generate a Global L1 Trigger with a much better momentum resolution, as showed in Figure 3.20.

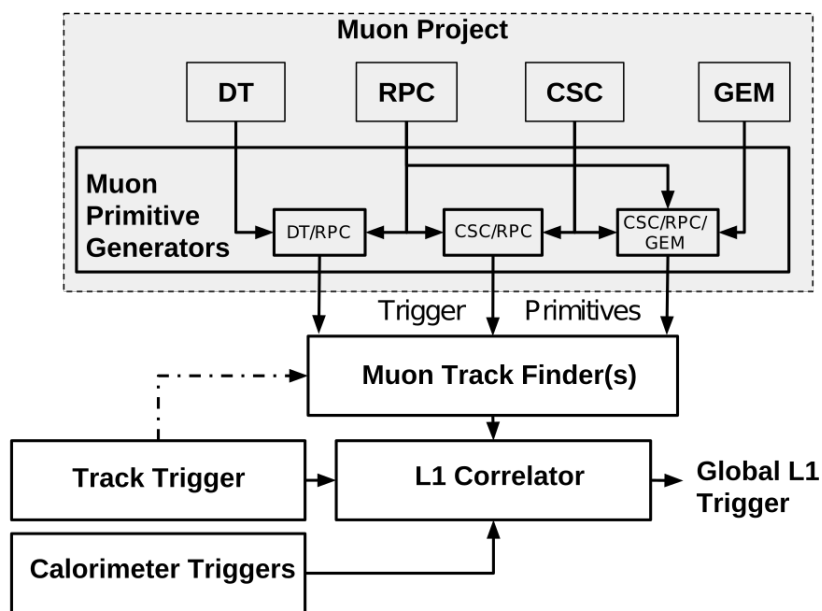


Figure 3.20: Data flow of the Level-1 Trigger during Phase-II operations.

In terms of muon trigger, 3 regions are considered due to their different track finding logic: the Barrel Muon Track Finder (BMTF), the Endcap Muon Track Finder (EMTF) for both the barrel and endcap regions, and finally the Overlap Muon Track Finder (OMTF) which concerns the pseudo-rapidity region in which there is a common coverage by both the barrel and endcap muon systems. This region can be seen in Figure 3.3 for $0.9 < |\eta| < 1.2$ and requires a specific more complex logic to provide with an efficient reconstruction of the muons due to the different orientation of the detectors and of the more complex magnetic field of this region that needs to be taken into account. The benefits of the upgrade for each of these track finders will be coming from different improvements and will be detailed sector by sector. The main contribution to the improvement of the BMTF is the time resolution improvement of RPC link systems that will allow to take profit of the full 1.5 ns resolution of the detectors. From the perspective of RPCs only, this improvement will help reducing the neutron induced background and slightly improve the bunch crossing assignment. The upgrade of DT electronics is also to take

1907 into account as the trigger primitive generator will be renewed through the use of TDCs that will
 1908 send the digitized signals directly to the back-end electronics instead of having an on-detector
 1909 trigger logic as it will be the case until the end of Phase-I. The front data of both DTs and RPCs
 1910 will be sent to the same back-end electronics. These upgrades were detailed in section 3.2 and will
 1911 lead to a more robust operation of the trigger in the barrel region. Indeed, the combination of RPC
 1912 hits together with DT primitives will bring improvement in the bunch crossing assignment and
 1913 improve the efficiency of the trigger in between the wheels were the quality of DT primitives is the
 1914 poorest. Moreover, having a redundant information is important in the case of failure and loss of
 1915 efficiency of one of either subsystems.

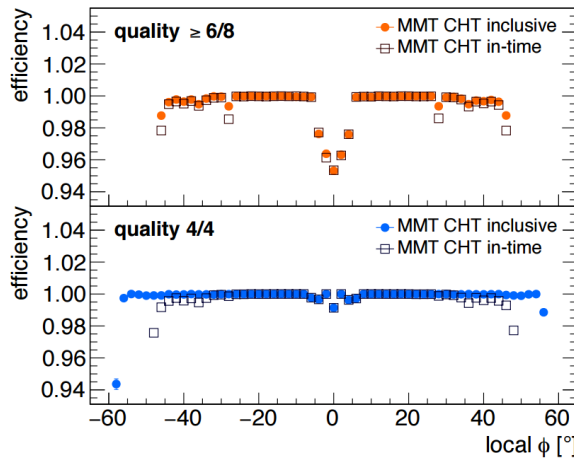


Figure 3.21: Comparison of Phase-II DT trigger primitives algorithmic efficiency for segments obtained with 2 super-layers ($\text{quality} \geq 6/8$) and 1 super-layer only ($\text{quality} = 4/4$). The simulation was done by generating 2×10^6 muons. The candidate tracks with correct time identification is showed with open symbols.

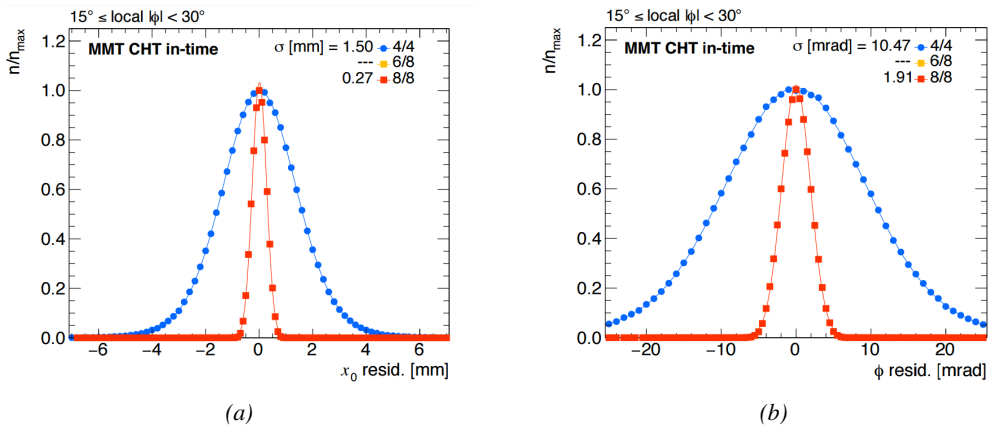


Figure 3.22: Simulated spatial (3.22a) and angular (3.22b) resolution of the algorithm using 8 aligned hits in both super-layers (quality = 8/8) and 4 aligned hits in only one super-layer (quality = 4/4). The contribution of intermediate quality tracks (6 aligned hits) is negligible in the angular range shown. [Be careful to update this caption as it uses a text to close to the published one.]

1916 The loss of single hit efficiency of DTs due to ageing will also force the DT to change the algorithm
 1917 use to identify tracks. So far, the identification was only performed at the level of a single DT
 1918 super-layer, which is composed of 4 single DT layers. In the perspective the single efficiency drops,
 1919 this will require to be upgraded to try to combine the data of more than a single super-layer to keep
 1920 a high muon track identification efficiency. In addition to this change in trigger primitive candidate
 1921 quality, new algorithms with higher efficiency are being developed. According to Figure 3.21, the
 1922 efficiency of the new algorithm, both in the cases using 1 or 2 super-layers, is higher than with the
 1923 current system [30]. Moreover, the overall efficiency of an algorithm requesting at least a muon
 1924 detected in 6 DT layers out of the 8 composing the 2 super-layers of a DT module would stay
 1925 comparable to the 4 DT layers out of 4 algorithm within the local bending angle range. On the
 1926 other hand, despite the slight loss of efficiency in the low angle range, the algorithm using more DT
 1927 layers achieves both higher spatial and angular resolution according to Figure 3.22.
 1928 With new detectors to cover the very forward region and the upgrade of RPC Link System, the
 1929 EMTF will be greatly improved. The current EMTF already use more sophisticated algorithms by
 1930 combining together RPC hits and CSC primitives and will also benefit from the improved time
 1931 resolution of the RPC system. The GEMs, in stations 1 and 2, and the iRPCs, in stations 3 and 4,
 1932 will be added into the EMTF algorithm. Both these contributions will help increasing the efficiency
 1933 of the L1 trigger in the endcap region in one hand, and help lowering the L1 trigger rate in the other
 1934 hand, especially in the most forward region. The improvement of the efficiency will come both
 1935 from the better time resolution of RPC link boards and from the addition of more hits along the
 1936 muon tracks and also a contribution from the GEMs to the lever arm of each track thanks to there
 1937 high angular resolution.

1938 The rate will be partly reduced in the forward region thanks to the better spatial resolution of
 1939 iRPCs, with respect to the current RPC system, that will reduce the ambiguity brought by multiple
 1940 local charged tracks in CSCs, as explained through Figure 3.24. Indeed, as the rates will increase,
 1941 the probability to record more than a single local charged track will greatly increase. This is due to
 1942 the fact that the trigger algorithm uses information from 3 consecutive bunch crossings to find
 1943 muon tracks. It is estimated that with iRPCs operated at 95% efficiency the resolution of
 1944 ambiguous events would be of the order of 99.7%.

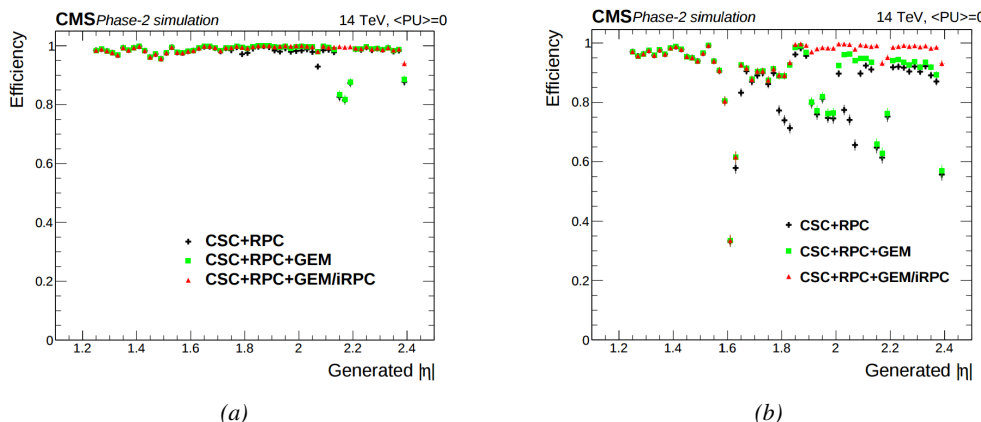


Figure 3.23: Efficiency of the L1 trigger in the endcap region after Phase-II upgrade in the case CSC/GEM/RPC hits are requested in at least 2 stations out of four (3.23a) and in all four stations (3.23b).

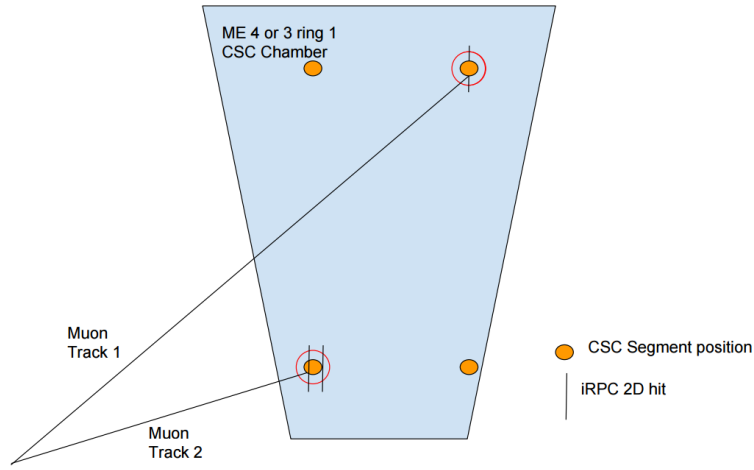


Figure 3.24: Resolution of the LCT ambiguous events thanks to the combination of CSC and iRPC readout data. Using CSCs only, 2 pairs of hits are possible.

1945 The addition of GEMs will improve greatly the measured muon momentum resolution by
 1946 improving the global resolution of the direction of muon tracks, as can be seen in Figure 3.25,
 1947 which will contribute to lowering the trigger rate and increase the efficiency, as can be seen from
 1948 Figure 3.26 that focuses especially in the most challenging pseudo-rapidity region. Data from both
 1949 CSCs and GEMs are combined into the OTMB to build on each station, GEM/CSC primitives
 1950 matching space and time information from both subsystems.

1951 Finally, the development of a track finder specific to the overlap region was already achieved during
 1952 the Phase-I upgrade of the L1-Trigger [31]. Nevertheless, the improvements of DT spatial
 1953 resolution and RPC timing will be carried and implemented into the OMTF.

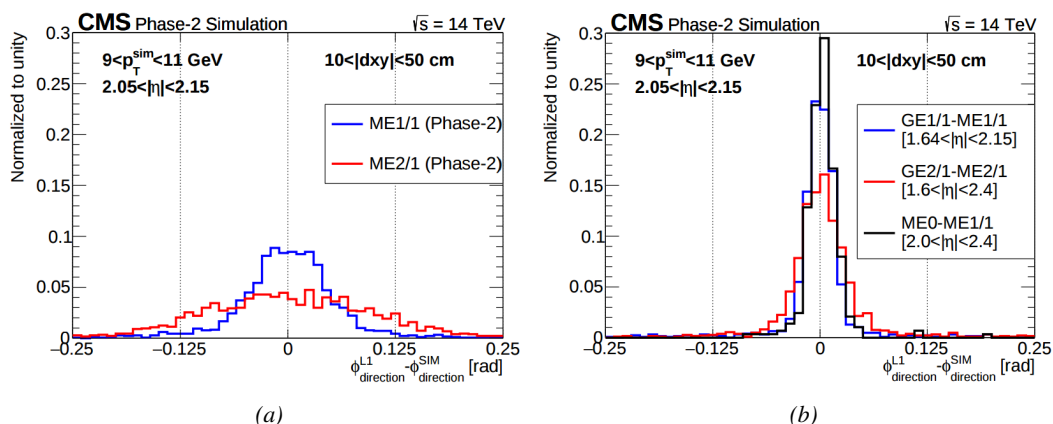


Figure 3.25: The angular resolution on reconstructed muon tracks in the GEM overlap region $2.0 < |\eta| < 2.15$ is compared for Phase-II conditions in the case CSC are alone (Figure 3.25a) and in the case the GEMs' data, including ME0, is combined to which of CSCs (Figure 3.25b).

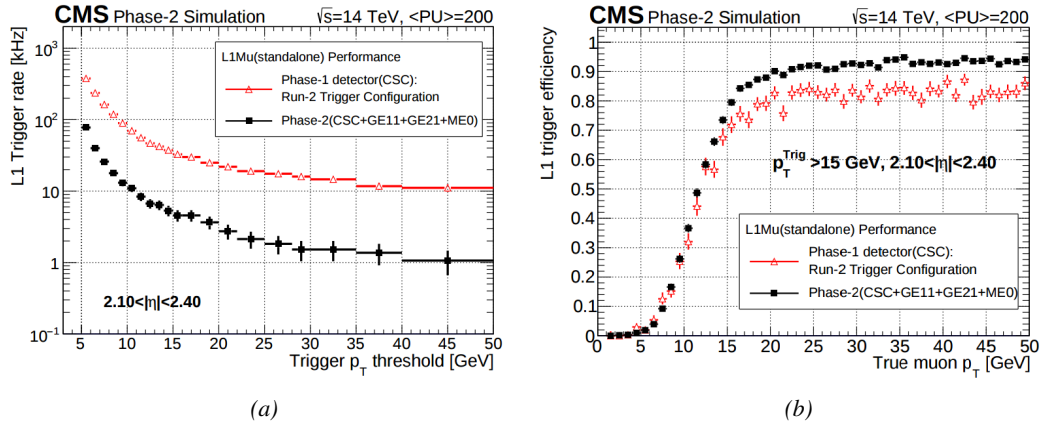


Figure 3.26: Comparison of L1 trigger performances for prompt muons with and without the addition of GEMs in the region $2.1 < |\eta| < 2.4$ at Phase-II conditions. GEMs would allow a reduction of the trigger accept rate by an order of magnitude (Figure 3.26a) while increasing the trigger efficiency (Figure 3.26b).

3.5 Ecofriendly gas studies

Future strict restrictions in the use of certain gases will affect the gaseous detectors of several experiment, including CMS. The European Commission adopted a new "F-gas regulation" in 2014 [32] with the goal to strongly control and reduce the use of fluorinated gases with high Global Warming Potential (GWP). Using CF_4 , $C_2H_2F_4$ and SF_6 , both CSC and RPC subsystems will need to address this problem by finding new gas mixture for the operation of their detectors. Finding a replacement for these gas component that were used for very specific reasons will be a great challenge. Indeed, CSCs use CF_4 in order to enhance the longevity of the detectors, increase the drift velocity of electrons and quench photons with a non-flammable gas mixture. RPCs use a mixture mainly composed of $C_2H_2F_4$, or $R134a$, that features a high effective Townsend coefficient and the great average fast charge allowing for operations with a high threshold, and contains a small fraction of SF_6 that is used for its electronegative properties that prevents the development of delta-rays in the gas volume that might trigger multiple ionization and avalanches.

	CSC	RPC
Greenhouse gases used	CF_4	$C_2H_2F_4$ and SF_6
Greenhouse gases fraction in the gas mixture	10%	95.2% and 0.3%
Global Warming Potential (relative to CO_2)	6500	1300 and 23900
Gas mixture re-circulation	Yes, 90%	Yes, 85%
Gas mixture replenishing rate (l/hr)	700	1100
F-gas recuperation	Yes, $\approx 40\%$	No
F-gas venting rate (l/hr)	42	1047 and 3.3
CO_2 -equivalent rate (m^3/h)	273	1440
Relative impact (entire muon system = 100%)	16%	84%

Table 3.1: Details of the greenhouse fluorinated gases used in CMS and of their GWP [23].

Nevertheless, all these gases have a very high GWP, as reported in Table 3.1, and only few options are left. The subsystems need to work on strongly decrease the loss of these gases due to leaks in

the gas system or completely change their gas mixture for more ecofriendly ones. Reducing the amount of F-gas released in the atmosphere due to leaks on the current gas system will require installation of a F-gas recuperation system on RPCs side and an upgrade of CSCs existing one in addition to the repair of existing leaks. With such measures, it is expected that the total rate of greenhouses gas vented in the atmosphere would represent only 1.6% of the current levels [23]. In the most critical case the F-gas were to be banned, it would be necessary to have replacement mixtures to operate CMS. CSC is presently investigating replacement for CF_4 such as CF_3I , C_4F_6 , IC_3F_6 , C_3F_8 or CHF_3 while RPCs, in collaboration with the ATLAS RPC group which uses the same gas mixture and, hence, faces similar restrictions, have identified CF_3I ($GWP \leq 1$) and $C_3H_2F_4$ ($GWP \leq 1$), referred to as HFO-1234ze, as potential candidates with mixtures containing CO_2 but more R&D needs to be conducted for both subsystems before concluding on the best alternative. No good alternative to the present mixtures will require very efficient abatement system in CMS to burn and convert the greenhouse gases into less harmful ones. This way, the air pollution would be strongly reduced.

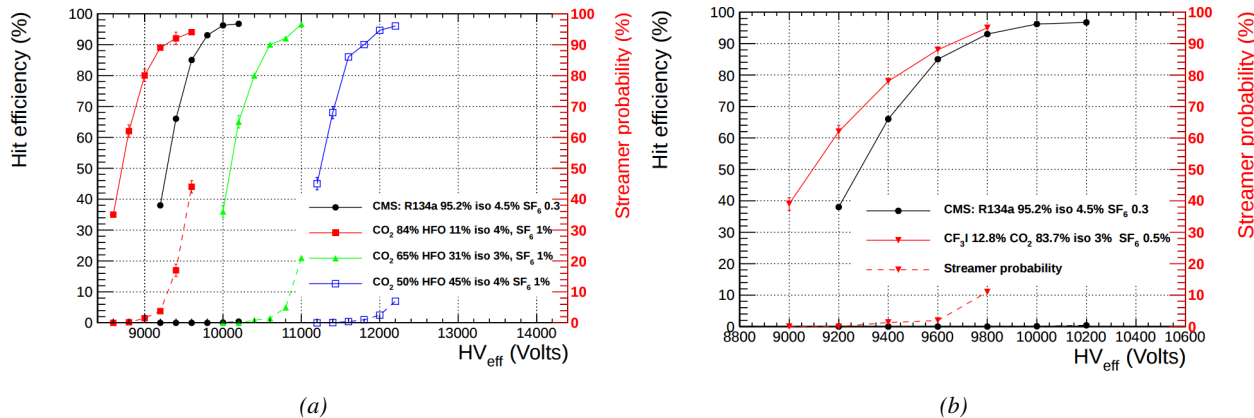


Figure 3.27: The efficiency (solid lines) and streamer probability (dashed lines) of HFO/CO₂ (Figure 3.27a) and CF₃I/CO₂ (Figure 3.27b) based gas mixtures as a function of the effective high-voltage are compared with the present CMS RPC gas mixture represented in black. The detector used for the study is a single gap RPC with similar properties than CMS RPCs. The streamer probability is defined as the proportion of events with a deposited charge greater than 20 pC.

The status of RPC studies are presented in Figure 3.27 in which the performance (efficiency and streamer probability) of an RPC operated with alternative gas mixtures is compared to the present CMS RPC mixture. Although the efficiency of detectors operated with mixtures containing CO_2/CF_3I or CO_2/HFO as a replacement for $C_2H_2F_4$ seem to reach similar levels than which of the detectors operated with the present mixture, the new gas mixtures feature a streamer probability (probability to have very large avalanches whose induced charge is greater than 20 pC) that far exceeds which of the present fluorinated mixture. The SF_6 , being a component of the mixture added in order to reduce the probability of large avalanches thanks to its electronegativity, doesn't seem to prevent streamers as efficiently even when used at levels more than 3 times higher than with the standard CMS RPC mixture. Nevertheless, it is important to note that these results were obtained with a single gap RPC while the use of a double gap RPC would reduce the operation voltage by 200 to 300 V, lowering the induced charge. A compromise in between good efficiency and acceptable level of streamer probability and the fine tuned composition of potential

¹⁹⁹⁶ replacement gas mixtures will be studied using a standard double-gap CMS RPC.

4

1997

1998

Physics of Resistive plate chambers

1999 A Resistive Plate Chamber (RPC) is a gaseous detector used in high-energy physics experiments as
2000 described in Chapter 3. It has been developed in 1981 by Santonico and Cardarelli [33], under the
2001 name of *Resistive Plate Counter*, as an alternative to the local-discharge spark counters proposed in
2002 1978 by Pestov and Fedotovich [34, 35]. Working with spark chambers implied using
2003 high-pressure gas and high mechanical precision which the RPC simplified by formerly using a gas
2004 mixture of argon and butane flowed at atmospheric pressure and a constant and uniform electric
2005 field propagated in between two parallel electrode plates. Moreover, a significant increase in rate
2006 capability was introduced by the use of electrode plate material with high bulk resistivity,
2007 preventing the discharge from growing throughout the whole gas gap. Indeed, the effect of using
2008 resistive electrodes is that the constant electric field is locally canceled out by the development of
2009 the discharge, limiting its growth.
2010 Through its development history, different operating modes [36–38], gas mixtures [33, 38–43] and
2011 new detector designs [44–46] have been discovered, leading to further improvement of the rate
2012 capability of such a detector. The low developing costs and easily achievable large detection areas
2013 offered by RPCs, as well as the wide range of possible designs, made them a natural choice to as
2014 muon chambers and/or trigger detectors in multipurpose experiments such as CMS [21] or
2015 ATLAS [47], time-of-flight detectors in ALICE [48], calorimeter with CALICE [49] or even
2016 detectors for volcanic muography with ToMuVol [50].

2017 4.1 Principle

2018 RPCs are ionisation detectors composed of two parallel resistive plate electrodes in between which
2019 a constant electric field is set. The space in between the electrodes, referred to as *gap*, is filled with
2020 a dense gas that is used to generate primary ionization into the gas volume. The free charge carriers
2021 (electrons and cations) created by the ionization of the gas molecules are then accelerated towards
2022 the electrodes by the electric field, as shown in Figure 4.1 [51]. RPCs being passive detectors, a
2023 current on pick-up copper read-out placed outside of the gas volume is induced by the charge

2024 accumulation during the growth of the avalanche resulting from the acceleration of the charge
 2025 carriers. As a consequence, the time resolution of the detector is substantially increased as the
 2026 output signal is generated while the electrons are still in movement. The advantage of a constant
 2027 electric field, over multi-wire proportional chambers, is that the electrons are being fully
 2028 accelerated from the moment charge carriers are freed and feel the full strength of the electric field
 2029 that doesn't depend on the distance to the readout and that the output signal doesn't need for the
 2030 electrons to be physically collected.

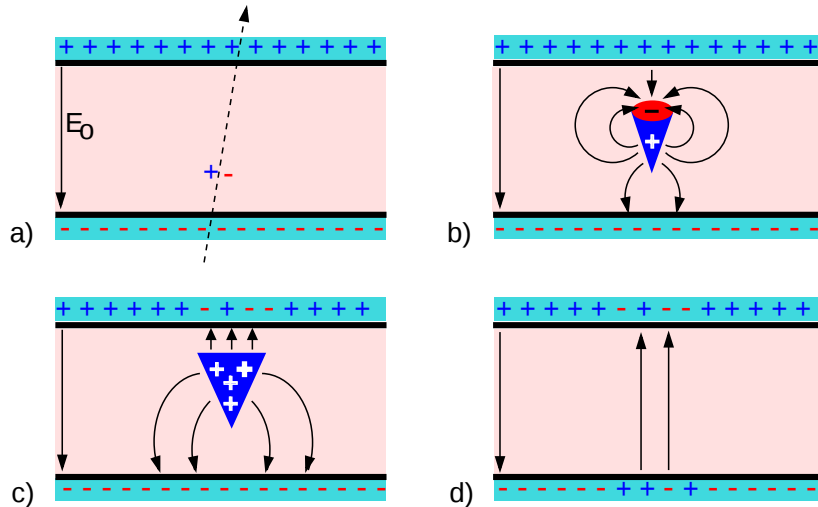


Figure 4.1: Different phases of the avalanche development in the RPC gas volume subjected to a constant electric field E_0 . a) An avalanche is initiated by the primary ionisation caused by the passage of a charged particle through the gas volume. b) Due to its growing size, the avalanche starts to locally influence the electric field. c) The electrons, lighter than the cations reach the anode first. d) The ions reach the cathode. While the charges have not recombined, the electric field in the small region around the avalanche stays affected and locally blinds the detector.

2031 After an avalanche developed in the gas, a time long compared to the development of a discharge is
 2032 needed to recombine the charge carriers in the electrode material due to their resistivity. This
 2033 property has the advantage of affecting the local electric field and avoiding sparks in the detector
 2034 but, on the other hand, the rate capability is intrinsically limited by the time constant τ_{RPC} of the
 2035 detector. Using a quasi-static approximation of Maxwell's equations for weakly conducting media,
 2036 it can be shown that the time constant τ_{RPC} necessary to the charge recombination at the interface
 2037 in between the electrode and the gas volume is given by the Formula 4.1 [52].

$$\tau_{RPC} = \frac{\epsilon_{electrode} + \epsilon_{gas}}{\sigma_{electrode} + \sigma_{gas}} \quad (4.1)$$

2038 A gas can be assimilated to vacuum, leading to $\epsilon_{gas} = \epsilon_0$ and $\sigma_{gas} = 0$, and the electrodes
 2039 permittivity and conductivity can be written as $\epsilon_{electrode} = \epsilon_r \epsilon_0$ and $\sigma_{electrode} = 1/\rho_{electrode}$,
 2040 showing the strong dependence of the time constant to the electrodes resistivity in Formula 4.2.

$$\tau_{RPC} = (\epsilon_r + 1)\epsilon_0 \times \rho_{electrode} \quad (4.2)$$

Very few materials with a low enough resistivity exist in nature. The resistivity targeted to build RPCs ranges from 10^9 to $10^{12} \Omega \cdot \text{cm}$. The most common RPC electrode materials are displayed in Table 4.1. When the doped glass and ceramics can offer short time constants of the order of 1 ms, the developing cost of such materials is quite high due to the very low demand. Thus, High-pressure laminate (HPL) is often the choice for high rate experiments using very large RPC detection areas. Other experiments working at cosmic muon fluxes can safely operate with ordinary float glass.

Material	$\rho_{\text{electrode}} (\Omega \cdot \text{cm})$	ϵ_r	$\tau_{\text{RPC}} (\text{ms})$
Float glass	10^{12}	~ 7	~ 700
High-pressure laminate	10^{10} to 10^{12}	~ 6	~ 6 to 600
Doped glass (LR S)	10^9 to 10^{11}	~ 10	~ 1 to 100
Doped ceramics (SiN/SiC)	10^9	~ 8.5	~ 1
Doped ceramics (Ferrite)	10^8 to 10^{12}	~ 20	~ 0.2 to 2000

Table 4.1: Properties of the most used electrode materials for RPCs.

4.2 Rate capability and time resolution of Resistive Plate Chambers

The electrode material plays a key role in the maximum intrinsic rate capability of RPCs. R&D is continuously being done to develop at always cheaper costs material with lower resistivity. Nevertheless, the amount of charge released, i.e. the size of the discharge, if reduced leads to a smaller blind area in the detector, increasing the rate capability of the detector. On the other hand, the drift velocity of electrons in the gas volume being quite stable with the applied electric field, the design of a detector and the associated read-out and pulse-processing electronics will be a major component of the time resolution of RPCs. Moreover, the sensitivity of the electronics will also help increasing the rate capability by lowering the gain the gas volume needs to be operated at, increasingly lowering the gas volume in which the signals will develop.

4.2.1 Operation modes

Being a gaseous detector using an accelerating electric field to amplify the signal of primary charge carriers, the RPC can be operated into different modes as the electric field intensity varies. Each mode offers different performances for such a detector, and it will be showed that the operating mode corresponding to the lowest electric field possible is best suited for high rate detectors working in collider experiments.

RPCs where developed early 1980s. At that time it was using an operating mode now referred to as *streamer mode*. Streamers are large discharges that develop in between the 2 electrodes enough to locally discharge the electrodes. If the electric field inside of the gas volume is strong enough, with electrons being fast compared to ions, a large and dense cloud of positive ions will develop nearby the anode and extend toward the cathode while the electrons are being collected, eventually leading to a streamer discharge due to the increase of field seen at the cathode. The field is then strong enough so that electrons are pulled out of the cathode. Electrodes, though they are a unique volume of resistive material, can be assimilated to capacitors. At the moment an electric field is applied in between their outer surfaces, the charge carriers inside of the volume will start moving leading to a situation where there is no voltage across the electrodes and a higher density of negative charges,

i.e. electrons, on the inner surface of the cathode. Finally, when a streamer discharge occurs, these electrons are partially released in the gas volume contributing to increase the discharge strength until the formation of a conductive plasma, the streamer. This can be understood through Figure 4.2 [36]. Streamer signals are very convenient in terms of read-out as no further amplification is required with output pulses amplitudes of the order of a few tens to few hundreds of mV as can be seen on Figure 4.3.

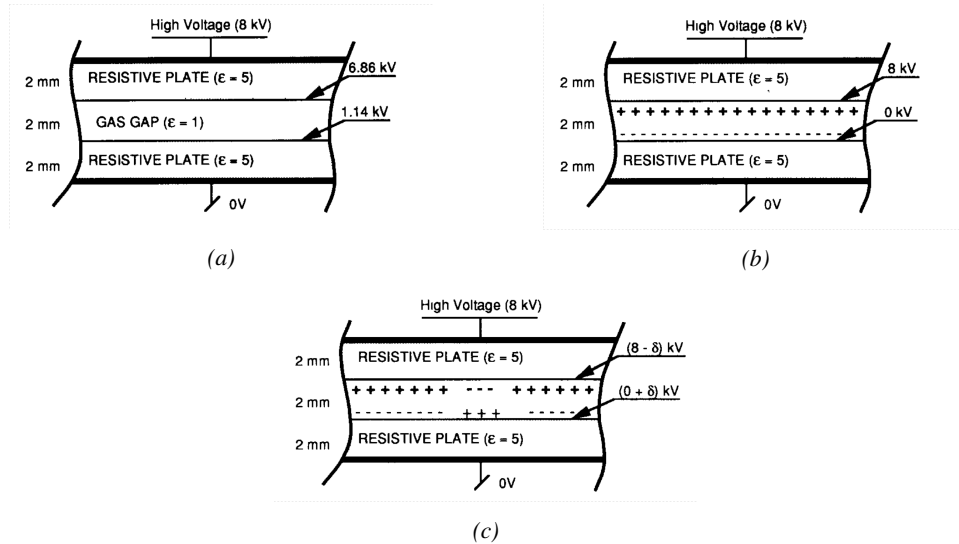


Figure 4.2: Movement of the charge carriers in an RPC. Figure 4.2a: Voltage across an RPC whose electrode have a relative permittivity of 5 at the moment the tension is applied. Figure 4.2b: After the charge carriers moved, the electrodes are charged and there is no voltage drop over the electrodes anymore. The full potential is applied on the gas gap only. Figure 4.2c: The streamer discharge initiated by a charged particle transports electrons and cations towards the anode and cathode respectively.

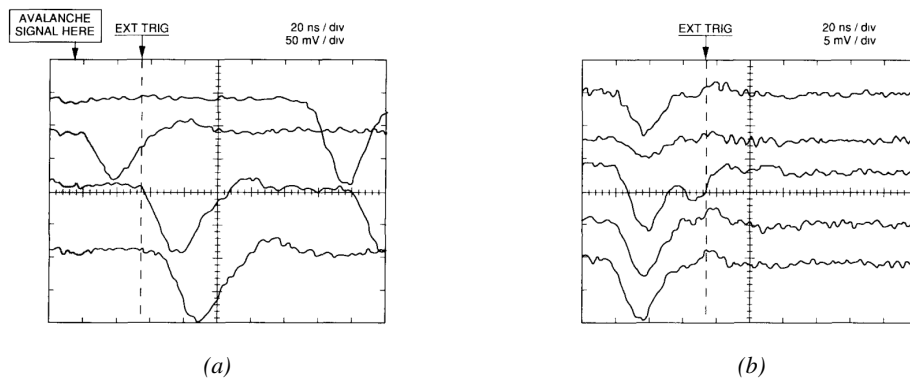


Figure 4.3: Typical oscilloscope pulses in streamer mode (Figure 4.3a) and avalanche mode (Figure 4.3b). In the case of streamer mode, the very small avalanche signal is visible.

When the electric field is reduced though, the electronic gain is small until the electrons get close enough to the anode and the positive ion cloud is much smaller. The electric field cannot rise to the

point a field emission of electrons on the cathode is possible. The resulting signal is weak, of the order of a few mv as shown on Figure 4.3, and requires amplification. This is the *avalanche mode* of RPC operation. This mode offers a higher rate capability by providing smaller discharges that don't affect the electrodes charge and are more locally contained in the gas volume as was demonstrated by Crotty with Figure 4.4 [36]. The detector only stays locally blind the time the charge carriers are recombined and there is no need for electrode recharge which is a long process affecting a large portion of the detector. Another advantage of avalanche signals over streamer is the great time consistency. Figure 4.3 shows very clearly that avalanche signals have a very small time jitter. Thus, using such a mode is a natural choice for experiments in which the detectors are required to have a high detection rate.

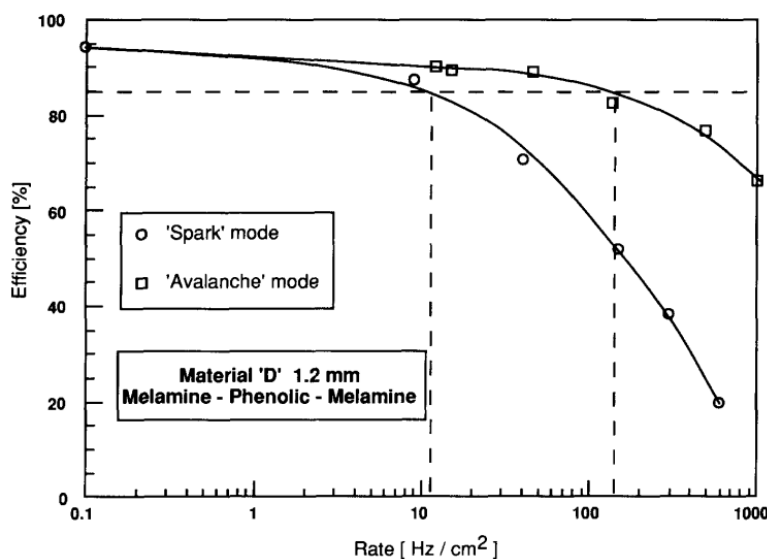


Figure 4.4: Rate capability comparison for the streamer and avalanche mode of operation. An order of magnitude in rate capability for a maximal efficiency drop of 10% is gained by using the avalanche mode over the streamer mode.

4.2.2 Standard gas mixture for RPCs operated in collider experiments

The first RPC working in streamer mode was operated with a 50/50 mixture of argon and butane [33], a standard mixture used at that time in multi-wire proportional chambers, taking profit of the good effective Townsend coefficient of argon to maximize the number of primary charge carriers freed in the gas by ionizing particles and of the quenching properties of butane. Before the discovery of the avalanche mode of RPC operation and concerned about the rate capability of RPCs operated in streamer mode, the performance improvement of the detectors through the increase of fast charge ratio in the signal development, decreasing the charge induced per avalanche as can be seen through Figure 4.5, was studied by adding Freon based gases, such as CF_3Br , into the typical Ar/C_4H_{10} gas mixture was studied and showed that a lower induced charge could lead to an improvement the rate capability [39]. This consideration lead to the discovery of the avalanche mode which confirmed that the smaller the induced charge, the better the rate capability of the RPCs [36]. This discovery could happen thanks to the increased number of lower induced charge

2105 events allowed by adding a fraction of strong quencher in the gas mixture.

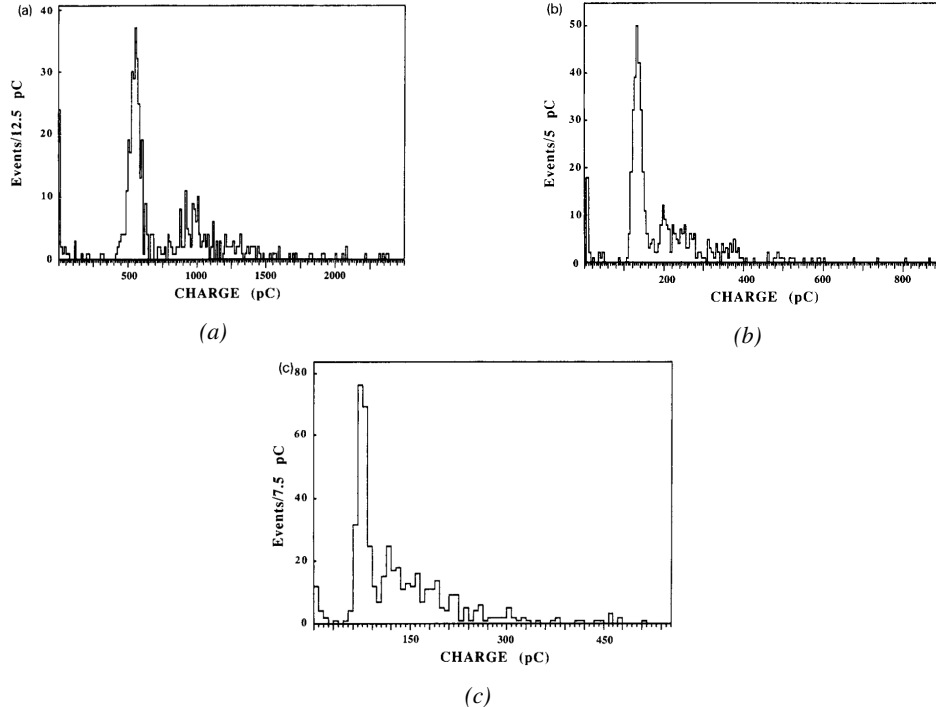


Figure 4.5: Comparison of the charge distribution of signals induced by cosmic muons in an RPC operated with a gas mixture of argon, butane and bromotrifluoromethane (CF₃Br). The Ar/C₄H₁₀ is kept constant at 60/40 in volume while the total amount of CF₃Br in the mixture is varied: 0% (Figure 4.5a), 4% (Figure 4.5b) and 8% (Figure 4.5c) [39].

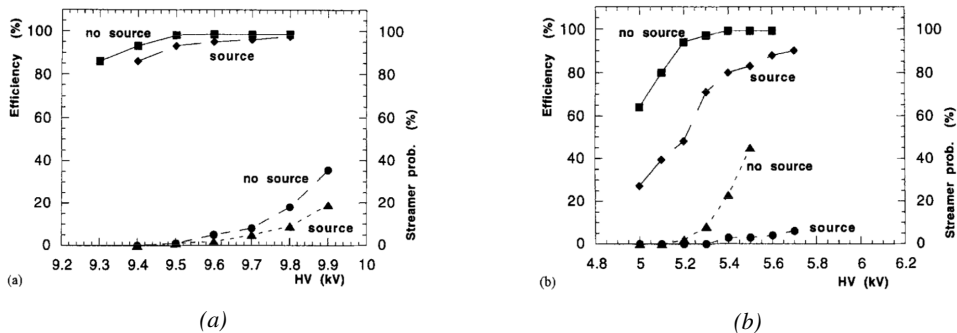


Figure 4.6: Comparison of the efficiency and streamer probability, defined as the fraction of events with an induced charge 10 times larger than that of the average avalanche, with and without irradiation by a 24 GBq ¹³⁷Cs source of an RPC successively operated with a 90/10 mixture C₂H₂F₄/i-C₄H₁₀ (Figure 4.6a) and a 70/5/10/15 mixture of Ar/i-C₄H₁₀/CO₂/C₂H₂F₄ (Figure 4.6b) [40].

2106 From this moment onward, more and more studies were conducted in order to find a gas mixture
2107 that would allow for the best suppression of streamers for the benefit of low charge avalanches.

Most R&D groups working with narrow gaps started using freon-based gas mixtures while users of wide gap RPCs kept using Ar/CO_2 based mixtures. The differences in between narrow and wide gaps will be later discussed in Section 4.2.3. The CF_3Br having a high GWP, tetrafluoroethane ($C_2H_2F_4$) was preferred to it as more suitable ecofriendly gas in the middle of the 90s. An advantage of this new freon component is that it featured a high primary ionization and a low operating voltage, as reported by Cardarelli [38]. Thus, the new gas mixtures used were mainly composed of tetrafluoroethane alone with lower content of isobutane in order to reduce the flammability of the mixtures in the case it were to be used in accelerator experiments for safety reasons. Performance and models about such mixtures were discussed in papers of Abbrescia [40, 41] and showed a better suitability of such a gas mixture, with respect to argon based ones, for operations with high radiation backgrounds leading to a need for high rate capability of the detectors, as can be seen from Figures 4.6 and 4.7. Indeed, although the operating voltage of a tetrafluoroethane based mixture is higher than which of an argon based mixture but the efficiency under irradiation is more stable, the voltage range with negligible streamer probability is much wider, and the fast charge ratio available is much greater, providing with more stable operation of the detector.

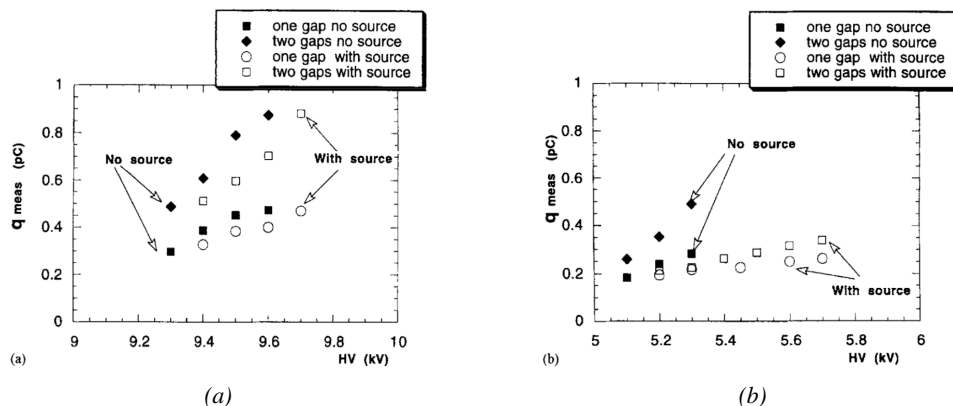


Figure 4.7: Comparison of the fast charge ratio with and without irradiation by a 24 GBq ^{137}Cs source of an RPC successively operated with a 90/10 mixture $C_2H_2F_4/i-C_4H_{10}$ (Figure 4.7a) and a 70/5/10/15 mixture of $Ar/i-C_4H_{10}/CO_2/C_2H_2F_4$ (Figure 4.7b). The results are provided for both single gap and double gap operation [40].

Aside of the improvement of the rate capability through linseed oil surface treatment of HPL electrodes, which allowed for a lower intrinsic noise rate and dark current of the detectors by improving the smoothness of the electrodes surface [53], it was later found that the streamers could be further suppressed by adding an electronegative compound into the gas mixture. The benefits of adding SF_6 in order to push the transitions from avalanche to streamers towards high voltages has been discussed in 1998 [42, 43] and eventually the high rate RPC destined to be used in accelerator physics would unanimously start using this compound into RPC gas mixtures. Being able to control the creation of streamers allows for slower ageing of the detector and lower power consumption as the currents driven by the electrodes consecutively to the induced charges would be smaller. In summary, the typical gas mixture RPCs are operated with is generally composed of the following 3 gas compounds, although, as mentioned in Chapter 3.5, research is being conducted into new more ecofriendly gas mixture using gases with a much lower Global Warming Potential:

- 2136 • Tetrafluoroethane ($C_2F_4H_2$), also referred to as *Freon* or *R134a*, is the principal compound
 2137 of the RPC gas mixtures, with a typical fraction above 90%. It is used for its high effective
 2138 Townsend coefficient and the great average fast charge that allows to operate the detector
 2139 with a high threshold with respect to argon, for example, that has similar effective Townsend
 2140 coefficient but suffers from a lower fast charge. To operate with similar conditions, argon
 2141 would require a higher electric field leading to a higher fraction of streamers, thus limiting
 2142 the rate capability of the detector [40, 41].
- 2143 • Isobutane (i- C_4H_{10}), only present in a few percent in the gas mixtures, is used for its UV
 2144 quenching properties [54] helping to prevent streamers due to UV photon emission during
 2145 the avalanche growth.
- 2146 • Sulfur hexafluoride, (SF_6), simply referred to as SF_6 , is used in very little quantities for its
 2147 high electronegativity. Excess of electrons are being absorbed by the compound and
 2148 streamers are suppressed [42, 43]. Nevertheless, a fraction of SF_6 higher than 1% will not
 2149 bring any extra benefit in terms of streamer cancelation power but will lead to higher
 2150 operating voltage [42], as can be understood through Figure 4.8.

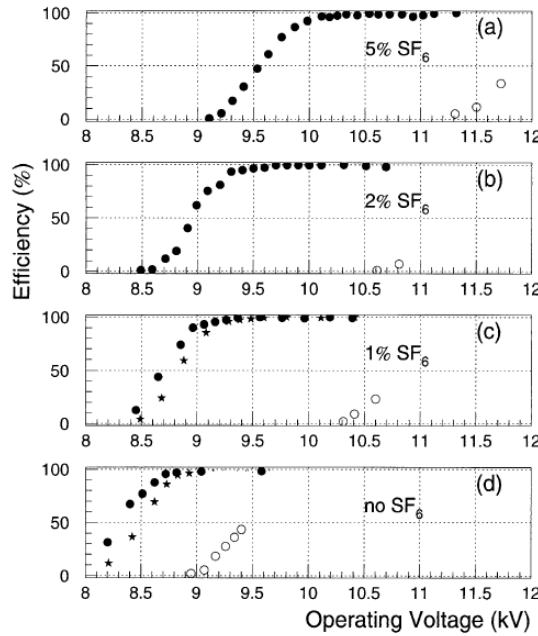


Figure 4.8: Efficiency (circles and stars with 30 mV and 100 mV thresholds respectively) and streamer probability (opened circles) as function of the operating voltage of a 2 mm single gap HPL RPC flushed with a gas mixture containing (a) 5%, (b) 2%, (c) 1% and (d) no SF_6 [42].

2151 In the last steps of R&D, the gas mixture of CMS RPCs was foreseen to be a 96.2/3.5/0.3
 2152 composition of $C_2H_2F_4/i-C_4H_{10}/SF_6$ [55] but finally it was slightly changed into a 95.2/4.5/0.3
 2153 mixture of the same gases [56]. A summary of the operation performance of the RPCs since the
 2154 start of LHC and of CMS data taking is given in Figure 4.9 [57]. The performance of the detectors
 2155 is regularly monitored and the operating voltages updated in order to obtain a very stable

2156 performance through time. Nevertheless, the detectors will face new challenges during Phase-II
 2157 during which they will be exposed to more extreme radiation conditions. Description of the longevity
 2158 tests with extreme irradiation and the conclusions regarding the operation of the present RPC
 2159 system will be given in Chapter 5.

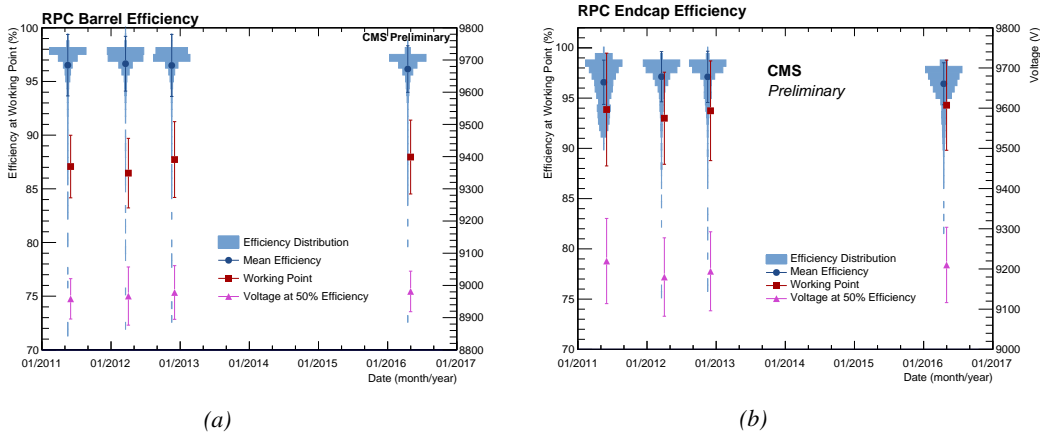


Figure 4.9: Evolution of the efficiency, working voltage, and voltage at 50% of maximum efficiency for CMS Barrel (Figure 4.9a) and Endcap (Figure 4.9b) RPCs obtained through yearly voltage scans since 2011. The working voltage of each RPC is updated after each voltage scan to ensure optimal operation [57].

2160 It was already discussed that in the future, it is likely that the use of freon gases could be banned.
 2161 As potential replacement for tetrafluoroethane was proposed the trifluoriodomethane (CF_3I), a
 2162 molecule with similar properties than CF_3Br which was replaced by the tetrafluoroethane, and the
 2163 1,3,3,3-tetrafluoropropene ($C_3H_2F_4$ or HFO-1234re), a molecule with similar properties than the
 2164 actual tetrafluoroethane and proposed as a replacement in refrigerating and air conditioning
 2165 systems [58]. These 2 gases have stronger quenching properties than $C_2H_2F_4$ which means a much
 2166 stronger electric field needs to be applied on the parallel electrodes of the RPCs in order to reach
 2167 full efficiency. But the power supply system of CMS RPC is limited to 15 kV and so is ATLAS
 2168 power supply system which is participating in a joined R&D. As can be seen from Figure 3.27,
 2169 reducing the working voltage was achieved by mixing the potential replacements together with
 2170 CO_2 . Introducing carbon dioxide into the mixture while keeping similar levels of isobutane and
 2171 SF_6 increases the streamer probability and the best candidate identified for a compromise in
 2172 between low enough working voltage and acceptable levels of streamers corresponds to a mixture
 2173 containing 50% of CO_2 , 45% of HFO, 4% of isobutane and 1% of SF_6 but is not yet considered
 2174 satisfactory. On the other hand, no good replacement for SF_6 has yet been identified. With its very
 2175 high Global Warming Potential (23900), even small fraction of this gas in the mixture (it only
 2176 represents 0.3% of CMS standard mixture but more than 5% of its overall GWP) substantially
 2177 increase the danger for the environment. Although finding a replacement for this gas is less critical
 2178 than for the tetrafluoroethane composing more than 90% of usual RPC standard mixtures, the
 2179 problem will need to be addressed.

²¹⁸⁰ **4.2.3 Detector designs and performance**

²¹⁸¹ Different RPC design have been used and each of them present its own advantages. Historically, the
²¹⁸² first type of RPC to have been developed is what is now referred to as *narrow gap* RPC [33, 59].

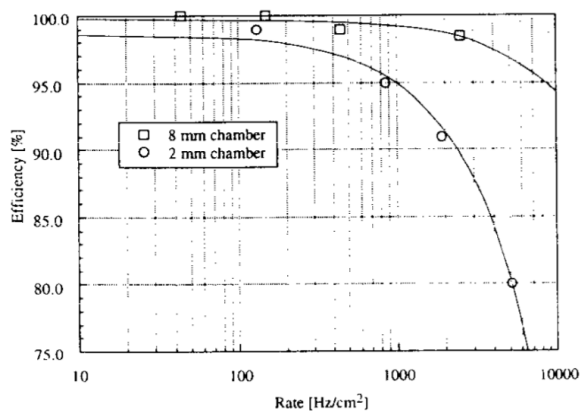


Figure 4.10: Comparison of the rate capability of 8 mm and 2 mm wide RPCs. The lines are linear fits on the data [59].

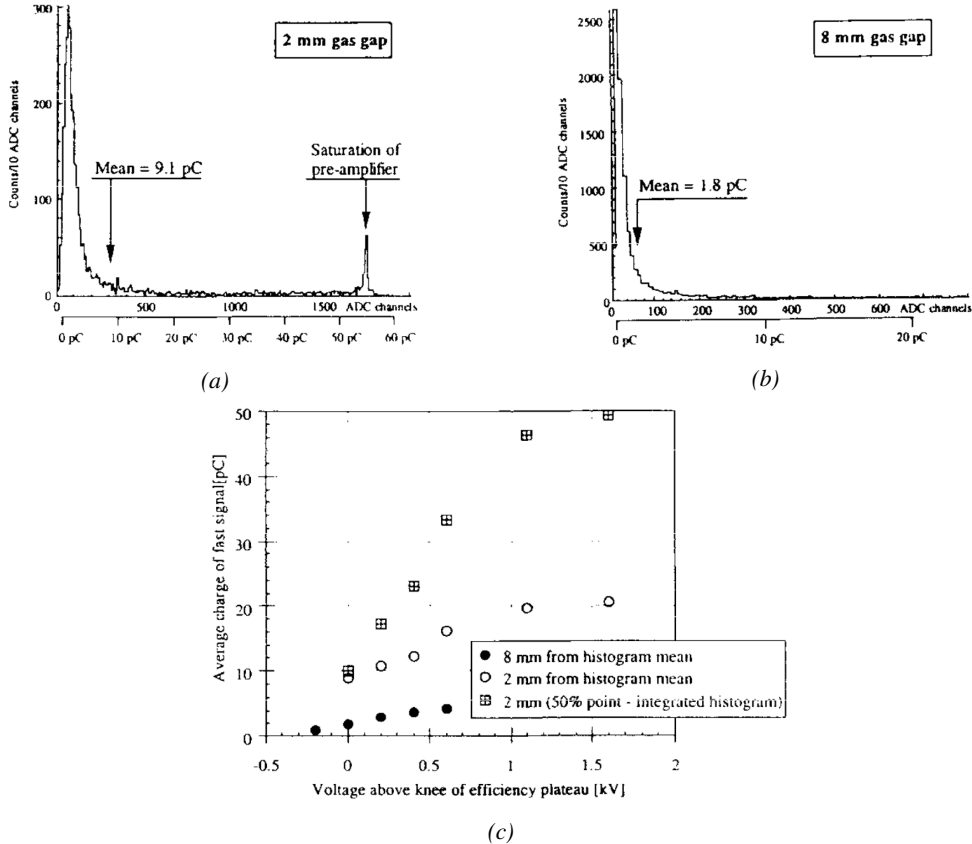


Figure 4.11: Distributions of the induced charge of fast signals on 2 mm (Figure 4.11a) and 8 mm (Figure 4.11b) RPCs exposed to a radiation rate of 100 Hz/cm^2 . Average induced charge of fast signals as a function of the high voltage applied on 2 mm and 8 mm RPCs (Figure 4.11c). In the case of the 2 mm RPC, a saturation of the pre-amplifier was observed. The average of the distribution is underestimated and the median is showed together with the average to account for this bias [59].

After the avalanche mode has been discovered [36], it has been showed that increasing the width of the gas gap lead to higher rate capability, due to lower charge deposition per avalanche, and lower power dissipation [59], as is showed in Figures 4.10 and 4.11. The distance in between the electrode being greater, a weaker electric field can be applied and a lower gain used as a longer gas volume will contribute to the signal induction on the read-out circuit. Nevertheless, by increasing the gas gap width, the time resolution of the detector decreases. This is a natural result if the increase of active gas volume in the detector is taken into account. Indeed, for a given detection threshold on the induced charge per signal, only the small fraction of gas closest to the cathode will provide enough gain to have a detectable signal. In the case of a wider gas volume, the active region is then larger and a larger time jitter is introduced with the variation of starting position of the avalanche, as discussed in [44] and showed in Figure 4.12.

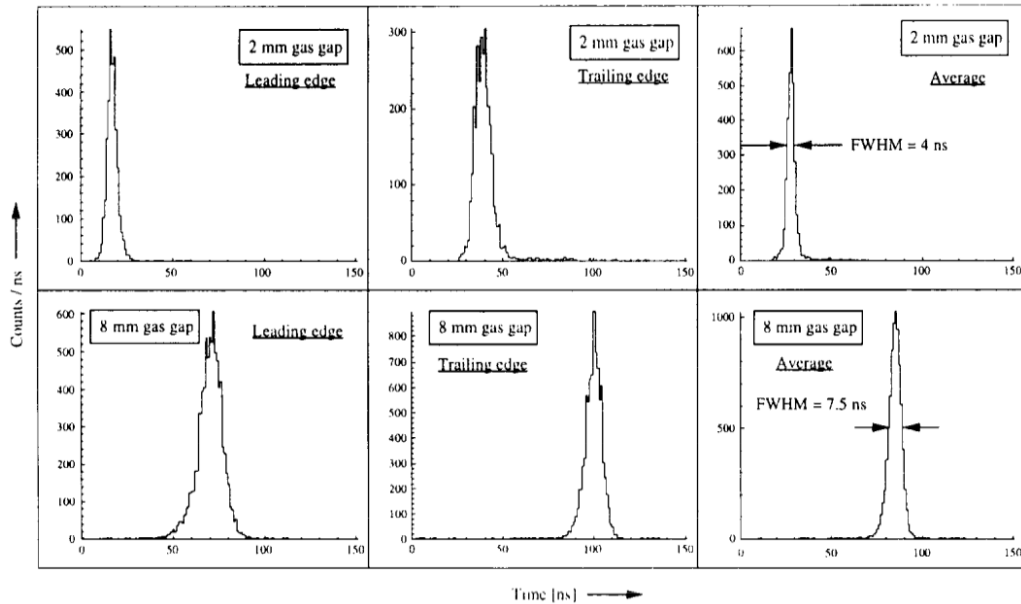


Figure 4.12: Time distributions of the leading, trailing, and average of both leading and trailing edges for 2 mm (top row) and 8 mm (bottom row) RPCs exposed to a 100 Hz/cm^2 radiation rate. The data was collected with RPCs operated at the voltage corresponding to the knee of the efficiency distribution, defined as the point where 95% of the maximum efficiency is obtained [59].

2194 To improve both the time resolution and the rate capability, different methods were used trying to
 2195 take advantage of both narrow and wide gap RPCs into a single design. Thus, double gap RPCs,
 2196 combining two narrow gaps into a single detector to increase the effective sensitive volume, and
 2197 multigap RPCs, which divided the large volume of a wide gap RPC into thinner sub-gaps by adding
 2198 intermediate electrodes in between the cathode and anode to improve the time resolution by
 2199 mimicking narrow gap RPCs, were developed starting from the middle of the 90s.

2200 4.2.3.1 Double gap RPC

2201 Made out of 2 narrow RPC detectors stacked on top of each other as shown in Figure 4.13, this
 2202 detector layout, popularized by the two multipurpose experiments CMS [21] and ATLAS [47] at
 2203 LHC, can be used as an OR system in which each individual chamber participates in the output
 2204 signal and increases the overall sensitive volume of the detector apparatus. Keeping the copper strip
 2205 read-out system at the ground, CMS and ATLAS, due to different goals, have chosen different
 2206 designs as CMS RPCs possess a 1D read-out while ATLAS RPCs offer a 2D read-out. The
 2207 difference comes from placing the read-out in between the gaps, the anodes facing each other, or to
 2208 have both RPC gaps in between 2 layers of read-out panels, one along the X-axis and one along the
 2209 Y-axis, the cathodes facing each other.

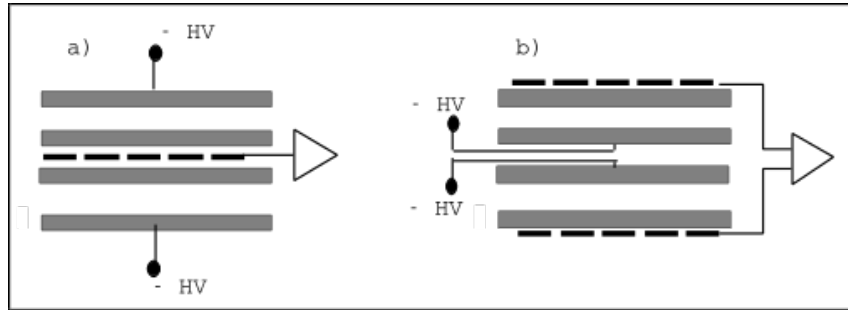


Figure 4.13: Possible double-gap RPC layouts: a) "standard" 1D double-gap RPC, as used in CMS experiment, where the anodes are facing each other and a 1D read-out plane is sandwiched in between them, b) double read-out double-gap RPC as used in ATLAS experiment, where the cathodes are facing each other and 2 read-out planes are used on the outer surfaces. This last layout can offer the possibility to use a 2D reconstruction by using orthogonal read-out planes.

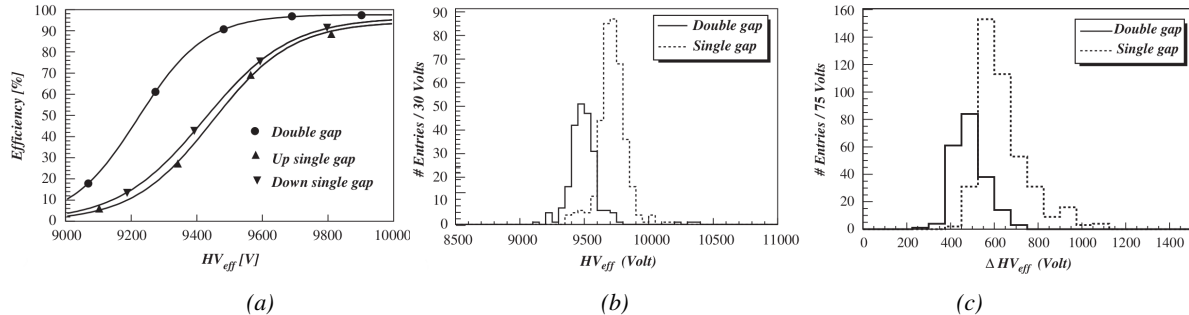


Figure 4.14: Comparison of performance of CMS double and single gap RPCs using cosmic muons [55].
Figure 4.14a: Comparison of efficiency sigmoids. Figure 4.14b: Voltage distribution at 95% of maximum efficiency. Figure 4.14c: $\Delta_{10\%}$ distribution.

The gain of such a detector is reduced by a factor 2 with respect to single-gap RPCs with an efficiency plateau reached at lower voltage, as visible on Figure 4.14, due to the two gas gaps contributing to the signal formation and offering a dynamic range closer to that of a wide gap RPC. A double gap is then fully efficient while the individual RPC gaps composing it are only 70 to 80% efficient. Naturally, by operating the double gap at a lower voltage, the rate capability is found to be increased as the induced charge per gap is then lower than in the case of a single gap detector also leading to a reduction of the streamer probability and a better extraction of the fast charge of the total signal as could be seen through previously presented Figure 4.7.

4.2.3.2 Multigap RPC (MRPC)

MRPCs are layouts in which floating sub electrode plates are placed into a wide gap RPC to divide the gas volume and create a sum of narrow gaps [44, 45]. Similarly to the double gap RPC for which the gain could be reduced by increasing the dynamic range, the multigap reduces the gain while keeping a total dynamic range similar to that of a wide gap RPC by reducing the size of each individual sub-gap composing the detector. The dynamic range, associated to the sensitive volume, and the comparison of each detector layout to the wide gap RPC is showed in Figure 4.15.

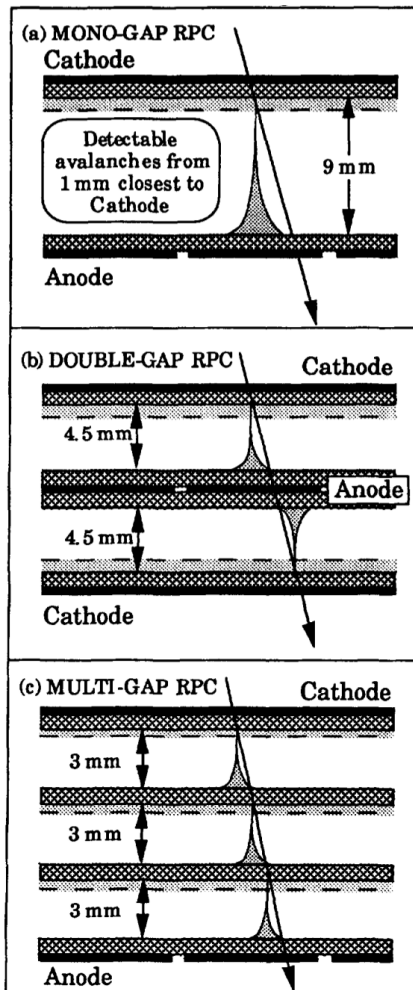


Figure 4.15: Representation of different RPC layouts (wide gap on Figure (a), double gap on Figure (b) and multigap on Figure (c)), of the corresponding sensitive volume in gray, and of the associated avalanche size [45].

2225 By operating the detector with thinner gaps, the time resolution is improved. Comparatively to the
 2226 time resolution presented in Figure 4.12 for the wide gap RPC of 8 mm, a complementary study
 2227 was conducted on multigaps using two 4 mm and four 2 mm subgaps and showed, via Figure 4.16,
 2228 an improvement of the time resolution with the reduction of the gap width and of the number of
 2229 gaps while the same sensitive volume was kept [45].

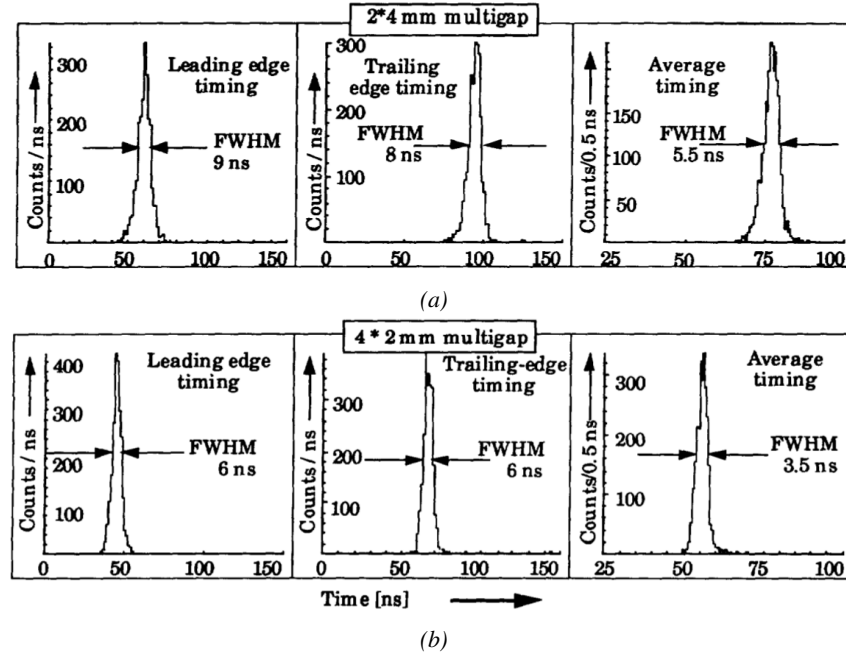


Figure 4.16: Time distributions of the leading, trailing, and average of both leading and trailing edges for multigap RPCs consisting in two 4 mm (Figure 4.16a) and four 2 mm (Figure 4.16b) exposed to a 100 Hz/cm² radiation rate. The data was collected with RPCs operated at the voltage corresponding to the knee of the efficiency distribution, defined as the point where 95% of the maximum efficiency is obtained [45].

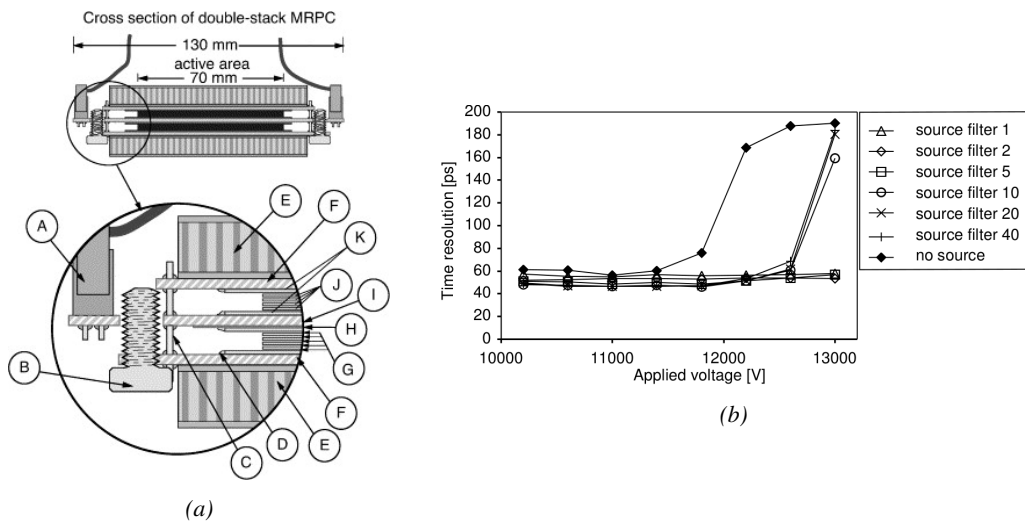


Figure 4.17: Presentation of a study of a possible ALICE MRPC cell using 250 µm gas gaps, 620 µm outer glass electrodes, and 550 µm inner floating electrodes (Figure 4.17a), and of its time resolution performance as a function of the applied high voltage for different radiation levels referred through different filter settings of the 740 GBq ¹³⁷Cs source the former CERN GIF facility [60].

2230 After the problem of streamers was solved by adding SF₆ into the gas mixture, the size of the

2231 MRPCs decreased as the research groups started applying the concept of dividing the gas volume
 2232 into subvolumes to the narrow gap RPCs leading to the now widely used micro gap MRPCs. The
 2233 time resolution of such a detector can reach of few tens of ps, with gas gaps of the order of a few
 2234 hundred μm as showed in Figure 4.17 representing a single cell of ALICE Time-of-flight (ToF)
 2235 system consisting of double MRPCs, as it was studied in the early 2000s [60].

2236 Sometimes used as a double multigap RPC, taking advantage of the OR of double gap RPCs to
 2237 both be able to operate a higher number of gaps while keeping a reasonable high voltage applied in
 2238 between the cathode and anode and to further reduce the gain, the MRPC is mainly used as ToF
 2239 detector [60–64] due to its excellent timing properties that allow to perform particle identification
 2240 as explained by Williams in [65]. The principle of particle identification using ToF is simply the
 2241 measurement of the velocity of a particle. Indeed, particles are defined by their mass (for the
 2242 parameter of interest here, their electric charge being measured using the bending angle of the
 2243 particles traveling through a magnetic field) and this mass can be calculated by measuring the
 2244 velocity β and momentum of the particle:

$$\beta = \frac{p}{\sqrt{p^2 + m^2}} \quad (4.3)$$

2245 Intuitively, it is trivial to understand that 2 different particles having the same momentum will have
 2246 a different velocity due to the mass difference and thus a different flight time T_1 and T_2 through the
 2247 detector and this is used to separate and identify particles. The better the time resolution of the ToF
 2248 system used, the stronger will the separation be:

$$T = \frac{L}{v} = \frac{L}{c \cdot \beta}, \quad \Delta T = T_1 - T_2 = \frac{L}{c} \left(\sqrt{1 + m_1^2/p^2} - \sqrt{1 + m_2^2/p^2} \right) \cong (m_1^2 - m_2^2) \frac{L}{2cp^2} \quad (4.4)$$

2249 An example of particle identification is given for the case of STAR experiment in Figure 4.18.

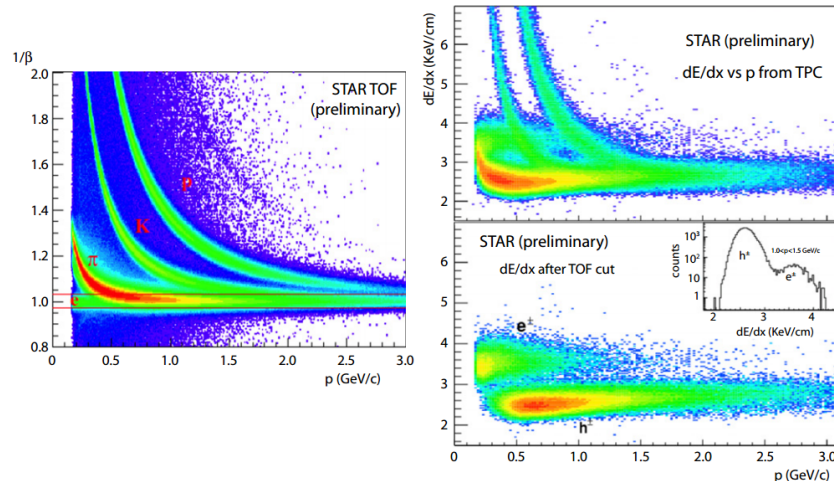


Figure 4.18: Particle identification applied to electrons in the STAR experiment. The identification is performed combining ToF and dE/dx measurements [65].

2250 Taking into account the distortion effect on the electric field inside of a MRPC built using micro
 2251 gaps due to the exposition to irradiation, distortion that can be understood by monitoring the current

2252 drawn by the detector which should stay constant at constant electric field, another benefice of
 2253 using such small gas gaps is the strong reduction of the average avalanche volume and thus of the
 2254 blind spot on MRPCs leading to an improved rate capability. Multigaps can sustain backgrounds of
 2255 several kHz/cm² as demonstrated in Figure 4.19.

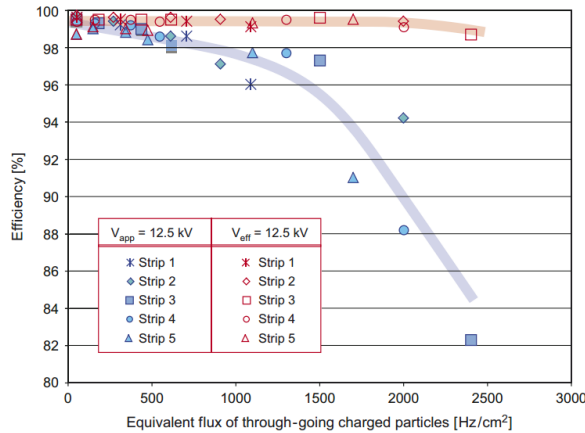


Figure 4.19: Comparison of the detector performance of ALICE ToF MRPC [66] at fixed applied voltage (in blue) and at fixed effective voltage (in red). The effective voltage is kept fixed by increasing the applied voltage accordingly to the current drawn by the detector.

2256 4.2.3.3 Charge distribution and performance limitations

2257 [This part could be moved in the next section of the chapter and deepened using the
 2258 perspective of the avalanche physics.]

2259 The direct consequence of the different RPC layouts is a variation of intrinsic time resolution of the
 2260 RPC as the gap size decreases and of the rate capability when the deposited charge per event is
 2261 spread over a larger number of amplification volumes, allowing for a reduction of the overall gain
 2262 of the detectors which is replaced by an on-electronics pre-amplification of the signals. in this
 2263 sense, an advantage is given to multigaps whose design use sub-millimeter gas volumes providing
 2264 very consistent signals.

2265 From the charge spectrum point of view, each layout has its own advantages. When the double-gap
 2266 has the highest induced over drifting charge ratio, as seen in Figure 4.20, the multigap has a charge
 2267 spectrum strongly detached from the origin, as visible in Figure 4.21. A high induced over drifting
 2268 charge ratio means that the double gap can be safely operated at high threshold or that at similar
 2269 threshold it can be operated with a twice smaller drifting charge, meaning a higher rate capability if
 2270 operated with sensitive enough electronics. On the other hand, the strong detachment of the charge
 2271 spectrum from the origin in the MRPC case allows to reach a higher efficiency with increasing
 2272 threshold as most of the induced charge is not low due to the convolution of several single gap
 2273 spectra. The range of stable efficiency increases with the number of gap, as presented in
 2274 Figure 4.22.

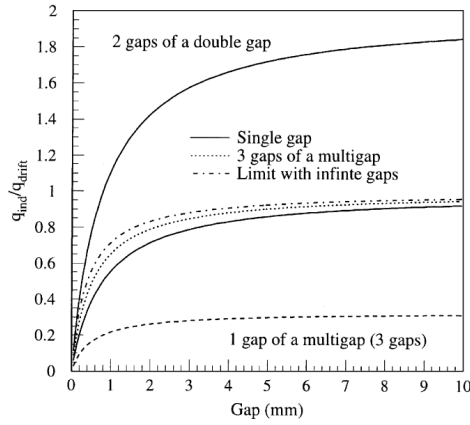


Figure 4.20: Ratio between total induced and drifting charge have been simulated for single gap, double-gap and multigap layouts [67]. The total induced charge for a double-gap RPC is a factor 2 higher than for a multigap.

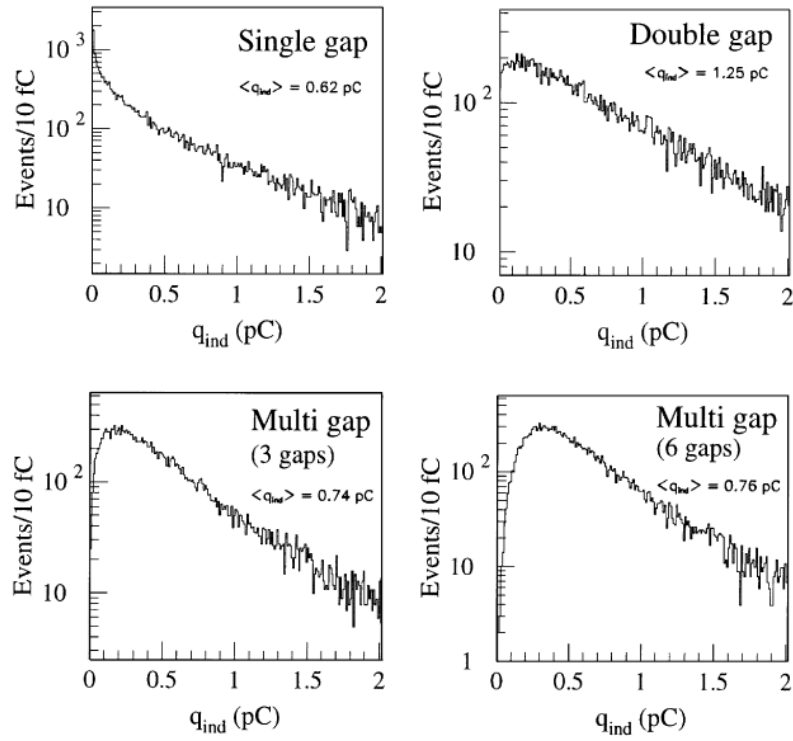


Figure 4.21: Charge spectra have been simulated for single gap, double-gap and multigap layouts [67]. It appears that when single gap shows a decreasing spectrum, double and multigap layouts exhibit a spectrum whose peak is detached from the origin. The detachment gets stronger as the number of gaps increases.

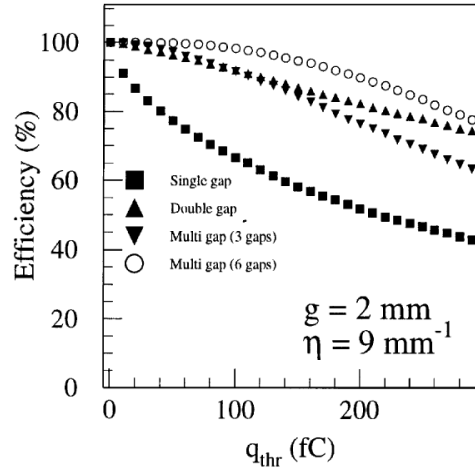


Figure 4.22: The maximal theoretical efficiency is simulated for single gap, double-gap and multigap layouts [67] at a constant gap thickness of 2 mm and using an effective Townsend coefficient of 9 mm^{-1} .

4.3 Signal formation

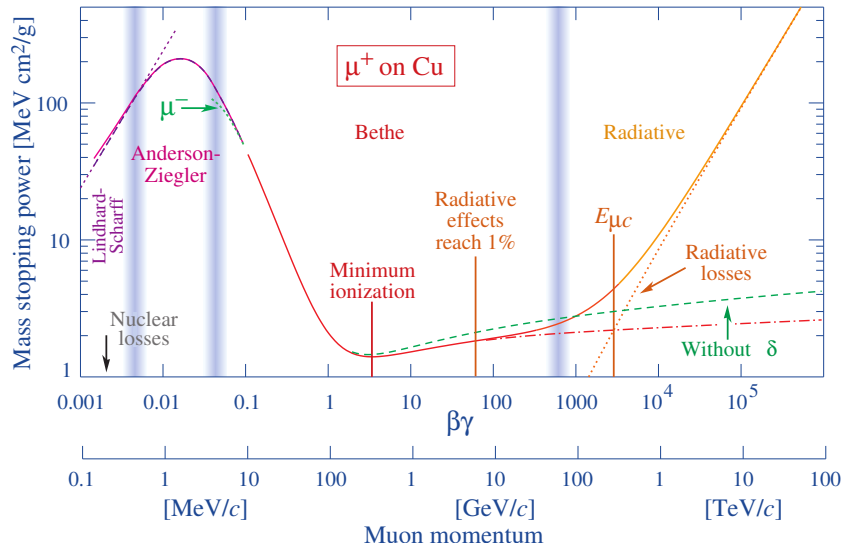


Figure 4.23: Mass stopping power as a function of $\beta\gamma = p/Mc$ for positive muons in copper [68]. The total stopping power is indicated with solid line and local components with dashed lines. The vertical bands are used to indicate boundaries between different approximations used at different energy range.

The physics of Resistive Plate Chambers still is far from being fully understood and work is regularly being accomplished in trying to model these detectors the best way possible by phenomenological models using well-defined physics [51, 69, 70]. These theoretical works have nevertheless lead to a better understanding of the key principles that account for RPCs signal

formation. As previously discussed, the typical mixture of such a detector is in great majority composed by a ionizing gas with some quenching properties and a low ionization potential to easily produce electrons, with the addition of UV quencher and electronegative compounds. The electronic avalanche formation will be triggered by a charged particle passing through the gas, typically a muon in the case of most uses of RPCs. The production of electrons in the gas of a detector is related to the energy lost by the incoming particle traveling through a material medium. The example of the mass stopping power of copper on muons is given in Figure 4.23 on which the different energy loss mechanisms at different energy ranges are visible. Once primary electrons have been freed in the gas volume, the electric field applied in between the electrodes of the RPC will make the charges move and there will be a competition in the gas in between the Townsend and attachment coefficient which describe the evolution of the number of electrons in an avalanche. While drifting through the gas, the electrons are also subjected to diffusion that will affect the evolution of the avalanches. Finally, when the avalanche is big enough, the accumulation of negative (electrons) and positive (ions) charges in the gas volume will start affecting the local electric field. This effect is known as space charge effect.

4.3.1 Energy loss at intermediate energies

Intuitively, a particle traveling through a medium will interact with its components, losing energy. When a muon travels through the gas of a gaseous detector, at the energy range usually observed, it interacts with the molecules of the gas leading to dissipation of the transferred energy in the form of inelastic diffusion or ionization. The photons and electron-ion pairs resulting from these interaction can trigger avalanches in the gas which will contribute to feed the avalanche growth thanks to the strong electric field applied in between the 2 electrodes of a RPC. The mass stopping power of moderately relativistic ($0.1 \lesssim \beta\gamma \lesssim 1000$) heavy particles ($M \gg m_e$) traveling through a medium via excitation and ionization processes was studied by Bethe in 1930 [71] and is well described by the so called the Bethe Formula given in Equation 4.5.

$$\left\langle -\frac{dE}{dx} \right\rangle = K z^2 \frac{Z}{A} \frac{1}{\beta^2} \left(\frac{1}{2} \ln \frac{2m_e c^2 \beta^2 \gamma^2 W_{max}}{I^2} - \beta^2 - \delta(\beta\gamma) \right) \quad (4.5)$$

The different parameters used in this equation are

E	- incident particle energy γMc^2	MeV
x	- mass per unit area	g cm^{-2}
N_A	- Avogadro's number	$6.022\ 140\ 857(74) \times 10^{23} \text{ mol}^{-1}$
c	- speed of light in vacuum	$299\ 792\ 458 \text{ m s}^{-1}$
μ_0	- permeability of free space	$4\pi \times 10^{-7} \text{ N A}^{-2}$
ϵ_0	- permittivity of free space $\epsilon_0 = 1/\mu_0 c^2$	$8.854\ 187\ 817\dots \times 10^{-12} \text{ F m}^{-1}$
α	- fine structure constant $\alpha = e^2/4\pi\epsilon_0\hbar c$	$1/137.035\ 999\ 139(31)$
r_e	- classical electron radius $r_e = e^2/4\pi\epsilon_0 m_e c^2$	$2.817\ 940\ 3227(19) \text{ fm}$
e	- elementary charge of the electron	$-1.6021766208(98) \times 10^{-19} \text{ C}$
$m_e c^2$	- electron mass $\times c^2$	$0.510\ 998\ 9461(31) \text{ MeV}$
K	- constant defined as $K = 4\pi N_A r_e^2 m_e c^2$	$0.307\ 075 \text{ MeV mol}^{-1} \text{ cm}^2$
z	- charge number of incident particle	
Z	- atomic number of absorbing medium	
A	- atomic mass of absorbing medium	g mol^{-1}
β	- velocity of particle $\beta = v/c$	
γ	- Lorentz factor $\gamma = (1 - \beta^2)^{-1/2}$	

W_{max}	-	maximum energy transfer through a single collision	MeV
I	-	mean excitation energy of absorbing medium	eV
$\delta(\beta\gamma)$	-	density effect correction to ionization energy loss	

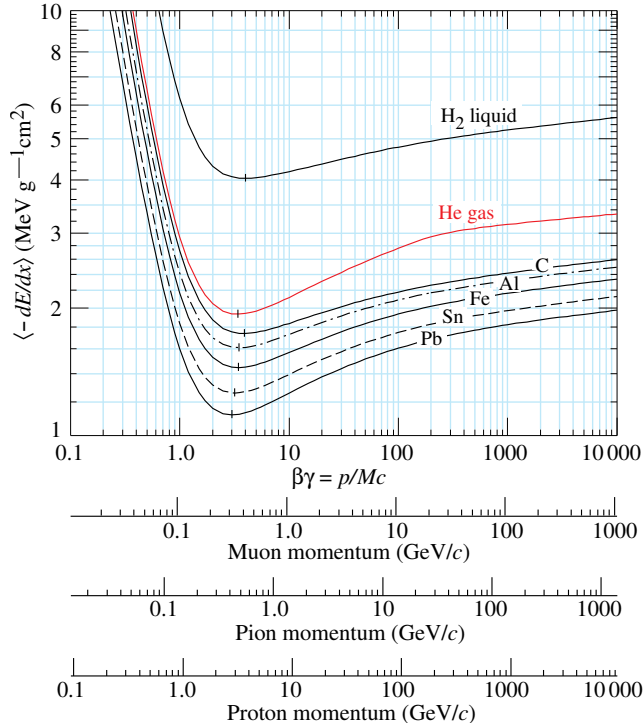


Figure 4.24: Mean mass stopping power for liquid hydrogen, as used in bubble chambers, gaseous helium, carbon, aluminum, iron, tin, and lead without the inclusion of radiative effect at higher $\beta\gamma$ necessary for pions and muons in denser materials [68].

In this equation, the maximum energy transfer W_{max} is defined as function of the incident particle mass M , expressed in MeV/c²

$$W_{max} = \frac{2m_e c^2 \beta^2 \gamma^2}{1 + 2\gamma m_e / M + (m_e / M)^2} \quad (4.6)$$

and the mean excitation energy I depends on the absorber and its determination is non-trivial but recommendation are given by the International Commission on Radiation Units & Measurements (ICRU) based on experimental measurements and interpolations as showed in Figure 4.25.

For the case of copper, the mean stopping power is visible in Figure 4.23. The mean stopping power corresponding only to the Bethe range for other materials is given in Figure 4.24 and shows that $\langle -dE/dx \rangle$ is similar for each material with a slow decrease with Z . The factor affecting the equation the most is β as the dependence on M is introduced at higher energies in the logarithm via the max transfer energy per single collision but in most practice cases, only the dependence on β is considered as most of the relativistic particles are closed to the lowest mean energy loss rate and are

²³¹⁸ referred to as minimum ionizing particles (mip's). The almost logarithmic relation in between the
²³¹⁹ mean energy loss rate for minimum ionizing particles and Z is showed in Figure 4.26.

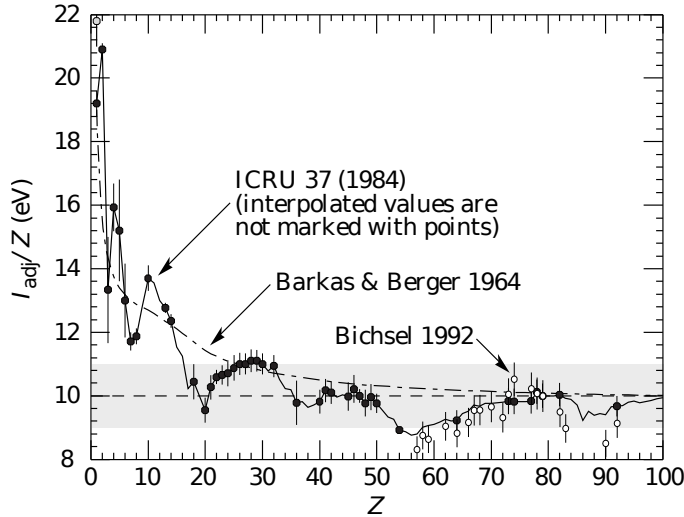


Figure 4.25: Mean excitation energies normalized to the atomic number as adopted by the ICRU [68, 72, 73].

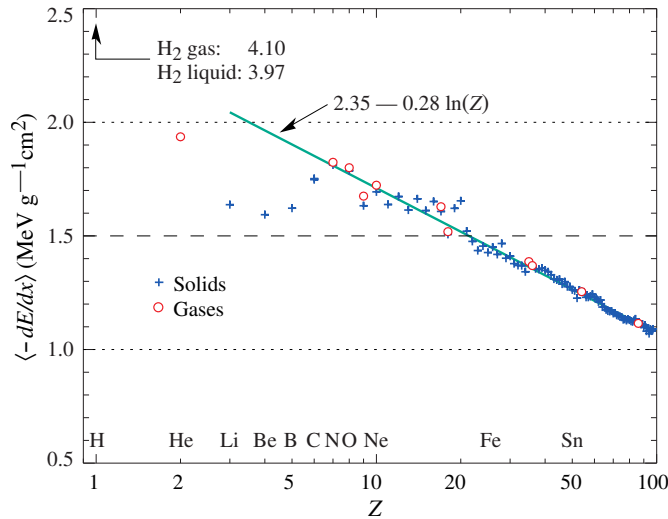


Figure 4.26: Mean mass stopping power at minimum ionization as a function of the atomic number [68].

²³²⁰ Finally, the term $\delta(\beta\gamma)/2$ corresponds to the density effect correction introduced to account for the
²³²¹ polarization of a real media that limits the spatial extension of the electric field of relativistic
²³²² particles. Indeed, as the energy of a particle increases, the associated electric field will flatten and
²³²³ extend. Due to this effect, the distant collision contribution to Equation 4.5 will increase as $\ln(\beta\gamma)$
²³²⁴ but the polarization of the media trunc this rise. At high energies, the correction is given by

²³²⁵ Equation 4.7

$$\delta/2 \longrightarrow \ln(\hbar\omega_p/I) + \ln(\beta\gamma) - 1/2 \quad (4.7)$$

²³²⁶ where $\hbar\omega_p$ represents the plasma energy that depends on the electron density of the media and the
²³²⁷ electron mass and can be calculated as $\sqrt{\rho\langle Z/A\rangle} \times 28.816$ eV. The introduction of this correction
²³²⁸ term reduces the increase of the mean stopping power at higher energies as can be seen in
²³²⁹ Figure 4.23. Moreover, due to poorer electron density, the effect is less visible on gases than on
²³³⁰ liquids and solids has van be seen from Figure 4.24.

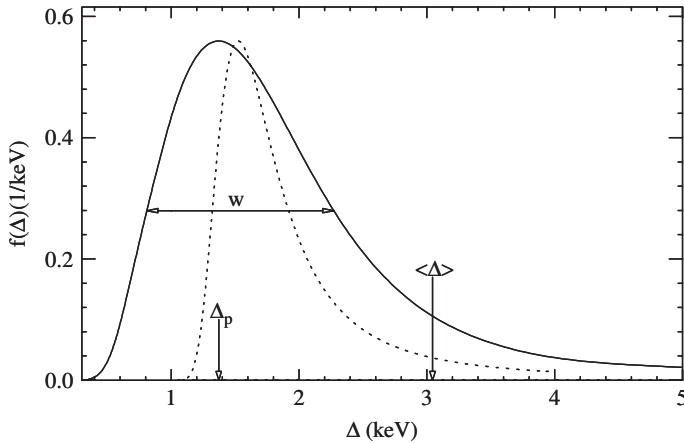


Figure 4.27: Example of straggling function $f(\Delta)$ of particles passing through 1.2 cm of Argon gas with a $\beta\gamma$ of 3.6 and represented with a solid line. The original Landau distribution is showed with a dashed line [74].

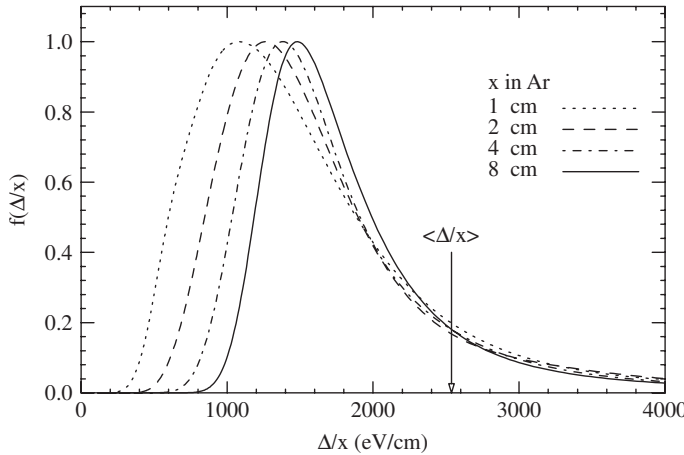


Figure 4.28: Evolution of straggling functions $f(\Delta)$ of particles passing through a volume of Argon gas with a $\beta\gamma$ of 3.6 with increasing thickness x [74].

²³³¹ The mean energy loss per collision can be difficult to measure for low data samples and is not
²³³² always representative of the energy loss distribution for a given incident particle energy. Hence, it is
²³³³ easier to access the most probable energy loss which is a lower value than than the average loss due

to the distribution of the energy transfer. This value is well described by a highly skewed Landau distribution for detectors with "moderate" thickness x , expressed in g mol⁻¹. But for gas volumes, a Landau distribution greatly underestimates the width w of the distribution and only succeeds to provide with a correct value for the most probable energy loss, as showed in Figure 4.27. Thus, the energy loss distribution is better represented by its most probable energy loss Δ_p and its full-width-at-half-maximum (FWHM) w . As showed by Figure 4.28, the distribution is affected by the thickness of the gas volume and the most probable energy loss normalized to the thickness is increased and the width decreased, converging towards the Landau distribution, whereas the mean energy loss is unchanged. Correction are brought to the original Landau equation in order to account better for the number of collisions leading to an increased width of the energy loss distribution [74].

In the case of gas mixtures, composed of several elements, using Bragg additivity it can be understood that the mean energy loss of the mixture is the sum of the mean energy losses in each individual element j layer of weight w_j .

$$\left\langle \frac{dE}{dx} \right\rangle = \sum w_j \left\langle \frac{dE}{dx} \right\rangle_j \quad (4.8)$$

4.3.2 Primary ionization

Using Bethe formula to understand the mean energy transfer of charged particle when traveling through a gas volume give an intuition of the physics that affect the particle but doesn't provide a detailed enough information about the individual ionizations along its tracks at a microscopic level. In order to simulate efficiently an RPC and hence understand the processes governing avalanches creation and growth, knowledge on the ionization process is necessary.

To convert the energy loss rate into a number of primary ionizations was developed in 1980 the Photo-Absorption Ionisation (PAI) model [75] based on the cross section of ionization of gas atoms to real photons and the dielectric constant of the medium through which the charged particles are going. Indeed, the interaction of charged particles with the gas molecules being of electromagnetic nature, it is mediated by quasi-real photons and, hence, the cross section to photon ionization is important to understand. This approach is nevertheless semi-classical as it relies on classical electrodynamics and it only gives access to the energy transfer to the gas atoms and no information on the energy dissipation and secondary emissions is available on the output of the model. The energy transferred to the medium is not all used for ionization. For an energy deposition Δ , the number of electron-ion pairs produced is:

$$\Delta = n_i W \quad (4.9)$$

W corresponds to the mean work per pair production that depends on the medium and is greater than the ionization potential leading to the conclusion that part of the transferred energy is dissipated through other processes [70, 76]. In order to understand the energy dissipation and the secondary emissions, the fine structure of each atom is taken into account. Through the PAI model, the incident charged particle interacts is assumed to interact with the full atom rather than with a single electron.

Although, considering that the particle interacts with a single electron, leads to the possibility to study the excited state of the atom once the photo-electron has been emitted with an energy corresponding to the transferred energy minus the binding energy of the electronic shell. The

resulting vacancies in the electronic shell will be filled through emission of photons or Auger electrons and can contribute to further ionization or excitation in the gas volume. Fluorescence photons are usually not considered as they only constitute a very small fraction of secondary emissions [77]. Assuming that the transferred energy is absorbed in its totality by a single electronic shell, the PAI model was modified to include relaxations and constitute the new Photo-Absorption Ionisation with Relaxation (PAIR) model [77]. In this model, the cross section corresponding to the whole atom is re-expressed using a sum of partial cross sections corresponding to the different electronic shells. When one or more electrons are knocked out of the atom, the vacancies are filled by electrons of the shell above with relaxation by Auger electron emission. These processes happen in cascade from the inner shell to the outer one until all the vacancies are filled and the energy has been released.

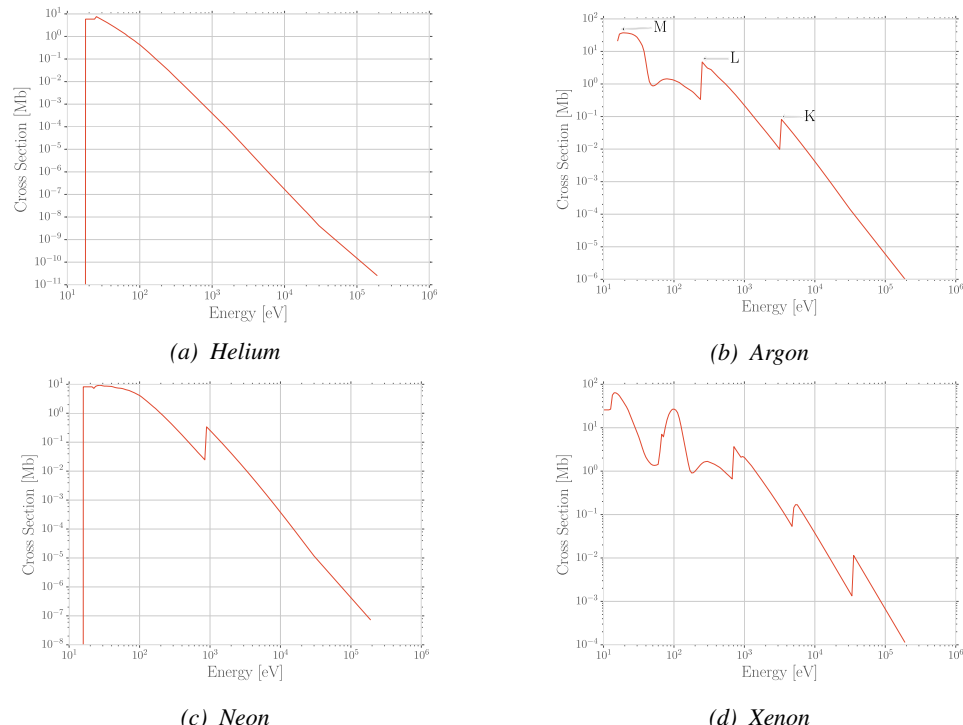


Figure 4.29: Photo-absorption cross section as computed by HEED for noble gases with different electric shell numbers [70].

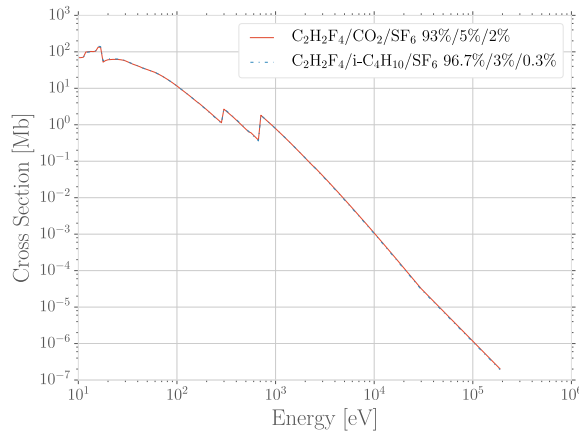


Figure 4.30: Photo-absorption cross section as computed by HEED for typical RPC gas mixtures [70]. The RPC mixture with CO₂ corresponds to the mixture used by CALICE SDHCAL [78] while the other one was foreseen for the experiment ATLAS [79] but has been changed since then.

This model is included in the program HEED developed at CERN [80] and called by Garfield, a program developed for the simulation of gaseous detectors. The results for the cross section for a few noble gases are given in Figure 4.29. It can be seen that for each shell, the cross section is increased. More complex patterns are seen with bigger atoms such as Xenon on Figure 4.29d. For gas mixtures, like the typical RPC mixtures, the cross section is showed in Figure 4.30. Both mixtures being mainly composed of C₂H₂F₄, the variations in between the 2 cross section profiles are very subtle and depends on the concentration of the other compounds.

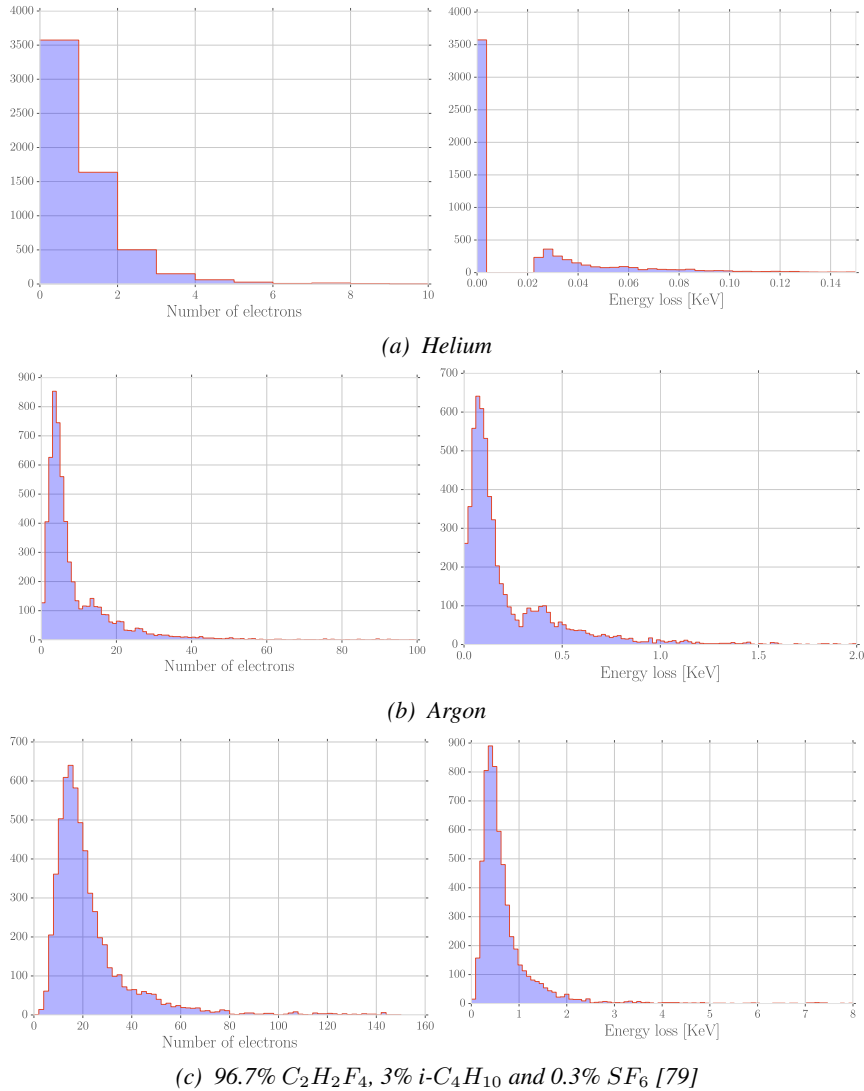


Figure 4.31: Distributions of number of electrons (left) and energy loss (right) for a 5 GeV/c muon passing through 1.2 mm of Helium (Figure 4.31a), Argon (Figure 4.31b) or a typical RPC gas mixture (Figure 4.31c) [70].

Once the cross section of interaction is known, it is possible to extract the distribution of energy loss and of the number of electron produced, as showed in Figure 4.31 for Helium, Argon, which is used in gaseous detectors, and for a typical RPC mixture [70]. The distributions are computed using HEED and show typical straggling function profiles with some complex structures that can be related to interaction of the incoming particle with the different electronic shells. Helium does not have a great photo-absorption cross-section according to Figure 4.29a and a muon will not be likely to lose a lot of energy and to create a lot of electrons whereas in a more complex atom like Argon, the cross-section is greater and will lead to a greater energy loss of muons and more electron produced. Finally, a complex gas mixture used in RPCs will offer an even greater cross-section, a wider energy loss distribution and will be able to produce more electrons. The same information is

seen by looking at the evolution of the mean number of cluster as a function of the lorentz factor associated to muons showed in Figure 4.32a. Indeed, the greater photo-absorption cross-section of RPC mixtures allow for a much greater amount of clusters to be created by charged particles. The size of these clusters is studied through Figure 4.32b which shows that, in most of the cases ($\approx 80\%$), the clusters only are composed of a single electron which is consistent with minimum ionizing particles.

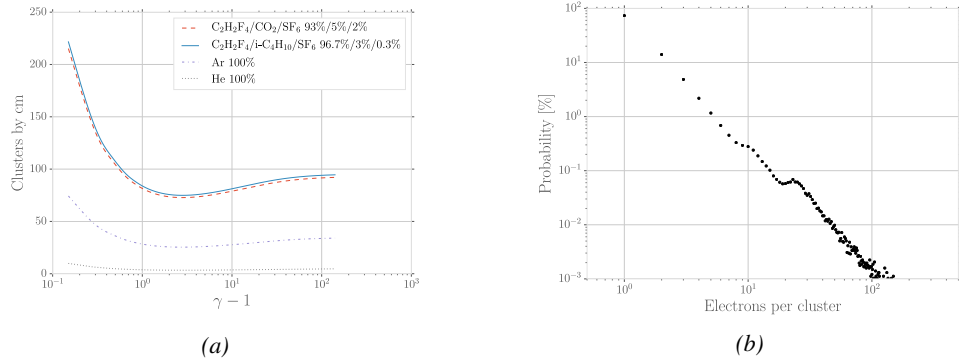


Figure 4.32: Figure 4.32a: Mean cluster density for muons through different gas volumes [70]. Figure 4.32b: Distribution of the number of electrons per cluster for a 5 GeV/c muon traveling through a mixture of 96.7% $C_2H_2F_4$, 3% $i-C_4H_{10}$ and 0.3% SF_6 [70, 79].

4.3.3 Development and propagation of avalanches

From the clusters released in the gas volume by the charged particles, free electrons will start drifting due to the electric applied in between the electrodes of the RPC. Gaining velocity and energy, these electrons in their turn will be able to ionize the gas. This process being repeated by all the produced electrons will trigger an avalanche to develop. The growth of the avalanche can be intuitively understood as a competition between 2 effects. Due to their increasing energy, electrons have a probability to trigger new ionizations by interacting with gas molecules. On the other hand, before the minimal amount of energy is reached, the electrons can get attached to a gas molecule instead. These two effects can be described using a simple model in which the multiplication and attachment processes are given by the Townsend coefficient α and the attachment coefficient η , assuming that the history of previous interactions in the gas does not influence new interactions. This model simply takes into account probabilities to have at the gas depth z for a given number n of free electrons in the gas $n + 1$ or $n - 1$ electrons at the depth $z + dz$ (respectively $n\alpha dz$ and $n\eta dz$). Then, the mean number of electrons \bar{n} and cations \bar{p} can be written for single compound gases as

$$\frac{d\bar{n}}{dz} = (\alpha - \eta)\bar{n}, \quad \frac{d\bar{p}}{dz} = \alpha\bar{n} \quad (4.10)$$

which, assuming the initial conditions $\bar{n}(0) = 1$ and $\bar{p}(0) = 0$, lead to the mean number of electrons and cations at a depth z

$$\bar{n}(z) = e^{(\alpha-\eta)z}, \quad \bar{p}(z) = \frac{\alpha}{\alpha - \eta} \left(e^{(\alpha-\eta)z} - 1 \right) \quad (4.11)$$

2424 The Townsend and attachment coefficient as a function of the applied electric field are given in
 2425 Figure 4.33 for a standard RPC gas mixture using Magboltz [81].

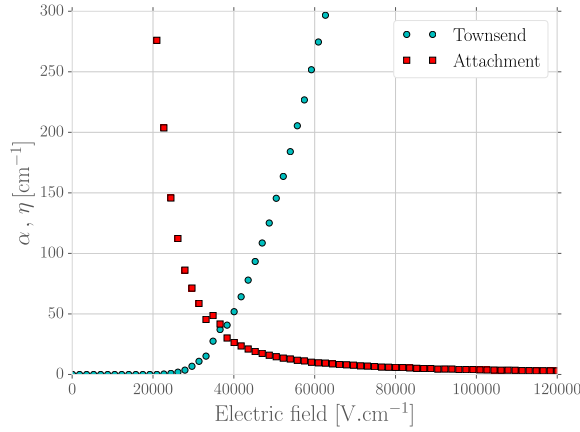


Figure 4.33: Townsend and attachment coefficient for a typical 96.7/3/0.3 mixture of $C_2H_2F_4/i-C_4H_{10}/SF_6$, at a temperature $T = 296.15\text{ K}$ and a pressure $P = 1013\text{ hPa}$ [70, 79].

2426 Nevertheless, there are more to the avalanche growth than simply these two factors. Throughout the
 2427 20th century, models have been developed to better understand the physics of discharges in gas. In
 2428 1937, Furry developed a model to describe electromagnetic cascades [82] that would be used for
 2429 electron avalanches in gas during the 1950s. Furry realized that the use of a Poisson law to describe
 2430 the distribution of shower sizes could not be accurate as he understood that the events occurring in
 2431 the development of a cascade are not independent from each other, as a Poisson law would suggest.
 2432 Indeed, part of the particles produce others and this process depends on both their original energy
 2433 and energy lost. Experimental results showed excess of small showers and an under estimate of very
 2434 large ones. To solve this problem, Furry proposed a distribution of sizes of following the likelihood
 2435 described in Equation 4.12, in which $\bar{n} = e^{\alpha z}$, compared with a Poisson law in Figure 4.34.

$$P(n, \bar{n}) = \bar{n}^{-1} (1 - \bar{n}^{-1})^{n-1} \quad (4.12)$$

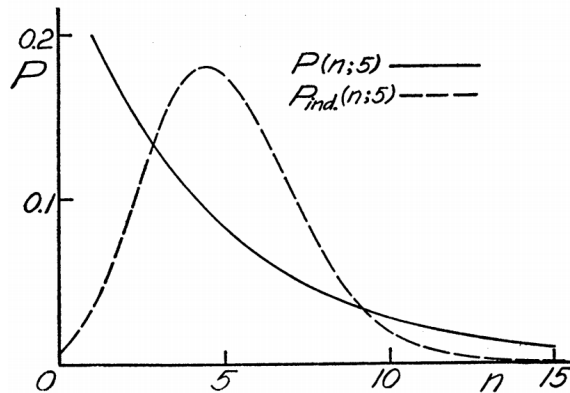


Figure 4.34: Comparison of the distribution law of Furry and the Poisson law for $\bar{n} = 5$ [82].

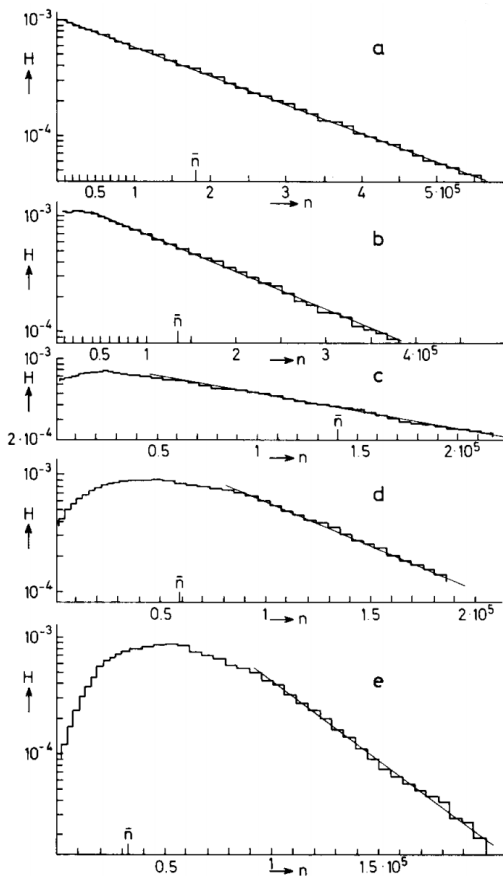


Figure 4.35: Single-electron avalanche size distribution in a proportionnal counter filled with methylal at different E/p values. (a) 70, (b) 76.5, (c) 105, (d) 186.5, (e) 426V/cm torr [83].

In this model, no extra energy is brought to the electrons in the showers, contrary to the case of a gaseous detector such as a RPC where an electric field accelerates them. Using the Furry model, Genz studied the fluctuations in electron avalanches in gaseous detectors [83]. Collisions leading to ionizations leave electrons with an energy much smaller than the ionization energy eU_i , where U_i is the ionization potential of a gas molecule. Hence, the electrons need to travel a distance $s = U_i/E$ along the electric field E to acquire a high enough energy to trigger a new ionization. For the probability of a new ionization to be independent from the path followed by the electrons since the previous ionization, the mean free path $1/\alpha$ of electrons in the gas has to be large compared to s and thus $E/\alpha \gg U_i$. The Townsend coefficient is related to the gas pressure leading to conditions on the value of E/p . Avalanches in gas are large compared to the showers Furry has studied in his original paper. For very large avalanche sizes, Equation 4.12 can be written as an exponential, as showed in Equation 4.13.

$$P(n, \bar{n}) = \bar{n}^{-1} e^{-n/\bar{n}} \quad (4.13)$$

This exponential behaviour is showed through Figure 4.35. In practice, to fully understand the avalanche growth, taking into account the path followed by electrons from one ionization to another will become necessary. In the same paper, Genz then discusses models using Polya distributions to

estimate the multiplication by looking at the size of the avalanche it self. Indeed, the number of charge carriers in the avalanche might become important enough to have an effect on the multiplication process. To account for this, it was proposed to use a varying Townsend coefficient such as described by Equation 4.14 depending on the position x in which θ is an empirical parameter leading to the probability distribution of Equation 4.15. In the limit case where θ goes to 0, the formula describes again the Furry model. But the data deviates from this model as well at large n values. Moreover, the introduction of an empirical parameters makes the model hard to interpret physically.

$$\alpha(n, x) = \alpha(x) \left(1 + \frac{\theta}{n}\right), \quad n > 0 \quad (4.14)$$

$$P(n, x) = \frac{1 + \theta}{\bar{n}} \frac{1}{\theta!} \left(\frac{n(1 + \theta)}{\bar{n}}\right)^{\theta} e^{-\frac{n(1 + \theta)}{\bar{n}}} \quad (4.15)$$

In order to have a model that describes reality better, the introduction of the attachment into the model is an important step. Despite its limitations, the Furry model had the advantage to describe well avalanches occurring when the attachment could be ignored. This is only natural that this model was then extended to included attachment. This was done by Riegler, Lippmann and Veenhof [79] which showed that what was important was to consider both the Townsend coefficient describing the multiplication *and* the attachment coefficient, not only the effective multiplication coefficient $\bar{\alpha} = \alpha - \eta$. The probability to see an avalanche started by a single electron grow to a size n after having traveled a distance z through the gas is given by Equation 4.16.

$$\begin{aligned} P(n, z) = & P(n - 1, z) (n - 1)\alpha dz (1 - (n - 1)\eta dz) \\ & + P(n, z) (1 - n\alpha dz) (1 - n\eta dz) \\ & + P(n, z) n\alpha dz n\eta dz \\ & + P(n + 1, z) (1 - (n + 1)\alpha dz) (n + 1)\eta dz \end{aligned} \quad (4.16)$$

The first term of this probability that from a state with $n - 1$ electrons, only 1 multiplies while the others don't get attached. Both the second and third terms describes the probability that from a state with already n electrons the total number of electrons stay the same. On the second term, no electron gets attached nor multiplies while on the third term, 1 electron gets multiplied and 1 gets attached to compensate. Finally, the fourth term describes the probability to fall from a state with $n + 1$ to a state with n electrons due to the attachment of a single electron. At the first order, the evaluation of the previous expression leads to Equation 4.17 which general solution is given in Equation 4.18 in which are introduced the variables $\bar{n}(z)$, defined as in Equation 4.11, and $k = \eta/\alpha$ making explicit the fact that the distribution not only depends on the effective Townsend coefficient.

$$\frac{dP(n, z)}{dz} = -P(n, z)n(\alpha + \eta) + P(n - 1, z)(n - 1)\alpha + P(n + 1, z)(n + 1)\eta \quad (4.17)$$

$$P(n, z) = \begin{cases} k^{\frac{\bar{n}(z)-1}{\bar{n}(z)-k}}, & n = 0 \\ \bar{n}(z) \left(\frac{1-k}{\bar{n}(z)-k}\right)^2 \left(\frac{\bar{n}(z)-1}{\bar{n}(z)-k}\right)^{n-1}, & n > 0 \end{cases} \quad (4.18)$$

The example given through Figure 4.36 shows the importance of each individual process in the growth of avalanches and the fluctuation of their size. The values of α and η will influence the probability distribution, as can be seen from Figure 4.36a. Then, Figure 4.36b shows that the

²⁴⁷⁹ fluctuation really takes place within the very first interactions. Indeed, when the avalanche contains
²⁴⁸⁰ a large enough amount of charge carriers (a few hundreds), its size then increases like $e^{z(\alpha-\eta)}$.

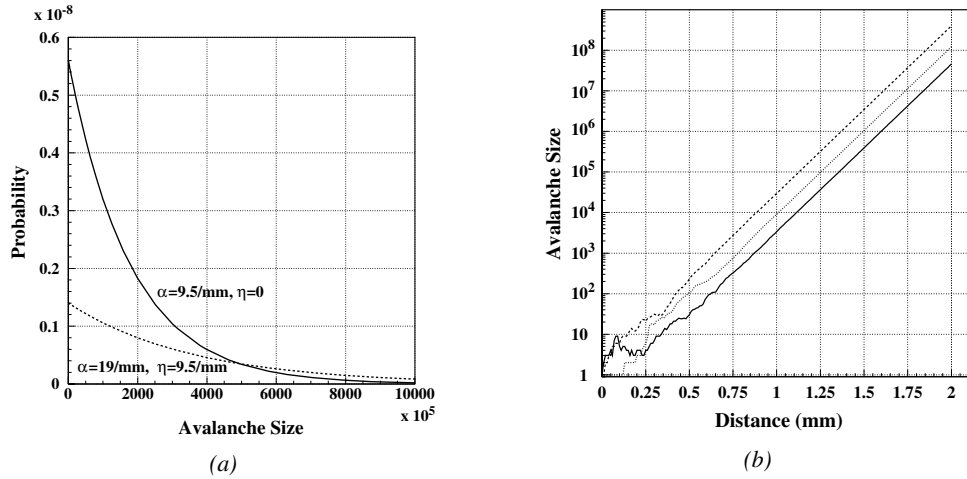


Figure 4.36: Figure 4.36a: Comparison of avalanche size distributions for different values of Townsend and attachment coefficients. The effective Townsend coefficient is the same for both distributions. Figure 4.36b: Fluctuation in avalanche size for avalanche started by a single electron with $\alpha = 13 \text{ mm}^{-1}$ and $\eta = 3.5 \text{ mm}^{-1}$ [79].

²⁴⁸¹ 4.3.4 Drift and diffusion of the electron cloud

²⁴⁸² During the growth of avalanches, an electron cloud drifting along the electric field through the gas
²⁴⁸³ will undergo thermal diffusion due to random collisions with the gas molecules. This phenomenon
²⁴⁸⁴ can be studied using Maxwell-Boltzmann distribution whose mean is defined by the thermal energy
²⁴⁸⁵ of the cloud $\langle E \rangle = 3/2kT$ with an extra component coming from the constant drift motion. The
²⁴⁸⁶ drift of electrons along the field lines is usually observed on a macroscopic scale through which the
²⁴⁸⁷ speed can be assimilated to a constant v_D which corresponds to the mean drift speed over a large
²⁴⁸⁸ number of collisions in the gas.

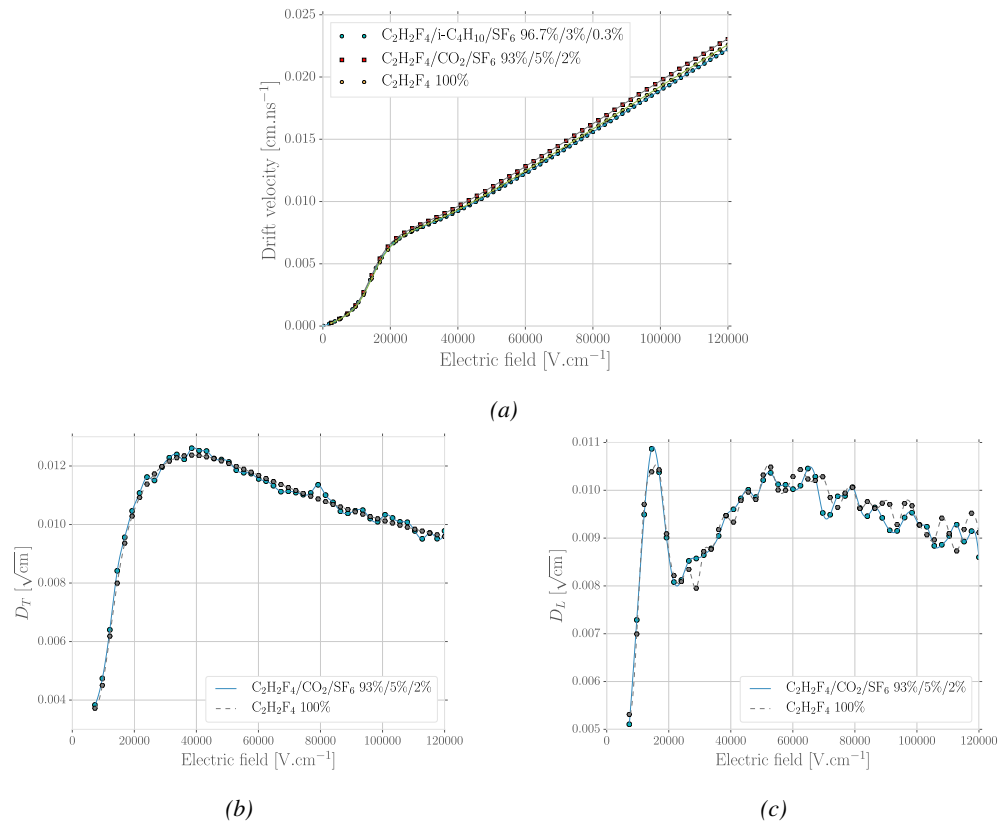


Figure 4.37: Figure 4.37a: Electron mean drift velocity v_D in pure $C_2H_2F_4$ and typical RPC gas mixtures. Figure 4.37b: Transverse diffusion coefficient in pure $C_2H_2F_4$ and a typical RPC gas mixture. Figure 4.37c: Longitudinal diffusion coefficient in pure $C_2H_2F_4$ and a typical RPC gas mixture. All results are given with a pressure $P = 760$ Torr and a temperature $T = 296.15$ K [70].

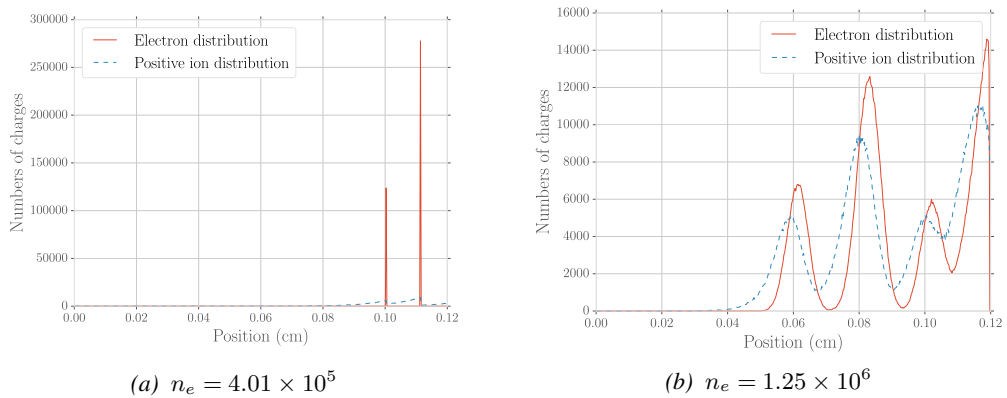


Figure 4.38: Comparison of the free charge carriers in the gas after a time $t = 7.90$ ns in the case where no diffusion is taken into account to simulate the avalanche (Figure 4.38a) and in the case where the diffusion is implemented (Figure 4.38b) [70].

Indeed, at the microscopic scale, the electrons are drifting over a distance δz while acquiring the corresponding kinetic energy $T = e_0 |\vec{E}| \delta z$ until they are slowed down by a collision in which they lose part of their energy. This process is repeated as long as electrons are free carriers. Starting from a point-like electron cloud, the Gaussian density distribution at \vec{r}_0 will be described by Formula 4.19 in which the width of the isotropic distribution is $\sigma = 2\bar{D}t$, with \bar{D} being a diffusion coefficient expressed in m^2/s [51].

$$\varphi(\vec{r}, t) = \frac{1}{(\sqrt{2\pi}\sigma(t))^3} \exp\left(-\frac{(\vec{r} - \vec{r}_0)^2}{2\sigma^2(t)}\right) \quad (4.19)$$

Now, if the constant drifting motion is added, the distribution is anisotropic and can be divided onto transversal (Formula 4.20) and longitudinal (Formula 4.21) terms, $\varphi(r, z, t) = \varphi_T(r, t)\varphi_L(z, t)$, with a cylindrical symmetry around the field axis [51]. The variables t and $\sigma_{T,L}(t)$ can be hidden to the profit of the diffusion coefficients by using the relations $v_D = l/t$ and $\sigma_{T,L}^2(t) = 2\bar{D}_{T,L}l/v_D$ and introducing new diffusion coefficients $D_{T,L} = \sqrt{2\bar{D}_{T,L}/v_D}$ in order to explicitly show the dependence of the Gaussian width in drifted distance l .

$$\varphi_T(r, t) = \frac{1}{D_T^2 l} \exp\left(-\frac{(r - r_0)^2}{2D_T^2 l}\right) \quad (4.20)$$

$$\varphi_L(z, t) = \frac{1}{\sqrt{2\pi l D_L}} \exp\left(-\frac{(z - z_0)^2}{2D_L^2 l}\right) \quad (4.21)$$

These coefficients, as well as the drift velocity of the electrons, can be calculated thanks to Magboltz as showed in Figure 4.37. The influence of the diffusion on the distribution of charge carriers throughout the gas volume is depicted in Figure 4.38. From very localised electron clusters in the gas in Figure 4.38a, a Gaussian diffusion is then visible in Figure 4.38b. Due to the interactions with gas molecules during the drift, diffusions can occur in the forward and backward direction. Electrons diffused backward will effectively drift over a longer distance and multiply more than electrons diffused forward that will see a shorter drift length. As an effect, the avalanche develops over a longer time and extends over a greater gas volume than in the case the electron cloud is considered as point like and without diffusion. Moreover, as a side effect to the longer growth of the avalanche due to backward longitudinal diffusion, the total production of electrons is increased.

4.3.5 Space charge effect & streamers

Now that have been considered the basic processes that influence the development of avalanches in a gaseous detector in the previous sections, it is now important to consider the influence of the charge carriers present in the avalanche on the electric field seen by the avalanche. Indeed, each charged particle induces an electric field and it is only natural that the increasing density of electrons and ions in the detector volume will affect the electric field. Thus, parameters such as the Townsend and attachment coefficients, drift velocity or diffusion coefficients will find themselves to be modified along the gas gap length due to this effect referred to as *space charge effect*. Figure 4.39 is a more detailed version of Figure 4.1 (b) in which three electric regions are distinguished [51]. When compared to the linear electric field of strength E_0 that is developed in between the detector's electrodes, the accumulation of negative charges (electrons) on the front of the avalanche will reinforce the effective electric field in between the anode of the avalanche front.

2524 Deeper in the gas volume, the positive charges (cations) slowly drift towards the cathode and can
 2525 induce together with the avalanche front opposite electric field loops. Finally, due to the density of
 2526 positive charges, the electric field seen in between the ions tails and the cathode charged with
 2527 negative charges is on average stronger than E_0 and compensate for the locally reversed field E_2 .
 2528 Lippmann roughly estimated by considering that 10^6 charges were contained in a sphere of radius
 2529 $r_d = 0.1$ mm that the space charge effect could change the electric field by 3% and the Townsend
 2530 and attachment coefficient up to 14% [51, 70].

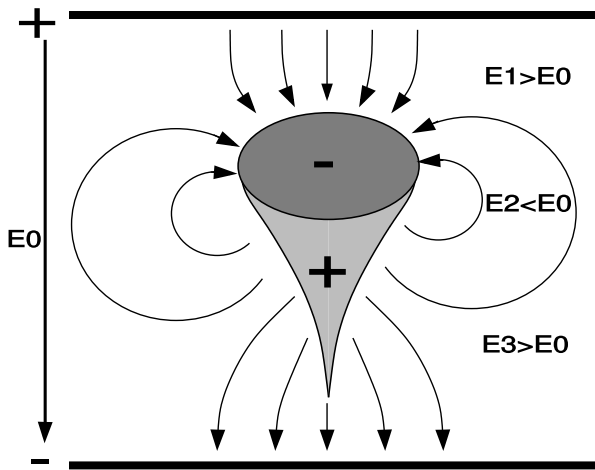


Figure 4.39: Schematic representation of an avalanche and of the electric field deformation it causes due to the local concentration of charge carriers [51].

2531 To account for the space charge effect, the electric potential and field of free charges are solved and
 2532 applied to each charges in the avalanche [51, 70]. As discussed by Français who has been working
 2533 on simulating RPCs similar to that used by the SDHCAL project of ILC, the computation of these
 2534 equations for each individual charge carrier to dynamically know the space charge field at every
 2535 stage of an avalanche development is a difficult task and would require far too much computation
 2536 time and a solution is to pre-compute an interpolation table keeping an adequately large number of
 2537 values of the space charge field for each positions in space thanks to which the values stored in the
 2538 interpolation table become very close to the analytic solution and allow for a much faster
 2539 simulation.

2540 The study of space charge effect through simulation shows that it can lead to a saturation of the
 2541 avalanche growth due to the deformation of the electric field, as showed through Figure 4.40.
 2542 Additionnally, a more precise understanding of the space charge effect is given through Figure 4.41
 2543 which looks at the distribution of charges and the distortion of the electric field at different steps of
 2544 the evolution of an avalanche in a RPC. At the moment a 5 GeV muon ionizes the gas, electron-ion
 2545 pairs are created in the gas in different clusters (Figure 4.41a). Later, the first clusters have reached
 2546 the anode while the clusters that where created the closest to the cathode are now big enough to
 2547 start influencing the electric field in the gap (Figure 4.41b). When a cluster is big enough, the
 2548 electric field in front of it locally increases a lot and contributes to a stronger but very localised
 2549 multiplication. At the same moment, the positive ions right behind the cluster avalanche front
 2550 decrease the electric field, saturating the electron multiplication on the tail of the electron cloud
 2551 (Figure 4.41c). Finally, when all the electrons have reached the anode and are relaxing, the electric

2552 field still is very deformed by the distribution of both positive and negative ions in the the gas
 2553 volume closest to the anode (Figure 4.41d).

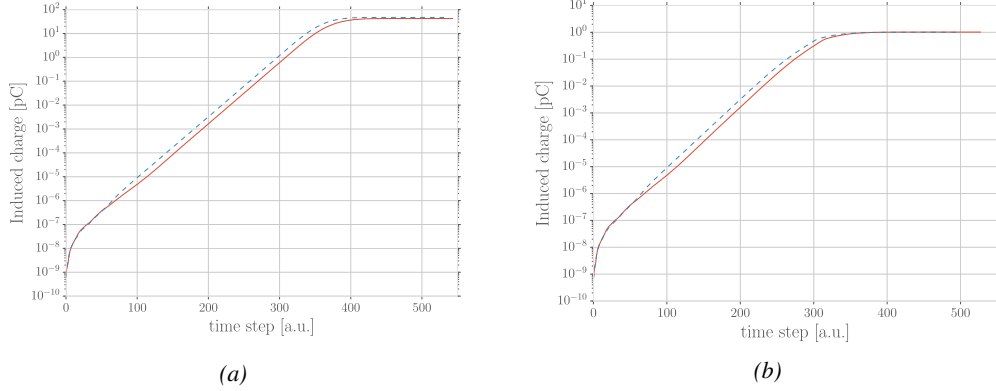


Figure 4.40: Evolution of the charge induced by an avalanche started by a single electron in a 1.2 mm thick RPC with an applied electric field of 54 kV/cm in the case space charge is not taken into account (Figure 4.40a) and in the case it is implemented into the simulation (Figure 4.40b). The total induced charge is correlated to the size of the avalanche [70].

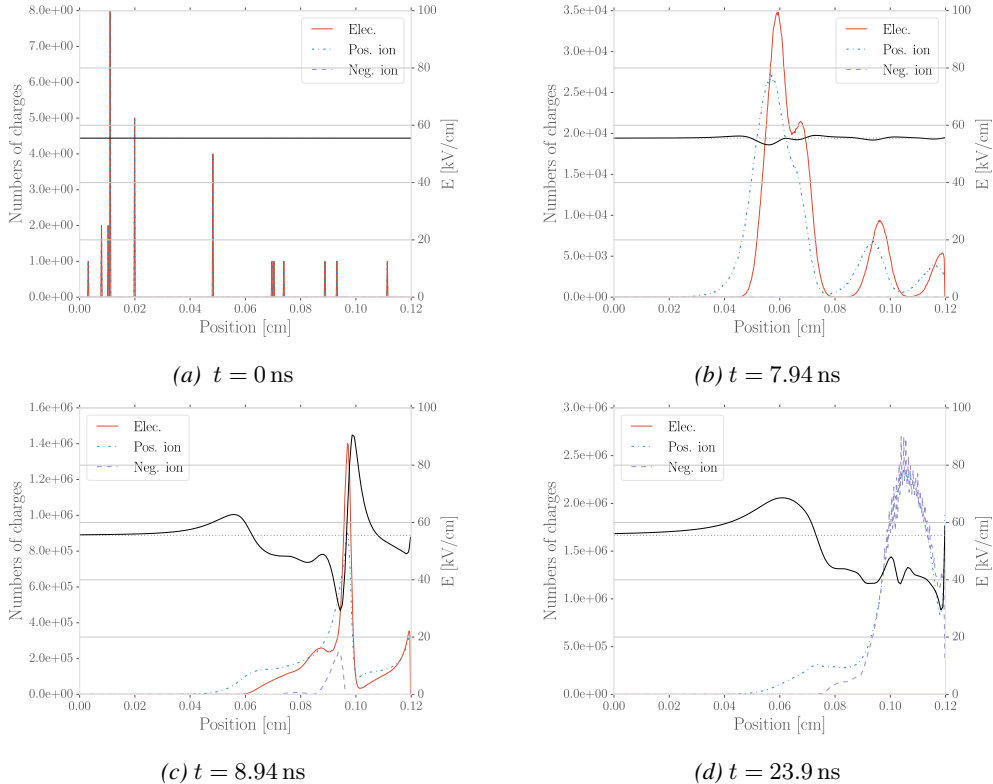


Figure 4.41: Distributions of charge carriers within the gas volume of a 1.2 mm thick RPC and the corresponding deformation of the electric field at different time steps with an applied electric field of 55.5 kV/cm [70].

The electric field following the development of an avalanche can stay perturbed for a long time with respect to the avalanche development due to the slow drift of the much heavier ions. This can result in powerful secondary avalanches triggered by the fluctuation of the electric field together with the emission of UV-photons leading to emission of electrons at the surface of the electrode. This is a slow phenomenon compared to the development of avalanches. Experimentally, it is observed that the stronger the electric field applied over the gap, the sooner after the avalanche, referred to as *precursor signal* in this context, and the stronger will the secondary avalanche be, possibly reaching the streamer regime. This could be due to the amount of UV-photons emitted by the growing precursor. These photons will be able to trigger new avalanches in a radius of a few mm around the precursor by knocking electrons from the cathode by photoelectric effect. The strong distortions of the electric field due to a large avalanche will be more likely to emit UV-photons as the electric field at the front of the precursor avalanche will be large, providing the electrons with a larger energy. Eventually, the new avalanches can grow to form streamers.

4.4 Effect of atmospherical conditions on the detector's performance

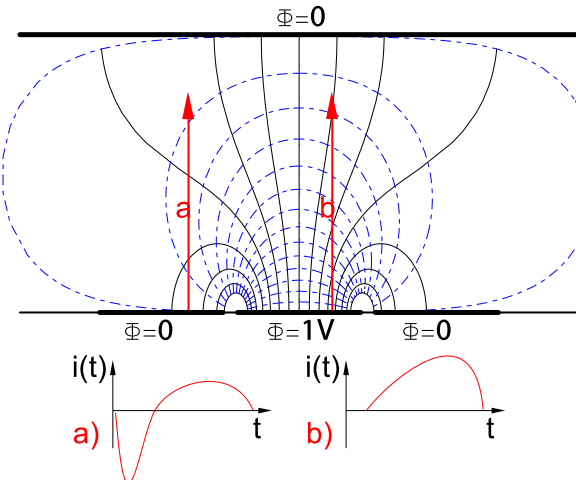


Figure 4.42: Representation of the weighting field in the volume of a RPC and the resulting induced current in the strip placed at 1 V and its neighbour connected to the ground. The induced current corresponds, as can be understood from Formula 4.22 [51].

Accordingly to Ramo's theorem, the movement of charge carriers, and in particular, the movement of a dense electron cloud toward the anode induces a current signal on one or more of the readout electrodes (strips or pads). The ions on the other hand induce only a very small current as their movement is much slower than which of the electrons. The current induced by $n_C l$ clusters of $N_j(t)$ charge carriers drifting at velocities $\vec{v}_{Dj}(t) = \vec{x}_j(t)$ at a time t is given by Formula 4.22 in which e_0 is the unit charge and \vec{E}_w is the *weighting field*.

$$i(t) = \sum_{j=1}^{n_C l} \vec{E}_w(x_j(t)) \cdot \vec{v}_{Dj}(t) e_0 N_j(t) \quad (4.22)$$

2575 The weighting field, that has been schematised in Figure 4.42, corresponds to the electric field that
 2576 would be observed in the gas gap if a readout electrode is placed at a potential of 1 V while keeping
 2577 all the other electrodes grounded. Then the induced charge in the readout can be simply obtained
 2578 by integrating Formula 4.22 over the duration T of the signal, as given by Formula 4.23.

$$Q(t) = \int_0^T \sum_{j=1}^{n_{cl}} \overrightarrow{E_{wj}}(\vec{x}_j(t)) \cdot \overrightarrow{v_{Dj}}(t) e_0 N_j(t) \quad (4.23)$$

2579 The signal induced in the readout of RPCs operated in avalanche mode is then sent into Front-End
 2580 Electronics in which they will be pre-amplified and discriminated. The discrimination and
 2581 digitization of signals in CMS FEE is described through Figure 4.43. On a first stage, analogic
 2582 signals are amplified, following the curve given on Figure 4.44, and then sent to the Constant
 2583 Fraction Discriminator (CFD) described in Figure 4.45. At the end of the chain, 100 ns long pulses
 2584 are sent in the LVDS output. The digital signals are both used as trigger for CMS and to evaluate
 2585 the performance of the detectors. The performance will depend on the applied HV, i.e. on the
 2586 electric field inside of the gas volume, but also on the threshold applied on the CFDs. Indeed, in
 2587 order to reduce the probability to measure noise, the threshold is set to a level where the noise is
 2588 strongly suppressed while the signals are not too affected. Typically, CMS FEEs are set to a
 2589 threshold of 215 mV after pre-amplification, corresponding to an input charge of about 140 fC.

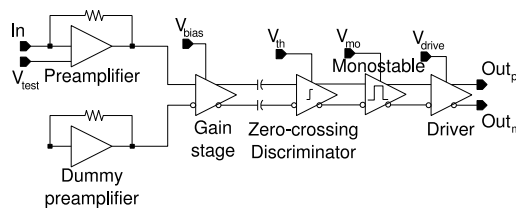


Figure 4.43: Schematics of CMS RPC FEE logic.

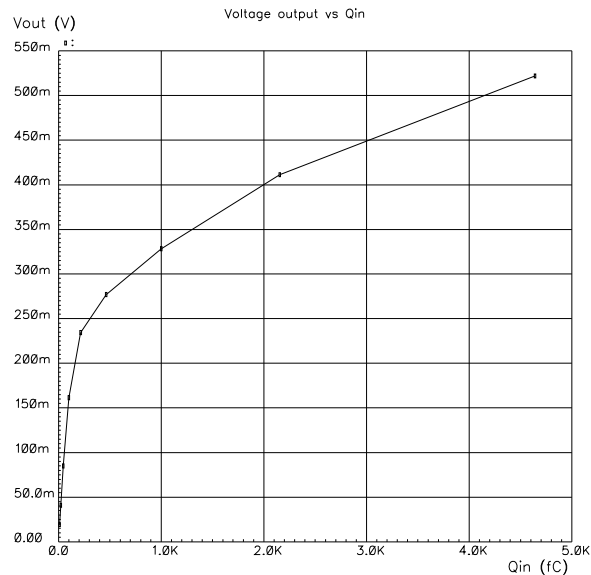


Figure 4.44: Equivalence in between the charge of the induced signal in input of the CMS FEE and the signal strength on the output of the pre-amplifier.

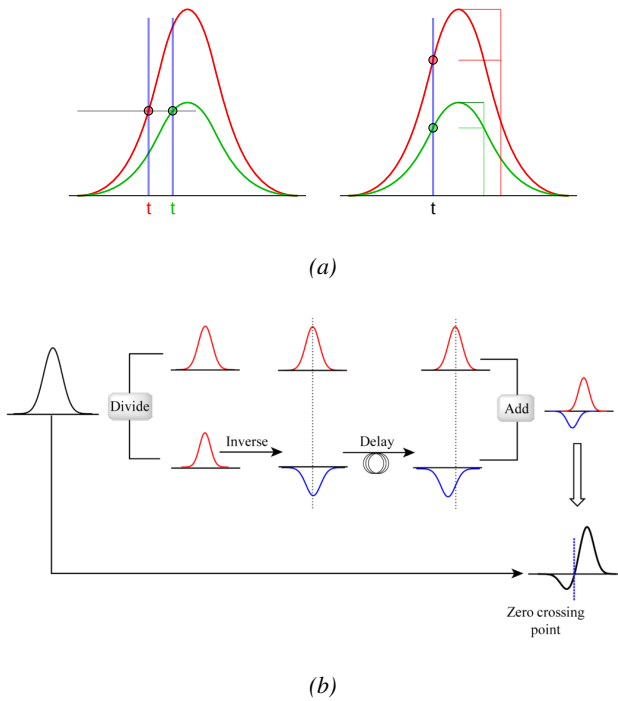


Figure 4.45: Description of the principle of a CFD. A comparison of threshold triggering (left) and constant fraction triggering (right) is shown in Figure 4.45a. Constant fraction triggering is obtained thanks to zero-crossing technique as explained in Figure 4.45b. The signal arriving at the input of the CFD is split into three components. A first one is delayed and connected to the inverting input of a first comparator. A second component is connected to the noninverting input of this first comparator. A third component is connected to the noninverting input of another comparator along with a threshold value connected to the inverting input. Finally, the output of both comparators is fed through an AND gate.

The performance of a detector is then simply measured relatively to which of a reference detector used as trigger as the ratio in between the number of events recorded in coincidence in the detector and the reference and the total amount of trigger events, $\epsilon = n_{events}/n_{triggers}$. An example of efficiency measured as a function of the effective voltage HV_{eff} is given in Figure 4.46 and can be fitted thanks to a sigmoidal function described as in Formula 4.24 and where ϵ_{max} is the maximal efficiency of the detector, λ is proportional to the slope at half maximum and HV_{50} is the value of the voltage when the efficiency reaches half of the maximum.

$$\epsilon(HV_{eff}) = \frac{\epsilon_{max}}{1 + e^{-\lambda(HV_{eff} - HV_{50})}} \quad (4.24)$$

CMS RPC also define two points on this sigmoid that called *knee* and *working point*. The corresponding voltages HV_{knee} is defined as the voltage at 95% of the maximum efficiency, and HV_{WP} is defined as in Formula 4.25.

$$HV_{WP} = HV_{knee} + \begin{cases} 100V & \text{(barrel)} \\ 150V & \text{(endcap)} \end{cases} \quad (4.25)$$

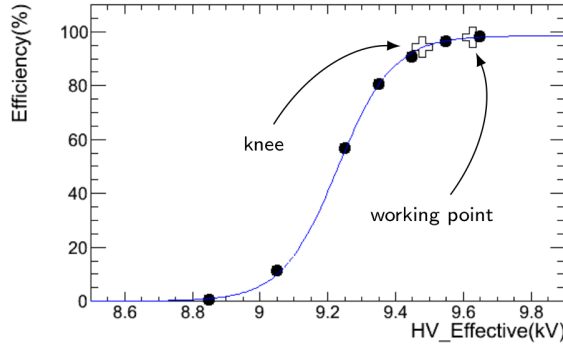


Figure 4.46: Typical efficiency sigmoid of a CMS RPC detector. The black dots correspond to the data, the blue line to the sigmoid fit and the opened cross to the knee and working extracted from the fit line.

Nevertheless, the voltage applied on a detector may vary due to a change in environmental conditions. Indeed, the variation of temperature and/or pressure will have effects on the gas density and the electrodes' resistivity which can be overcome by changing the electric field accordingly. The variation in temperature and pressure are depicted respectively in Figure 4.47 and Figure 4.48. A standard procedure to correct for temperature and pressure variations is to keep the factor $HV \cdot T/P$ constant using Formula 4.26 [84, 85] with reference values for T_0 and P_0 . For example, CMS uses $T_0 = 293.15$ K and $P_0 = 965$ hPa.

$$HV_{app} = HV_{eff} \frac{P_0}{P} \frac{T}{T_0} \quad (4.26)$$

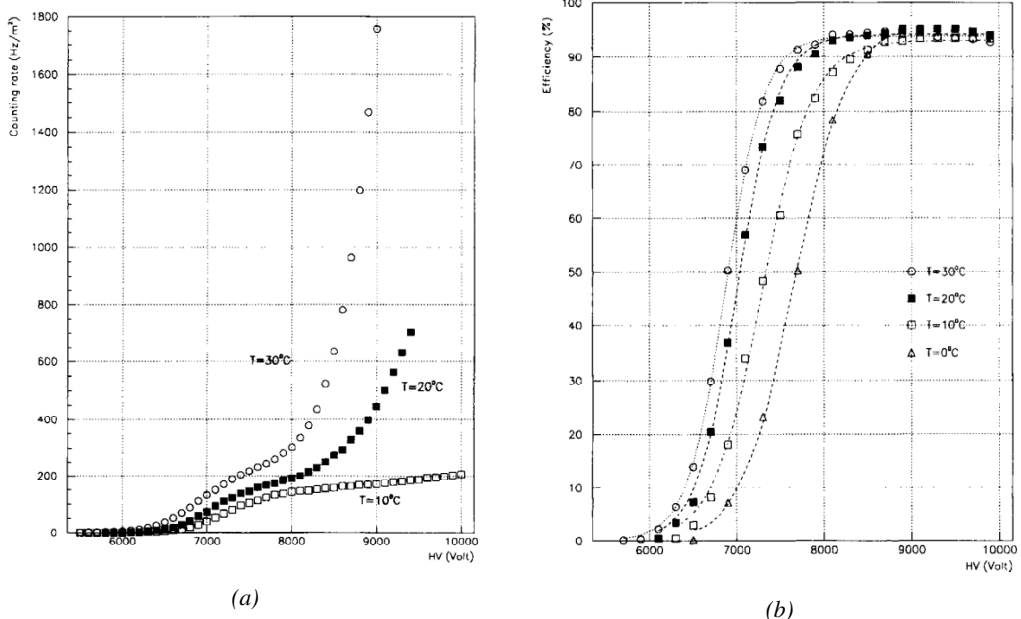


Figure 4.47: Effect of the temperature variation on the rate (Figure 4.47a) and the efficiency (Figure 4.47b) of a RPC [84].

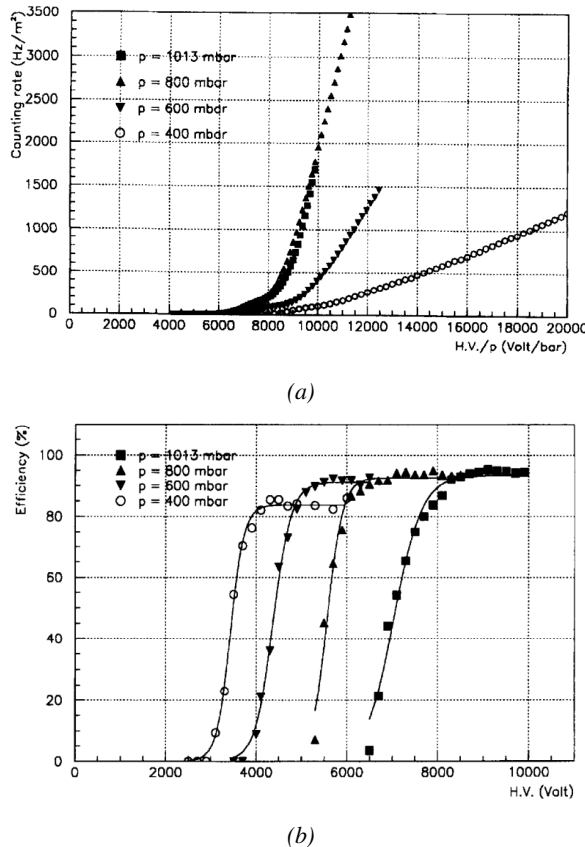


Figure 4.48: Effect of the pressure variation on the rate (Figure 4.48a) and the efficiency (Figure 4.48b) of a RPC [85].

It was actually found that such a simple procedure would overcorrect the applied voltage in the case the variations of temperature or pressure were too important [86–89]. CMS, considering that the temperature variations in the detector cavern were very small, decided only to improve the pressure correction, giving rise to Formula 4.27 [86] while on the other hand, ATLAS decided to have a more robust correction for both parameters and uses Formula 4.28 instead [89]. The coefficients α , in the case of CMS, and α, β , in the case of ATLAS, are extracted from fit on available dataset obtained during the operation of the detectors.

$$HV_{app} = HV_{eff} \left(1 - \alpha + \alpha \frac{P_0}{P} \right) \frac{T}{T_0}, \quad \alpha = 0.8 \quad (4.27)$$

$$HV_{eff} = HV_{app} \left(1 + \alpha \frac{\Delta T}{T_0} \right) \left(1 - \beta \frac{\Delta P}{P_0} \right), \quad \alpha = 0.5, \beta = 0.71 \quad (4.28)$$

5

2614

2615

2616

Longevity studies and Consolidation of the present CMS RPC subsystem

2617 The RPC system, located in both barrel and endcap regions, provides a fast, independent muon
2618 trigger with a looser p_T threshold over a large portion of the pseudorapidity range ($|\eta| < 1.6$).
2619 During HL-LHC operations the expected conditions in terms of background and pile-up will make
2620 the identification and correct p_T assignment a challenge for the muon system. The goal of RPC
2621 upgrade is to provide additional hits to the Muon system with precise timing. All these
2622 informations will be elaborated by the trigger system in a global way enhancing the performance of
2623 the trigger in terms of efficiency and rate control. The RPC Upgrade is based on two projects: an
2624 improved Link Board System and the extension of the RPC coverage up to $|\eta| = 2.4$.
2625 The extension of the RPC system up to $|\eta| = 2.1$ was already planned in the CMS TDR and staged
2626 because of budget limitations and expected background rates higher than the rate capability of the
2627 present CMS RPCs in that region. An extensive R&D program has been done in order to develop
2628 an improved RPC that fulfills the CMS requirements. Two new RPC layers in the innermost ring of
2629 stations 3 and 4 will be added with benefits to the neutron-induced background reduction and
2630 efficiency improvement for both trigger and offline reconstruction.
2631 The Link Board system is responsible to process, synchronize and zero-suppress the signals coming
2632 from the RPC front end boards. The Link Board components have been produced between 2006
2633 and 2007 and will be subjected to ageing and failure in the long term. The upgraded Link Board
2634 system will overcome the ageing problems and will allow for a more precise timing information to
2635 the RPC hits from 25 to 1 ns.

2636 **5.1 Testing detectors under extreme conditions**

2637 The upgrade from LHC to HL-LHC will increase the peak luminosity from $10^{34} \text{ cm}^{-2} \text{ s}^{-1}$ to reach
2638 $5 \times 10^{34} \text{ cm}^{-2} \text{ s}^{-1}$, increasing in the same way the total expected background to which the RPC
2639 system will be subjected to. Composed of low energy gammas and neutrons from $p\text{-}p$ collisions,

2640 low momentum primary and secondary muons, puch-through hadrons from calorimeters, and
 2641 particles produced in the interaction of the beams with collimators, the background will mostly
 2642 affect the regions of CMS that are the closest to the beam line, i.e. the RPC detectors located in the
 2643 endcaps.

2644 Data collected in 2016 allowed to study the values of the background rate in all RPC system. In
 2645 Figure 5.1, the distribution of the chamber background hit rate per unit area is shown at a
 2646 luminosity of $5 \times 10^{34} \text{ cm}^{-2}\text{s}^{-1}$ linearly. The maximum rate per unit area at HL-LHC conditions is
 2647 expected to be of the order of 600 Hzcm^{-2} , including a safety factor 3. Nevertheless, Fluka
 2648 simulations were conducted in order to understand the background at HL-LHC conditions. The
 2649 comparison to the data has shown, in Figure 5.2, a discrepancy of a factor 2 even though the order
 2650 of magnitude is consistent.

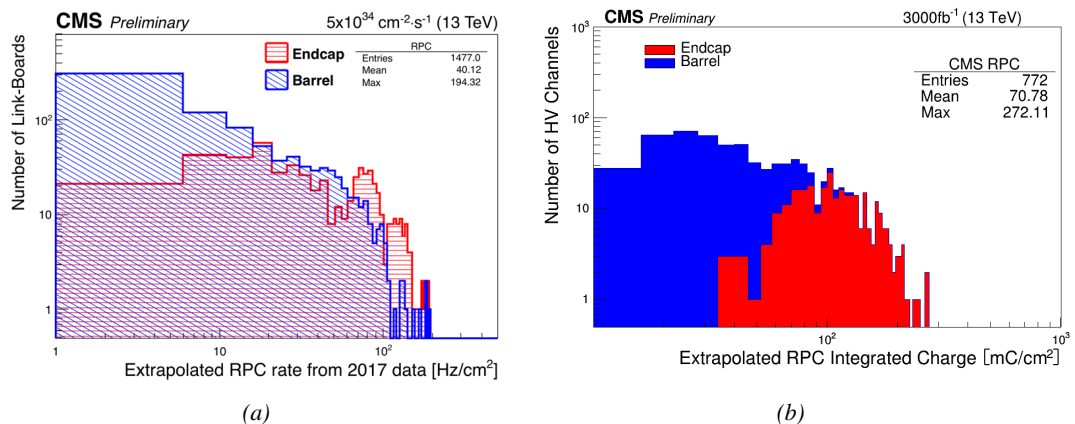


Figure 5.1: Figure 5.1a: The integrated charge per region (Barrel, Endcap) is extrapolated to HL-LHC integrated luminosity (3000 fb^{-1}) using the data accumulated in 2016 in every HV channels. Figure 5.1b: The hit rate per region (Barrel, Endcap) is linearly extrapolated to HL-LHC highest instantaneous luminosity ($5 \times 10^{34} \text{ cm}^{-2}\text{s}^{-1}$) using the rate as a function of instantaneous luminosity recorded by RPCs in 2017 showing a linear dependence.

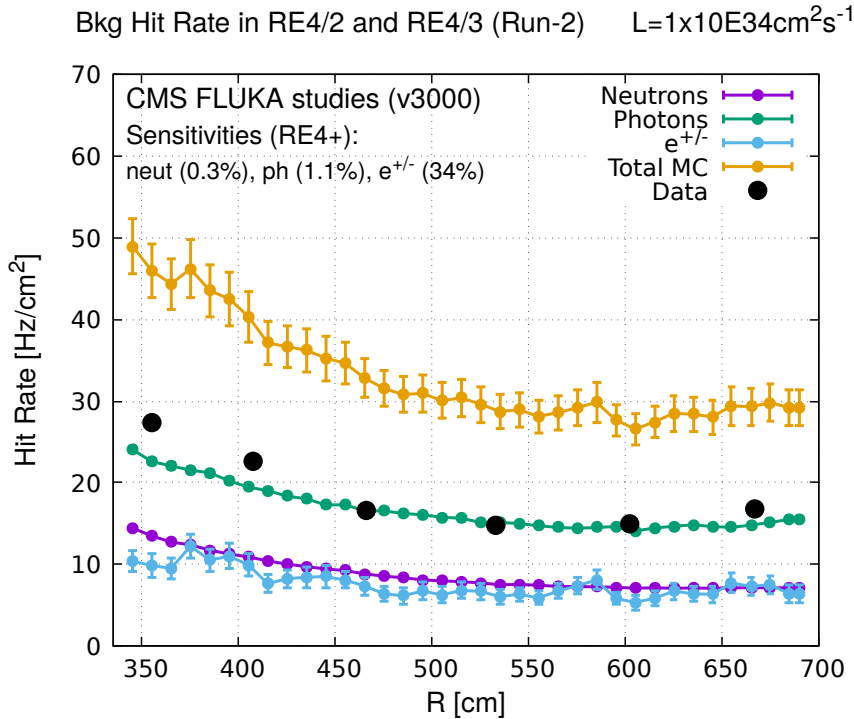


Figure 5.2: Background Fluka simulation compared to 2016 Data at $L = 10^{34} \text{ cm}^{-2} \text{s}^{-1}$ in the fourth endcap disk region. A mismatch in between simulation and data can be observed.

In the past, extensive long-term tests were carried out at several gamma and neutron facilities certifying the detector performance. Both full size and small prototype RPCs have been irradiated with photons up to an integrated charge of $\sim 0.05 \text{ C/cm}^2$ and $\sim 0.4 \text{ C/cm}^2$, respectively [90, 91]. During Run-I, the RPC system provided stable operation and excellent performance and did not show any aging effects for integrated charge of the order of 0.01 C/cm^2 . Projections on currents from 2016 Data, has allowed to determine that the total integrated charge, by the end of HL-LHC, would be of the order of 1 C/cm^2 , including a safety factor 3.

5.1.1 The Gamma Irradiation Facilities

5.1.1.1 GIF

Located in the SPS West Area at the downstream end of the X5 test beam, the Gamma Irradiation Facility (GIF) was a test area in which particle detectors were exposed to a particle beam in presence of an adjustable gamma background [92]. Its goal was to reproduce background conditions these detectors would suffer in their operating environment at LHC. GIF layout is shown in Figure 5.3. Gamma photons are produced by a strong ¹³⁷Cs source installed in the upstream part of the zone inside a lead container. The source container includes a collimator, designed to irradiate a $6 \times 6 \text{ m}^2$ area at 5 m maximum to the source. A thin lens-shaped lead filter helps providing with a uniform outgoing flux in a vertical plane, orthogonal to the beam direction. The principal collimator hole provides a pyramidal aperture of $74^\circ \times 74^\circ$ solid angle and provides a photon flux in a pyramidal volume along the beam axis. The photon rate is controlled by further lead filters

allowing the maximum rate to be limited and to vary within a range of four orders of magnitude. Particle detectors under test are then placed within the pyramidal volume in front of the source, perpendicularly to the beam line in order to profit from the homogeneous photon flux. Adjusting the background flux of photons can then be done by using the filters and choosing the position of the detectors with respect to the source.

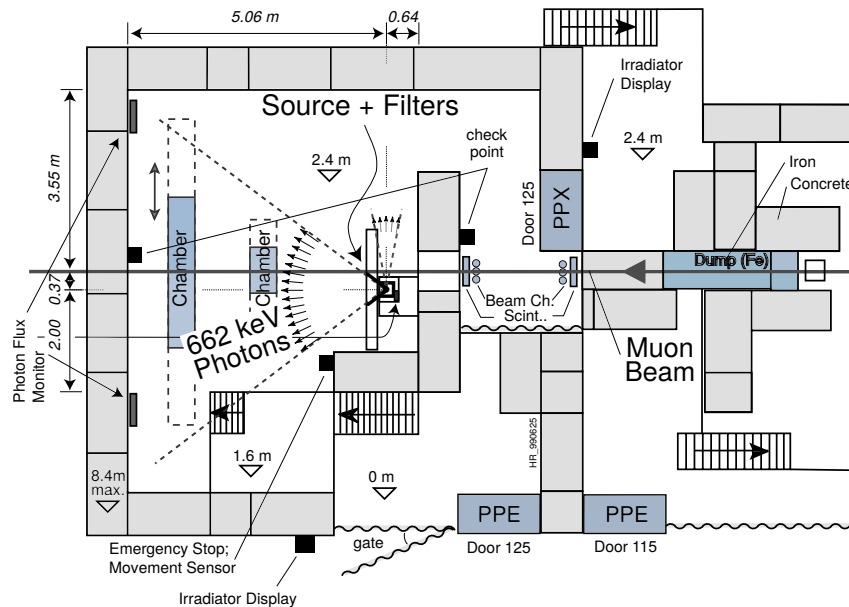


Figure 5.3: Layout of the test beam zone called X5c GIF at CERN. Photons from the radioactive source produce a sustained high rate of random hits over the whole area. The zone is surrounded by 8 m high and 80 cm thick concrete walls. Access is possible through three entry points. Two access doors for personnel and one large gate for material. A crane allows installation of heavy equipment in the area.

As described on Figure 5.4, the ^{137}Cs source emits a 662 keV photon in 85% of the decays. An activity of 740 GBq was measured on the 5th March 1997. To estimate the strength of the flux in 2014, it is necessary to consider the nuclear decay through time associated to the Cesium source whose half-life is well known ($t_{1/2} = (30.05 \pm 0.08)$ y). The GIF tests were done in between the 20th and the 31st of August 2014, i.e. at a time $t = (17.47 \pm 0.02)$ y resulting in an attenuation of the activity from 740 GBq in 1997 to 494 GBq in 2014.

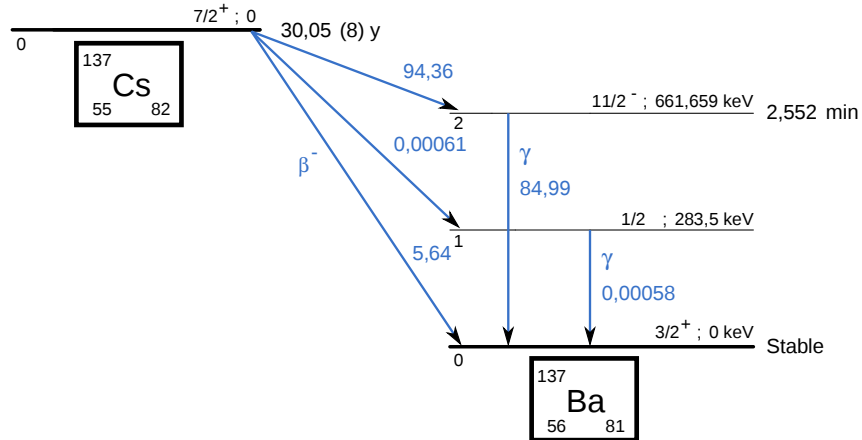


Figure 5.4: ^{137}Cs decays by β^- emission to the ground state of ^{137}Ba ($BR = 5.64\%$) and via the 662 keV isomeric level of ^{137}Ba ($BR = 94.36\%$) whose half-life is 2.55min.

5.1.1.2 GIf++

The new Gamma Irradiation Facility (GIF++), located in the SPS North Area at the downstream end of the H4 test beam, has replaced its predecessor during LS1 and has been operational since spring 2015 [93]. Like GIF, GIF++ features a ^{137}Cs source of 662 keV gamma photons, their fluence being controlled with a set of filters of various attenuation factors. The source provides two separated large irradiation areas for testing several full-size muon detectors with continuous homogeneous irradiation, as presented in Figure 5.5.

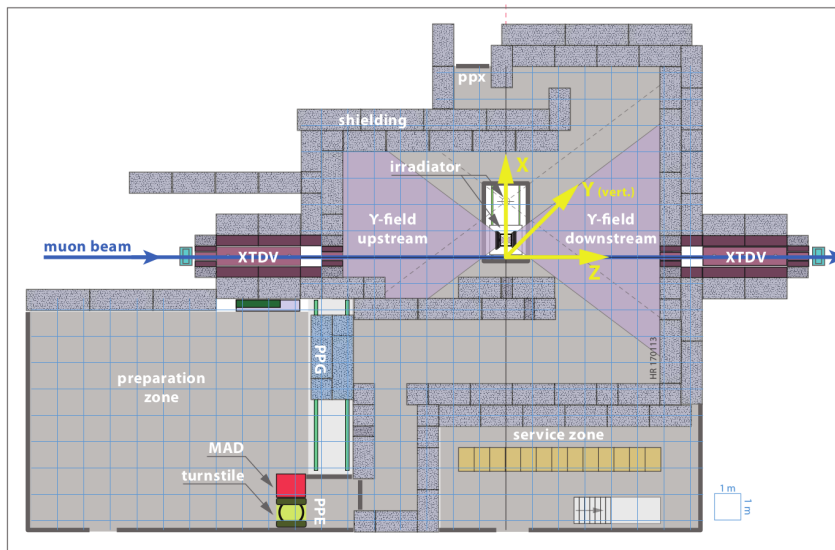


Figure 5.5: Floor plan of the GIf++ facility. When the facility downstream of the GIf++ takes electron beam, a beam pipe is installed along the beam line (z -axis). The irradiator can be displaced laterally (its center moves from $x = 0.65$ m to 2.15 m), to increase the distance to the beam pipe.

The source activity was measured to be about 13.5 TBq in March 2016. The photon flux being far

2689 greater than HL-LHC expectations, GIF++ provides an excellent facility for accelerated aging tests
 2690 of muon detectors.

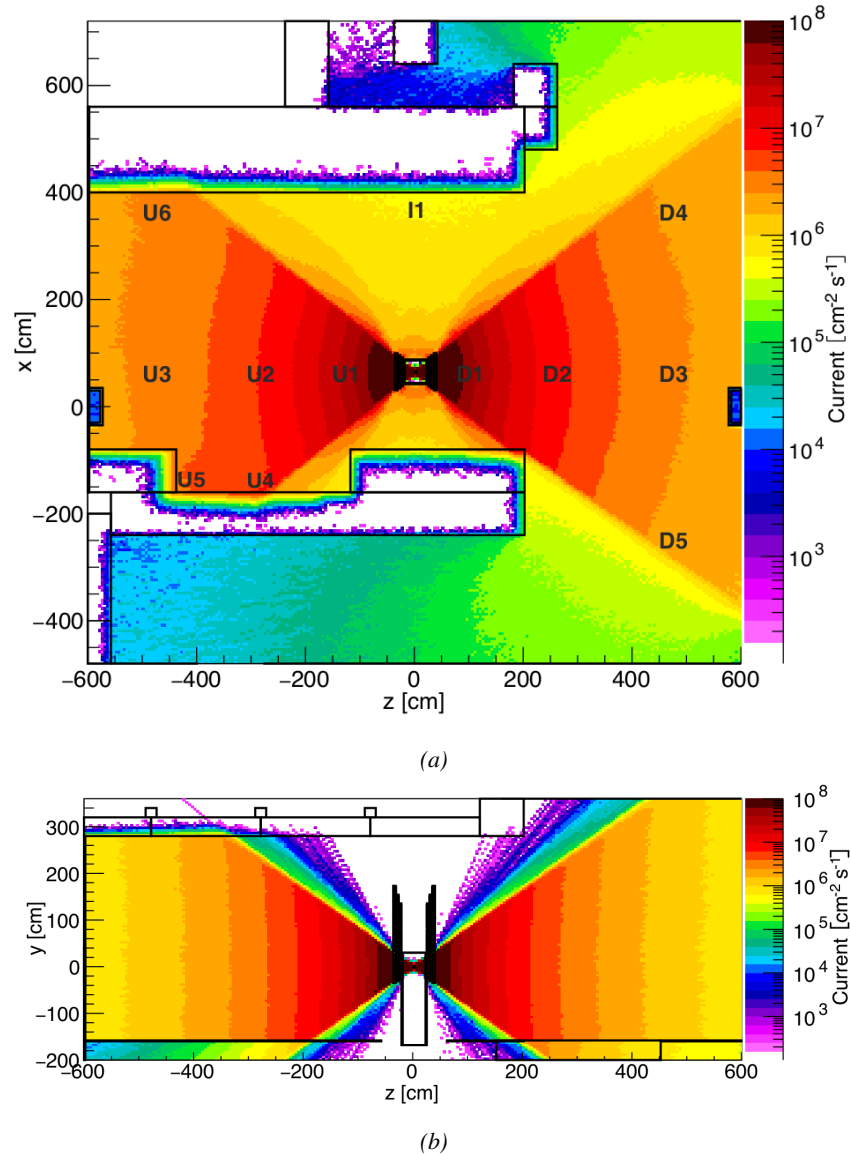


Figure 5.6: Simulated unattenuated current of photons in the xz plane (Figure 5.6a) and yz plane (Figure 5.6b) through the source at $x = 0.65$ m and $y = 0$ m. With angular correction filters, the current of 662 keV photons is made uniform in xy planes.

2691 The source is situated in the muon beam line with the muon beam being available a few times a
 2692 year. The H4 beam, composed of muons with a momentum of about 150 GeV/c, passes through
 2693 the GIF++ zone and is used to study the performance of the detectors. Its flux is of
 2694 104 particles/s/cm² focused in an area similar to 10×10 cm². Therefore, with properly adjusted
 2695 filters, one can imitate the HL-LHC background and study the performance of muon detectors with

2696 their trigger/readout electronics in HL-LHC environment.

2697 5.2 Preliminary tests at GIF

2698 5.2.1 Resistive Plate Chamber test setup

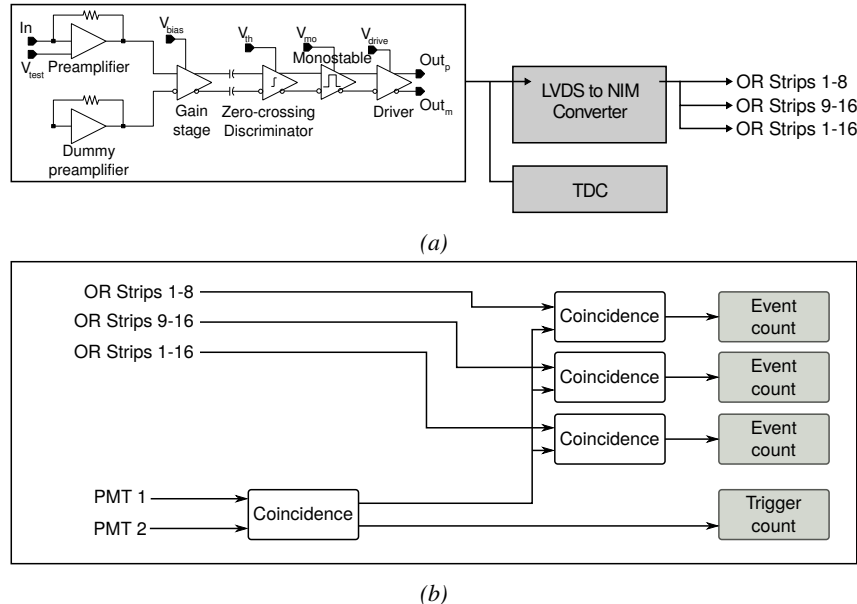


Figure 5.7: Signals from the RPC strips are shaped by the FEE described on Figure 5.7a. Output LVDS signals are then read-out by a TDC module connected to a computer or converted into NIM and sent to scalers. Figure 5.7b describes how these converted signals are put in coincidence with the trigger.

2699 During summer 2014, preliminary tests have been conducted in the GIF area on a newly produced
 2700 RE4/2 chamber labelled RE-4-2-BARC-161. This chamber has been placed into a trolley covered
 2701 with a tent. The position of the RPC inside the tent and of the tent related to the source is described
 2702 in Figure 5.8. To test this CMS RPC, three different absorber settings were used. First of all,
 2703 measurements were done with fully opened source. Then, to complete this preliminary study, the
 2704 gamma flux has been attenuated from a factor 2 and a factor 5. The expected gamma flux at the
 2705 level of our detector will be discussed in subsection ??.

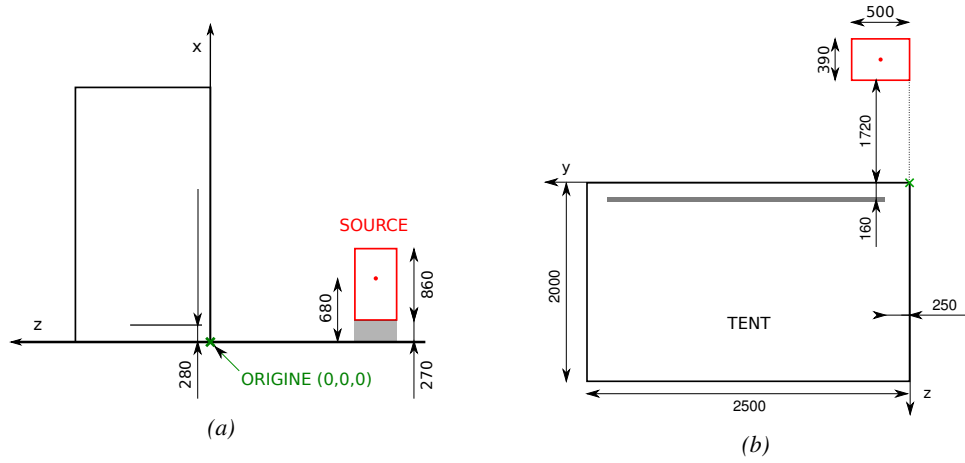


Figure 5.8: Description of the RPC setup. Dimensions are given in mm. A tent containing RPCs is placed at 1720 mm from the source container. The source is situated in the center of the container. RE-4-2-BARC-161 chamber is 160 mm inside the tent. This way, the distance between the source and the chambers plan is 2060 mm. Figure 5.8a provides a side view of the setup in the xz plane while Figure 5.8b shows a top view in the yz plane.



Figure 5.9: RE-4-2-BARC-161 chamber is inside the tent as described in Figure 5.8. In the top right, the two scintillators used as trigger can be seen. This trigger system has an inclination of 10° relative to horizontal and is placed above half-partition B2 of the RPCs. PMT electronics are shielded thanks to lead blocks placed in order to protect them without stopping photons from going through the scintillators and the chamber.

At the time of the tests, the beam not being operational anymore, a trigger composed of 2 plastic scintillators has been placed in front of the setup with an inclination of 10° with respect to the detector plane in order to look at cosmic muons. Using this particular trigger layout, shown on Figure 5.9, leads to a cosmic muon hit distribution into the chamber similar to the one in

2710 Figure 5.10. Measured without gamma irradiation, two peaks can be seen on the profil of partition
 2711 B, centered on strips 52 and 59. Section 5.2.3 will help us understand that these two peaks are due
 2712 respectively to forward and backward coming cosmic particles where forward coming particles are
 2713 first detected by the scintillators and then the RPC while the backward coming muons are first
 2714 detected in the RPC.

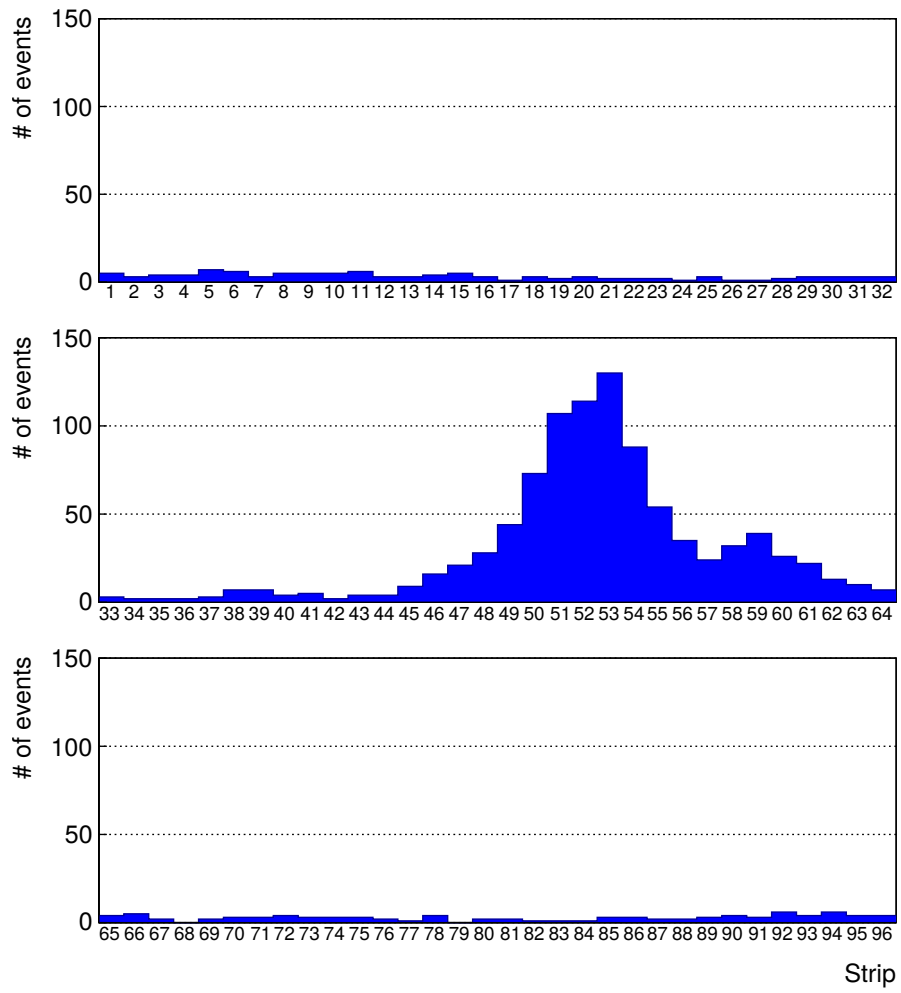


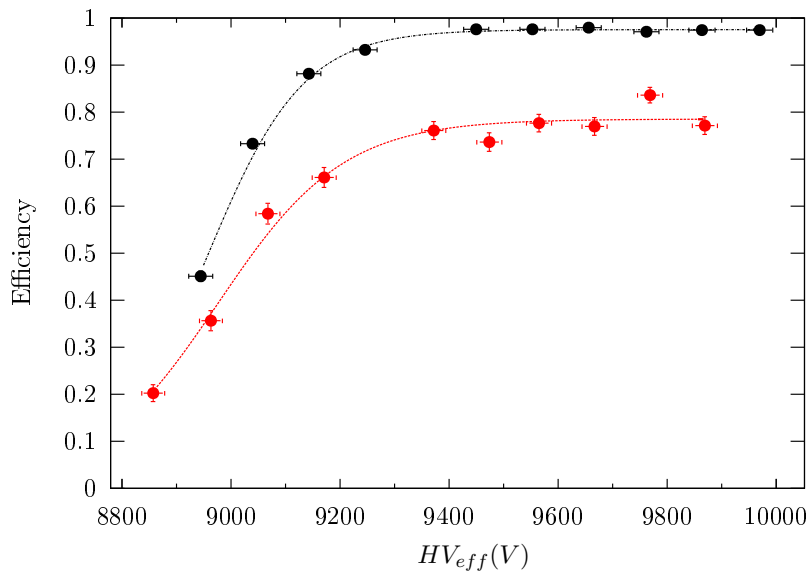
Figure 5.10: Hit distributions over all 3 partitions of RE-4-2-BARC-161 chamber is showed on these plots. Top, middle and bottom figures respectively correspond to partitions A, B, and C. These plots show that some events still occur in other half-partitions than B2, which corresponds to strips 49 to 64, in front of which the trigger is placed, contributing to the inefficiency of detection of cosmic muons. In the case of partitions A and C, the very low amount of data can be interpreted as noise. On the other hand, it is clear that a little portion of muons reach the half-partition B1, corresponding to strips 33 to 48.

2715 **5.2.2 Data Acquisition**

2716 **5.2.3 Geometrical acceptance of the setup layout to cosmic muons**

2717 In order to profit from a constant gamma irradiation, the detectors inside of the GIF bunker need to
 2718 be placed in a plane orthogonal to the beam line. The muon beam that used to be available was
 2719 meant to test the performance of detectors under test. This beam not being active anymore, another
 2720 solution to test detector performance had to be used. Thus, it has been decided to use cosmic muons
 2721 detected through a telescope composed of two scintillators. Lead blocks were used as shielding to
 2722 protect the photomultipliers from gammas as can be seen from Figure 5.9.

2723 An inclination has been given to the cosmic telescope to maximize the muon flux. A good
 2724 compromise had to be found between good enough muon flux and narrow enough hit distribution to
 2725 be sure to contain all the events into only one half partitions as required from the limited available
 2726 readout hardware. Nevertheless, a consequence of the misplaced trigger, that can be seen as a loss
 2727 of events in half-partition B1 in Figure 5.10, is an inefficiency. Nevertheless, the inefficiency of
 2728 approximately 20% highlighted in Figure 5.11 by comparing the performance of chamber
 2729 BARC-161 in 904 and at GIF without irradiation seems too important to be explained only by the
 2730 geometrical acceptance of the setup itself. Simulations have been conducted to show how the setup
 2731 brings inefficiency.



2732 *Figure 5.11: Results are derived from data taken on half-partition B2 only. On the 18th of June 2014, data
 2733 has been taken on chamber RE-2-BARC-161 at building 904 (Preressin Site) with cosmic muons providing us a
 2734 reference efficiency plateau of $(97.54 \pm 0.15)\%$ represented by a black curve. A similar measurement has been
 done at GIF on the 21st of July with the same chamber giving a plateau of $(78.52 \pm 0.94)\%$ represented by a red curve.*

2732 **5.2.3.1 Description of the simulation layout**

2733 The layout of GIF setup has been reproduced and incorporated into a Monte Carlo (MC) simulation
 2734 to study the influence of the disposition of the telescope on the final distribution measured by the

2735 RPC. A 3D view of the simulated layout is given into Figure 5.12. Muons are generated randomly
 2736 in a horizontal plane located at a height corresponding to the lowest point of the PMTs. This way,
 2737 the needed size of the plane in order to simulate events happening at very big azimuthal angles (i.e.
 2738 $\theta \approx \pi$) can be kept relatively small. The muon flux is designed to follow the usual $\cos^2\theta$
 2739 distribution for cosmic particle. The goal of the simulation is to look at muons that pass through the
 2740 muon telescope composed of the two scintillators and define their distribution onto the RPC plane.
 2741 During the reconstruction, the RPC plane is then divided into its strips and each muon track is
 2742 assigned to a strip.

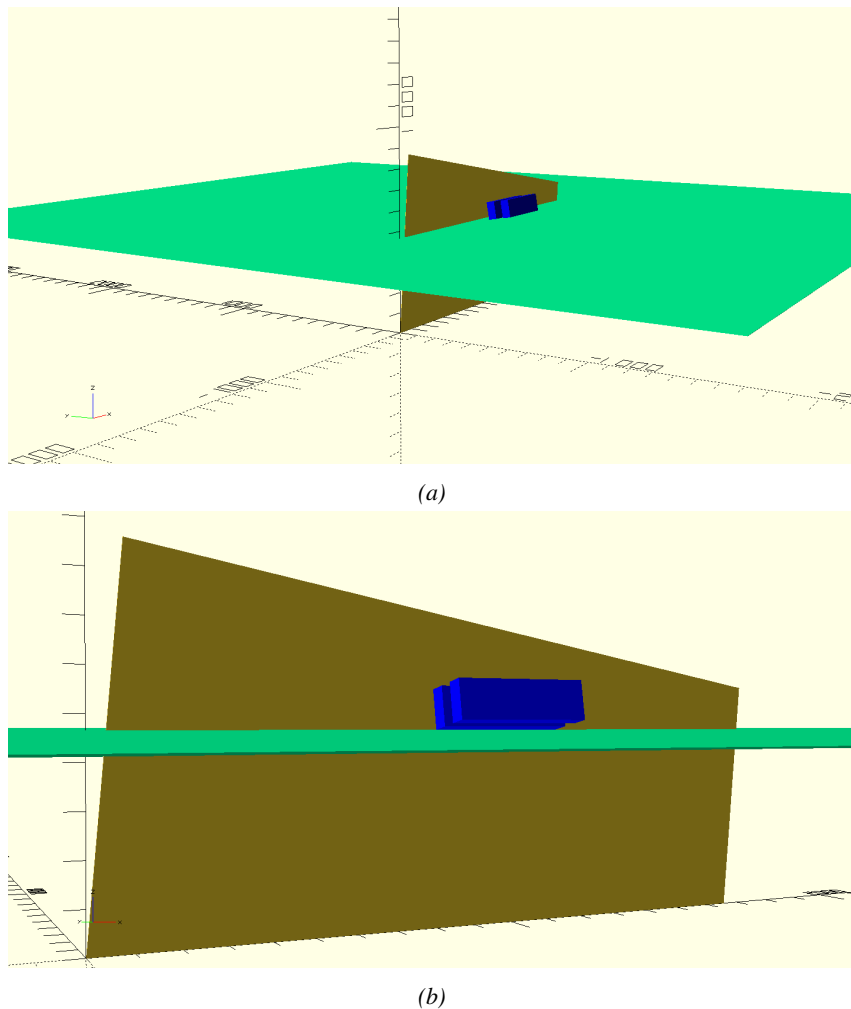


Figure 5.12: Representation of the layout used for the simulations of the test setup. The RPC is represented as a yellow trapezoid while the two scintillators as blue cuboids looking at the sky. A green plane corresponds to the muon generation plane within the simulation. Figure 5.8a shows a global view of the simulated setup. Figure 5.8b shows a zoomed view that allows to see the 2 scintillators as well as the full RPC plane.

2743 In order to further refine the quality of the simulation and understand deeper the results the
 2744 dependance of the distribution has been studied for a range of telescope inclinations. Moreover, the
 2745 threshold applied on the PMT signals has been included into the simulation in the form of a cut. In

the approximation of uniform scintillators, it has been considered that the threshold can be understood as the minimum distance particles need to travel through the scintillating material to give a strong enough signal. Particles that travel a distance smaller than the set "threshold" are thus not detected by the telescope and cannot trigger the data taking. Finally, the FEE threshold also has been considered in a similar way. The mean momentum of horizontal cosmic rays is higher than those of vertical ones but the stopping power of matter for momenta ranging from 1 GeV to 1 TeV stays comparable. It is then possible to assume that the mean number of primary e^- /ion pairs per unit length will stay similar and thus, depending on the applied discriminator threshold, muons with the shortest path through the gas volume will deposit less charge and induce a smaller signal on the pick-up strips that could eventually not be detected. These two thresholds also restrain the overall geometrical acceptance of the system.

5.2.3.2 Simulation procedure

The simulation software has been designed using C++ and the output data is saved into ROOT histograms. Simulations start for a threshold T_{scint} varying in a range from 0 to 45 mm in steps of 5 mm, where $T_{scint} = 0$ mm corresponds to the case where there isn't any threshold apply on the input signal while $T_{scint} = 45$ mm, which is the scintillator thickness, is the case where muons cannot arrive orthogonally onto the scintillator surface. For a given T_{scint} , a set of RPC thresholds are considered. The RPC threshold, T_{RPC} varies from 2 mm, the thickness of the gas volume, to 3 mm in steps of 0.25 mm. For each $(T_{scint}; T_{RPC})$ pair, $N_\mu = 10^8$ muons are randomly generated inside the muon plane described in the previous paragraph with an azimuthal angle θ chosen to follow a $\cos^2\theta$ distribution.

Planes are associated to each surface of the scintillators. Knowing muon position into the muon plane and its direction allows us, by assuming that muons travel in a straight line, to compute the intersection of the muon track with these planes. Applying conditions to the limits of the surfaces of the scintillator faces then gives us an answer to whether or not the muon passed through the scintillators. In the case the muon has indeed passed through the telescope, the path through each scintillator is computed and muons whose path was shorter than T_{scint} are rejected and are thus considered as having not interacted with the setup.

On the contrary, if the muon is labeled as good, its position within the RPC plane is computed and the corresponding strip, determined by geometrical tests in the case the distance through the gas volume was enough not to be rejected because of T_{RPC} , gets a hit and several histograms are filled in order to keep track of the generation point on the muon plane, the intersection points of the reconstructed muons within the telescope, or on the RPC plane, the path traveled through each individual scintillator or the gas volume, as well as other histograms. Moreover, muons fill different histograms whether they are forward or backward coming muons. They are discriminated according to their direction components. When a muon is generated, an (x, y, z) position is assigned into the muon plane as well as a $(\theta; \phi)$ pair that gives us the direction it's coming from. This way, muons satisfying the condition $0 \leq \phi < \pi$ are designated as backward coming muons while muons satisfying $\pi \leq \phi < 2\pi$ as forward coming muons.

This simulation is then repeated for different telescope inclinations ranging in between 4 and 20° and varying in steps of 2° . Due to this inclination and to the vertical position of the detector under test, the muon distribution reconstructed in the detector plane is asymmetrical. The choice as been made to chose a skew distribution formula to fit the data built as the multiplication of gaussian and sigmoidal curves together. A typical gaussian formula is given as 5.1 and has three free parameters

2790 as A_g , its amplitude, \bar{x} , its mean value and σ , its root mean square. Sigmoidal curves as given by
 2791 formula 5.2 are functions converging to 0 and A_s as x diverges. The inflection point is given as x_i
 2792 and λ is proportional to the slope at $x = x_i$. In the limit where $\lambda \rightarrow \infty$, the sigmoid becomes a
 2793 step function.

$$g(x) = A_g e^{\frac{-(x-\bar{x})^2}{2\sigma^2}} \quad (5.1)$$

$$s(x) = \frac{A_s}{1 + e^{-\lambda(x-x_i)}} \quad (5.2)$$

2794 Finally, a possible representation of a skew distribution is given by formula 5.3 and is the product
 2795 of 5.1 and 5.2. Naturally, here $A_{sk} = A_g \times A_s$ and represents the theoretical maximum in the limit
 2796 where the skew tends to a gaussian function.

$$sk(x) = g(x) \times s(x) = A_{sk} \frac{e^{\frac{-(x-\bar{x})^2}{2\sigma^2}}}{1 + e^{-\lambda(x-x_i)}} \quad (5.3)$$

2797 5.2.3.3 Results

2798 Influence of T_{scint} on the muon distribution

2799 Influence of T_{RPC} on the muon distribution

2800 Influence of the telescope inclination on the muon distribution

2801 Comparison to data taken at GIF without irradiation

2802 5.2.4 Photon flux at GIF

2803 5.2.4.1 Expectations from simulations

2804 In order to understand and evaluate the γ flux in the GIF area, simulations had been conducted in
 2805 1999 and published by S. Agosteo et al [92]. Table 5.1 presented in this article gives us the γ flux
 2806 for different distances D to the source. This simulation was done using GEANT and a Monte Carlo
 2807 N-Particle (MCNP) transport code, and the flux F is given in number of γ per unit area and unit
 2808 time along with the estimated error from these packages expressed in %.

Nominal ABS	Photon flux F [$\text{cm}^{-2}\text{s}^{-1}$]			
	at $D = 50 \text{ cm}$	at $D = 155 \text{ cm}$	at $D = 300 \text{ cm}$	at $D = 400 \text{ cm}$
1	$0.12 \times 10^8 \pm 0.2\%$	$0.14 \times 10^7 \pm 0.5\%$	$0.45 \times 10^6 \pm 0.5\%$	$0.28 \times 10^6 \pm 0.5\%$
2	$0.68 \times 10^7 \pm 0.3\%$	$0.80 \times 10^6 \pm 0.8\%$	$0.25 \times 10^6 \pm 0.8\%$	$0.16 \times 10^6 \pm 0.6\%$
5	$0.31 \times 10^7 \pm 0.4\%$	$0.36 \times 10^6 \pm 1.2\%$	$0.11 \times 10^6 \pm 1.2\%$	$0.70 \times 10^5 \pm 0.9\%$

Table 5.1: Total photon flux ($E\gamma \leq 662 \text{ keV}$) with statistical error predicted considering a ^{137}Cs activity of 740 GBq at different values of the distance D to the source along the x -axis of irradiation field [92].

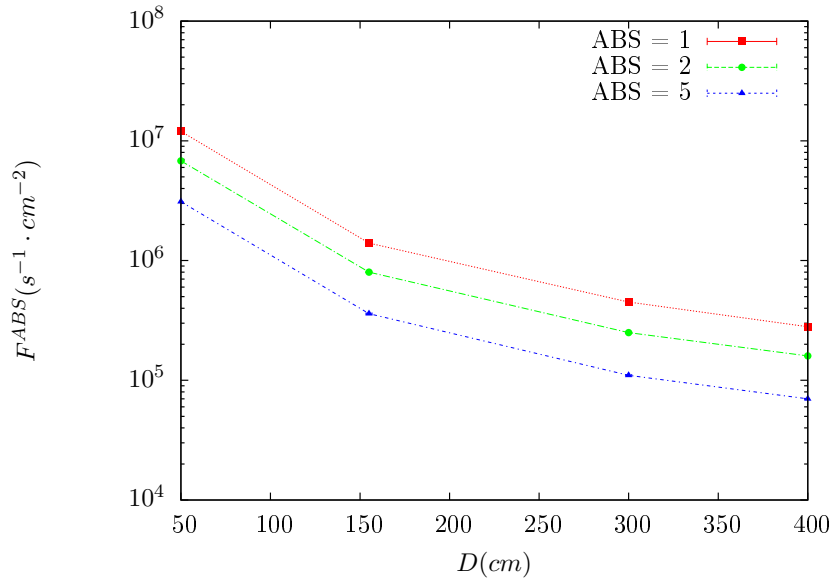


Figure 5.13: γ flux $F(D)$ is plot using values from table 5.1. As expected, the plot shows similar attenuation behaviours with increasing distance for each absorption factors.

The simulation doesn't directly provide us with an estimated flux at the level of our RPC. First of all, it is needed to extract the value of the flux from the available data contained in the original paper and then to estimate the flux in 2014 at the time the experimentation took place. Figure 5.13 that contains the data from Table 5.1. In the case of a pointlike source emitting isotropic and homogeneous gamma radiations, the gamma flux F at a distance D to the source with respect to a reference point situated at D_0 where a known flux F_0 is measured will be expressed like in Equation 5.4, assuming that the flux decreases as $1/D^2$, where c is a fitting factor.

$$F^{ABS} = F_0^{ABS} \times \left(\frac{cD_0}{D} \right)^2 \quad (5.4)$$

By rewriting Equation 5.4, it comes that :

$$c = \frac{D}{D_0} \sqrt{\frac{F^{ABS}}{F_0^{ABS}}} \quad (5.5)$$

$$\Delta c = \frac{c}{2} \left(\frac{\Delta F^{ABS}}{F^{ABS}} + \frac{\Delta F_0^{ABS}}{F_0^{ABS}} \right) \quad (5.6)$$

Finally, using Equation 5.5 and the data in Table 5.1 with $D_0 = 50$ cm as reference point, we can build Table 5.2. It is interesting to note that c for each value of D doesn't depend on the absorption factor.

Nominal ABS	Correction factor c		
	at $D = 155$ cm	at $D = 300$ cm	at $D = 400$ cm
1	$1.059 \pm 0.70\%$	$1.162 \pm 0.70\%$	$1.222 \pm 0.70\%$
2	$1.063 \pm 1.10\%$	$1.150 \pm 1.10\%$	$1.227 \pm 0.90\%$
5	$1.056 \pm 1.60\%$	$1.130 \pm 1.60\%$	$1.202 \pm 1.30\%$

Table 5.2: Correction factor c is computed thanks to formulae 5.5 taking as reference $D_0 = 50$ cm and the associated flux F_0^{ABS} for each absorption factor available in table 5.1.

2820 For the range of D/D_0 values available, it is possible to use a simple linear fit to get the evolution of
 2821 c . The linear fit will then use only 2 free parameters, a and b , as written in Equation 5.7. This gives
 2822 us the results showed in Figure 5.14. Figure 5.14b confirms that using only a linear fit to extract c is
 2823 enough as the evolution of the rate that can be obtained superimposes well on the simulation points.

$$c \left(\frac{D}{D_0} \right) = a \frac{D}{D_0} + b \quad (5.7)$$

$$F^{ABS} = F_0^{ABS} \left(a + \frac{b D_0}{D} \right)^2 \quad (5.8)$$

$$\Delta F^{ABS} = F^{ABS} \left[\frac{\Delta F_0^{ABS}}{F_0^{ABS}} + 2 \frac{\Delta a + \Delta b \frac{D_0}{D}}{a + \frac{b D_0}{D}} \right] \quad (5.9)$$

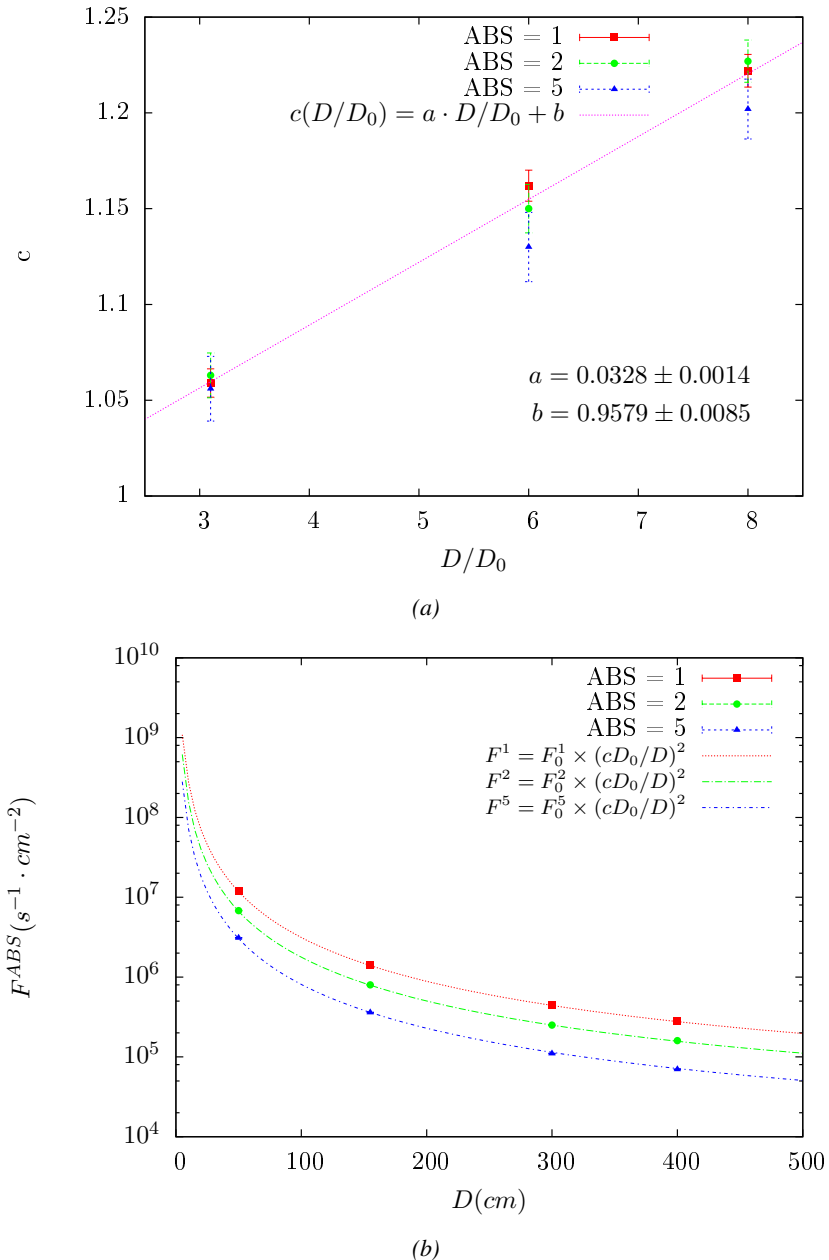


Figure 5.14: Figure 5.14a shows the linear approximation fit done via formulae 5.7 on data from table 5.2. Figure 5.14b shows a comparison of this model with the simulated flux using a and b given in figure 5.14a in formulae 5.4 and the reference value $D_0 = 50$ cm and the associated flux for each absorption factor F_0^{ABS} from table 5.1

In the case of the 2014 GIF tests, the RPC plane is located at a distance $D = 206$ cm to the source. Moreover, to estimate the strength of the flux in 2014, it is necessary to consider the nuclear decay through time associated to the Cesium source whose half-life is well known ($t_{1/2} = (30.05 \pm 0.08)$ y). The very first source activity measurement has been done on the 5th of March

2828 1997 while the GIF tests where done in between the 20th and the 31th of August 2014, i.e. at a
 2829 time $t = (17.47 \pm 0.02)$ y resulting in an attenuation of the activity from 740 GBq in 1997 to
 2830 494 GBq in 2014. All the needed information to extrapolate the flux through our detector in 2014
 2831 has now been assembled, leading to the Table 5.3. It is interesting to note that for a common RPC
 2832 sensitivity to γ of 2×10^{-3} , the order of magnitude of the estimated hit rate per unit area is of the
 2833 order of the kHz for the fully opened source. Moreover, taking profit of the two working absorbers,
 2834 it will be possible to scan background rates at 0 Hz, ~ 300 Hz as well as ~ 600 Hz. Without source,
 2835 a good estimate of the intrinsic performance will be available. Then at 300 Hz, the goal will be to
 2836 show that the detectors fulfill the performance certification of CMS RPCs. Then a first idea of the
 2837 performance of the detectors at higher background will be provided with absorption factors 2
 2838 (~ 600 Hz) and 1 (no absorption). *[Here I will also put a reference to the plot showing the
 2839 estimated background rate at the level of RE3/1 in the case of HL-LHC but this one being in
 another chapter, I will do it later.]*

Nominal ABS	Photon flux F [cm $^{-2}$ s $^{-1}$]			Hit rate/unit area [Hzcm $^{-2}$] at $D^{2014} = 206$ cm
	at $D_0^{1997} = 50$ cm	at $D^{1997} = 206$ cm	at $D^{2014} = 206$ cm	
1	$0.12 \times 10^8 \pm 0.2\%$	$0.84 \times 10^6 \pm 0.3\%$	$0.56 \times 10^6 \pm 0.3\%$	1129 ± 32
2	$0.68 \times 10^7 \pm 0.3\%$	$0.48 \times 10^6 \pm 0.3\%$	$0.32 \times 10^6 \pm 0.3\%$	640 ± 19
5	$0.31 \times 10^7 \pm 0.4\%$	$0.22 \times 10^6 \pm 0.3\%$	$0.15 \times 10^6 \pm 0.3\%$	292 ± 9

Table 5.3: The data at D_0 in 1997 is taken from [92]. In a second step, using Equations 5.8 and 5.9, the flux at D can be estimated in 1997. Then, taking into account the attenuation of the source activity, the flux at D can be estimated at the time of the tests in GIF in 2014. Finally, assuming a sensitivity of the RPC to γ $s = 2 \times 10^{-3}$, an estimation of the hit rate per unit area is obtained.

2841 **5.2.4.2 Dose measurements**

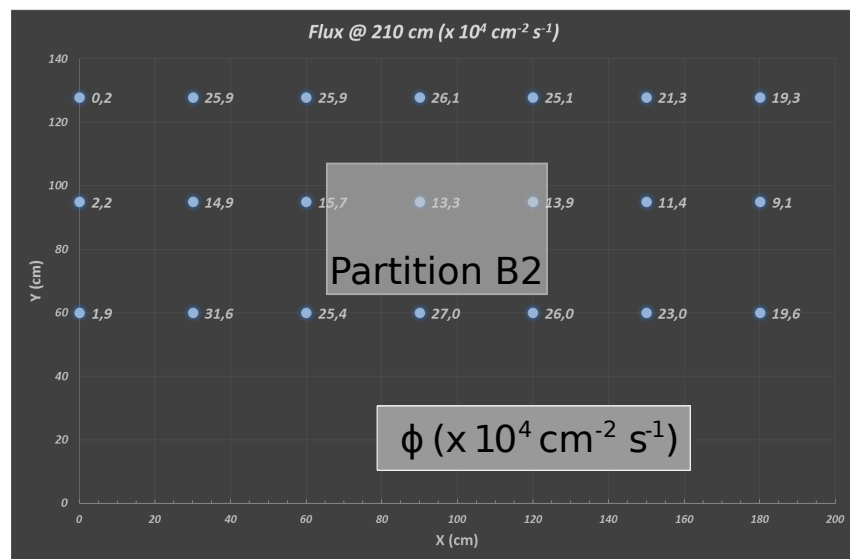


Figure 5.15: Dose measurements has been done in a plane corresponding to the tents front side. This plan is 1900 mm away from the source. As explained in the first chapter, a lens-shaped lead filter provides a uniform photon flux in the vertical plan orthogonal to the beam direction. If the second line of measured fluxes is not taken into account because of lower values due to experimental equipments in the way between the source and the tent, the uniformity of the flux is well showed by the results.

2842 **5.2.5 Results and discussions**

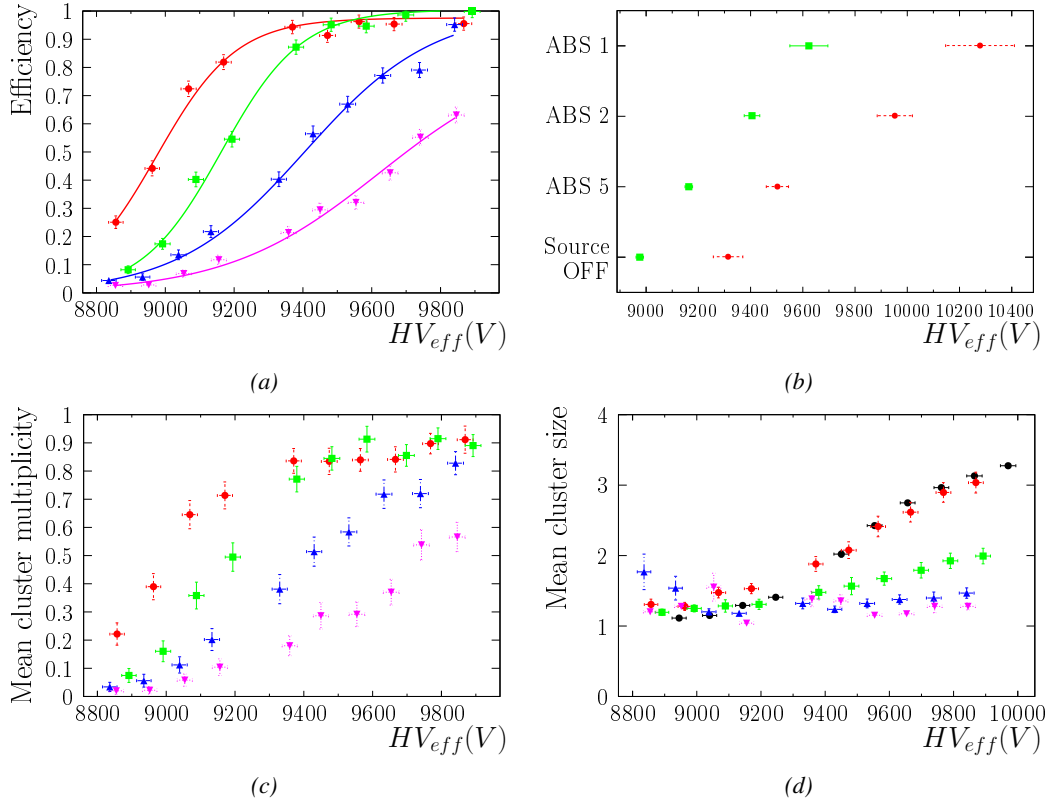


Figure 5.16

2843 **5.3 Longevity tests at GIF++**

2844 Longevity studies imply a monitoring of the performance of the detectors probed using a high
 2845 intensity muon beam in a irradiated environment by periodically measuring their rate capability, the
 2846 dark current running through them and the bulk resistivity of the Bakelite composing their
 2847 electrodes. GIF++, with its very intense ^{137}Cs source, provides the perfect environment to perform
 2848 such kind of tests. Assuming a maximum acceleration factor of 3, it is expected to accumulate the
 2849 equivalent charge in 1.7 years.

2850 As the maximum background is found in the endcap, the choice naturally was made to focus the
 2851 GIF++ longevity studies on endcap chambers. Most of the RPC system was installed in 2007.
 2852 Nevertheless, the large chambers in the fourth endcap (RE4/2 and RE4/3) have been installed
 2853 during LS1 in 2014. The Bakelite of these two different productions having different properties,
 2854 four spare chambers of the present system were selected, two RE2,3/2 spares and two RE4/2
 2855 spares. Having two chambers of each type allows to always keep one of them non irradiated as
 2856 reference, the performance evolution of the irradiated chamber being then compared through time
 2857 to the performance of the non irradiated one.
 2858 The performance of the detectors under different level of irradiation is measured periodically

2859 during dedicated test beam periods using the H4 muon beam. In between these test beam periods,
 2860 the two RE2,3/2 and RE4/2 chambers selected for this study are irradiated by the ^{137}Cs source in
 2861 order to accumulate charge and the gamma background is monitored, as well as the currents. The
 2862 two remaining chambers are kept non-irradiated as reference detectors. Due to the limited gas flow
 2863 in GIF++, the RE4 chamber remained non-irradiated until end of November 2016 where a new
 2864 mass flow controller has been installed allowing for bigger volumes of gas to flow in the system.
 2865 Figures 5.17 and 5.18 give us for different test beam periods, and thus for increasing integrated
 2866 charge through time, a comparison of the maximum efficiency, obtained using a sigmoid-like
 2867 function, and of the working point of both irradiated and non irradiated chambers [55]. No aging is
 2868 yet to see from this data, the shifts in γ rate per unit area in between irradiated and non irradiated
 2869 detectors and RE2 and RE4 types being easily explained by a difference of sensitivity due to the
 2870 various Bakelite resistivities of the HPL electrodes used for the electrode production.
 2871 Collecting performance data at each test beam period allows us to extrapolate the maximum
 2872 efficiency for a background hit rate of $300 \text{ s}^{-1} \text{ cm}^{-2}$ corresponding to the expected HL-LHC
 2873 conditions. Aging effects could emerge from a loss of efficiency with increasing integrated charge
 2874 over time, thus Figure 5.19 helps us understand such degradation of the performance of irradiated
 2875 detectors in comparison with non irradiated ones. The final answer for an eventual loss of efficiency
 2876 is given in Figure 5.20 by comparing for both irradiated and non irradiated detectors the efficiency
 2877 sigmoids before and after the longevity study. Moreover, to complete the performance information,
 2878 the Bakelite resistivity is regularly measured thanks to Ag scans (Figure 5.21) and the noise rate is
 2879 monitored weekly during irradiation periods (Figure 5.22). At the end of 2016, no signs of aging
 2880 were observed and further investigation is needed to get closer to the final integrated charge
 2881 requirements proposed for the longevity study of the present CMS RPC sub-system.

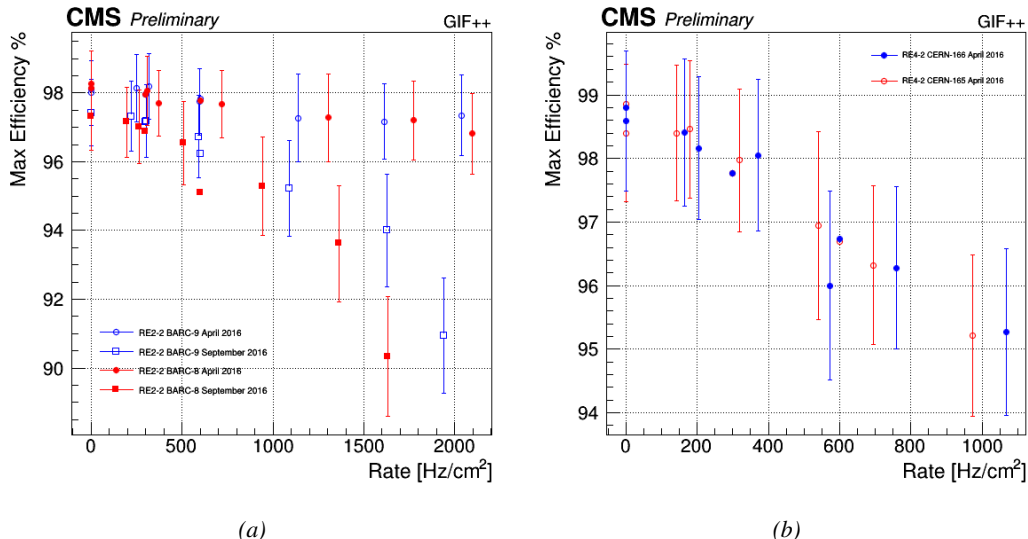


Figure 5.17: Evolution of the maximum efficiency for RE2 (5.17a) and RE4 (5.17b) chambers with increasing extrapolated γ rate per unit area at working point. Both irradiated (blue) and non irradiated (red) chambers are shown.

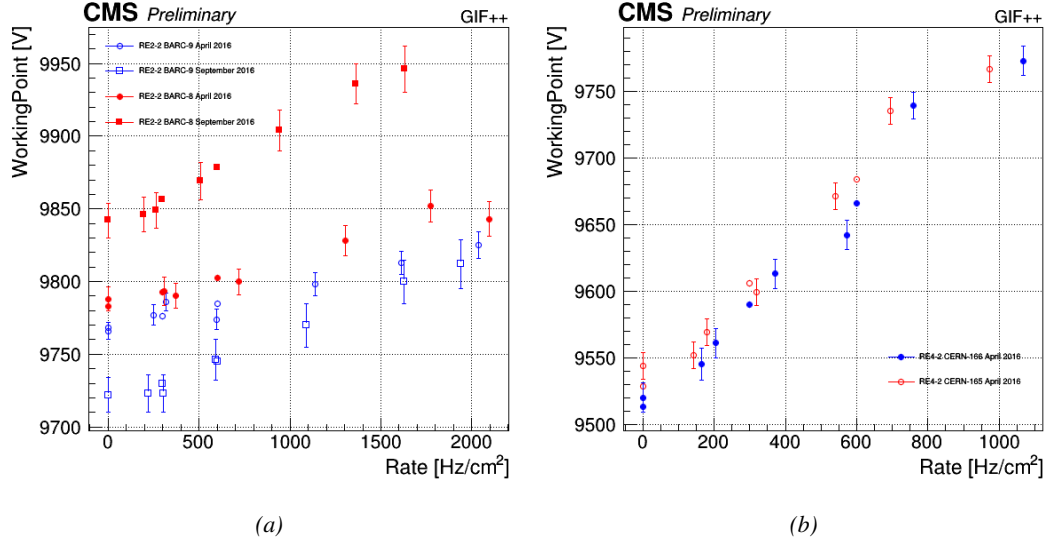


Figure 5.18: Evolution of the working point for RE2 (5.18a) and RE4 (5.18b) with increasing extrapolated γ rate per unit area at working point. Both irradiated (blue) and non irradiated (red) chambers are shown.

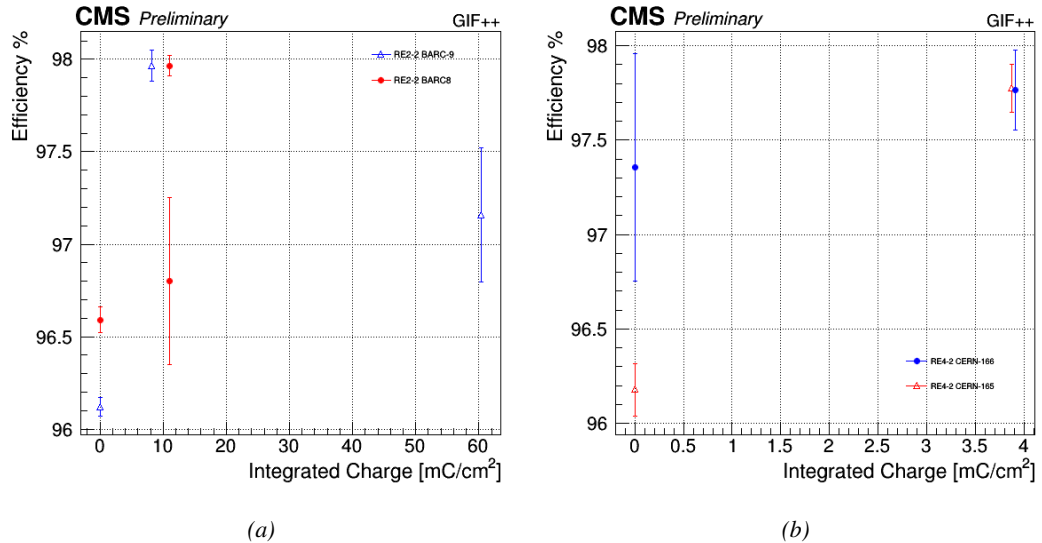


Figure 5.19: Evolution of the maximum efficiency at HL-LHC conditions, i.e. a background hit rate per unit area of 300 Hz/cm², with increasing integrated charge for RE2 (5.19a) and RE4 (5.19b) detectors. Both irradiated (blue) and non irradiated (red) chambers are shown. The integrated charge for non irradiated detectors is recorded during test beam periods and stays small with respect to the charge accumulated in irradiated chambers.

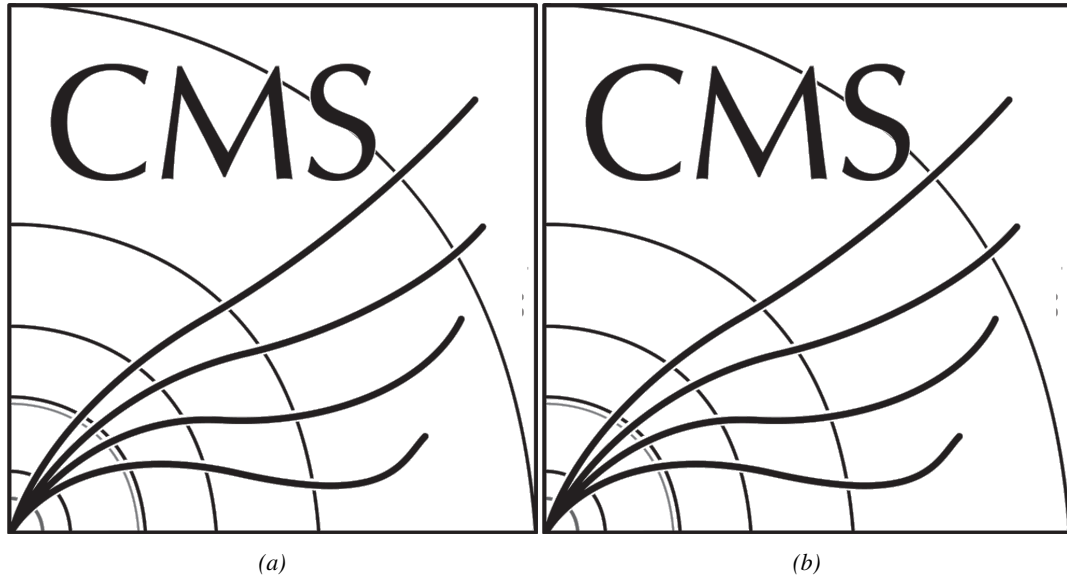


Figure 5.20: Comparison of the efficiency sigmoid before (triangles) and after (circles) irradiation for RE2 (5.20a) and RE4 (5.20b) detectors. Both irradiated (blue) and non irradiated (red) chambers are shown.

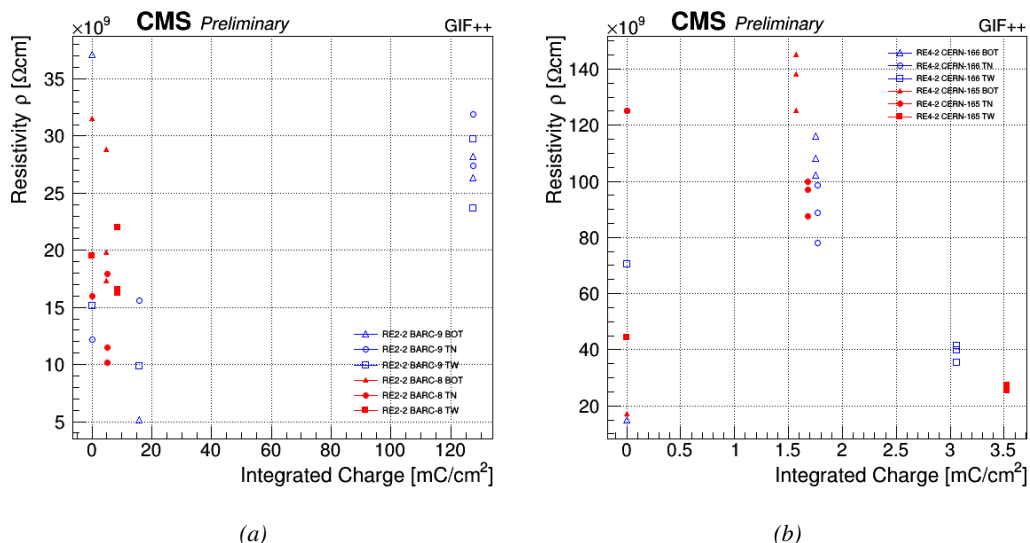


Figure 5.21: Evolution of the Bakelite resistivity for RE2 (5.21a) and RE4 (5.21b) detectors. Both irradiated (blue) and non irradiated (red) chambers are shown.

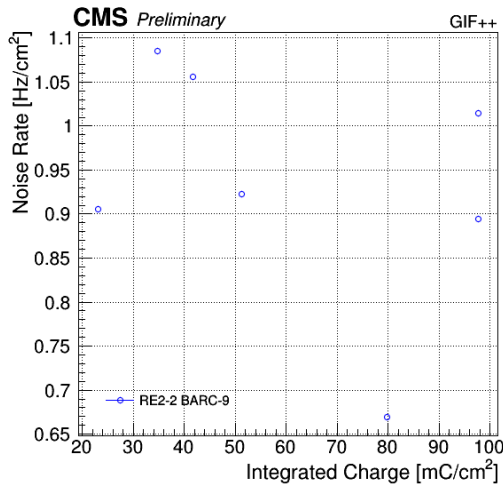


Figure 5.22: Evolution of the noise rate per unit area for the irradiated chamber RE2-2-BARC-9 only.

5.3.1 Description of the Data Acquisition

For the longevity studies, four spare chambers of the present system are used. Two spare RPCs of the RE2,3 stations as well as two spare RPCs from the new RE4 stations have been mounted in a Trolley. Six RE4 gaps are also placed in the trolley. The trolley is placed inside the GIF++ in the upstream region of the bunker, taking the cesium source as a reference. The trolley is oriented for the detection surface of the chambers to be orthogonal to the beam line. The system can be moved along the orthogonal plane in order to have the beam in all η -partitions. For the aging the trolley is moved outside the beam line and is placed in a distance of 5.2 m to the source, which irradiates the bunker using an attenuation filter of 2.2 which corresponds to a fluence of 10^7 gamma/cm². During GIF++ operation, the data collected can be divided into different categories as several parameters are monitored in addition to the usual RPC performance data. On one hand, to know the performance of a chamber, it is need to measure its efficiency and to know the background conditions in which it is operated. To do this, the hit signals from the chamber are recorded and stored in a ROOT file via a DAQ software. On the other hand, it is also very important to monitor parameters such as environmental pressure and temperature, gas temperature and humidity, RPC HV, LV, and currents, or even source and beam status. This is done through the GIF++ web DCS that stores this information in a database. Two different types of tests are conducted on RPCs via the DAQ. Indeed, the performance of the detectors is measured periodically during dedicated test beam periods using the H4 muon beam. In between these test beam periods, when the beam is not available, the chambers are irradiated by the ^{137}Cs in order to accumulate deposited charge and the gamma background is measured. RPCs under test are connected through LVDS cables to V1190A TDC modules manufactured by CAEN. These modules, located in the rack area outside of the bunker, get the logic signals sent by the chambers and save them into their buffers. Due to the limited size of the buffers, the collected data is regularly erased and replaced. A trigger signal is needed for the TDC modules to send the useful data to the DAQ computer via a V1718 CAEN USB communication module. In the case of performance test, the trigger signal used for data acquisition is generated by the

2909 coincidence of three scintillators. A first one is placed upstream outside of the bunker, a second one
 2910 is placed downstream outside of the bunker, while a third one is placed in front of the trolley, close
 2911 by the chambers. Every time a trigger is sent to the TDCs, i.e. every time a muon is detected,
 2912 knowing the time delay in between the trigger and the RPC signals, signals located in the right time
 2913 window are extracted from the buffers and saved for later analysis. Signals are taken in a time
 2914 window of 400 ns centered on the muon peak (here we could show a time spectrum). On the other
 2915 hand, in the case of background rate measurement, the trigger signal needs to be "random" not to
 2916 measure muons but to look at gamma background. A trigger pulse is continuously generated at a
 2917 rate of 300 Hz using a dual timer. To integrate an as great as possible time, all signals contained
 2918 within a time window of 10us prior to the random trigger signal are extracted form the buffers and
 2919 saved for further analysis (here another time spectrum to illustrate could be useful, maybe even
 2920 place both spectrum together as a single Figure).
 2921 The signals sent to the TDCs correspond to hit collections in the RPCs. When a particle hits a RPC,
 2922 it induce a signal in the pickup strips of the RPC readout. If this signal is higher than the detection
 2923 threshold, a LVDS signal is sent to the TDCs. The data is then organised into 4 branches keeping
 2924 track of the event number, the hit multiplicity for the whole setup, and the time and channel profile
 2925 of the hits in the TDCs.

2926 **5.3.2 RPC current, environmental and operation parameter monitoring**

2927 In order to take into account the variation of pressure and temperature between different data taking
 2928 periods the applied voltage is corrected following the relationship :

$$2929 HV_{eff} = HV_{app} \times \left(0.2 + 0.8 \cdot \frac{P_0}{P} \times \frac{T}{T_0} \right) \quad (5.10)$$

2929 where T_0 (=293 K) and P_0 (=990 mbar) are the reference values.

2930 **5.3.3 Measurement procedure**

- 2931 Insert a short description of the online tools (DAQ, DCS, DQM).
- 2932 Insert a short description of the offline tools : tracking and efficiency algorithm.
- 2933 Identify long term aging effects we are monitoring the rates per strip.

2934 **5.3.4 Longevity studies results**

6

2935

2936

Conclusions and outlooks

2937 **6.1 Conclusions**

2938 **6.2 Outlooks**

A

2939

2940

A data acquisition software for CAEN VME TDCs

2941

2942 Certifying detectors in the perspective of HL-LHC required to develop tools for the GIF++
2943 experiment. Among them was the C++ Data Acquisition (DAQ) software that allows to make the
2944 communications in between a computer and TDC modules in order to retrieve the RPC data [94].
2945 In this appendix, details about this software, as of how the software was written, how it functions
2946 and how it can be exported to another similar setup, will be given.

2947 A.1 GIF++ DAQ file tree

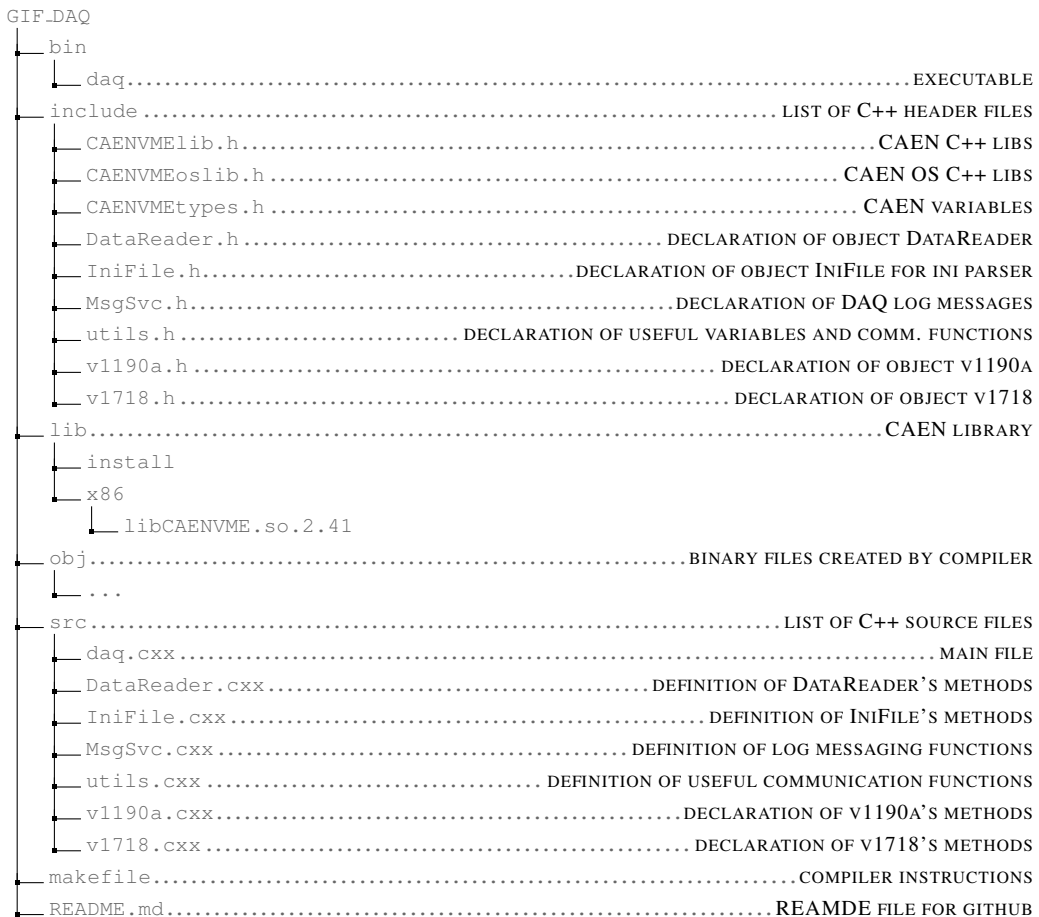
2948 GIF++ DAQ source code is fully available on github at
2949 https://github.com/afagot/GIF_DAQ. The software requires 3 non-optional
2950 dependencies:

- 2951 • CAEN USB Driver, to mount the VME hardware,
2952 • CAEN VME Library, to communicate with the VME hardware, and
2953 • ROOT, to organize the collected data into a TTree.

2954 The CAEN VME library will not be packaged by distributions and will need to be installed
2955 manually. To compile the GIF++ DAQ project via a terminal, from the DAQ folder use the
2956 command:

2957 `make`

2958 The source code tree is provided below along with comments to give an overview of the files'
2959 content. The different objects created for this project (`v1718`, `v1190a`, `IniFile` & `DataReader`) will
2960 be described in details in the following sections.



2961 A.2 Usage of the DAQ

2962 GIF++ DAQ, as used in GIF++, is not a standalone software. Indeed, the system being more
 2963 complexe, the DAQ only is a sub-layer of the software architecture developped to control and
 2964 monitor the RPCs that are placed into the bunker for performance study in an irradiated
 2965 environment. The top layer of GIF++ is a Web Detector Control System (webDCS) application.
 2966 The DAQ is only called by the webDCS when data needs to be acquired. The webDCS operates the
 2967 DAQ through command line. To start the DAQ, the webDCS calls:

2968 bin/daq /path/to/the/log/file/in/the/output/data/folder

2969 where /path/to/the/log/file/in/the/output/data/folder is the only argument required. This
 2970 log file is important for the webDCS as this file contains all the content of the communication of the
 2971 webDCS and the different systems monitored by the webDCS. Its content is constantly displayed
 2972 during data taking for the users to be able to follow the operations. The communication messages
 2973 are normally sent to the webDCS log file via the functions declared in file `MsgSvc.h`, typically
 2974 `MSG_INFO(string message)`.

2975 A.3 Description of the readout setup

2976 The CMS RPC setup at GIF++ counts 5 V1190A Time-to-Digital Converter (TDC) manufactured
 2977 by CAEN [95]. V1190A are VME units accepting 128 independent Multi-Hit/Multi-Event TDC
 2978 channels whose signals are treated by 4 100 ps high performance TDC chips developped by CERN
 2979 / ECP-MIC Division. The communication between the computer and the TDCs to transfer data is
 2980 done via a V1718 VME master module also manufactured by CAEN and operated from a USB
 2981 port [96]. These VME modules are all hosted into a 6U VME 6021 powered crate manufactured by
 2982 W-Ie-Ne-R than can accomodate up to 21 VME bus cards [97]. These 3 components of the DAQ
 2983 setup are shown in Figure A.1.

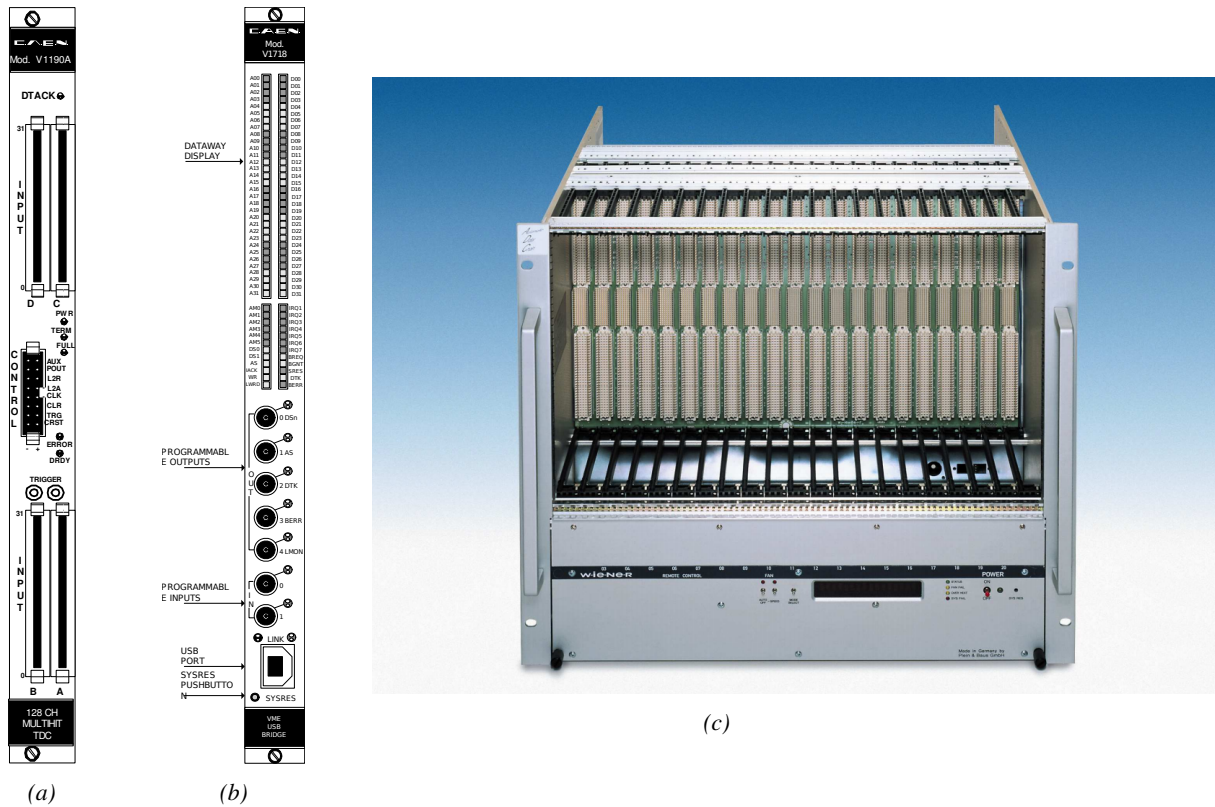


Figure A.1: (A.1a) View of the front panel of a V1190A TDC module [95]. (A.1b) View of the front panel of a V1718 Bridge module [96]. (A.1c) View of the front panel of a 6U 6021 VME crate [97].

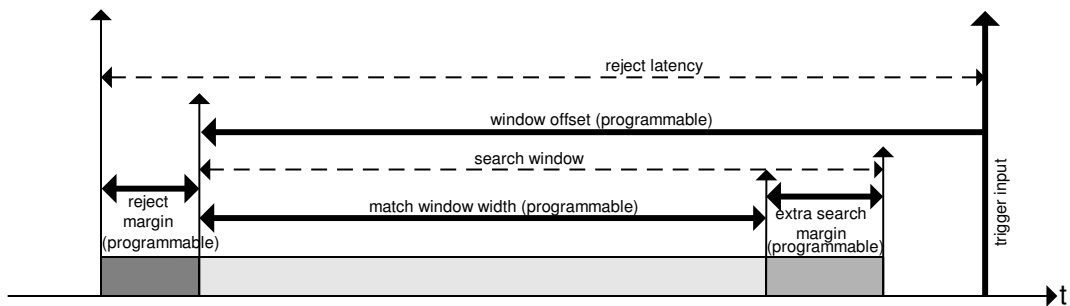
2984 A.4 Data read-out

2985 To efficiently perform a data readout algorithm, C++ objects to handle the VME modules (TDCs
 2986 and VME bridge) have been created along with objects to store data and read the configuration file
 2987 that comes as an input of the DAQ software.

2988 A.4.1 V1190A TDCs

2989 The DAQ used at GIF takes profit of the *Trigger Matching Mode* offered by V1190A modules. This
 2990 setting is enabled through the method `v1190a::SetTrigMatching (int ntdcs)` where `ntdcs` is the
 2991 total number of TDCs in the setup this setting needs to be enabled for (Source Code A.1). A trigger
 2992 matching is performed in between a trigger time tag, a trigger signal sent into the TRIGGER input
 2993 of the TDC visible on Figure A.1a, and the channel time measurements, signals recorded from the
 2994 detectors under test in our case. Control over this data acquisition mode, explained through
 2995 Figure A.2, is offered via 4 programmable parameters:

- 2996 • **match window:** the matching between a trigger and a hit is done within a programmable
 time window. This is set via the method
`void v1190a::SetTrigWindowWidth(Uint windowHeight, int ntdcs)`
- 2999 • **window offset:** temporal distance between the trigger tag and the start of the trigger
 matching window. This is set via the method
`void v1190a::SetTrigWindowWidth(Uint windowHeight, int ntdcs)`
- 3002 • **extra search margin:** an extended time window is used to ensure that all matching hits are
 found. This is set via the method
`void v1190a::SetTrigSearchMargin(Uint searchMargin, int ntdcs)`
- 3005 • **reject margin:** older hits are automatically rejected to prevent buffer overflows and to speed
 up the search time. This is set via the method
`void v1190a::SetTrigRejectionMargin(Uint rejectMargin, int ntdcs)`



3008 Figure A.2: Module V1190A Trigger Matching Mode timing diagram [95].

3009 Each of these 4 parameters are given in number of clocks, 1 clock being 25 ns long. It is easy to
 understand at this level that there are 3 possible functioning settings:

- 3010 • **1:** the match window is entirely contained after the trigger signal,
- 3011 • **2:** the match window overlaps the trigger signal, or
- 3012 • **3:** the match window is entirely contained before the trigger signal as displayed on
 Figure A.2.

3014 In both the first and second cases, the sum of the window width and of the offset can be set to a
3015 maximum of 40 clocks, which corresponds to 1 μ s. Evidently, the offset can be negative, allowing
3016 for a longer match window, with the constraint of having the window ending at most 1 μ s after the
3017 trigger signal. In the third case, the maximum negative offset allowed is of 2048 clocks (12 bit)
3018 corresponding to 51.2 μ s, the match window being strictly smaller than the offset. In the case of
3019 GIF++, the choice has been made to use this last setting by delaying the trigger signal. During the
3020 studies performed in GIF++, both the efficiency of the RPCs, probed using a muon beam, and the
3021 noise or gamma background rate are monitored. The extra search and reject margins are left unused.
3022 To probe the efficiency of RPC detectors, the trigger time tag is provided by the coincidence of
3023 scintillators when a bunch of muons passes through GIF++ area is used to trigger the data
3024 acquisition. For this measurement, it is useful to reduce the match window width only to contain
3025 the muon information. Indeed, the delay in between a trigger signal and the detection of the
3026 corresponding muon in the RPC being very constant (typically a few tens of ns due to jitter and
3027 cable length), the muon signals are very localised in time. Thus, due to a delay of approximately
3028 325 ns in between the muons and the trigger, the settings were chosen to have a window width of
3029 24 clocks (600 ns) centered on the muon peak thanks to a negative offset of 29 clocks (725 ns).
3030 On the other hand, monitoring the rates don't require for the DAQ to look at a specific time window.
3031 It is important to integrate enough time to have a robust measurement of the rate as the number of
3032 hits per time unit. The triggering signal is provided by a pulse generator at a frequency of 300 Hz
3033 to ensure that the data taking occurs in a random way, with respect to beam physics, to probe only
3034 the irradiation spectrum on the detectors. The match window is set to 400 clocks (10 μ s) and the
3035 negative offset to 401 clocks as it needs to exceed the value of the match window.

```

class v1190a
{
    private :
        long Handle;
        vector<Data32> Address;
        CVDataWidth DataWidth;
        CVAAddressModifier AddressModifier;

    public:

        v1190a(long handle, IniFile *inifile, int ntdcs);
        ~v1190a();
        Data16 write_op_reg(Data32 address, int code, string error);
        Data16 read_op_reg(Data32 address, string error);
        void Reset(int ntdcs);
        void Clear(int ntdcs);
        void TestWR(Data16 value,int ntdcs);
        void CheckTDCStatus(int ntdcs);
        void CheckCommunication(int ntdcs);
        void SetTDCTestMode(Data16 mode,int ntdcs);
        void SetTrigMatching(int ntdcs);
        void SetTrigTimeSubtraction(Data16 mode,int ntdcs);
        void SetTrigWindowWidth(Uint windowHeight,int ntdcs);
        void SetTrigWindowOffset(Uint windowOffset,int ntdcs);
        void SetTrigSearchMargin(Uint searchMargin,int ntdcs);
        void SetTrigRejectionMargin(Uint rejectMargin,int ntdcs);
        void GetTrigConfiguration(int ntdcs);
        void SetTrigConfiguration(IniFile *inifile,int ntdcs);
        void SetTDCDetectionMode(Data16 mode,int ntdcs);
        void SetTDCResolution(Data16 lsb,int ntdcs);
        void SetTDCDeadTime(Data16 time,int ntdcs);
        void SetTDCHeadTrailer(Data16 mode,int ntdcs);
        void SetTDCEventSize(Data16 size,int ntdcs);
        void SwitchChannels(IniFile *inifile,int ntdcs);
        void SetIRQ(Data32 level, Data32 count,int ntdcs);
        void SetBlockTransferMode(Data16 mode,int ntdcs);
        void Set(IniFile *inifile,int ntdcs);
        void CheckStatus(CVErrorCodes status) const;
        int ReadBlockD32(Uint tdc, const Data16 address,
                           Data32 *data, const Uint words, bool ignore_berr);
        Uint Read(RAWData *DataList,int ntdcs);
};

3036

```

3037 *Source Code A.1: Description of C++ object v1190a.*

3038 The v1190a object, defined in the DAQ software as in Source Code A.1, offers the possibility to
 3039 concatenate all TDCs in the readout setup into a single object containing a list of hardware
 3040 addresses (addresses to access the TDCs' buffer through the VME crate) and each constructor and
 3041 method acts on the list of TDCs.

3042 **A.4.2 DataReader**

3043 Enabled thanks to v1190a::SetBlockTransferMode(Data16 mode, **int** ntdcs), the data transfer
 3044 is done via Block Transfer (BLT). Using BLT allows to transfer a fixed number of events called a
 3045 **block**. This is used together with an Almost Full Level (AFL) of the TDCs' output buffers, defined
 3046 through v1190a::SetIRQ(Data32 level, Data32 count, **int** ntdcs). This AFL gives the

3047 maximum amount of 32735 words (16 bits, corresponding to the depth of a TDC output buffer) that
 3048 can written in a buffer before an Interrupt Request (IRQ) is generated and seen by the VME Bridge,
 3049 stopping the data acquisition to transfer the content of each TDC buffers before resuming. For each
 3050 trigger, 6 words or more are written into the TDC buffer:

- 3051 • **a global header** providing information of the event number since the beginning of the data
 acquisition,
- 3053 • **a TDC header,**
- 3054 • **the TDC data** (*if any*), 1 for each hit recorded during the event, providing the channel and
 the time stamp associated to the hit,
- 3056 • **a TDC error** providing error flags,
- 3057 • **a TDC trailer,**
- 3058 • **a global trigger time tag** that provides the absolute trigger time relatively to the last reset,
 and
- 3060 • **a global trailer** providing the total word count in the event.

3061 As previously described in Section ??, CMS RPC FEEs provide us with 100 ns long LVDS output
 3062 signals that are injected into the TDCs' input. Any avalanche signal that gives a signal above the
 3063 FEEs threshold is thus recorded by the TDCs as a hit within the match window. Each hit is assigned
 3064 to a specific TDC channel with a time stamp, with a precision of 100 ps. The reference time,
 3065 $t_0 = 0$, is provided by the beginning of the match window. Thus for each trigger, coming from a
 3066 scintillator coïncidence or the pulse generator, a list of hits is stored into the TDCs' buffers and will
 3067 then be transferred into a ROOT Tree.

3068 When the BLT is used, it is easy to understand that the maximum number of words that have been
 3069 set as ALF will not be a finite number of events or, at least, the number of events that would be
 3070 recorded into the TDC buffers will not be a multiple of the block size. In the last BLT cycle to
 3071 transfer data, the number of events to transfer will most probably be lower than the block size. In
 3072 that case, the TDC can add fillers at the end of the block but this option requires to send more data
 3073 to the computer and is thus a little slower. Another solution is to finish the transfer after the last
 3074 event by sending a bus error that states that the BLT reached the last event in the pile. This method
 3075 has been chosen in GIF++.

3076 Due to irradiation, an event in GIF++ can count up to 300 words per TDC. A limit of 4096 words
 3077 (12 bits) has been set to generate IRQ which represent from 14 to almost 700 events depending on
 3078 the average of hits collected per event. Then the block size has been set to 100 events with enabled
 3079 bus errors. When an AFL is reached for one of the TDCs, the VME bridge stops the acquisition by
 3080 sending a BUSY signal.

3081 The data is then transferred one TDC at a time into a structure called `RAWData` (Source Code A.2).

```
struct RAWData {
    vector<int>           *EventList;
    vector<int>           *NHitsList;
    vector<int>           *QFlagList;
    vector<vector<int>>   *ChannelList;
    vector<vector<float>> *TimeStampList;
};
```

3083 *Source Code A.2: Description of data holding C++ structure RAWData.*

3084 In order to organize the data transfer and the data storage, an object called `DataReader` was created
 3085 (Source Code A.3). On one hand, it has `v1718` and `v1190a` objects as private members for
 3086 communication purposes, such as VME modules settings via the configuration file `*iniFile` or
 3087 data read-out through `v1190a::Read()` and on the other hand, it contains the struture `RAWData` that
 3088 allows to organise the data in vectors reproducing the tree structre of a ROOT file.

```
3084       class DataReader
 3085       {
 3086        private:
 3087        bool      StopFlag;
 3088        IniFile *iniFile;
 3089        Data32     MaxTriggers;
 3090        v1718     *VME;
 3091        int       nTDCs;
 3092        v1190a    *TDCs;
 3093        RAWData   TDCData;

 3094       public:
 3095        DataReader();
 3096        virtual ~DataReader();
 3097        void      SetIniFile(string inifilename);
 3098        void      SetMaxTriggers();
 3099        Data32     GetMaxTriggers();
 3100        void      SetVME();
 3101        void      SetTDC();
 3102        int       GetQFlag(Uint it);
 3103        void      Init(string inifilename);
 3104        void      FlushBuffer();
 3105        void      Update();
 3106        string    GetFileName();
 3107        void      WriteRunRegistry(string filename);
 3108        void      Run();
 3109   };
```

3090 *Source Code A.3: Description of C++ object DataReader.*

3091 Each event is tranferred from `TDCData` and saved into branches of a ROOT `TTree` as 3 integers that
 3092 represent the event ID (`EventCount`), the number of hits read from the TDCs (`nHits`), and the
 3093 quality flag that provides information for any problem in the data transfer (`qflag`), and 2 lists of
 3094 `nHits` elements containing the fired TDC channels (`TDCh`) and their respective time stamps
 3095 (`TDCTS`), as presented in Source Code A.4. The ROOT file file is named using information
 3096 contained into the configuration file, presented in section A.5.2. The needed information is
 3097 extracted using method `DataReader::GetFileName()` and allow to build the output filename format
 3098 `ScanXXXXXX_HVX_DAQ.root` where `ScanXXXXXX` is a 6 digit number representing the scan number
 3099 into GIF++ database and `HVX` the HV step within the scan that can be more than a single digit. An
 3100 example of ROOT data file is provided with Figure A.3.

```

RAWData TDCData;
TFile *outputFile = new TFile(outputFileName.c_str(), "recreate");
TTree *RAWDataTree = new TTree("RAWData", "RAWData");

int EventCount = -9;
int nHits = -8;
int qflag = -7;
vector<int> TDCCh;
vector<float> TDCTS;

RAWDataTree->Branch("EventNumber",&EventCount, "EventNumber/I");
RAWDataTree->Branch("number_of_hits",&nHits, "number_of_hits/I");
RAWDataTree->Branch("Quality_flag",&qflag, "Quality_flag/I");
RAWDataTree->Branch("TDC_channel",&TDCCh);
RAWDataTree->Branch("TDC_TimeStamp",&TDCTS);

3101
//...
//Here read the TDC data using v1190a::Read() and place it into
//TDCData for as long as you didn't collect the requested amount
//of data.
//...

for(Uint i=0; i<TDCData.EventList->size(); i++){
    EventCount = TDCData.EventList->at(i);
    nHits = TDCData.NHitsList->at(i);
    qflag = TDCData.QFlagList->at(i);
    TDCCh = TDCData.ChannelList->at(i);
    TDCTS = TDCData.TimeStampList->at(i);
    RAWDataTree->Fill();
}

```

3102 *Source Code A.4: Highlight of the data transfer and organisation within DataReader::Run() after the data has been collected into TDCData.*

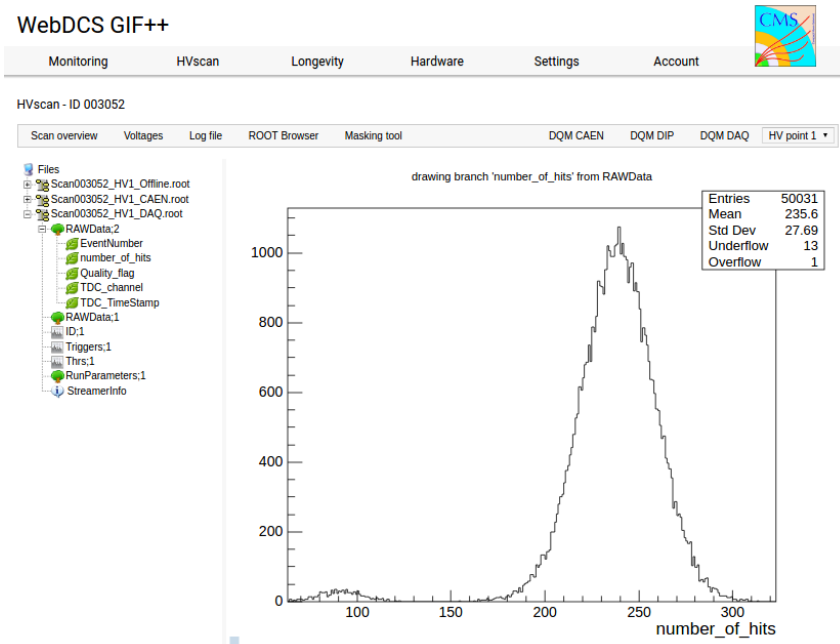


Figure A.3: Structure of the ROOT output file generated by the DAQ. The 5 branches (EventNumber, number_of_hits, Quality_flag, TDC_channel and TDC_TimeStamp) are visible on the left panel of the ROOT browser. On the right panel is visible the histogram corresponding to the variable nHits. In this specific example, there were approximately 50k events recorded to measure the gamma irradiation rate on the detectors. Each event is stored as a single entry in the TTree.

3103 A.4.3 Data quality flag

3104 Among the parameters that are recorded for each event, the quality flag, defined in Source
 3105 Code A.5, is determined on the fly by checking the data recorded by every single TDC. From
 3106 method `v1190a::Read()`, it can be understood that the content of each TDC buffer is readout one
 3107 TDC at a time. Entries are created in the data list for the first TDC and then, when the second buffer
 3108 is readout, events corresponding to entries that have already been created to store data for the
 3109 previous TDC are added to the existing list element. On the contrary, when an event entry has not
 3110 been yet created in the data list, a new entry is created.

```
3111    typedef enum _QualityFlag {
 3112     GOOD        = 1,
 3113     CORRUPTED = 0
 3114 } QualityFlag;
```

3115 *Source Code A.5: Definition of the quality flag `enum`.*

3116 It is possible that each TDC buffer contains a different number of events. In cases where the first
 3117 element in the buffer list is an event for corresponds to a new entry, the difference in between the
 3118 entry from the buffer and the last entry in the data list is recorded and checked. If it is greater than 1,
 what should never be the case, the quality flag is set to `CORRUPTED` for this TDC and an empty entry
 is created in the place of the missing ones. Missing entries are believe to be the result of a bad hold
 on the TDC buffers at the moment of the readout. Indeed, the software hold is effective only on 1

3119 TDC at a time and no solution as been found yet to completely block the writting in the buffers
 3120 when an IRQ is received.
 3121 At the end of each BLT cycle, the ID of the last entry stored for each TDC buffer is not recorded.
 3122 When starting the next cycle, if the first entry in the pile corresponds to an event already existing in
 3123 the list, the readout will start from this list element and will not be able to check the difference in
 3124 between this entry's ID and the one of the last entry that was recorded for this TDC buffer in the
 3125 previous cycle. In the case events were missing, the flag stays at its initial value of 0, which is
 3126 similar to CORRUPTED and it is assumed that then this TDC will not contribute to number_of_hits,
 3127 TDC_channel or TDC_TimeStamp.
 3128 Finally, since there will be 1 RAWData entry per TDC for each event (meaning nTDCs entries,
 3129 referring to DataReader private attribute), the individual flags of each TDC will be added together.
 3130 The final format is an integer composed nTDCs digits where each digit is the flag of a specific TDC.
 3131 This is constructed using powers of 10 like follows:

3132 TDC 0: QFlag = $10^0 \times \text{QualityFlag}$
 3133 TDC 1: QFlag = $10^1 \times \text{QualityFlag}$
 3134 ...
 3135 TDC N: QFlag = $10^N \times \text{QualityFlag}$

3136 and the final flag to be with N digits:

3137 QFlag = n....3210
 3138 each digit being 1 or 0. Below is given an example with a 4 TDCs setup.

3139 If all TDCs were good : QFlag = 1111,
 3140 but if TDC 2 was corrupted : QFlag = 1011.

3141 When data taking is over and the data contained in the dynamical RAWData structure is transferred to
 3142 the ROOT file, all the 0s are changed into 2s by calling the method DataReader::GetQFlag(). This
 3143 will help translating the flag without knowing the number of TDCs beforehand. Indeed, a flag 111
 3144 could be due to a 3 TDC setup with 3 good individual TDC flags or to a more than 3 TDC setup
 3145 with TDCs those ID is greater than 2 being CORRUPTED, thus giving a 0.
 3146 The quality flag has been introduced quite late, in October 2017 only, to the list of GIF++ DAQ
 3147 parameters to be recorded into the output ROOT file. Before this addition, the missing data,
 3148 corrupting the quality for the offline analysis, was contributing to artificially fill data with lower
 3149 multiplicity. Looking at TBranch number_of_hits provides an information about the data of the
 3150 full GIF++ setup. When a TDC is not able to transfer data for a specific event, the effect is a
 3151 reduction of the total number of hits recorded in the full setup, this is what can be seen from
 3152 Figure A.4. After offline reconstruction detector by detector, the effect of missing events can be
 3153 seen in the artificially filled bin at multiplicity 0 shown in Figure A.5. Nonetheless, for data with high
 3154 irradiation levels, as it is the case for Figure A.5a, discarding the fake multiplicity 0 data can be
 3155 done easily during the offline analysis. At lower radiation, the missing events contribution becomes
 3156 more problematic as the multiplicity distribution overlaps the multiplicity 0 and that in the same
 3157 time the proportion of missing events decreases. Attempts to fit the distribution with a Poisson or

3158 skew distribution function were not conclusive and this very problem has been at the origin of the
 3159 quality flag that allows to give a non ambiguous information about each event quality.

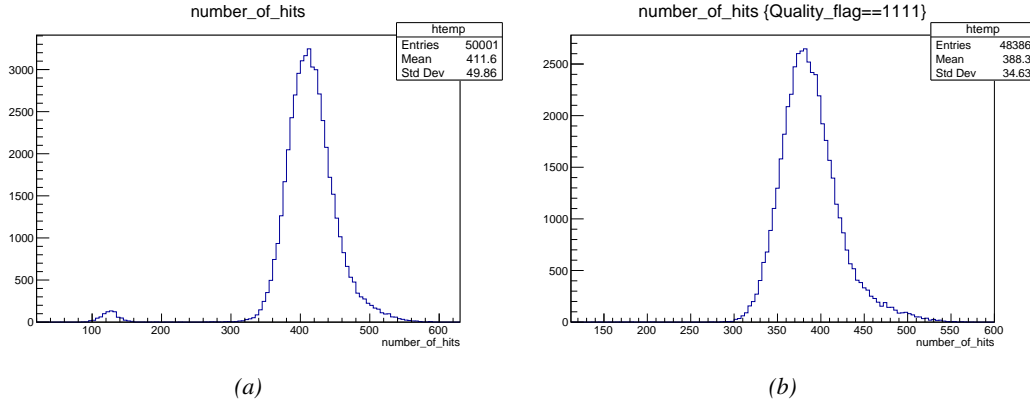


Figure A.4: The effect of the quality flag is explained by presenting the content of TBranch number_of_hits of a data file without Quality_flag in Figure A.4a and the content of the same TBranch for data corresponding to a Quality_flag where all TDCs were labelled as GOOD in Figure A.4b taken with similar conditions. It can be noted that the number of entries in Figure A.4b is slightly lower than in Figure A.4a due to the excluded events.

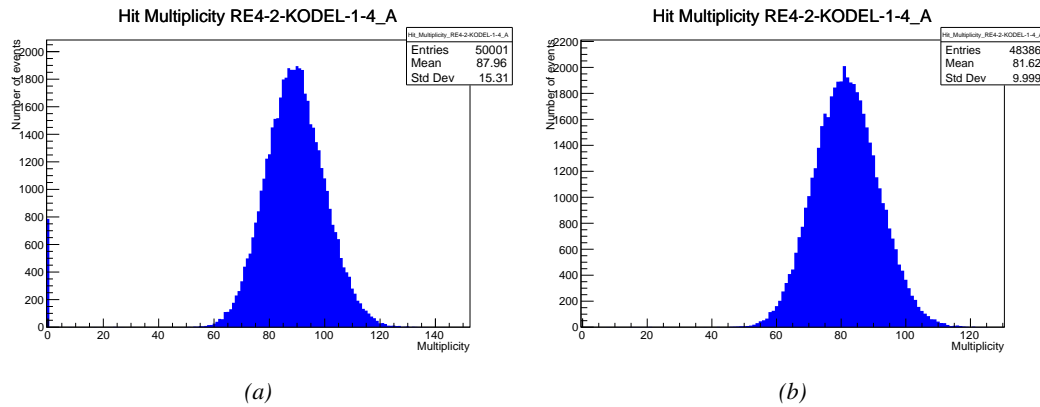


Figure A.5: Using the same data as previously showed in Figure A.4, the effect of the quality flag is explained by presenting the reconstructed hit multiplicity of a data file without Quality_flag in Figure A.5a and the reconstructed content of the same RPC partition for data corresponding to a Quality_flag where all TDCs were labelled as GOOD in Figure A.5b taken with similar conditions. The artificial high content of bin 0 is completely suppressed.

3160 A.5 Communications

3161 To ensure data readout and dialog in between the machine and the TDCs or in between the
 3162 webDCS and the DAQ, different communication solutions were used. First of all, it is important to
 3163 have a module to allow the communication in between the TDCs and the computer from which the
 3164 DAQ operates. When this communication is effective, shifters using the webDCS to control data

3165 taking can thus send instructions to the DAQ.

3166 A.5.1 V1718 USB Bridge

3167 In the previous section, the data transfer as been discussed. The importance of the `v1718` object
 3168 (Source Code A.6), used as private member of `DataReader`, was not explicited. VME master
 3169 modules are used for communication purposes as they host the USB port that connects the powered
 3170 crate buffer to the computer were the DAQ is installed. From the source code point of view, this
 3171 object is used to control the communication status, by reading the returned error codes with
 3172 `v1718::CheckStatus()`, or to check for IRQs coming from the TDCs through `v1718::CheckIRQ()`.
 3173 Finally, to ensure that triggers are blocked at the hardware level, a NIM pulse is sent out of one of
 3174 the 5 programmable outputs (`v1718::SendBUSY()`) to the VETO of the coïncidence module where
 3175 the trigger signals originate from. As long as this signal is ON, no trigger can reach the TDCs
 3176 anymore.

```
3176
  class v1718{
    private:
      int Handle;           // Data
      Data32 Data;          // Interrupt level
      CVIRQLevels Level;   // Addressing Mode
      CVAddressModifier AM; // Data Format
      CVDataWidth dataSize; // Base Address
      Data32 BaseAddress;   // Base Address

    public:
      v1718(IniFile *inifile);
      ~v1718();
      long GetHandle(void) const;
      int GetData(Data16 data);
      Data16 GetData(void);
      int SetLevel(CVIRQLevels level);
      CVIRQLevels GetLevel(void);
      int SetAM(CVAddressModifier am);
      CVAddressModifier GetAM(void);
      int SetDatasize(CVDataWidth datasize);
      CVDataWidth GetDataSize(void);
      int SetBaseAddress(Data16 baseaddress);
      Data16 GetBaseAddress(void);
      void CheckStatus(CVErrorCodes status) const;
      bool CheckIRQ();
      void SetPulsers();
      void SendBUSY(BusyLevel level);
  };

```

3178 *Source Code A.6: Description of C++ object v1718.*

3179 A.5.2 Configuration file

3180 The DAQ software takes as input a configuration file written using INI standard [98]. This file is
 3181 partly filled with the information provided by the shifters when starting data acquisition using the
 3182 webDCS, as shown by Figure A.6. This information is written in section [`General`] and will later
 3183 be stored in the ROOT file that contains the DAQ data as can be seen from Figure A.3. Indeed,
 3184 another `TTree` called `RunParameters` as well as the 2 histograms `ID`, containing the scan number,
 3185 start and stop time stamps, and `Triggers`, containing the number of triggers requested by the

3186 shifter, are available in the data files. Moreover, `ScanID` and `HV` are then used to construct the file
 3187 name thanks to the method `DataReader::GetFileName()`.

Chamber	RE2-2-NPD-BARC-8	RE4-2-CERN-105	RE2-2-NPD-BARC-9	RE4-2-CERN-105	RE4-2-KODEL-1-4	Max triggers
HV _{eff} 1	8600	8500	8600	8500	6500	
HV _{eff} 2	8700	8600	8700	8600	6600	
HV _{eff} 3	8800	8700	8800	8700	6700	
HV _{eff} 4	8900	8800	8900	8800	6800	
HV _{eff} 5	9000	8900	9000	8900	6900	
HV _{eff} 6	9100	9000	9100	9000	7000	
HV _{eff} 7	9200	9100	9200	9100	7100	
HV _{eff} 8	9300	9200	9300	9200	7200	
HV _{eff} 9	9400	9300	9400	9300	7300	
HV _{eff} 10	9500	9400	9500	9400	7400	

Figure A.6: WebDCS DAQ scan page. On this page, shifters need to choose the type of scan (Rate, Efficiency or Noise Reference scan), the gamma source configuration at the moment of data taking, the beam configuration, and the trigger mode. These information will be stored in the DAQ ROOT output. Are also given the minimal measurement time and waiting time after ramping up of the detectors is over before starting the data acquisition. Then, the list of HV points to scan and the number of triggers for each run of the scan are given in the table underneath.

3188 The rest of the information is written beforehand in the configuration file template, as explicated in
 3189 Source Code A.7, and contains the hardware addresses to the different VME modules in the setup
 3190 as well as settings for the TDCs. As the TDC settings available in the configuration file are not
 3191 supposed to be modified, an improvement would be to remove them from the configuration file and
 3192 to hardcode them inside of the DAQ code itself or to place them into a different INI file that would
 3193 host only the TDC settings to lower the probability for a bad manipulation of the configuration file
 3194 that can be modified from one of webDCS' menus.

```
[General]
TdcS=4
ScanID=$scanid
HV=$HV
RunType=$runtype
MaxTriggers=$maxtriggers
Beam=$beam
[VMEInterface]
Type=V1718
BaseAddress=0xFF0000
Name=VmeInterface
[TDC0]
Type=V1190A
BaseAddress=0x00000000
Name=Tdc0
StatusA00-15=1
StatusA16-31=1
StatusB00-15=1
StatusB16-31=1
StatusC00-15=1
StatusC16-31=1
StatusD00-15=1
StatusD16-31=1
[TDC1]
Type=V1190A
BaseAddress=0x11110000
Name=Tdc1
StatusA00-15=1
StatusA16-31=1
StatusB00-15=1
StatusB16-31=1
StatusC00-15=1
StatusC16-31=1
StatusD00-15=1
StatusD16-31=1
[TDC2]
Type=V1190A
BaseAddress=0x22220000
Name=Tdc2
StatusA00-15=1
StatusA16-31=1
StatusB00-15=1
StatusB16-31=1
StatusC00-15=1
StatusC16-31=1
StatusD00-15=1
StatusD16-31=1
[TDC3]
Type=V1190A
BaseAddress=0x44440000
Name=Tdc3
StatusA00-15=1
StatusA16-31=1
StatusB00-15=1
StatusB16-31=1
StatusC00-15=1
StatusC16-31=1
StatusD00-15=1
StatusD16-31=1
[TDCSettings]
TriggerExtraSearchMargin=0
TriggerRejectMargin=0
TriggerTimeSubtraction=0b1
TdcDetectionMode=0b01
TdcResolution=0b10
TdcDeadTime=0b00
TdcHeadTrailer=0b1
TdcEventSize=0b1001
TdcTestMode=0b0
BLTMode=1
```

Source Code A.7: INI configuration file template for 4 TDCs. In section [General], the number of TDCs is explicitated and information about the ongoing run is given. Then, there are sections for each and every VME modules. There buffer addresses are given and for the TDCs, the list of channels to enable is given. Finally, in section [TDCSettings], a part of the TDC settings are given.

3197 In order to retrieve the information of the configuration file, the object `IniFile` has been
 3198 developed to provide an INI parser, presented in Source Code A.8. It contains private methods
 3199 returning a boolean to check the type of line written in the file, whether a comment, a group header
 3200 or a key line (`IniFile::CheckIfComment()`, `IniFile::CheckIfGroup()` and
 3201 `IniFile::CheckIfToken()`). The key may sometimes be referred to as *token* in the source code.
 3202 Moreover, the private element `FileData` is a map of `const string` to `string` that allows to store
 3203 the data contained inside the configuration file via the public method `IniFile::GetFileData()`
 3204 following the formatting (see method `IniFile::Read()`):

```
3205   string group, token, value;
  // Get the field values for the 3 strings.
  // Then concatenate group and token together as a single string
  // with a dot separation.
  token = group + "." + token;
  FileData[token] = value;
```

3206 More methods have been written to translate the different keys into the right variable format when
 3207 used by the DAQ. For example, to get a `float` value out of the configuration file data, knowing the
 3208 group and the key needed, the method `IniFile::floatType()` can be used. It takes 3 arguments
 3209 being the group name and key name (both `string`), and a default `float` value used as exception in
 3210 the case the expected combination of group and key cannot be found in the configuration file. This
 3211 default value is then used and the DAQ continues on working after sending an alert in the log file
 3212 for further debugging.

```

typedef map< const string, string > IniFileData;

class IniFile{
    private:
        bool          CheckIfComment (string line);
        bool          CheckIfGroup(string line, string& group);
        bool          CheckIfToken(string line, string& key, string& value);
        string         FileName;
        IniFileData   FileData;
        int           Error;

    public:
        IniFile();
        IniFile(string filename);
        virtual      ~IniFile();

        // Basic file operations
        void          SetFileName(string filename);
        int           Read();
        int           Write();
        IniFileData   GetFileData();

        // Data readout methods
        Data32         addressType (string groupname, string keyname, Data32
3213      defaultValue);
        long          intType     (string groupname, string keyname, long
        defaultValue);
        long long    longType    (string groupname, string keyname, long long
        defaultValue );
        string         stringType  (string groupname, string keyname, string
        defaultValue );
        float         floatType   (string groupname, string keyname, float
        defaultValue );

        // Error methods
        string         GetErrorMsg();
    };

```

3214 *Source Code A.8: Description of C++ object `IniFile` used as a parser for INI file format.*

3215 A.5.3 WebDCS/DAQ intercommunication

3216 When shifters send instructions to the DAQ via the configuration file, it is the webDCS itself that
 3217 gives the start command to the DAQ and then the 2 softwares use inter-process communication
 3218 through file to synchronise themselves. This communication file is represented by the variable
 3219 **const** string __runstatuspath.

3220 On one side, the webDCS sends commands or status that are readout by the DAQ:

- 3221 ● INIT, status sent when launching a scan and read via function `CtrlRunStatus(...)`,
- 3222 ● START, command to start data taking and read via function `CheckSTART()`,
- 3223 ● STOP, command to stop data taking at the end of the scan and read via function `CheckSTOP()`,
 3224 and
- 3225 ● KILL, command to kill data taking sent by user and read via function `CheckKILL()`

3226 and on the other, the DAQ sends status that are controled by the webDCS:

- 3227 ● DAQ_RDY, sent with `SendDAQReady()` to signify that the DAQ is ready to receive commands
3228 from the webDCS,
- 3229 ● RUNNING, sent with `SendDAQRunning()` to signify that the DAQ is taking data,
- 3230 ● DAQ_ERR, sent with `SendDAQError()` to signify that the DAQ didn't receive the expected
3231 command from the webDCS or that the launch command didn't have the right number of
3232 arguments,
- 3233 ● RD_ERR, sent when the DAQ wasn't able to read the communication file, and
- 3234 ● WR_ERR, sent when the DAQ wasn't able to write into the communication file.

3235 **A.5.4 Example of inter-process communication cycle**

3236 Under normal conditions, the webDCS and the DAQ processes exchange commands and status via
3237 the file hosted at the address `__runstatuspath`, as explained in subsection A.5.3. An example of
3238 cycle is given in Table A.1. In this example, the steps 3 to 5 are repeated as long as the webDCS
3239 tells the DAQ to take data. A data taking cycle is the equivalent as what is called a *Scan* in GIFT++
3240 jargon, referring to a set of runs with several HV steps. Each repetition of steps 3 to 5 is then
3241 equivalent to a single *Run*.

3242 At any moment during the data taking, for any reason, the shifter can decide that the data taking
3243 needs to be stopped before it reached the end of the scheduled cycle. Thus at any moment on the
3244 cycle, the content of the inter-process communication file will be changed to `KILL` and the DAQ
3245 will shut down right away. The DAQ checks for `KILL` signals every 5s after the TDCs configuration
3246 is over. So far, the function `CheckKILL()` has been used only inside of the data taking loop of
3247 method `DataReader::Run()` and thus, if the shifter decides to KILL the data taking during the TDC
3248 configuration phase or the HV ramping in between 2 HV steps, the DAQ will not be stopped
3249 smoothly and a *force kill* command will be sent to stop the DAQ process that is still awake on the
3250 computer. Improvements can be brought on this part of the software to make sure that the DAQ can
3251 safely shutdown at any moment.

3252 **A.6 Software export**

3253 In section A.2 was discussed the fact that the DAQ as written in its last version is not a standalone
3254 software. It is possible to make it a standalone program that could be adapted to any VME setup
3255 using V1190A and V1718 modules by creating a GUI for the software or by printing the log
3256 messages that are normally printed in the webDCS through the log file, directly into the terminal.
3257 This method was used by the DAQ up to version 3.0 moment where the webDCS was completed.
3258 Also, it is possible to check branches of DAQ v2.X to have example of communication through a
3259 terminal.

3260 DAQ v2.X is nonetheless limited in its possibilities and requires a lot of offline manual
3261 interventions from the users. Indeed, there is no communication of the software with the detectors'
3262 power supply system that would allow for a user a predefine a list of voltages to operate the
3263 detectors at and loop over to take data without any further manual intervention. In v2.X, the data is
3264 taken for a single detector setting and at the end of each run, the softwares asks the user if he

step	actions of webDCS	status of DAQ	<code>__runstatuspath</code>
1	launch DAQ ramp voltages ramping over wait for currents stabilization	readout of IniFile configuration of TDCs	INIT
2		configuration done send DAQ ready wait for START signal	DAQ_RDY
3	waiting time over send START		START
4	wait for run to end monitor DAQ run status	data taking ongoing check for KILL signal	RUNNING
5		run over send DAQ_RDY wait for next DCS signal	DAQ_RDY
6	ramp voltages ramping over wait for currents stabilization		DAQ_RDY
3	waiting time over send START		START
4	wait for run to end monitor DAQ run status	update IniFile information data taking ongoing check for KILL signal	RUNNING
5		run over send DAQ_RDY wait for next DCS signal	DAQ_RDY
7	send command STOP	DAQ shuts down	STOP

Table A.1: Inter-process communication cycles in between the webDCS and the DAQ through file string signals.

3265 intends on taking more runs. If so, the software invites the user to set the operating voltages
3266 accordingly to what is necessary and to manual update the configuration file in consequence. This
3267 working mode can be a very first approach before an evolution and has been successfully used by
3268 colleagues from different collaborations.
3269 For a more robust operation, it is recommended to develop a GUI or a web application to interface
3270 the DAQ. Moreover, to limit the amount of manual interventions, and thus the probability to make
3271 mistakes, it is also recommended to add an extra feature into the DAQ by installing the HV Wrapper
3272 library provided by CAEN of which an example of use in a similar DAQ software developed by a
3273 master student of UGent, and called TinyDAQ, is provided on UGent's github. Then, this HV
3274 Wrapper will help you communicating with and give instructions to a CAEN HV powered crate
3275 and can be added into the DAQ at the same level where the communication with the user was made
3276 in DAQ v2.X. In case you are using another kind of power system for your detectors, it is stringly
3277 advised to use HV modules or crates that can be remotely controled via a using C++ libraries.

B

3278

3279

Details on the offline analysis package

3280 The data collected in GIF++ thanks to the DAQ described in Appendix A is difficult to interpret by
3281 a human user that doesn't have a clear idea of the raw data architecture of the ROOT data files. In
3282 order to render the data human readable, a C++ offline analysis tool was designed to provide users
3283 with detector by detector histograms that give a clear overview of the parameters monitored during
3284 the data acquisition [99]. In this appendix, details about this software in the context of GIF++, as of
3285 how the software was written and how it functions will be given.

3286 B.1 GIF++ Offline Analysis file tree

3287 GIF++ Offline Analysis source code is fully available on github at
3288 https://github.com/afagot/GIF_OfflineAnalysis. The software requires ROOT
3289 as non-optionnal dependency as it takes ROOT files in input and write an output ROOT file
3290 containing histograms. To compile the GIF++ Offline Analysis project is compiled with cmake. To
3291 compile, first a build/ directory must be created to compile from there:

```
3292     mkdir build  
3293     cd build  
3294     cmake ..  
3295     make  
3296     make install
```

3293 To clean the directory and create a new build directory, the bash script cleandir.sh can be used:

```
3294     ./cleandir.sh
```

3295 The source code tree is provided below along with comments to give an overview of the files'
3296 content. The different objects created for this project (`Infrastructure`, `Trolley`, `RPC`, `Mapping`,
3297 `RPCHit`, `RPCCluster` and `Inifile`) will be described in details in the following sections.

```
GIFOfflineAnalysis  
└── bin
```



3298 B.2 Usage of the Offline Analysis

3299 In order to use the Offline Analysis tool, it is necessary to know the Scan number and the HV Step
 3300 of the run that needs to be analysed. This information needs to be written in the following format:
 3301 Scan00XXXX_HVY

3302 where XXXX is the scan ID and y is the high voltage step (in case of a high voltage scan, data will be
 3303 taken for several HV steps). This format corresponds to the base name of data files in the database
 3304 of the GIF++ webDCS. Usually, the offline analysis tool is automatically called by the webDCS at
 3305 the end of data taking or by a user from the webDCS panel if an update of the tool was brought.
 3306 Nonetheless, an expert can locally launch the analysis for tests on the GIF++ computer, or a user can
 3307 get the code on his local machine from github and download data from the webDCS for his own

3308 analysis. To launch the code, the following command can be used from the `GIF_OfflineAnalysis`
 3309 folder:

```
3310 bin/offlineanalysis /path/to/Scan00XXXX_HVY
```

3311 where, `/path/to/Scan00XXXX_HVY` refers to the local data files. Then, the offline tool will by itself
 3312 take care of finding all available ROOT data files present in the folder, as listed below:

- 3313 ● `Scan00XXXX_HVY_DAQ.root` containing the TDC data as described in Appendix ?? (events, hit
 3314 and timestamp lists), and
- 3315 ● `Scan00XXXX_HVY_CAEN.root` containing the CAEN mainframe data recorded by the
 3316 monitoring tool webDCS during data taking (HVs and currents of every HV channels). This
 3317 file is created independently of the DAQ.

3318 **B.2.1 Output of the offline tool**

3319 **B.2.1.1 ROOT file**

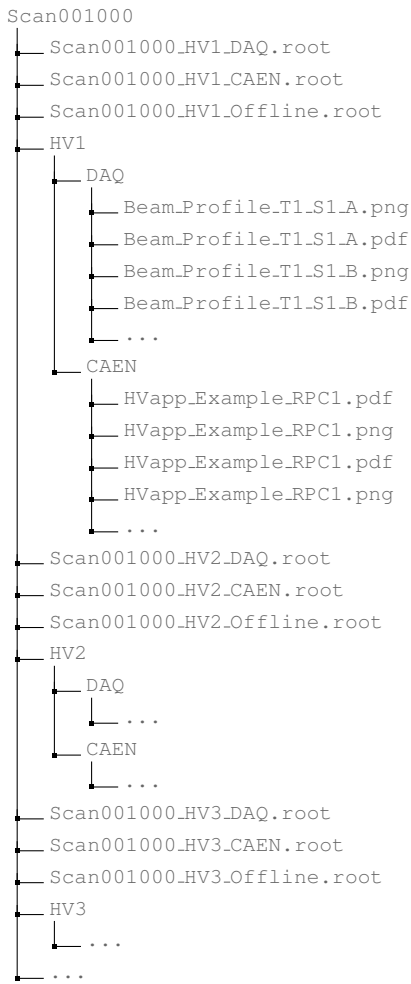
3320 The analysis gives in output ROOT datafiles that are saved into the data folder and called using the
 3321 naming convention `Scan00XXXX_HVY_Offline.root`. Inside those, a list of `TH1` histograms can be
 3322 found. Its size will vary as a function of the number of detectors in the setup as each set of
 3323 histograms is produced detector by detector. For each partition of each chamber, can be found:

- 3324 ● `Time_Profile_Tt_Sc_p` shows the time profile of all recorded events (number of events per
 3325 time bin),
- 3326 ● `Hit_Profile_Tt_Sc_p` shows the hit profile of all recorded events (number of events per
 3327 channel),
- 3328 ● `Hit_Multiplicity_Tt_Sc_p` shows the hit multiplicity (number of hits per event) of all
 3329 recorded events (number of occurrences per multiplicity bin),
- 3330 ● `Strip_Mean_Noise_Tt_Sc_p` shows noise/gamma rate per unit area for each strip in a
 3331 selected time range. After filters are applied on `Time_Profile_Tt_Sc_p`, the filtered version
 3332 of `Hit_Profile_Tt_Sc_p` is normalised to the total integrated time and active detection area
 3333 of a single channel,
- 3334 ● `Strip_Activity_Tt_Sc_p` shows noise/gamma activity for each strip (normalised version of
 3335 previous histogram - strip activity = strip rate / average partition rate),
- 3336 ● `Strip_Homogeneity_Tt_Sc_p` shows the *homogeneity* of a given partition (homogeneity =
 3337 $\exp(-\text{strip rates standard deviation}(\text{strip rates in partition}/\text{average partition rate}))$),
- 3338 ● `mask_Strip_Mean_Noise_Tt_Sc_p` shows noise/gamma rate per unit area for each masked
 3339 strip in a selected time range. Offline, the user can control the noise/gamma rate and decide
 3340 to mask the strips that are judged to be noisy or dead. This is done via the *Masking Tool*
 3341 provided by the webDCS,
- 3342 ● `mask_Strip_Activity_Tt_Sc_p` shows noise/gamma activity per unit area for each masked
 3343 strip with respect to the average rate of active strips,

- 3344 ● NoiseCSize_H_Tt_Sc_p shows noise/gamma cluster size, a cluster being constructed out of
3345 adjacent strips giving a signal at the *same time* (hits within a time window of 25 ns),
- 3346 ● NoiseCMult_H_Tt_Sc_p shows noise/gamma cluster multiplicity (number of reconstructed
3347 clusters per event),
- 3348 ● Chip_Mean_Noise_Tt_Sc_p shows the same information than Strip_Mean_Noise_Tt_Scp
3349 using a different binning (1 chip corresponds to 8 strips),
- 3350 ● Chip_Activity_Tt_Sc_p shows the same information than Strip_Activity_Tt_Scp using
3351 chip binning,
- 3352 ● Chip_Homogeneity_Tt_Sc_p shows the homogeneity of a given partition using chip binning,
- 3353 ● Beam_Profile_Tt_Sc_p shows the estimated beam profile when taking efficiency scan. This
3354 is obtained by filtering Time_Profile_Tt_Sc_p to only consider the muon peak where the
3355 noise/gamma background has been subtracted. The resulting hit profile corresponds to the
3356 beam profile on the detector channels,
- 3357 ● L0_Efficiency_Tt_Sc_p shows the level 0 efficiency that was estimated **without** muon
3358 tracking,
- 3359 ● MuonCSize_H_Tt_Sc_p shows the level 0 muon cluster size that was estimated **without** muon
3360 tracking, and
- 3361 ● MuonCMult_H_Tt_Sc_p shows the level 0 muon cluster multiplicity that was estimated
3362 **without** muon tracking.

3363 In the histogram labels, t stands for the trolley number (1 or 3), c for the chamber slot label in
3364 trolley t and p for the partition label (A, B, C or D depending on the chamber layout) as explained
3365 in Chapter 5.3.

3366 In the context of GIF++, an extra script called by the webDCS is called to extract the histograms
3367 from the ROOT files. The histograms are then stored in PNG and PDF formats into the
3368 corresponding folder (a single folder per HV step, so per ROOT file). the goal is to then display the
3369 histograms on the Data Quality Monitoring (DQM) page of the webDCS in order for the users to
3370 control the quality of the data taking at the end of data taking. An example of histogram
3371 organisation is given bellow:



3372 ***Here can put some screens from the webDCS to show the DQM and the plots available to users.***

3373 **B.2.1.2 CSV files**

3374 Moreover, up to 3 CSV files can be created depending on which ones of the 3 input files were in the
 3375 data folder:

- 3376 • `Offline-Corrupted.csv`, is used to keep track of the amount of data that was corrupted and
 3377 removed from old data format files that don't contain any data quality flag.
- 3378 • `Offline-Current.csv`, contains the summary of the currents and voltages applied on each
 3379 RPC HV channel.
- 3380 • `Offline-L0-EffC1.csv`, is used to write the efficiencies, cluster size and cluster multiplicity
 3381 of efficiency runs. Note that L0 refers here to *Level 0* and means that the results of efficiency
 3382 and clusterization are a first approximation calculated without performing any muon tracking
 3383 in between the different detectors. This offline tool provides the user with a preliminary
 3384 calculation of the efficiency and of the muon event parameters. Another analysis software

3385 especially dedicated to muon tracking is called on selected data to retrieve the results of
 3386 efficiency and muon clusterization using a tracking algorithm to discriminate noise or gamma
 3387 from muons as muons are the only particles that pass through the full setup, leaving hits than
 3388 can be used to reconstruct their tracks.

- 3389 • `Offline-Rate.csv`, is used to write the noise or gamma rates measured in the detector
 3390 readout partitions.

3391 Note that these 4 CSV files are created along with their *headers* (`Offline-[...]-Header.csv`
 3392 containing the names of each data columns) and are automatically merged together when the offline
 3393 analysis tool is called from the webDCS, contrary to the case where the tool is runned locally from
 3394 the terminal as the merging bash script is then not called. Thus, the resulting files, used to make
 3395 official plots, are:

- 3396 • `Corrupted.csv`,
 3397 • `Current.csv`,
 3398 • `L0-EffCl.csv`.
 3399 • `Rate.csv`.

3400 B.3 Analysis inputs and information handling

3401 The usage of the Offline Analysis tool as well as its output have been presented in the previous
 3402 section. It is now important to dig further and start looking at the source code and the inputs
 3403 necessary for the tool to work. Indeed, other than the raw ROOT data files that are analysed, more
 3404 information needs to be imported inside of the program to perform the analysis such as the
 3405 description of the setup inside of GIFT++ at the time of data taking (number of trolleys, of RPCs,
 3406 dimensions of the detectors, etc...) or the mapping that links the TDC channels to the corresponding
 3407 RPC channels in order to translate the TDC information into human readable data. 2 files are used
 3408 to transmit all this information:

- 3409 • `Dimensions.ini`, that provides the necessary setup and RPC information, and
 3410 • `ChannelsMapping.csv`, that gives the link between the TDC and RPC channels as well as the
 3411 *mask* for each channel (masked or not?).

3412 B.3.1 Dimensions file and IniFile parser

3413 This input file, present in every data folder, allows the analysis tool to know of the number of active
 3414 trolleys, the number of active RPCs in those trolleys, and the details about each RPCs such as the
 3415 number of RPC gaps, the number of pseudo-rapidity partitions (for CMS-like prototypes), the
 3416 number of strips per partition or the dimensions. To do so, there are 3 types of groups in the INI file
 3417 architecture. A first general group, appearing only once at the head of the document, gives
 3418 information about the number of active trolleys as well as their IDs, as presented in Source
 3419 Code B.1. For each active trolley, a group similar to Source Code B.2 can be found containing
 3420 information about the number of active detectors in the trolley and their IDs. Each trolley group as
 3421 a `Tt` name format, where `t` is the trolley ID. Finally, for each detector stored in slots of an active

3422 trolley, there is a group providing information about their names and dimensions, as shown in
 3423 Source Code B.3. Each slot group as a `TtSs` name format, where `s` is the slot ID of trolley `t` where
 3424 the active RPC is hosted.

```
[General]
3425 nTrolleys=2
TrolleysID=13
```

3426 *Source Code B.1: Example of [General] group as might be found in Dimensions.ini. In GIF++, only 2 trolleys are available to hold RPCs and place them inside of the bunker for irradiation. The IDs of the trolleys are written in a signle string as "13" and then read character by character by the program.*

```
[T1]
3427 nSlots=4
SlotsID=1234
```

3428 *Source Code B.2: Example of trolley group as might be found in Dimensions.ini. In this example, the file tells that there are 4 detectors placed in the holding slots of the trolley T1 and that their IDs, written as a single string variable, are 1, 2, 3 and 4.*

```
[T1S1]
Name=RE2-2-NPD-BARC-8
Partitions=3
Gaps=3
Gap1=BOT
Gap2=TN
Gap3=TW
3429 AreaGap1=11694.25
AreaGap2=6432
AreaGap3=4582.82
Strips=32
ActiveArea-A=157.8
ActiveArea-B=121.69
ActiveArea-C=93.03
```

3430 *Source Code B.3: Example of slot group as might be found in Dimensions.ini. In this example, the file provides information about a detector named RE2-2-NPD-BARC-8, having 3 pseudo-rapidity readout partitions and stored in slot S1 of trolley T1. This is a CMS RE2-2 type of detector. This information will then be used for example to compute the rate per unit area calculation.*

3431 This information is readout and stored in a C++ object called `IniFile`, that parses the information
 3432 in the INI input file and stores it into a local buffer for later use. This INI parser is the exact same
 3433 one that was previously developped for the GIF++ DAQ and described in Appendix A.5.2.

3434 B.3.2 TDC to RPC link file and Mapping

3435 The same way the INI dimension file information is stored using `map`, the channel mapping and
 3436 mask information is stored and accessed through `map`. First of all, the mapping CSV file is
 3437 organised into 3 columns separated by tabulations (and not by comas, as expected for CSV files as
 3438 it is easier using streams to read tab or space separated data using C++):

```
3439   RPC_channel      TDC_channel      mask
```

3440 using as formatting for each field:

```
3441   TSCCC      TCCC      M
```

3442 TSCCC is a 5-digit integer where τ is the trolley ID, s the slot ID in which the RPC is held insite the
 3443 trolley τ and ccc is the RPC channel number, or *strip* number, that can take values up to
 3444 3-digits depending on the detector,

3445 TCCC is a 4 digit integer where τ is the TDC ID, ccc is the TDC channel number that can take
 3446 values in between 0 and 127, and

3447 M is a 1-digit integer indicating if the channel should be considered ($M = 1$) or discarded ($M = 0$)
 3448 during analysis.

3449 This mapping and masking information is readout and stored thanks to the object `Mapping`,
 3450 presented in Source Code B.4. Similarly to `IniFile` objects, this class has private methods. The
 3451 first one, `Mapping::CheckIfNewLine()` is used to find the newline character '`\n`' or return
 3452 character '`\r`' (depending on which kind of operating system interacted with the file). This is used
 3453 for the simple reason that the masking information has been introduced only during the year 2017
 3454 but the channel mapping files exist since 2015 and the very beginning of data taking at GIP++. This
 3455 means that in the older data folders, before the upgrade, the channel mapping file only had 2
 3456 columns, the RPC channel and the TDC channel. For compatibility reasons, this method helps
 3457 controling the character following the readout of the 2 first fields of a line. In case any end of line
 3458 character is found, no mask information is present in the file and the default $M = 1$ is used. On the
 3459 contrary, if the next character was a tabulation or a space, the mask information is present.
 3460 Once the 3 fields have been readout, the second private method `Mapping::CheckIfTDCCh()` is used
 3461 to control that the TDC channel is an existing TDC channel. Finally, the information is stored into
 3462 3 different maps (`Link`, `ReverseLink` and `Mask`) thanks to the public method `Mapping::Read()`.
 3463 `Link` allows to get the RPC channel by knowing the TDC channel while `ReverseLink` does the
 3464 opposite by returning the TDC channel by knowing the RPC channel. Finally, `Mask` returns the
 3465 mask associated to a given RPC channel.

```
3466 typedef map<UInt, UInt> MappingData;

3467 class Mapping {
3468     private:
3469         bool           CheckIfNewLine(char next);
3470         bool           CheckIfTDCCh(UInt channel);
3471         string        FileName;
3472         MappingData Link;
3473         MappingData ReverseLink;
3474         MappingData Mask;
3475         int            Error;
3476
3477     public:
3478         Mapping();
3479         Mapping(string baseName);
3480         ~Mapping();
3481
3482         void SetFileName(const string filename);
3483         int  Read();
3484         UInt GetLink(UInt tdcchannel);
3485         UInt GetReverse(UInt rpcchannel);
3486         UInt GetMask(UInt rpcchannel);
3487     };
3488 
```

3467 *Source Code B.4: Description of C++ object `Mapping` used as a parser for the channel mapping and mask file.*

3468 B.4 Description of GIF++ setup within the Offline Analysis tool

3469 In the previous section, the tool input files have been discussed. The dimension file information is
 3470 stored in a map hosted by the `IniFile` object. But this information is then used to create a series of
 3471 new objects that helps defining the GIF++ infrastructure directly into the Offline Analysis. Indeed,
 3472 from the `RPC`, to the more general `Infrastructure`, every element of the GIF++ infrastrucutre is
 3473 recreated for each data analysis based on the information provided in input. All this information
 3474 about the infrastructure will be used to assign each hit signal to a specific strip channel of a specific
 3475 detector, and having a specific active area. This way, rate per unit area calculation is possible.

3476 B.4.1 RPC objects

3477 `RPC` objects have been developped to represent physical active detectors in GIF++ at the moment of
 3478 data taking. Thus, there are as many `RPC` objects created during the analysis than there were active
 3479 `RPCs` tested during a run. Each `RPC` hosts the information present in the corresponding INI slot
 3480 group, as shown in B.3, and organises it using a similar architecture. This can be seen from
 3481 Source Code B.5.

3482 To make the object more compact, the lists of gap labels, of gap active areas and strip active areas
 3483 are stored into `vector` dynamical containers. `RPC` objects are always contructed thanks to the
 3484 dimension file information stored into the `IniFILE` and their ID, using the format `TtSs`. Using the
 3485 `RPC` ID, the constructor calls the methods of `IniFILE` to initialise the `RPC`. The other constructors
 3486 are not used but exist in case of need. Finally, some getters have been written to access the different
 3487 private parameters storing the detector information.

```
3488 class RPC{
    private:
        string          name;           //RPC name as in webDCS database
        Uint            nGaps;          //Number of gaps in the RPC
        Uint            nPartitions;    //Number of partitions in the RPC
        Uint            nStrips;         //Number of strips per partition
        vector<string> gaps;          //List of gap labels (BOT, TOP, etc...)
        vector<float>  gapGeo;         //List of gap active areas
        vector<float>  stripGeo;       //List of strip active areas

    public:
        RPC();
        RPC(string ID, IniFILE* geofile);
        RPC(const RPC& other);
        ~RPC();
        RPC& operator=(const RPC& other);

        string GetName();
        Uint  GetNGaps();
        Uint  GetNPartitions();
        Uint  GetNStrips();
        string GetGap(Uint g);
        float GetGapGeo(Uint g);
        float GetStripGeo(Uint p);
    };
}
```

3489 *Source Code B.5: Description of C++ objects `RPC` that describe each active detectors used during data taking.*

3490 **B.4.2 Trolley objects**

3491 Trolley objects have been developped to represent physical active trolleys in GIFT++ at the moment
 3492 of data taking. Thus, there are as many trolley objects created during the analysis than there were
 3493 active trolleys hosting tested RPCs during a run. Each Trolley hosts the information present in the
 3494 corresponding INI trolley group, as shown in B.2, and organises it using a similar architecture. In
 3495 addition to the information hosted in the INI file, these object have a dynamical container of `RPC`
 3496 objects, representing the active detectors the active trolley was hosting at the time of data taking.
 3497 This can been seen from Source Code B.6.

3498 Trolley objects are always contructed thanks to the dimension file information stored into the
 3499 `IniFILE` and their ID, using the format `Tt`. Using the Trolley ID, the constructor calls the methods
 3500 of `IniFile` to initialise the Trolley. Retrieving the information of the RPC IDs via `SlotsID`, a new
 3501 `RPC` is constructed and added to the container `RPCs` for each character in the ID `string`. The other
 3502 constructors are not used but exist in case of need. Finally, some getters have been written to access
 3503 the different private parameters storing the trolley and detectors information.

```
class Trolley{
    private:
        Uint           nSlots; //Number of active RPCs in the considered trolley
        string         SlotsID; //Active RPC IDs written into a string
        vector<RPC*> RPCs;   //List of active RPCs

    public:
        //Constructors, destructor and operator =
        Trolley();
        Trolley(string ID, IniFile* geofile);
        Trolley(const Trolley& other);
        ~Trolley();
        Trolley& operator=(const Trolley& other);

        //Get GIFTrolley members
        Uint   GetNSlots();
        string GetSlotsID();
        Uint   GetSlotID(Uint s);

        //Manage RPC list
        RPC*   GetRPC(Uint r);
        void   DeleteRPC(Uint r);

        //Methods to get members of RPC objects stored in RPCs
        string GetName(Uint r);
        Uint   GetNGaps(Uint r);
        Uint   GetNPartitions(Uint r);
        Uint   GetNStrips(Uint r);
        string GetGap(Uint r, Uint g);
        float  GetGapGeo(Uint r, Uint g);
        float  GetStripGeo(Uint r, Uint p);
    };
}
```

3505 *Source Code B.6: Description of C++ objects Trolley that describe each active trolley used during data taking.*

3506 B.4.3 Infrastructure object

3507 The `Infrastructure` object has been developped to represent the Gif++ bunker area dedicated to
 3508 CMS RPC experiments. With this very specific object, all the information about the CMS RPC
 3509 setup within Gif++ at the moment of data taking is stored. It hosts the information present in the
 3510 corresponding INI general group, as shown in B.1, and organises it using a similar architecture. In
 3511 addition to the information hosted in the INI file, this object have a dynamical container of `Trolley`
 3512 objects, representing the active tolleys in Gif++ area. This can be seen from Source Code B.7.
 3513 The `Infrastructure` object is always contructed thanks to the dimension file information stored
 3514 into the `IniFile`. Retrieving the information of the trolley IDs via `TrolleysID`, a new `Trolley` is
 3515 constructed and added to the container `Trolleys` for each character in the ID string. By extension,
 3516 it is easy to understand that the process described in Section B.4.2 for the construction of RPCs
 3517 takes place when a trolley is constructed. The other constructors are not used but exist in case of
 3518 need. Finally, some getters have been written to access the different private parameters storing the
 3519 infrastructure, tolleys and detectors information.

```
3519
  class Infrastructure {
    private:
      Uint           nTrolleys; //Number of active Trolleys in the run
      string         TrolleysID; //Active trolley IDs written into a string
      vector<Trolley*> Trolleys; //List of active Trolleys (struct)

    public:
      //Constructors and destructor
      Infrastructure();
      Infrastructure(IniFile* geofile);
      Infrastructure(const Infrastructure& other);
      ~Infrastructure();
      Infrastructure& operator=(const Infrastructure& other);

      //Get Infrastructure members
      Uint   GetNTrolleys();
      string GetTrolleysID();
      Uint   GetTrolleyID(Uint t);

      //Manage Trolleys
      Trolley* GetTrolley(Uint t);
      void     DeleteTrolley(Uint t);

      //Methods to get members of GifTrolley objects stored in Trolleys
      Uint   GetNSlots(Uint t);
      string GetSlotsID(Uint t);
      Uint   GetSlotID(Uint t, Uint s);
      RPC*  GetRPC(Uint t, Uint r);

      //Methods to get members of RPC objects stored in RPCs
      string GetName(Uint t, Uint r);
      Uint   GetNGaps(Uint t, Uint r);
      Uint   GetNPartitions(Uint t, Uint r);
      Uint   GetNStrips(Uint t, Uint r);
      string GetGap(Uint t, Uint r, Uint g);
      float  GetGapGeo(Uint t, Uint r, Uint g);
      float  GetStripGeo(Uint t, Uint r, Uint p);
  };

```

3521 *Source Code B.7: Description of C++ object `Infrastructure` that contains the full information about CMS
 RPC experiment in Gif++.*

3522 B.5 Handeling of data

3523 As discussed in Appendix A.4.2, the raw data as a `TTree` architecture where every entry is related to
 3524 a trigger signal provided by a muon or a random pulse, whether the goal of the data taking was to
 3525 measure the performance of the detector or the noise/gamma background respectively. Each of
 3526 these entries, referred also as events, contain a more or less full list of hits in the TDC channels to
 3527 which the detectors are connected. To this list of hits corresponds a list of time stamps, marking the
 3528 arrival of the hits within the TDC channel.

3529 The infrastructure of the CMS RPC experiment within `GIF++` being defined, combining the
 3530 information about the raw data with the information provided by both the mapping/mask file and
 3531 the dimension file allows to build new physical objects that will help in computing efficiency or
 3532 rates.

3533 B.5.1 RPC hits

3534 The raw data stored in the ROOT file as output of the `GIF++` DAQ, is readout by the analysis tool
 3535 using the structure `RAWData` presented in Source Code B.9 that differs from the structure presented
 3536 in Appendix A.4.2 as it is not meant to hold all of the data contained in the ROOT file. In this
 3537 sense, this structure is in the case of the offline analysis tool not a dynamical object and will only be
 3538 storing a single event contained in a single entry of the `TTree`.

```
3539 class RPCHit {
  private:
    Uint Channel;      //RPC channel according to mapping (5 digits)
    Uint Trolley;      //0, 1 or 3 (1st digit of the RPC channel)
    Uint Station;      //Slot where is held the RPC in Trolley (2nd digit)
    Uint Strip;        //Physical RPC strip where the hit occured (last 3
    → digits)
    Uint Partition;   //Readout partition along eta segmentation
    float TimeStamp;  //Time stamp of the arrival in TDC

  public:
    //Constructors, destructor & operator =
    RPCHit();
    RPCHit(Uint channel, float time, Infrastructure* Infra);
    RPCHit(const RPCHit& other);
    ~RPCHit();
    RPCHit& operator=(const RPCHit& other);

    //Get RPCHit members
    Uint GetChannel();
    Uint GetTrolley();
    Uint GetStation();
    Uint GetStrip();
    Uint GetPartition();
    float GetTime();
};

typedef vector<RPCHit> HitList;
typedef struct GIFHitList { HitList rpc[NTROLLEYS][NSLOTS][NPARTITIONS]; } → GIFHitList;

bool SortHitbyStrip(RPCHit h1, RPCHit h2);
bool SortHitbyTime(RPCHit h1, RPCHit h2);
```

```
3541 struct RAWData{
    int iEvent; //Event i
    int TDCNHits; //Number of hits in event i
    int QFlag; //Quality flag list (1 flag digit per TDC)
    vector<UInt> *TDCCh; //List of channels giving hits per event
    vector<float> *TDCTS; //List of the corresponding time stamps
};
```

Source Code B.9: Description of C++ structure RAWData.

3543 Each member of the structure is then linked to the corresponding branch of the ROOT data tree, as
3544 shown in the example of Source Code B.10, and using the method `GetEntry(int i)` of the ROOT
3545 class `TTree` will update the state of the members of `RAWData`.

```
3546 TTree* dataTree = (TTree*)dataFile.Get("RAWData");
RAWData data;

dataTree->SetBranchAddress("EventNumber", &data.iEvent);
dataTree->SetBranchAddress("number_of_hits", &data.TDCNHits);
dataTree->SetBranchAddress("Quality_flag", &data.QFlag);
dataTree->SetBranchAddress("TDC_channel", &data.TDCCh);
dataTree->SetBranchAddress("TDC_TimeStamp", &data.TDCTS);
```

Source Code B.10: Example of link in between RAWData and TTree.

The data is then analysed entry by entry and to each element of the TDC channel list, a `RPCHit` is constructed by linking each TDC channel to the corresponding RPC channel thanks to the `Mapping` object. The information carried by the RPC channel format allows to easily retrieve the trolley and slot from which the hit was recorded (see section B.3.2). Using these 2 values, the readout partition can be found by knowing the strip channel and comparing it with the number of partitions and strips per partition stored into the `Infrastructure` object.

Thus `RPCHit` objects are then stored into 3D dynamical list called `GIFHitList` (Source Code B.9) where the 3 dimensions refer to the 3 layers of the readout in `GIF++` : in the bunker there are *trolleys* (`T`) holding detectors in *slots* (`S`) and each detector readout is divided into 1 or more pseudo-rapidity *partitions* (`P`). Using these 3 information allows to assign an address to each readout partition and this address will point to a specific hit list.

3559 B.5.2 Clusters of hits

All the hits contained in the ROOT file have been sorted into the different hit lists through the `GIFHitList`. At this point, it is possible to start looking for clusters. A cluster is a group of adjacent strips getting hits within a time window of 25 ns. These strips are then assumed to be part of the same physical avalanche signal generated by a muon passing through the chamber or by the interaction of a gamma stopping into the electrodes of the RPCs.

To keep the cluster information, `RPCCluster` objects have been defined as shown in Source Code B.11. Using the information of each individual `RPCHit` taken out of the hit list, it stores the cluster size (number of adjacent strips composing the cluster), the first and last hit, the center for spatial reconstruction and finally the start and stop time stamps as well as te time spread in between the first and last hit.

```

3570
class RPCCluster{
    private:
        Uint ClusterSize; //Size of cluster #ID
        Uint FirstStrip; //First strip of cluster #ID
        Uint LastStrip; //Last strip of cluster #ID
        float Center; //Center of cluster #ID ((first+last)/2)
        float StartStamp; //Time stamp of the earliest hit of cluster #ID
        float StopStamp; //Time stamp of the latest hit of cluster #ID
        float TimeSpread; //Time difference between earliest and latest hits
                           //of cluster #ID

    public:
        //Constructors, destructor & operator =
        RPCCluster();
        RPCCluster(HitList List, Uint cID, Uint cSize, Uint first, Uint firstID);
        RPCCluster(const RPCCluster& other);
        ~RPCCluster();
        RPCCluster& operator=(const RPCCluster& other);

        //Get Cluster members
        Uint GetID();
        Uint GetSize();
        Uint GetFirstStrip();
        Uint GetLastStrip();
        float GetCenter();
        float GetStart();
        float GetStop();
        float GetSpread();
    };

    typedef vector<RPCCluster> ClusterList;

    //Other functions to build cluster lists out of hit lists
    void BuildClusters(HitList &cluster, ClusterList &clusterList);
    void Clusterization(HitList &hits, TH1 *hcSize, TH1 *hcMult);
}

```

Source Code B.11: Description of C++ object cluster.

To investigate the hit list of a given detector partition, the function `Clusterization()` defined in `include/Cluster.h` needs the hits in the list to be time sorted. This is achieved by calling function `sort()` of library `<algorithm>` using the comparator `SortHitbyTime(RPCHit h1, RPCHit h2)` defined in `include/RPCHit.h` that returns `true` if the time stamp of hit `h1` is lower than that of `h2`. A first isolation of strips is made only based on time information. All the hits within the 25 ns window are taken separately from the rest. Then, this sub-list of hits is sorted this time by ascending strip number, using this time the comparator `SortHitbyStrip(RPCHit h1, RPCHit h2)`. Finally, the groups of adjacent strips are used to construct `RPCCluster` objects that are then stored in a temporary list of clusters that is at the end of the process used to know how many clusters were reconstructed and to fill their sizes into an histogram that will allows to know the mean size of muon or gamma clusters.

3583 B.6 DAQ data Analysis

All the ingredients to analyse GIF++ data have been defined. This section will focus on the different part of the analysis performed on the data, from determining the type of data the tool is dealing with to calculating the rate in each detector or reconstructing muon or gamma clusters.

3587 B.6.1 Determination of the run type

3588 In GIF++, both the performance of the detectors in detecting muons in an irradiated environment
 3589 and the gamma background can be independantly measured. These corresponds to different run
 3590 types and thus, to different TDC settings giving different data to look at.
 3591 In the case of performance measurements, the trigger for data taking is provided by the coincidence
 3592 of several scintillators when muons from the beam passing through the area are detected. Data is
 3593 collected in a 600 ns wide window around the arrival of muons in the RPCs. The expected time
 3594 distribution of hits is shown in Figure B.1a. The muon peak is clearly visible in the center of the
 3595 distribution and is to be extracted from the gamma background that composes the flat part of the
 3596 distribution.
 3597 On the other hand, gamma background or noise measurements are focussed on the non muon
 3598 related physics and the trigger needs to be independant from the muons to give a good
 3599 measurement of the gamma/noise distribution as seen by the detectors. The trigger is then provided
 3600 by a pulse generator at a frequency of 300 Hz whose pulse is not likely to be on time with a muon.
 3601 In order to increase the integrated time without increasing the acquisition time too much, the width
 3602 of the acquisition windows are increased to 10 μ s. The time distribution of the hits is expected to be
 3603 flat, as shown by Figure B.1b.

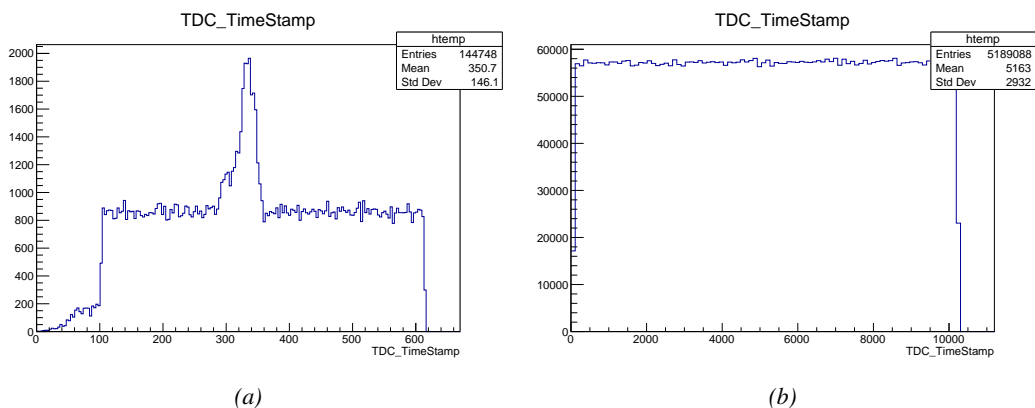


Figure B.1: Example of expected hit time distributions in the cases of efficiency (Figure B.1a) and noise/gamma rate per unit area (Figure B.1b) measurements as extracted from the raw ROOT files. The unit along the x-axis corresponds to ns. The fact that "the" muon peak is not well defined in Figure B.1a is due to the contribution of all the RPCs being tested at the same time that don't necessarily have the same signal arrival time. Each individual peak can have an offset with the ones of other detectors. The inconsistancy in the first 100 ns of both time distributions is an artefact of the TDCs and are systematically rejected during the analysis.

3604 The ROOT files include a TTree called RunParameters containing, among other things, the
 3605 information related to the type of run. The run type can then be accessed as described by Source
 3606 Code B.12 and the function IsEfficiencyRun() is then used to determine if the run file is an
 3607 efficiency run or, on the contrary, another type of run (noise or gamma measurement).

```
3608 TTree* RunParameters = (TTree*)dataFile.Get("RunParameters");
TString* RunType = new TString();
RunParameters->SetBranchAddress("RunType", &RunType);
RunParameters->GetEntry(0);
```

3609 *Source Code B.12: Access to the run type contained in TTree* RunParameters.*

3610 Finally, the data files will have a slightly different content whether it was collected before or after
 3611 October 2017 and the upgrade of the DAQ software that brought a new information into the ROOT
 3612 output. This is discussed in Appendix A.4.3 and implies that the analysis will differ a little
 3613 depending on the data format. Indeed, as no information on the data quality is stored, in older data
 3614 files, the corrections for missing events has to be done at the end of the analysis. The information
 3615 about the type of data format is stored in the variable `bool isNewFormat` by checking the list of
 3616 branches contained in the data tree via the methods `TTree::GetListOfBranches()` and
 3617 `TCollection::Contains()`.

3618 B.6.2 Beam time window calculation for efficiency runs

3619 Knowing the run type is important first of all to know the width of the acquisition window to be
 3620 used for the rate calculation and finally to be able to seek for muons. Indeed, the peak that appears
 3621 in the time distribution for each detectors is then fitted to extract the most probable time window in
 3622 which the tool should look for muon hits. The data outside of this time window is then used to
 3623 evaluate the noise or gamma background the detector was subjected to during the data taking.
 3624 Computing the position of the peak is done calling the function `SetBeamWindow()` defined in file
 3625 `src/RPCHit.cc` that loops a first time on the data. The data is first sorted in a 3D array of 1D
 3626 histograms (`GIFH1Array`, see `include/types.h`). Then the location of the highest bin is determined
 3627 using `TH1::GetMaximumBin()` and is used to define a window in which a gaussian fit will be applied
 3628 to compute the peak width. This window is a 80 ns defined by Formula B.1 around the central bin.

$$t_{center}(ns) = bin \times width_{bin}(ns) \quad (B.1a)$$

$$[t_{low}; t_{high}] = [t_{center} - 40; t_{center} + 40] \quad (B.1b)$$

3629 Before the fit is performed, the average number of noise/gamma hits per bin is evaluated using the
 3630 data outside of the fit window. Excluding the first 100 ns, the average number of hits per bin due to
 3631 the noise or gamma is defined by Formula B.2 after extracting the amount of hits in the time
 3632 windows $[100; t_{low}]$ and $[t_{high}; 600]$ thanks to the method `TH1::Integral()`. This average number
 3633 of hits is then subtracted to every bin of the 1D histogram, in order to *clean* it from the noise or
 3634 gamma contribution as much as possible to improve the fit quality. Bins where $\langle n_{hits} \rangle$ is greater
 3635 than the actual bin content are set to 0.

$$\Delta t_{noise}(ns) = 600 \overbrace{-t_{high} + t_{low}}^{-80ns} - 100 = 420ns \quad (B.2a)$$

$$\langle n_{hits} \rangle = width_{bin}(ns) \times \frac{\sum_{t=100}^{t_{low}} + \sum_{t=t_{high}}^{600}}{\Delta t_{noise}(ns)} \quad (B.2b)$$

3636 Finally, the fit parameters are extracted and saved for each detector in 3D arrays of `float`
 3637 (`muonPeak`, see `include/types.h`), a first one for the mean arrival time of the muons, `PeakTime`,
 3638 and a second one for the width of the peak, `PeakWidth`. The width is defined as 6σ of the gaussian
 3639 fit. The same settings are applied to every partitions of the same detector. To determine which one
 3640 of the detector's partitions is directly illuminated by the beam, the peak height of each partition is
 3641 compared and the highest one is then used to define the peak settings.

3642 B.6.3 Data loop and histogram filling

3643 3D arrays of histogram are created to store the data and display it on the DQM of GIFT++ webDCS
 3644 for the use of shifters. These histograms, presented in section B.2.1.1, are filled while looping on
 3645 the data. Before starting the analysis loop, it is necessary to control the entry quality for the new file
 3646 formats featuring QFlag. If the QFlag value for this entry shows that 1 TDC or more have a
 3647 CORRUPTED flag, then this event is discarded. The loss of statistics is low enough to be neglected.
 3648 QFlag is controlled using the function IsCorruptedEvent() defined in src/utils.cc. As explained
 3649 in Appendix A.4.3, each digit of this integer represent a TDC flag that can be 1 or 2. Each 2 is the
 3650 sign of a CORRUPTED state. Then, the data is accessed entry by entry in the ROOT TTree using
 3651 RAWData and each hit in the hit list is assigned to a detector channel and saved in the corresponding
 3652 histograms. In the first part of the analysis, in which the loop over the ROOT file's content is
 3653 performed, the different steps are:

3654 **1- RPC channel assignment and control:** a check is done on the RPC channel extracted thanks
 3655 to the mapping via the method Mapping::GetLink(). If the channel is not initialised and is 0, or if
 3656 the TDC channel was greater than 5127, the hit is discarded. This means there was a problem in the
 3657 mapping. Often a mapping problem leads to the crash of the offline tool.

3658 **2- Creation of a RPCHit object:** to easily get the trolley, slot and partition in which the hit has
 3659 been assigned, this object is particularly helpful.

3660 **3- General histograms are filled:** the hit is filled into the time distribution and the general hit
 3661 distribution histograms, and if the arrival time is within the first 100 ns, it is discarded and nothing
 3662 else happens and the loop proceeds with the next hit in the list.

3663 **4- Multiplicity counter:** the hit multiplicity counter of the corresponding detectors incremented.

3664 **5-a- Efficiency runs - Is the hit within the peak window? :** if the peak is contained in the peak
 3665 window previously defined in section B.6.2, the hit is filled into the beam hit profile histogram of
 3666 the corresponding chamber, added into the list of muon hits and increments the counter of *in time*
 3667 hits. The term *in time* here refers to the hits that are likely to be muons by arriving in the expected
 3668 time window. If the hit is outside of the peak window, it is filled into the noise profile histogram of
 3669 the corresponding detector, added into the list of noise/gamma hits and increments the counter of
 3670 noise/gamma hits.

3671 **5-b- Noise/gamma rate runs - Noise histograms are filled:** the hit is filled into the noise profile
 3672 histogram of the corresponding detector, added into the list of noise/gamma hits and increments the
 3673 counter of noise/gamma hits.

3674 After the loop on the hit list of the entry is over, the next step is to clusterize the 3D lists filled in
 3675 the previous steps. A 3D loop is then started over the active trolley, slot and RPC partitions to
 3676 access these objects. Each NoiseHitList and MuonHitList, in case of efficiency run, are
 3677 clusterized as described in section B.5.2. There corresponding cluster size and multiplicity
 3678 histograms are filled at the end of the clustering process. Then, the efficiency histogram is filled in
 3679 case of efficiency run. The selection is simply made by checking whether the RPC detected signals
 3680 in the peak window during this event. Nevertheless, it is useful to highlight that at this level, it is

3681 not possible yet to discriminate in between a muon hit and noise or gamma hit. Thus, MuonCSIZE_H,
 3682 MuonCMult_H and Efficiency0_H are subjected to noise and gamma contamination. This
 3683 contamination will be estimated and corrected at the moment the results will be written into output
 3684 CSV files. Finally, the loop ends on the filling of the general hit multiplicity histogram.

3685 **B.6.4 Results calculation**

3686 As mentioned in section B.2.1, the analysis of DAQ data provides the user with 3 CSV files and a
 3687 ROOT file associated to each and every ROOT data file. The fourth CSV file is provided by the
 3688 extraction of the CEAN main frame data monitored during data tacking and will be discussed later.
 3689 After looping on the data in the previous part of the analysis macro, the output files are created and
 3690 a 3D loop on each RPC readout partitions is started to extract the histograms parameters and
 3691 compute the final results.

3692 **B.6.4.1 Rate normalisation**

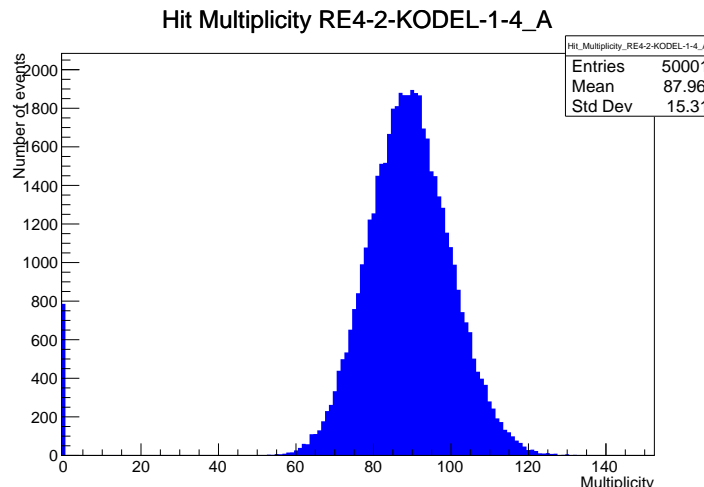


Figure B.2: The effect of the quality flag is explained by presenting the reconstructed hit multiplicity of a data file without Quality_flag. The artificial high content of bin 0 is the effect of corrupted data.

3693 To analyse old data format files, not containing any quality flag, it is needed to estimate the amount
 3694 of corrupted data via a fit as the corrupted data will always fill events with a fake "0 multiplicity".
 3695 Indeed, as no hits were stored in the DAQ ROOT files, these events artificially contribute to fill the
 3696 bin corresponding to a null multiplicity, as shown in Figure B.2. In the case the mean of the hit
 3697 multiplicity distribution is high, the contribution of the corrupted data can easily be evaluated for
 3698 later correction by comparing the level of the bin at multiplicity 0 and of a skew fit curve that
 3699 should indicate a value consistent with 0. A skew fit has been chosen over a Poisson fit as it was
 3700 giving better results for lower mean multiplicity values. Nevertheless, for low irradiation cases, as
 3701 explained in Appendix A.4.3, the hit multiplicity distribution mean is, on the contrary, rather small
 3702 and the probability to record events without hits can't be considered small anymore, leading to a
 3703 difficult and non-reliable estimation of the corruption. As can be seen in Source Code B.13,
 3704 conditions have been applied to prevent bad fits and wrong corruption estimation in cases where :

- 3705 ● The difference in between the data for multiplicity 1 and the corresponding fit value should
3706 be lower than 1% of the total amount of data : $\frac{|n_{m=1} - sk(1)|}{N_{tot}} < 0.01$ where $n_{m=1}$ is the
3707 number of entries with multiplicity 1, $sk(1)$ the value of the skew fit, as defined by
3708 Formula 5.3, for multiplicity 1 and N_{tot} the total number of entries.

- 3709 ● The amount of data contained in the multiplicity 0 bin should not exceed 40% : $\frac{n_{m=0}}{N_{tot}} \leq 0.4$
3710 where $n_{m=0}$ is the number of entries with multiplicity 0. This number has been determined
3711 to be the maximum to be able to separate the excess of data due to corruption from the hit
3712 multiplicity distribution.

3713 Those 2 conditions need to be fulfilled to estimate the corruption of old data format files. If the fit
3714 was successful, the level of corruption is written in `Offline-Corrupted.csv` and the number of
3715 corrupted entries, refered as the integer `nEmptyEvent`, is subtracted from the total number of entries
3716 when the rate normalisation factor is computed as explicitated in Source Code B.13. Note that for
3717 new data format files, the number of corrupted entries being set to 0, the definition of `rate_norm`
3718 stays valid.

```

if(!isNewFormat){
    TF1* GaussFit = new TF1("gaussfit","[0]*exp(-0.5*((x-[1])/[2])**2)",0,Xmax);
    GaussFit->SetParameter(0,100);
    GaussFit->SetParameter(1,10);
    GaussFit->SetParameter(2,1);
    HitMultiplicity_H.rpc[T][S][p]->Fit(GaussFit,"LIQR","");
    HitMultiplicity_H.rpc[T][S][p]->Fit(GaussFit,"LIQR","");
}

TF1* SkewFit = new TF1("skewfit","[0]*exp(-0.5*((x-[1])/[2])**2) / (1 +
→ exp(-[3]*(x-[4])))",0,Xmax);
SkewFit->SetParameter(0,GaussFit->GetParameter(0));
SkewFit->SetParameter(1,GaussFit->GetParameter(1));
SkewFit->SetParameter(2,GaussFit->GetParameter(2));
SkewFit->SetParameter(3,1);
SkewFit->SetParameter(4,1);
HitMultiplicity_H.rpc[T][S][p]->Fit(SkewFit,"LIQR","");
HitMultiplicity_H.rpc[T][S][p]->Fit(SkewFit,"LIQR","");
double fitValue = SkewFit->Eval(1,0,0,0);
double dataValue = (double)HitMultiplicity_H.rpc[T][S][p]->GetBinContent(2);
double difference = TMath::Abs(dataValue - fitValue);
double fitTOdataVSentries_ratio = difference / (double)nEntries;
bool isFitGOOD = fitTOdataVSentries_ratio < 0.01;

3719 double nSinglehit = (double)HitMultiplicity_H.rpc[T][S][p]->GetBinContent(1);
double lowMultRatio = nSinglehit / (double)nEntries;
bool isMultLOW = lowMultRatio > 0.4;

if(isFitGOOD && !isMultLOW){
    nEmptyEvent = HitMultiplicity_H.rpc[T][S][p]->GetBinContent(1);
    nPhysics = (int)SkewFit->Eval(0,0,0,0);
    if(nPhysics < nEmptyEvent)
        nEmptyEvent = nEmptyEvent-nPhysics;
}
}

double corrupt_ratio = 100.*(double)nEmptyEvent / (double)nEntries;
outputCorrCSV << corrupt_ratio << '\t';

float rate_norm = 0.;
float stripArea = GIFIInfra->GetStripGeo(tr,sl,p);

if(IsEfficiencyRun(RunType)){
    float noiseWindow = BMTDCWINDOW - TIMEREJECT - 2*PeakWidth.rpc[T][S][p];
    rate_norm = (nEntries-nEmptyEvent)*noiseWindow*1e-9*stripArea;
} else
    rate_norm = (nEntries-nEmptyEvent)*RDMNOISEWDW*1e-9*stripArea;

```

Source Code B.13: Definition of the rate normalisation variable. It takes into account the number of non corrupted entries and the time window used for noise calculation, to estimate the total integrated time, and the strip active area to express the result as rate per unit area.

3721 B.6.4.2 Rate and activity

3722 At this point, the strip rate histograms, `StripNoiseProfile_H.rpc[T][S][p]`, only contain an
 3723 information about the total number of noise or rate hits each channel received during the data
 3724 taking. As described in Source Code B.14, a loop on the strip channels will be used to normalise
 3725 the content of the rate distribution histogram for each detector partitions. The initial number of hits
 3726 recorded for a given bin will be extracted and 2 values will be computed:

- 3727 ● the strip rate, defined as the number of hits recorded in the bin normalised like described in
 3728 the previous section, using the variable `rate_norm`, and

- 3729 ● the strip activity, defined as the number of hits recorded in the bin normalised to the average
 3730 number of hits per bin contained in the partition histogram, using the variable `averageNhit`.
 3731 This value provides an information on the homogeneity of the detector response to the
 3732 gamma background or of the detector noise. An activity of 1 corresponds to an average
 3733 response. Above 1, the channel is more active than the average and bellow 1, the channel is
 3734 less active.

```

int nNoise = StripNoiseProfile_H.rpc[T][S][p]->GetEntries();
float averageNhit = (nNoise>0) ? (float)(nNoise/nStripsPart) : 1.;

for(Uint st = 1; st <= nStripsPart; st++){
    float stripRate =
        StripNoiseProfile_H.rpc[T][S][p]->GetBinContent(st)/rate_norm;
    float stripAct =
        StripNoiseProfile_H.rpc[T][S][p]->GetBinContent(st)/averageNhit;

    StripNoiseProfile_H.rpc[T][S][p]->SetBinContent(st,stripRate);
    StripActivity_H.rpc[T][S][p]->SetBinContent(st,stripAct);
}

```

3736 *Source Code B.14: Description of the loop that allows to set the content of each strip rate and strip activity
 channel for each detector partition.*

3737 On each detector partitions, which are readout by a single FEE, all the channels are not processed
 3738 by the same chip. Each chip can give a different noise response and thus, histograms using a chip
 3739 binning are used to investigate chip related noise behaviours. The average values of the strip rate or
 3740 activity grouped into a given chip are extracted using the using the function `GetChipBin()` and
 3741 stored in dedicated histograms as described in Source Codes B.15 and B.16 respectively.

```

float GetChipBin(TH1* H, Uint chip){
    Uint start = 1 + chip*NSTRIPSCHIP;
    int nActive = NSTRIPSCHIP;
    float mean = 0.;

    for(Uint b = start; b <= (chip+1)*NSTRIPSCHIP; b++){
        float value = H->GetBinContent(b);
        mean += value;
        if(value == 0.) nActive--;
    }

    if(nActive != 0) mean /= (float)nActive;
    else mean = 0.;

    return mean;
}

```

3743 *Source Code B.15: Function used to compute the content of a bin for an histogram using chip binning.*

```

3744     for(UInt ch = 0; ch < (nStripsPart/NSTRIPSCHIP); ch++) {
      ChipMeanNoiseProf_H.rpc[T][S][p]->
          SetBinContent(ch+1,GetChipBin(StripNoiseProfile_H.rpc[T][S][p],ch));
      ChipActivity_H.rpc[T][S][p]->
          SetBinContent(ch+1,GetChipBin(StripActivity_H.rpc[T][S][p],ch));
}

```

Source Code B.16: Description of the loop that allows to set the content of each chip rate and chip activity bins for each detector partition knowing the information contained in the corresponding strip distribution histograms.

The activity variable is used to evaluate the homogeneity of the detector response to background or of the detector noise. The homogeneity h_p of each detector partition can be evaluated using the formula $h_p = \exp(-\sigma_p^R / \langle R \rangle_p)$, where $\langle R \rangle_p$ is the partition mean rate and σ_p^R is the rate standard deviation calculated over the partition channels. The more homogeneously the rates are distributed and the smaller will σ_p^R be, and the closer to 1 will h_p get. On the contrary, if the standard deviation of the channel's rates is large, h_p will rapidly get to 0. This value is saved into histograms as shown in Source Code B.17 and could in the future be used to monitor through time, once extracted, the evolution of every partition homogeneity. This could be of great help to understand the apparition of eventual hot spots due to ageing of the chambers subjected to high radiation levels. The monitored homogeneity information could then be combined with a monitoring of the activity of each individual channel in order to have a finer information. Monitoring tools have been suggested and need to be developed for this purpose.

```

3758     float MeanPartSDev = GetTH1StdDev(StripNoiseProfile_H.rpc[T][S][p]);
      float strip_homog = (MeanPartRate==0)
          ? 0.
          : exp(-MeanPartSDev/MeanPartRate);
      StripHomogeneity_H.rpc[T][S][p]->Fill("exp -#left (#frac{\#sigma_{Strip}
          → Rate}){(\#mu_{Strip Rate})}\#right)",strip_homog);
      StripHomogeneity_H.rpc[T][S][p]->GetYaxis()->SetRangeUser(0.,1.);

      float ChipStDevMean = GetTH1StdDev(ChipMeanNoiseProf_H.rpc[T][S][p]);
      float chip_homog = (MeanPartRate==0)
          ? 0.
          : exp(-ChipStDevMean/MeanPartRate);
      ChipHomogeneity_H.rpc[T][S][p]->Fill("exp -#left (#frac{\#sigma_{Chip}
          → Rate}){(\#mu_{Chip Rate})}\#right)",chip_homog);
      ChipHomogeneity_H.rpc[T][S][p]->GetYaxis()->SetRangeUser(0.,1.);

```

Source Code B.17: Storage of the homogeneity into dedicated histograms.

3760 B.6.4.3 Strip masking tool

The offline tool is automatically called at the end of each data taking to analyse the data and offer the shifter DQM histograms to control the data quality. After the histograms have been published online in the DQM page, the shifter can decide to mask noisy or dead channels that will contribute to bias the final rate calculation by editing the mask column of `ChannelsMapping.csv` as can be seen in Figure B.3.

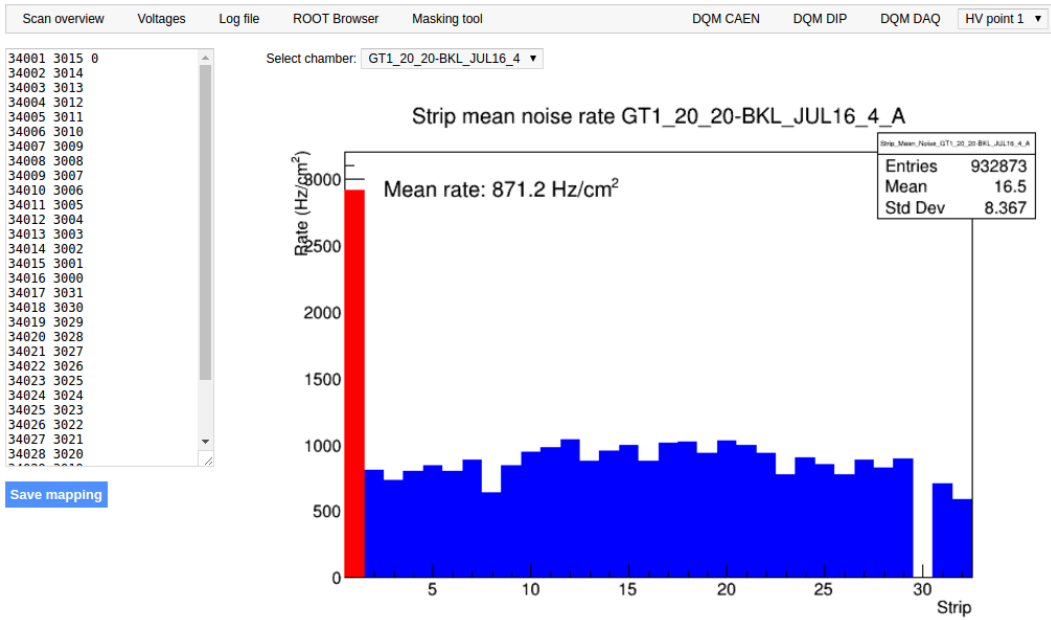


Figure B.3: Display of the masking tool page on the webDCS. The window on the left allows the shifter to edit ChannelsMapping.csv. To mask a channel, it only is needed to set the 3rd field corresponding to the strip to mask to 0. It is not necessary for older mapping file formats to add a 1 for each strip that is not masked as the code is versatile and the default behaviour is to consider missing mask fields as active strips. The effect of the mask is directly visible for noisy channels as the corresponding bin turns red. The global effect of masking strips will be an update of the rate value showed on the histogram that will take into consideration the rejected channels.

3766 From the code point of view, the function `GetTH1Mean()` is used to retrieve the mean rate partition
 3767 by partition after the rates have been calculated strip by strip and filled into the histograms
 3768 `StripNoiseProfile_H.rpc[T][S][p]`, as described through Source Code B.18.
 3769 Once the mask for each rejected channel has been updated, the shifter can manually run the offline
 3770 tool again to update the DQM plots, now including the masked strips, as well the rate results
 3771 written in the output CSV file `Offline-Rate.csv`. If not done during the shifts, the strip masking
 3772 procedure needs to be carefully done by the person in charge of data analysis on the scans that were
 3773 selected to produce the final results.

```

float GetTH1Mean(TH1* H){
    int nBins = H->GetNbinsX();
    int nActive = nBins;
    float mean = 0.;

    for(int b = 1; b <= nBins; b++){
        float value = H->GetBinContent(b);
        mean += value;
        if(value == 0.) nActive--;
    }

    if(nActive != 0) mean /= (float)nActive;
    else mean = 0.;

    return mean;
}

```

Source Code B.18: The function `GetTH1Mean()` is used to return the mean along the y-axis of `TH1` histograms containing rate information. In order to take into account masked strips whose rate is set to 0, the function looks for masked channels and decrement the number of active channels for each null value found.

3776 B.6.4.4 Output CSV files filling

3777 All the histograms have been filled. Parameters will then be extracted from them to compute the
 3778 final results that will later be used to produce plots. Once the results have been computed, the very
 3779 last step of the offline macro is to write these values into the corresponding CSV outputs. Aside of
 3780 the file `Offline-Corrupted.csv`, 2 CSV files are being written by the macro `OfflineAnalysis()`,
 3781 `Offline-Rates.csv` and `Offline-L0-EffCl.csv` that respectively contain information about noise
 3782 or gamma rates, cluster size and multiplicity, and about level 0 reconstruction of the detector
 3783 efficiency, muon cluster size and multiplicity. Details on the computation and file writing are
 3784 respectively given in Sources Codes B.19 and B.20.

3785 **Noise/gamma background variables** are computed and written in the output file for each
 3786 detector partitions. A detector average of the hit and cluster rate is also provided, as shown through
 3787 Sources Code B.19. The variables that are written for each partition are:

- 3788 • The mean partition hit rate per unit area, `MeanPartRate`, that is extracted from the histogram
 3789 `StripNoiseProfile_H` as the mean value along the y-axis, as described in section B.6.4.3.
 3790 No error is recorded for the hit rate as this is considered a single measurement. No statistical
 3791 error can be associated to it and the systematics are unknown.
- 3792 • The mean cluster size, `cSizePart`, is extracted from the histogram `NoiseCSize_H` and it's
 3793 statistical error, `cSizePartErr`, is taken to be 2σ of the total distribution.
- 3794 • The mean cluster multiplicity per trigger, `cMultPart`, is extracted from the histogram
 3795 `NoiseCMult_H` and it's statistical error, `cMultPartErr`, is taken to be 2σ of the total
 3796 distribution. It is important to point to the fact that this variable gives an information that is
 3797 dependent on the buffer window width used for each trigger for the calculation.
- 3798 • The mean cluster rate per unit area, `ClustPartRate`, is defined as the mean hit rate

3799 normalised to the mean cluster size and it's statistical error, `ClustPartRateErr`, is then
 3800 obtained using the relative statistical error on the mean cluster size.

```

for (UInt tr = 0; tr < GIFInfra->GetNTrolleys(); tr++) {
    UInt T = GIFInfra->GetTrolleyID(tr);

    for (UInt sl = 0; sl < GIFInfra->GetNSlots(tr); sl++) {
        UInt S = GIFInfra->GetSlotID(tr,sl) - 1;

        float MeanNoiseRate = 0.;
        float ClusterRate = 0.;
        float ClusterSDev = 0.;

        for (UInt p = 0; p < GIFInfra->GetNPartitions(tr,sl); p++) {
            float MeanPartRate = GetTH1Mean(StripNoiseProfile_H.rpc[T][S][p]);
            float cSizePart = NoiseCSize_H.rpc[T][S][p]->GetMean();
            float cSizePartErr = (NoiseCSize_H.rpc[T][S][p]->GetEntries()==0)
                ? 0.
                : 2*NoiseCSize_H.rpc[T][S][p]->GetStdDev() /
                    sqrt(NoiseCSize_H.rpc[T][S][p]->GetEntries());
            float cMultPart = NoiseCMult_H.rpc[T][S][p]->GetMean();
            float cMultPartErr = (NoiseCMult_H.rpc[T][S][p]->GetEntries()==0)
                ? 0.
                : 2*NoiseCMult_H.rpc[T][S][p]->GetStdDev() /
                    sqrt(NoiseCMult_H.rpc[T][S][p]->GetEntries());
            float ClustPartRate = (cSizePart==0) ? 0.
                : MeanPartRate/cSizePart;
            float ClustPartRateErr = (cSizePart==0) ? 0.
                : ClustPartRate * cSizePartErr/cSizePart;

            outputRateCSV << MeanPartRate << '\t'
                << cSizePart << '\t' << cSizePartErr << '\t'
                << cMultPart << '\t' << cMultPartErr << '\t'
                << ClustPartRate << '\t' << ClustPartRateErr << '\t';

            RPCarea += stripArea * nStripsPart;
            MeanNoiseRate += MeanPartRate * stripArea * nStripsPart;
            ClusterRate += ClustPartRate * stripArea * nStripsPart;
            ClusterSDev += (cSizePart==0)
                ? 0.
                : ClusterRate*cSizePartErr/cSizePart;
        }

        MeanNoiseRate /= RPCarea;
        ClusterRate /= RPCarea;
        ClusterSDev /= RPCarea;

        outputRateCSV << MeanNoiseRate << '\t'
            << ClusterRate << '\t' << ClusterSDev << '\t';
    }
}

```

Source Code B.19: Description of rate result calculation and writing into the CSV output `Offline-Rate.csv`. Are saved into the file for each detector, the mean partition rate, cluster size and cluster mutiplicity, along with their errors, for each partition and as well as a detector average.

3803 **Muon performance variables** are computed and written in the output file for each detector
 3804 partitions as shown through Sources Code B.20. The variables that are written for each partition

3805 are:

- 3806 • The muon efficiency, `eff`, extracted from the histogram `Efficiency0_H`. It is reminded that
 3807 this offline tool doesn't include any tracking algorithm to identify muons from the beam and
 3808 only relies on the hits arriving in the time window corresponding to the beam time. The
 3809 content of the efficiency histogram is thus biased by the noise/gamma background
 3810 contribution into this window and is thus corrected by estimating the muon data content in
 3811 the peak region knowing the noise/gamma content in the rate calculation region. Both time
 3812 windows being different, the choice was made to normalise the noise/gamma background
 3813 calculation window to its equivalent beam window in order to have comparable values using
 3814 the variable `windowRatio`. Finally, to estimate the data ratio in the peak region, the variable
 3815 `DataRatio` is defined as the ratio in between the estimated mean cluster multiplicity of the
 3816 muons in the peak region, `MuonCM`, and of the total mean cluster multiplicity in the peak
 3817 region, `PeakCM`. `MuonCM` is itself defined as the difference in between the total mean cluster
 3818 multiplicity in the peak region and the normalised mean noise/gamma cluster multiplicity
 3819 calculated outside of the peak region. The statistical error related to the efficiency, `eff_err`,
 3820 is computed using a binomial distribution, as the efficiency measure the probability of
 3821 "success" and "failure" to detect muons.

- 3822 • The mean muon cluster size, `MuonCS`, is calculated using the total mean cluster size and
 3823 multiplicity in the peak region, respectively extracted from histograms `MuonCSize_H` and
 3824 `MuonCMult_H`, the noise/gamma background mean cluster size and normalised multiplicity,
 3825 extracted from `NoiseCSize_H` and `NoiseCMult_H`, and of the estimated muon cluster
 3826 multiplicity `MuonCM` previously explicated. The associated statistical error, `MuonCM_err`, is
 3827 calculated using the propagation of errors of the mentioned variables.

- 3828 • The mean muon cluster multiplicity in the peak region, `MuonCM`, explicated above whose
 3829 statistical error, `MuonCM_err`, is the sum of statistical error associated to the total mean cluster
 3830 multiplicity in the peak reagion, `PeakCM_err`, and of the mean noise/gamma cluster size,
 3831 `NoiseCM_err`.

- 3832 In addition to these 2 CSV files, the histograms are saved in ROOT file
 3833 `Scan00XXXX_HVY_Offline.root` as explained in section B.2.1.1.

```

for (UInt tr = 0; tr < GIFIInfra->GetNTrolleys(); tr++) {
    UInt T = GIFIInfra->GetTrolleyID(tr);
    for (UInt sl = 0; sl < GIFIInfra->GetNSlots(tr); sl++) {
        UInt S = GIFIInfra->GetSlotID(tr,sl) - 1;
        for (UInt p = 0; p < GIFIInfra->GetNPartitions(tr,sl); p++) {
            float noiseWindow =
                BMTDCWINDOW - TIMEREJECT - 2*PeakWidth.rpc[T][S][p];
            float peakWindow = 2*PeakWidth.rpc[T][S][p];
            float windowRatio = peakWindow/noiseWindow;

            float PeakCM = MuonCMult_H.rpc[T][S][p]->GetMean();
            float PeakCS = MuonCSize_H.rpc[T][S][p]->GetMean();
            float NoiseCM = NoiseCMult_H.rpc[T][S][p]->GetMean() *windowRatio;
            float NoiseCS = NoiseCSize_H.rpc[T][S][p]->GetMean();
            float MuonCM = (PeakCM<NoiseCM) ? 0. : PeakCM-NoiseCM;
            float MuonCS = (MuonCM==0 || PeakCM*PeakCS<NoiseCM*NoiseCS)
                ? 0.
                : (PeakCM*PeakCS-NoiseCM*NoiseCS) / MuonCM;
            float PeakCM_err = (MuonCMult_H.rpc[T][S][p]->GetEntries()==0.)
                ? 0.
                : 2*MuonCMult_H.rpc[T][S][p]->GetStdDev() /
                    sqrt(MuonCMult_H.rpc[T][S][p]->GetEntries());
            float PeakCS_err = (MuonCSize_H.rpc[T][S][p]->GetEntries()==0.)
                ? 0.
                : 2*MuonCSize_H.rpc[T][S][p]->GetStdDev() /
                    sqrt(MuonCSize_H.rpc[T][S][p]->GetEntries());
            float NoiseCM_err = (NoiseCMult_H.rpc[T][S][p]->GetEntries()==0.)
                ? 0.
                : windowRatio*2*NoiseCMult_H.rpc[T][S][p]->GetStdDev() /
                    sqrt(NoiseCMult_H.rpc[T][S][p]->GetEntries());
            float NoiseCS_err = (NoiseCSize_H.rpc[T][S][p]->GetEntries()==0.)
                ? 0.
                : 2*NoiseCSize_H.rpc[T][S][p]->GetStdDev() /
                    sqrt(NoiseCSize_H.rpc[T][S][p]->GetEntries());
            float MuonCM_err = (MuonCM==0) ? 0. : PeakCM_err+NoiseCM_err;
            float MuonCS_err = (MuonCS==0 || MuonCM==0) ? 0.
                : (PeakCS*PeakCM_err + PeakCM*PeakCS_err +
                    NoiseCS*NoiseCM_err + NoiseCM*NoiseCS_err +
                    MuonCS*MuonCM_err) / MuonCM;

            float DataRatio = MuonCM/PeakCM;
            float DataRatio_err = (MuonCM==0) ? 0.
                : DataRatio*(MuonCM_err/MuonCM + PeakCM_err/PeakCM);
            float eff = DataRatio*Efficiency0_H.rpc[T][S][p]->GetMean();
            float eff_err = DataRatio*2*Efficiency0_H.rpc[T][S][p]->GetStdDev() /
                sqrt(Efficiency0_H.rpc[T][S][p]->GetEntries()) +
                Efficiency0_H.rpc[T][S][p]->GetMean()*DataRatio_err;

            outputEffCSV << eff << '\t' << eff_err << '\t'
                << MuonCS << '\t' << MuonCS_err << '\t'
                << MuonCM << '\t' << MuonCM_err << '\t';
        }
    }
}

```

3834

Source Code B.20: Description of efficiency result calculation and writing into the CSV output Offline-L0-EffCl.csv. Are saved into the file for each detector, the efficiency, corrected taking into account the background in the peak window of the time profile, muon cluster size and muon cluster multiplicity, along with their errors, for each partition and as well as a detector average.

3835

3836 B.7 Current data Analysis

3837 Detectors under test at GIF++ are connected both to a CAEN HV power supply and to a CAEN
3838 ADC that reads the currents inside of the RPC gaps bypassing the supply cable. During data taking,
3839 the webDCS records into a ROOT file called `Scan00XXXX_HVY_CAEN.root` histograms with the
3840 monitored parameters of both CAEN devices. Are recorded for each RPC channels (in most cases,
3841 a channel corresponds to an RPC gap):

- 3842 • the effective voltage, HV_{eff} , set by the webDCS using the PT correction on the CAEN
3843 power supply,
- 3844 • the applied voltage, HV_{app} , monitored by the CAEN power supply, and the statistical error
3845 related to the variations of this value through time to follow the variation of the
3846 environmental parameters defined as the RMS of the histogram divided by the square root of
3847 the number of recorded points,
- 3848 • the monitored current, I_{mon} , monitored by the CAEN power supply, and the statistical error
3849 related to the variations of this value through time to follow the variation of the
3850 environmental parameters defined as the RMS of the histogram divided by the square root of
3851 the number of recorded points,
- 3852 • the corresponding current density, J_{mon} , defined as the monitored current per unit area,
3853 $J_{mon} = I_{mon}/A$, where A is the active area of the corresponding gap,
- 3854 • the ADC current, I_{ADC} , recorded through the CAEN ADC module that monitors the dark
3855 current in the gap itself. First of all, the resolution of such a module is better than that of
3856 CAEN power supplies and moreover, the current is not read-out through the HV supply line
3857 but directly at the chamber level giving the real current inside of the detector. The statistical
3858 error is defined as the RMS of the histogram distribution divided by the square root of the
3859 number of recorded points.

3860 Once extracted through a loop over the element of GIF++ infrastructure via the C++ macro
3861 `GetCurrent()`, these parameters, organised in 9 columns per detector HV supply line, are written in
3862 the output CSV file `Offline-Current.csv`. The macro can be found in the file `Current.cc`.

References

- [1] T. Massam et al. “Experimental observation of antideuteron production”. In: *Il Nuovo Cimento A* 63 (1965), pp. 10–14.
- [2] UA1 Collaboration. “Experimental observation of isolated large transverse energy electrons with associated missing energy at $s = 540 \text{ GeV}$ ”. In: *Physics Letters B* 122 (1983), pp. 103–116.
- [3] UA2 Collaboration. “Observation of single isolated electrons of high transverse momentum in events with missing transverse energy at the CERN pp collider”. In: *Physics Letters B* 122 (1983), pp. 476–485.
- [4] UA1 Collaboration. “Experimental observation of lepton pairs of invariant mass around $95 \text{ GeV}/c^2$ at the CERN SPS collider”. In: *Physics Letters B* 126 (1983), pp. 398–410.
- [5] UA2 Collaboration. “Evidence for $Z_0 \rightarrow e^+e^-$ at the CERN pp collider”. In: *Physics Letters B* 129 (1983), pp. 130–140.
- [6] ALEPH Collaboration. “Determination of the number of light neutrino species”. In: *Physics Letters B* 231 (1989), pp. 519–529.
- [7] CERN, ed. (1985).
- [8] CERN, ed. (1986).
- [9] CERN, ed. (1994).
- [10] CERN, ed. (1998).
- [11] CERN, ed. (1999).
- [12] CERN. Geneva. LHC Experiments Committee. *Letter of Intent for A Large Ion Collider Experiment [ALICE]*, note = CERN-LHCC-93-016. Tech. rep. ALICE Collaboration, 1993.
- [13] CERN. Geneva. LHC Experiments Committee. *ATLAS : technical proposal for a general-purpose pp experiment at the Large Hadron Collider at CERN*, note = CERN-LHCC-94-43. Tech. rep. ATLAS Collaboration, 1994.
- [14] CERN. Geneva. LHC Experiments Committee. *CMS : letter of intent by the CMS Collaboration for a general purpose detector at LHC*, note = CERN-LHCC-92-003. Tech. rep. CMS Collaboration, 1992.
- [15] CERN. Geneva. LHC Experiments Committee. *LHCb : letter of intent*. Tech. rep. CERN-LHCC-95-5. LHCb Collaboration, 1995.
- [16] L. Evans and P. Bryant. “LHC Machine”. In: *JINST* 3 (2008). S08001.
- [17] CMS Collaboration ATLAS Collaboration. “Combined Measurement of the Higgs Boson Mass in pp Collisions at $\sqrt{s} = 7$ and 8 TeV with the ATLAS and CMS Experiments”. In: *Physical Review Letters* 114 (2015). 191803.
- [18] LHCb Collaboration. “Observation of $J/\psi p$ Resonances Consistent with Pentaquark States in $\Lambda_b^0 \rightarrow J/\psi K^- p$ Decays”. In: *Physical Review Letters* 115 (2015). 072001.

- 3899 [19] LHCb Collaboration. “Observation of $J/\psi\phi$ Structures Consistent with Exotic States from
3900 Amplitude Analysis of $B^+ \rightarrow J/\psi\phi K^+$ Decays”. In: *Physical Review Letters* 118 (2017).
3901 022003.
- 3902 [20] CERN. Geneva. *High-Luminosity Large Hadron Collider (HL-LHC) Technical Design*
3903 *Report V. 0.1*. Tech. rep. CERN-2017-007-M. 2017.
- 3904 [21] CERN. Geneva. LHC Experiments Committee. *The CMS muon project : Technical Design*
3905 *Report*. Tech. rep. CERN-LHCC-97-032. CMS Collaboration, 1997.
- 3906 [22] CERN. Geneva. LHC Experiments Committee. *CMS, the Compact Muon Solenoid : technical proposal*. Tech. rep. CERN-2015-005. 2015.
- 3908 [23] CERN. Geneva. LHC Experiments Committee. *The Phase-2 Upgrade of the CMS Muon*
3909 *Detectors*. Tech. rep. CERN-LHCC-2017-012, CMS-TDR-016. CMS Collaboration, 2017.
- 3910 [24] CERN. Geneva. LHC Experiments Committee. *High-Luminosity Large Hadron Collider*
3911 *(HL-LHC) Preliminary Design Report*. Tech. rep. CERN-LHCC-94-38. CMS Collaboration,
3912 1994.
- 3913 [25] CERN. Geneva. LHC Experiments Committee. *The Phase-2 Upgrade of the CMS Level-1*
3914 *Trigger - Interim Report to the LHCC*. Tech. rep. CERN-LHCC-2017-013, CMS-TDR-017.
3915 CMS Collaboration, 2017.
- 3916 [26] CERN. Geneva. LHC Experiments Committee. *Technical Proposal for the Phase-II*
3917 *Upgrade of the CMS Detector*. Tech. rep. CERN-LHCC-2015-010, CMS-TDR-15-02. CMS
3918 Collaboration, 2015.
- 3919 [27] A. Gelmi. *CMS iRPC at HL-LHC: background study*. 2018. URL: https://indico.cern.ch/event/732794/contributions/3021836/attachments/1657792/2654574/iRPC_bkg_study_Upgrade29_05_18.pdf.
- 3922 [28] F.Sauli. “GEM: A new concept for electron amplification in gas detectors”. In: *Nucl. Instr.*
3923 *Meth. Phys. Res.* 386 (1997), pp. 531–534.
- 3924 [29] CERN. Geneva. LHC Experiments Committee. *CMS Technical Design Report for the Muon*
3925 *Endcap GEM Upgrade*. Tech. rep. CERN-LHCC-2015-012, CMS-TDR-013. CMS
3926 Collaboration, 2015.
- 3927 [30] The CMS collaboration. “The performance of the CMS muon detector in proton-proton
3928 collisions at $\sqrt{s} = 7$ TeV at the LHC”. In: *JINST* 8 (2013). P11002.
- 3929 [31] P.Bortignon. “Design and performance of the upgrade of the CMS L1 muon trigger”. In:
3930 *Nucl. Instr. Meth. Phys. Res.* 824 (2016), pp. 256–257.
- 3931 [32] The European Parliament and the Council of the European Union. “Regulation (EU) No
3932 517/2014 of 16 April 2014 on fluorinated greenhouse gases and repealing Regulation (EC)
3933 No 842/2006”. In: *Official Journal of the European Union* 150 (2014), pp. 195–230.
- 3934 [33] R. Santonico and R. Cardarelli. “Development of resistive plate counters”. In: *Nucl. Instr.*
3935 *Meth. Phys. Res.* 187 (1981), pp. 377–380.
- 3936 [34] Yu.N. Pestov and G.V. Fedotovich. *A picosecond time-of-flight spectrometer for the*
3937 *VEPP-2M based on local-discharge spark counter*. Tech. rep. SLAC-TRANS-0184. SLAC,
3938 1978.
- 3939 [35] W.W. Ash, ed. *Spark Counter With A Localized Discharge*. Vol. SLAC-R-250. 1982,
3940 pp. 127–131.
- 3941 [36] I. Crotty et al. “The non-spark mode and high rate operation of resistive parallel plate
3942 chambers”. In: *NIMA* 337 (1993), pp. 370–381.

BIBLIOGRAPHY

- [3943] [37] I. Crotty et al. “Further studies of avalanche mode operation of resistive parallel plate
3944 chambers”. In: *NIMA* 346 (1994), pp. 107–113.
- [3945] [38] R. Cardarelli et al. “Avalanche and streamer mode operation of resistive plate chambers”.
3946 In: *NIMA* 382 (1996), pp. 470–474.
- [3947] [39] R. Cardarelli et al. “Performance of a resistive plate chamber operating with pure CF_3Br ”.
3948 In: *NIMA* 333 (1993), pp. 399–403.
- [3949] [40] M. Abbrescia et al. “Performance of a Resistive Plate Chamber operated in avalanche mode
3950 under ^{137}Cs irradiation”. In: *NIMA* 392 (1997), pp. 155–160.
- [3951] [41] M. Abbrescia et al. “Properties of C2H2F4-based gas mixture for avalanche mode operation
3952 of resistive plate chambers”. In: *NIMA* 398 (1997), pp. 173–179.
- [3953] [42] P. Camarri et al. “Streamer suppression with SF6 in RPCs operated in avalanche mode”. In:
3954 *NIMA* 414 (1998), pp. 317–324.
- [3955] [43] E. Cerron Zeballos et al. “Effect of adding SF6 to the gas mixture in a multigap resistive
3956 plate chamber”. In: *NIMA* 419 (1998), pp. 475–478.
- [3957] [44] E. Cerron Zeballos et al. “A new type of resistive plate chamber: The multigap RPC”. In:
3958 *NIMA* 374 (1996), pp. 132–135.
- [3959] [45] M.C.S. Williams. “The development of the multigap resistive plate chamber”. In: *Nucl.
3960 Phys. B* 61 (1998), pp. 250–257.
- [3961] [46] H. Czyrkowski et al. “New developments on resistive plate chambers for high rate
3962 operation”. In: *NIMA* 419 (1998), pp. 490–496.
- [3963] [47] CERN. Geneva. LHC Experiments Committee. *ATLAS muon spectrometer: Technical
3964 design report*. Tech. rep. CERN-LHCC-97-22. ATLAS Collaboration, 1997.
- [3965] [48] CERN. Geneva. LHC Experiments Committee. *ALICE Time-Of-Flight system (TOF) :
3966 Technical Design Report*. Tech. rep. CERN-LHCC-2000-012. ALICE Collaboration, 2000.
- [3967] [49] The CALICE collaboration. “First results of the CALICE SDHCAL technological
3968 prototype”. In: *JINST* 11 (2016).
- [3969] [50] PoS, ed. *Density Imaging of Volcanoes with Atmospheric Muons using GRPCs*.
3970 International Europhysics Conference on High Energy Physics - HEP 2011. 2011.
- [3971] [51] C. Lippmann. “Detector Physics of Resistive Plate Chambers”. PhD thesis. Johann
3972 Wolfgang Goethe-Universität, 2003.
- [3973] [52] W. Riegler. “Induced signals in resistive plate chambers”. In: *NIMA* 491 (2002),
3974 pp. 258–271.
- [3975] [53] M. Abbrescia et al. “Effect of the linseed oil surface treatment on the performance of
3976 resistive plate chambers”. In: *NIMA* 394 (1997), pp. 13–20.
- [3977] [54] G.Battistoni et al. “Sensitivity of streamer mode to single ionization electrons”. In: *NIMA*
3978 235 (1985), pp. 91–97.
- [3979] [55] M. Abbrescia et al. “Cosmic ray tests of double-gap resistive plate chambers for the CMS
3980 experiment”. In: *NIMA* 550 (2005), pp. 116–126.
- [3981] [56] JINST, ed. *Performance of the Resistive Plate Chambers in the CMS experiment*. The 9th
3982 International Conference on Positioin Sensitive Detectors. 2012.
- [3983] [57] PoS, ed. *The CMS RPC detector performance during Run-II data taking*. The European
3984 Physical Society Conference on High Energy Physics (EPS-HEP2017). 2018.

- 3985 [58] Honeywell International Inc. *Solstice(R) ze Refrigerant (HFO-1234ze): The Environmental*
 3986 *Alternative to Traditional Refrigerants*. Tech. rep. FPR-003/2015-01. 2015.
- 3987 [59] E. Cerron Zeballos et al. “A comparison of the wide gap and narrow gap resistive plate
 3988 chamber”. In: *NIMA* 373 (1996), pp. 35–42.
- 3989 [60] ALICE Collaboration. “A study of the multigap RPC at the gamma irradiation facility at
 3990 CERN”. In: *NIMA* 490 (2002), pp. 58–70.
- 3991 [61] B. Bonner et al. “A multigap resistive plate chamber prototype for time-of-flight for the
 3992 STAR experiment at RHIC”. In: *NIMA* 478 (2002), pp. 176–179.
- 3993 [62] S. Yang et al. “Test of high time resolution MRPC with different readout modes for the
 3994 BESIII upgrade”. In: *NIMA* 763 (2014), pp. 190–196.
- 3995 [63] A. Akindinov et al. “RPC with low-resistive phosphate glass electrodes as a candidate for
 3996 the CBM TOF”. In: *NIMA* 572 (2007), pp. 676–681.
- 3997 [64] JINST, ed. *Development of the MRPC for the TOF system of the MultiPurpose Detector*.
 3998 RPC2016: XII Workshop on Resistive Plate Chambers and Related Detectors. 2016.
- 3999 [65] M.C.S. Williams. “Particle identification using time of flight”. In: *Journal of Physics G* 39
 4000 (2012).
- 4001 [66] A. Alici et al. “Aging and rate effects of the Multigap RPC studied at the Gamma Irradiation
 4002 Facility at CERN”. In: *NIMA* 579 (2007), pp. 979–988.
- 4003 [67] M. Abbrescia et al. “The simulation of resistive plate chambers in avalanche mode: charge
 4004 spectra and efficiency”. In: *NIMA* 431 (1999), pp. 413–427.
- 4005 [68] C. Patrignani et al. (Particle Data Group). “Review of Particle Physics”. In: *Chin. Phys. C*
 4006 C40 (2016), p. 100001.
- 4007 [69] JINST, ed. *Description and simulation of physics of Resistive Plate Chambers*. RPC2016:
 4008 XII Workshop on Resistive Plate Chambers and Related Detectors. 2016.
- 4009 [70] V. Français. “Description and simulation of the physics of Resistive Plate Chambers”.
 4010 PhD thesis. LPC - Laboratoire de Physique Corpusculaire - Clermont-Ferrand, 2017.
- 4011 [71] H. Bethe. “Zur Theorie des Durchgangs schneller Korpuskularstrahlen durch Materie”. In:
 4012 *Annalen der Physik* 397 (1930), pp. 325–400.
- 4013 [72] International Commission on Radiation Units and Measurements. *Stopping Powers for*
 4014 *Electrons and Positions*. Tech. rep. Report 37. 1984.
- 4015 [73] International Commission on Radiation Units and Measurements. *Stopping Power and*
 4016 *Ranges for Protons and Alpha Particles*. Tech. rep. Report 49. 1994.
- 4017 [74] H. Bichsel. “A method to improve tracking and particle identification in TPCs and silicon
 4018 detectors”. In: *NIMA* 562 (2006), pp. 154–197.
- 4019 [75] W. W. M. Allison and J. H. Cobb. “Relativistic charged particle identification by energy
 4020 loss”. In: *Annual Review of Nuclear and Particle Science* 30 (1980), 253–298.
- 4021 [76] International Commission on Radiation Units and Measurements. *Average energy to*
 4022 *produce an ion pair*. Tech. rep. Report 31. 1994.
- 4023 [77] I.B. Smirnov. “Modeling of ionization produced by fast charged particles in gases”. In:
 4024 *NIMA* 554 (2005), pp. 474–493.
- 4025 [78] <https://doi.org/10.1088/1742-6596/587/1/012035>.
- 4026 [79] W. Riegler et al. “Detector physics and simulation of resistive plate chambers”. In: *NIMA*
 4027 500 (2003), pp. 144–162.

BIBLIOGRAPHY

- 4028 [80] I.B. Smirnov. *HEED++ simulation program*. 2010. URL:
4029 `\href{http://ismirnov.web.cern.ch/ismirnov/heed}{http://ismirnov.web.cern.ch/ismirnov/heed}`.
4030
- 4031 [81] S.F. Biagi. “Monte Carlo simulation of electron drift and diffusion in counting gases under
4032 the influence of electric and magnetic fields”. In: *NIMA* 421 (1999), pp. 234–240.
4033 [82] W. H. Furry. “On Fluctuation Phenomena in the Passage of High Energy Electrons through
4034 Lead”. In: *Phys. Rev.* 52 (1937), pp. 569–581.
4035 [83] H. Genz. “Single electron detection in proportional gas counters”. In: *Nucl. Instr. and Meth.*
4036 112 (1973), pp. 83–90.
4037 [84] M. Abbrescia et al. “Resistive plate chambers performances at cosmic rays fluxes”. In:
4038 *NIMA* 359 (1995), pp. 603–609.
4039 [85] M. Abbrescia et al. “Resistive plate chambers performances at low pressure”. In: *NIMA* 394
4040 (1997), pp. 341–348.
4041 [86] M. Abbrescia. “Operation, performance and upgrade of the CMS Resistive Plate Chamber
4042 system at LHC”. In: *NIMA* 732 (2013), pp. 195–198.
4043 [87] F. Thyssen. “Commissioning, Operation and Performance of the CMS Resistive Plate
4044 Chamber System”. PhD thesis. Universiteit Gent, 2014.
4045 [88] M. Bianco. “ATLAS RPC certification and commissioning with cosmic rays”. PhD thesis.
4046 Università del Salento, 2007.
4047 [89] M. Bianco. “ATLAS RPC certification with cosmic rays”. In: *NIMA* 602 (2009),
4048 pp. 700–704.
4049 [90] M. Abbrescia et al. “Study of long-term performance of CMS RPC under irradiation at the
4050 CERN GIF”. In: *NIMA* 533 (2004), pp. 102–106.
4051 [91] H.C. Kim et al. “Quantitative aging study with intense irradiation tests for the CMS forward
4052 RPCs”. In: *NIMA* 602 (2009), pp. 771–774.
4053 [92] S. Agosteo et al. “A facility for the test of large-area muon chambers at high rates”. In:
4054 *NIMA* 452 (2000), pp. 94–104.
4055 [93] PoS, ed. *CERN GIF ++ : A new irradiation facility to test large-area particle detectors for*
4056 *the high-luminosity LHC program*. Vol. TIPP2014. 2014, pp. 102–109.
4057 [94] A. Fagot. *GIF++ DAQ v4.0*. 2017. URL: https://github.com/afagot/GIF_DAQ.
4058 [95] CAEN. *Mod. V1190-VX1190 A/B, 128/64 Ch Multihit TDC*. 14th ed. 2016.
4059 [96] CAEN. *Mod. V1718 VME USB Bridge*. 9th ed. 2009.
4060 [97] W-Ie-Ne-R. *VME 6021-23 VXI*. 5th ed. 2016.
4061 [98] Wikipedia. *INI file*. 2017. URL: https://en.wikipedia.org/wiki/INI_file.
4062 [99] S. Carrillo A. Fagot. *GIF++ Offline Analysis v6*. 2017. URL:
4063 https://github.com/afagot/GIF_OfflineAnalysis.